CFD analysis and optimisation of unidirectional radial turbine geometry for application with oscillating water column wave energy converters

by

Nazanin Ansarifard

National Centre of Maritime Engineering and Hydrodynamics
Australian Maritime College

Submitted in fulfilment of the requirements for the degree of Doctor of Philosophy

University of Tasmania, May 2019

DECLARATIONS

AUTHORITY OF ACCESS

This thesis may be available for loan and limited copying and communication in accordance with the Copyright Act 1968.

STATEMENT OF ORIGINALITY

This thesis contains no material that has been accepted for a degree or diploma by the university or other institution. To the best of my knowledge and belief, this thesis contains no material previously published or written by another person, except where due acknowledgement is made in the text.

Signed:

Nazanin Ansarifard

Date: ___06/05/2019_____

STATEMENT OF CO-AUTHORSHIP

Chapters 2-5 of this thesis have been prepared as scientific papers. In all cases 3D modelling, numerical simulations, data analysis and manuscript preparation were the primary responsibility of the candidate. However, the work was performed in collaboration with supervisors and co-authors. Details of contributions are outlined below:

Paper 1, A radial inflow air turbine design for a vented oscillating water column:

Located in chapter 2

Candidate was the primary author and with S.S Kianejad, provided technical support in performing the simulations in Star-CCM+. Alan Fleming and Shuhong Chai contributed to manuscript preparation and drafted significant parts of paper.

[Candidate 80%, Kianejad 6%, Fleming 10%, Chai 4%]

Paper 2, Optimisation study on the downstream section of a radial inflow turbine (Conference paper):

Located in chapter 3

Candidate was the primary author. Alan Fleming, Alan Henderson and Shuhong Chai contributed to the conception and design of the research paper.

[Candidate 85%, Fleming 6%, Henderson 6%, Chai 3%]

Paper 3*, Radial turbine geometry optimisation for a vented oscillating water column:*

Located in chapter 3

Candidate was the primary author on this paper. S.S Kianejad and Alan Henderson provided technical support in switching to ANSYS CFX and performing the design optimisation studies. Alan Fleming, Alan Henderson and Shuhong Chai contributed to the manuscript preparation of this paper.

[Candidate 79%, Kianejad 6%, Fleming 6%, Henderson 6%, Chai 3%]

Paper 4*, Design optimisation of an outflow radial turbine for a twin turbine OWC wave energy converter:*

Located in chapter 4

Candidate was the primary author and with Alan Fleming contributed to the planning execution and preparation of the research project and subsequent paper. Alan Fleming, Alan Henderson, S.S Kianejad and Shuhong Chai contributed to the manuscript preparation of this paper.

[Candidate 82%, Fleming 6%, Henderson 5%, Kianejad 4%, Chai 3%]

Paper 5*, Comparison of inflow and outflow radial air turbines in vented and bidirectional OWC systems:*

Located in chapter 5

Candidate was the primary author. Alan Fleming contributed to the analysis and interpretation of the research data and contributed to the interpretation of the work by critically revising the paper. Alan Fleming, Alan Henderson, S.S Kianejad and Shuhong Chai contributed to the manuscript preparation of this paper.

[Candidate 82%, Fleming 7%, Henderson 4%, Kianejad 4%, Chai 3%]

We the undersigned agree with the above stated "proportion of work undertaken" for each of the above published (or submitted) peer-reviewed manuscripts contributing to this thesis:

Signed:

Dr Alan Fleming

Supervisor

National Centre of Maritime

Engineering and Hydrodynamics

University of Tasmania

Date: _____10/05/2019_____

Signed:

Prof. Shuhong Chai

Principal

Australian Maritime College

University of Tasmania

Date: _____10/05/2019_____

ACKNOWLEDGEMENT

Firstly, I thank supervisory team (Alan Fleming, Alan Henderson and Shuhong Chai) for their knowledge, support and patience. Their worthwhile advice enlightened the journey of PhD in my mind and helped me to gradually fade the unknowns and emerge spark of the knowledge.

I appreciate the guidance of Alan Fleming for bringing me back on course when I ventured too far off topic. He built a connection between my research topic and industry concerns and provided advice regarding future opportunities, recent ocean renewable energy projects, relevant networks and conferences.

I thank Alan Henderson for his technical advice on switching to ANSYS programme and on performing the optimisation studies in that platform. I also thank Shuhong Chai for her worthwhile advice regarding the early career opportunities during PhD and after graduation (students' supervision and teaching).

I thank Dr Hung Nguyen, who was initially my primary supervisor, he provided me the direction necessary to win the initial scholarship in 2015 and advised me to work in a multidisciplinary area. I thank him for being the one who trusted me in this journey.

I thank S.S Kianejad for his support in discussing and solving the problems raised during the 3D modelling or numerical simulations.

I thank Jarrah Orphin for providing experimental data for the analysis performed in chapter 5 of this thesis, and Wave Swell Energy (WES) who owned the vented OWC prototype.

Finally, I thank my family for their on-going support in every situation and decision I have made in my life. My Parents who have done all they could for my happiness without expecting anything in return. My spouse, Sadra, who has always been inspiring and supporting during the hard moments and has been a true friend to me.

ABSTRACT

An oscillating-water-column (OWC) is a popular device for harnessing the power of ocean waves. A key component in the system is the air turbine, which operates as the power take-off unit (PTO) converting pneumatic power to mechanical. The turbine is probably the most complicated geometry in the system and is mainly designed in either an axial or radial configuration.

The efficiency of a conventional radial impulse turbine (bidirectional version) rarely reaches more than 40%, which makes it a less efficient choice than axial turbines. However, the radial configuration has some advantageous features compared with the axial turbine, such as lower bearing loads and easier manufacturing. Current research on unidirectional radial impulse turbines shows a higher resistance to backflow and negative torque than the axial turbines, which is particularly useful in a twin-turbine configuration of the OWC system. The work described in this thesis is concerned with efficiency improvement of unidirectional radial air turbines using computational engineering approaches.

In this research, optimisation techniques were used in conjunction with Computational-Fluid-Dynamics (CFD) simulations to maximize efficiency of a unidirectional radial turbine for a vented OWC (where air flows through the turbine in only one direction). A parametric turbine geometry was created by varying geometrical features to control the shape of upstream guide vanes, rotor blades, downstream guide vanes and the duct section. This method led to flexibility in design and adjustment of rotating and stationary elements. The optimised design obtained significantly improved torque production for a single flow direction due to its highly-asymmetric rotor blades and well-adjusted inlet guide vanes. A parameter sensitivity analysis was performed using the response surface method and the optimum geometry of the turbine was obtained from a large design space (containing over 140 design cases for the inflow turbine and around 80 design cases for the outflow turbine).

This research provides a detailed analysis on the impact of each parameter on the turbine performance and is conducted in four steps. First, identifying the design drawbacks and sources of energy loss in the initial geometry of a unidirectional radial turbine and suggesting design modifications. Second, studying the turbine performance in a vented OWC and finding the optimum design of the turbine in the centripetal configuration (inflow mode). Third, studying the turbine performance in the vented OWC and optimising the turbine design for maximized efficiency in centrifugal configuration (outflow mode). Finally, comparing the global efficiency of the optimised inflow and outflow radial turbines considering their application with the vented OWC and twin-turbine OWC configurations.

This study contributed to a significant increase in energy capture of unidirectional radial impulse turbines compared to their bidirectional version, where the optimised centripetal and centrifugal turbine configurations of this research obtain peak steady-state efficiencies of 80% and 74% respectively (almost double the global efficiency of a conventional bidirectional radial turbine).

The integration of the turbine-chamber under an oscillating flow regime was studied by considering the operation of unidirectional turbines in twin-turbine-OWC and vented-OWC configurations. Extrapolated hydrodynamic experimental data of irregular waves in King Island test site, Tasmania, were utilized with the turbine flow resistance simulated by an orifice plate. The flow and damping characteristics of the inflow and outflow turbine geometries were evaluated regarding the given optimum operation of the OWC chamber.

The unsteady performance evaluation of the turbines is made by comparing their power extraction under fixed and controlled RPM schemes. Comparison of the unidirectional turbines of this research concluded that the inflow turbine due to having a higher direct efficiency yields better performance than the outflow turbine in a vented-OWC system. However, it operates less effectively in a twin-turbine-OWC configuration due to the effects of backflow and negative torque in the reverse operational mode. The outflow turbine offers interesting features such as smaller size in full scale, higher backflow prevention and less sensitivity to RPM variations. In addition, it was found that the unidirectional inflow turbine integrated in a vented OWC obtains comparable power extraction to a bidirectional-turbine-OWC system fitted with a state-of-the-art bi-directional turbine.

Finally, this research shows that the concept of unidirectional radial turbine integrated in a vented OWC can be a more economical choice than the twin-turbine concept, due to eliminating the cost associated with the extra turbine (and extra generator). It also encourages a simpler turbine design with lower energy losses compared to the bidirectional turbine-OWC concept for a comparable power extraction.

Key words: Unidirectional radial air turbine, Design optimisation, Efficiency maximization, Vented oscillating water column, Computational fluid dynamics.

TABLE OF CONTENTS

LIST OF FIGURES

LIST OF TABLES

ABBREVIATIONS

2D	Two-dimensional
3D	Three-dimensional
AMC	Australian Maritime College
CFD	Computational Fluid Dynamics
DGV	Downstream Guide Vane
DS	Downstream Section
ERR	Error
GA	Genetic Aggregation
KRG	Kriging
LE	Leading Edge
MOGA	Multi-Objective Genetic Algorithm
MTB	Model Test Basin
OWC	Oscillating Water Column
Pa	Pascal
PS	Pressure Side
PTO	Power Take-Off
RB	Rotor Blades
RMS	Root Mean Squared
RS	Response Surface
SRS	Standard Response Surface
SS	Suction Side
TE	Trailing Edge
UGV	Upstream Guide Vane
UTAS	University of Tasmania
WEC	Wave Energy Convertor

NOMENCLATURE

A_R	Turbine flow passage area at $r_R = 2\pi r_R h$
A_o	Sectional area of the orifice
C_A	Input coefficient
C_H	Non-dimensional pressure ($C_H = \frac{\Delta p_0}{\rho \omega^2 D_R^{\ 2}}$)
C_{Losses}	Pressure losses coefficient
C_P	Non-dimensional power ($C_p = \frac{T_0 \omega}{\rho \omega^3 D_R^{\ 5}}$)
C_q	Non-dimensional flow rate ($C_q = \frac{Q}{\omega D_R^{\ 3}}$)
C_T	Torque coefficient
D	Diameter
$D_{Overall}$	Turbine overall diameter
D_R	Rotor mean diameter
D_s	Specific diameter
E_{Rl}	Rotor losses
h	Height of flow path of turbine
l_r	Chord length of the blade
$M-1$	Bidirectional radial turbine (used for validation)
$M-2$	Unidirectional radial turbine (centripetal)
$M-3$	Unidirectional radial turbine with increased height of casing
N	Number of guide vanes
N_s	Specific speed
P	Power
p_0	Total pressure
$p_{\max}$	Pressure amplitude of the OWC oscillations
p_{t-in}	Total pressure at the inlet

Δp_0	Total to static pressure drop
Δp_d	Total to static pressure drop inside the duct
Δp_R	Total pressure changes across the rotor
Q	Volumetric flow rate
$Q_{\max}$	Peak flow rate of the OWC oscillations
q	Volumetric flow rate through a turbine (in a wave cycle)
r	Radius
Re	Reynolds number ($\mathrm{Re} = \omega r^2_{in} / \upsilon$)
r_{in}	Inlet radius of the rotor
r_{out}	Outlet radius of the rotor
r_R	Mean radius of the rotor ($r_R = \frac{r_{in} + r_{out}}{2}$)
t	Time of the OWC oscillations
T	The period of the OWC oscillations
T_0	Output torque
U	Blade speed at r_R ($U = r_R \times \omega$)
V	Absolute velocity
V_d	Air velocity at the duct inlet
V_R	Air velocity at r_R
V_u	Tangential velocity
W	Relative velocity
Z	Number of blades
ρ	Density of air
ϕ	Flow coefficients
σ_R	Solidity
ω	Angular velocity
Ψ	Damping ($\Psi = C_q D_R^2 / \sqrt{\rho C_H}$)
υ	Kinematic viscosity of air
η	Turbine efficiency

1 INTRODUCTION

The ever-increasing demand for energy in the modern world, combined with the desire to reduce carbon emission, has led to a renewed interest to develop technologies in harnessing clean energy resources such as offshore renewable energy. Ocean waves are a promising source of offshore renewable energy with significant power and availability throughout the year. Research on potential of wave energy revealed a higher levelized energy supplied by ocean waves compared to wind and solar power resources (Waters, 2008). In addition, the availability of wave energy is more wide-spread than the tidal energy form (Frid et al., 2012).

Australia with thousands of kilometres of coastline has an abundant and attractive wave energy resource, particularly at its southern coastlines (Yusaf et al., 2011, Fadaeenejad et al., 2014). It was reported by the Commonwealth Scientific and Industrial Research Organisation (CSIRO) that the ocean waves have potential to contribute up to 11 per cent of Australia's energy demands within three decades (Hemer and Griffin, 2010).

Design choice for a wave energy converter (WEC) depends on the location and mode of extraction. Various regions and principal modes of power extraction require different design solutions, thus in contrast to wind energy, it is unlikely to converge on a single form of wave energy converter (WEC) geometry (Falnes, 2002, Harris et al., 2004, Cruz, 2007). One of the most extensively investigated classes of WECs is the oscillating water column (OWC). An OWC consists of a chamber partially submerged in water and opened to the incident waves at the bottom. From the top, the chamber is connected to atmosphere through a duct and a turbine located inside it. The incident waves cause oscillations on the free surface of the chamber and drive the airflow trapped on top of the water column through the turbine.

The wave-to-wire efficiency of the OWC is obtained through three stages of energy conversion; wave to pneumatic, pneumatic to mechanical and mechanical to electrical. The middle stage (conversion of pneumatical to mechanical power) is performed using the air turbine and has a significant contribution to the economic feasibility of the OWC technology. Different turbine configurations such as axial, radial and mixed-flow were studied for application with OWC's flow regime. Unidirectional flow turbines such as Francis turbine and axial-flow turbine were found to need a rectifying system for application with OWCs. Masuda (1986) was first to equip the conventional turbines (employed in the small navigation buoys) with a system of non-return valves (Falcão and Gato, 2012). However, this system added complexity and maintenance difficulties to the design and difficulties in engineering implementation (Falcão, 2010, Heath, 2012b, Takao and Setoguchi, 2012). The non-return valves system, which were inherently able to convert bidirectional airflow to unidirectional. Self-rectifying

air turbines employed in OWC projects are categorized in two main classes: axial-flow turbines such as Wells, impulse, Dennis Auld, twin-rotor and hydro-air configuration; and radial-flow turbines including impulse, bi-radial and twin-rotor configuration (Falcão and Henriques, 2014, Falcão and Henriques, 2016a, O'Sullivan et al., 2011, Lopes et al., 2019).

Design customization of turbines for OWC application involved preliminary design studies regarding optimum efficiency, size and speed. In this approach, the turbomachinery performance is predicted through a set of calculations considering non-dimensional parameters of specific speed N_s and specific diameter D_s. The size and rotational speed of the turbine for application with an OWC is obtained through matching the damping of the turbine and chamber. The damping is associated with the relationship between the pressure drop and flow rate through the element. For a well-matched turbine-chamber connection, the turbine should produce a close damping to the optimum damping of the OWC chamber at its design efficiency point. Design techniques based on N_s-D_s diagram were used to design the turbine for a broad performance range. Inioue et al. (2000) investigated the efficiency improvement of axial impulse turbines from the viewpoint of specific speed and specific diameter. They explained the low efficiency of axial impulse turbines at higher flow coefficients according to Balje diagrams (Balje, 1981), and concluded that high efficiency can be found in a limited range of N_s-D_s diagram (Thakker et al., 2009). In addition, efficiency maximization of a radial-flow turbine was studied for application in an OWC by A. Falcao et al. (2015), in which, the total-to-static efficiency of the turbine (under design conditions) was defined as a function of specific speed and specific diameter using the Balje diagram of the radial-inflow gas turbines (Hall and Dixon, 2013, Logan Jr, 2013).

In a conventional OWC, bidirectional turbines are used to operate in bidirectional reciprocating air flow (Drew et al., 2009, Heath, 2012a). However, the symmetrical design of bidirectional turbines with respect to the plane perpendicular to the rotor axis, leads to limitations such as relatively low efficiency, high mechanical losses and poor starting characteristics (Darabi and Poriavali, 2007, Takao et al., 2002, Halder et al., 2015). A topology utilizing a pair of unidirectional turbines, as an alternative to the bidirectional turbine, was proposed by Jayashankar et al. (2009a). They performed numerical investigations on a twin-turbine-OWC configuration for the Indian wave power plant and stated that this topology ensures high efficiency over a wide range of flow. In addition, separating the turbines causes them to rotate at different speeds which leads to an efficient power conversion in various wave climates (Dudhgaonkar et al., 2011). In this configuration, a common electrical generator can be used for both turbines (Figure 1.1) or, alternately, two separate generators can be coupled to each turbine. The turbines are similar to single-stage conventional turbines (Mala et al., 2011b), with a row of guide

vanes followed by a bladed rotor, useful to operate in unidirectional flow. Since the turbine is planned to operate in a single direction of flow, asymmetrical rotor blades are employed in the turbine design (Okuhara et al., 2014). In addition, the duct geometry is divided in two channels to lead the airflow through each turbine separately. As Figure 1.1 shows, turbine 1 (T_1) works in the inhalation mode and turbine 2 (T_2) works during the reverse direction. Each turbine operates effectively over a half cycle of the wave (direct mode), while the other turbine is not producing any energy (reverse mode). According to research by Setoguchi et al. (2006b), it was found that an axial unidirectional turbine is able to deliver higher instant efficiency over a wide range of flow coefficients than the bidirectional impulse turbine. However, lack of valve to stop the air flow through the idle turbine in this concept has caused major drawbacks. The negative torque (since the idle turbine consumes energy to maintain its rotation), and noise due to one-third of the total flow passing through the turbine in the reverse mode.

In addition, when a shared generator is used in the twin-turbine concept and both turbines have the same axis of rotation, the efficiency is reduced due to windage losses (Pereiras et al., 2013). Alternatively, in the configuration with two separate generators, the cost related to the second turbine and the extra generator is a negative point.

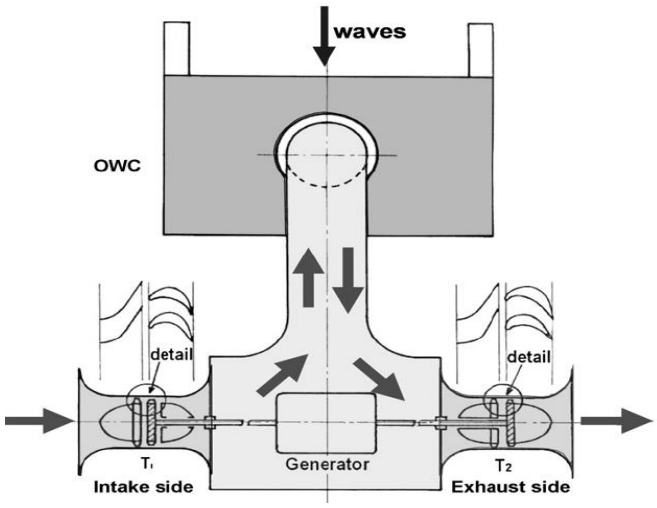

Figure 1.1 Twin unidirectional turbine configuration (Mala et al., 2011b).

A new patented self-rectifying air turbine was introduced by Falcao et al. (2015), based on numerical studies and with the aim of delivering higher efficiency. It was a twin rotor concept, consisted of two rows of axially offset rotating blades, and was able to be configured as radial-flow or axial-flow turbines as shown in Figure 1.2 and Figure 1.3, respectively. Both rows of blades are mounted on the same shaft and are integrated with corresponding guide vanes. The reciprocal airflow

is converted to unidirectional flow using a double set of circumferentially-adjusted curved ducts and a pair of axially-sliding valves.

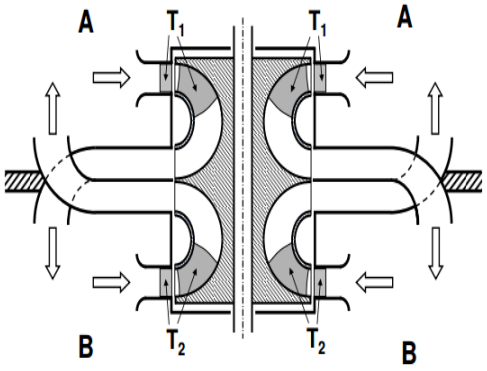

Figure 1.2 Twin-rotor turbine with radial rotors (A. Falcao et al., 2015).

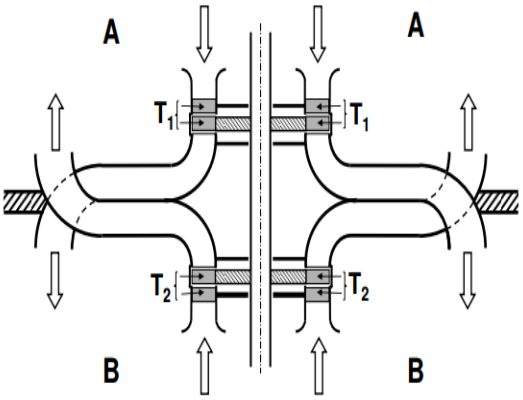

Figure 1.3 Twin-rotor turbine with axial-flow rotors (A. Falcao et al., 2015).

In the twin-rotor impulse turbine (illustrated in Figure 1.2), the aerodynamic losses at the entrance to the downstream guide vanes are low or completely prevented. In addition, compared to other types of turbine, the twin-rotor design is axially very compact, mechanically simple and reliable and able to extract energy of highly energetic sea states with large air pressure oscillations. Experimental studies showed that radial configuration of this machine can attain a peak efficiency of 86% (single-rotor configuration) and 73% (twin-rotor configuration) under design condition in unidirectional steady flow (Lopes et al., 2019), however this turbine is yet to be manufactured and operated in full-scale.

Recent research shows that design customization for operation in unidirectional flow is not limited to the turbine geometry, but the OWC chamber is also modified in a way to permit a single direction of air flow through the turbine. Fleming et al. (2017) experimentally tested a vented concept of OWC referred as UniWave in collaboration with Wave Swell Energy (WSE), the company owning the prototype. In this concept, under negative air chamber pressure, air passes through the turbine. While for positive air chamber pressure, air escapes the system through one-way valves (more detail on the vented OWC concept is provided in chapters 2 to 5 of this thesis). The interesting point about this concept is that although pneumatic energy is extracted during a half cycle of the wave, wave power extraction occurs over the entire wave cycle. This is due to the temporary energy storage in the form of additional water column heave inside the OWC chamber. Therefore, the air flow direction through the turbine is primarily unidirectional; an asymmetric pressure profile with large negative and small positive pressure drops. This typical pressure output provides opportunities to simplify the turbine technology, by using a single turbine and concentration on unidirectional air flow. However, for an economically feasible OWC concept, it is necessary to customize the turbine design for optimum

efficiency and for the OWC to still achieve resonance with the incident wave field (matching turbine damping with the OWC) (Fleming et al., 2017).

The research presented in this thesis is focused on design optimisation of unidirectional turbines for the typical operation of the vented OWC model of WSE. A radial impulse turbine was selected as the turbine geometry due to the following features:

- Research on radial impulse turbines is still in progress, currently this configuration is reported with a poor global efficiency compared to the axial turbines (50% versus 70%) (El Marjani et al., 2008, Setoguchi and Takao, 2006a, Rodríguez et al., 2019).
- The unidirectional turbines used in the twin-turbine concept of OWC are mainly of axial type and there is scope for use of unidirectional radial turbines for this concept (Jayashankar et al., 2009b, Takao et al., 2011a, Mala et al., 2011a).
- A radial turbine configuration has advantageous features compared to the axial configuration such as lower loads on bearing, easier manufacturing and higher backflow prevention (when used in the twin-turbine concept) (de O Falcão, 2002, Pereiras et al., 2011a, Tease et al., 2007).

Various sections of the turbine geometry and two different configurations of the unidirectional radial turbine were investigated for design modifications. Design of experiments (DOE) techniques were used with CFD simulations to optimise performance of the turbine. DOE is based on a Central Composite Design (CCD) test plan involving all the input variables that are likely to affect the turbine's performance (Guide, 2011). DOE samples a design space (using a limited number of points) and uses a statistical model (with low uncertainty in model estimation and high accuracy in prediction) to determine input variables' impact (Durgude et al., 2016). It is then followed by a designed experiment test plan (response surface) with the objective of optimising the turbine's performance. The response surface allows to perform sensitivity analysis to determine variation of the output parameter as a function of the input variables. Sensitivity analysis reduces the computational cost of the optimisation by identifying the most important variables in a large list of input variables and can lead to more intellectual choices among the input parameters in future studies (Uy and Telford, 2009).

The main questions behind this research were:

1- How does limiting air flow to a single direction affect the radial turbine's energy capture in OWC wave energy converter?
2- How is the overall performance of the turbine-OWC concept affected by the inward or outward direction of the flow in the radial turbine domain?

3- Does integrating a unidirectional-air-flow turbine into the vented OWC design enable greater power extraction compared to a conventional bi-directional OWC in an oscillating flow regime?

This thesis is presented in a chapterised format, meaning that the chapters have initially been prepared as research papers and submitted to recognised journals of the field. At the first page of each chapter, it is clearly mentioned whether the paper is published or is under review by the journal. The chapter body is then the most recent version of the manuscript. The structure of this thesis is as follows:

- Chapter 2 identifies the design drawbacks of a unidirectional radial air turbine (centripetal configuration), by investigating the energy losses in various sections of the turbine and suggests design modifications. (This chapter provides a background for turbine design improvement in chapter 3)
- Chapter 3 presents a study on design modification of the centripetal radial air turbine configuration (inflow turbine). It utilizes design optimisation methods with CFD simulations to improve the efficiency of the inflow turbine configuration. (This chapter presents the answer to research questions 1 and 2 regarding the inward-flow direction in a radial turbine domain.)
- Chapter 4 provides an analysis on design modification of a centrifugal radial air turbine configuration (outflow turbine). It combines design optimisation techniques with CFD simulations to improve the efficiency of the outflow turbine configuration. (This chapter presents the answer to research questions 1 and 2 regarding the outward-flow direction in a radial turbine domain.)
- Chapter 5 compares the inflow and outflow configurations in chapters 3 and 4 regarding their operation in vented and bidirectional OWC systems. It also evaluates turbines' operation using extrapolated experimental data of irregular waves simulated to match conditions at a King Island test site (in Tasmania) and provides a means to compare the performance of different turbines integrated into an OWC. (This chapter presents the answer to research questions 1 and 3, where power extraction of a unidirectional turbine in a single flow direction (as happens in the vented OWC concept) is compared to a conventional bidirectional OWC equipped with an efficient twin-rotor turbine.)
- Chapters 6 and 7 state the main conclusions and provide some ideas for further work on design of turbines for OWCs.

2 IDENTIFYING THE DESIGN DRAWBACKS OF A UNIDIRECTIONAL RADIAL AIR TURBINE (CENTRIPETAL TURBINE CONFIGURATION)

This chapter is published in the journal of Energy, the citation for the paper is:

Ansarifard, N., Kianejad, S., Fleming, A., & Chai, S. (2019). A radial inflow air turbine design for a vented oscillating water column. Energy, 166, 380-391.
(https://doi.org/10.1016/j.energy.2018.10.068)

Abstract

The focus of this paper is on analysing a unidirectional radial air-inflow-turbine design using Computational-Fluid-Dynamics (CFD) suitable for application with a vented-OWC. It is found that downstream of the rotor can cause significant energy losses due to its narrow flow passage. Two configurations of an inward-flow radial turbine were also compared. In the first configuration the height of casing was kept constant throughout the turbine domain and in the second configuration the sectional area from inlet to the outlet of the turbine domain was kept constant by gradually increasing the height of casing. The latter configuration obtained a ten percent gain in peak efficiency compared to the first, due to fewer energy losses at the downstream section and comparably higher torque for the same flow-coefficient. Introduction of downstream-guide-vanes was found to reduce the flow congestion, which offers a wider operational range for the radial-inflow design.

2.1 Introduction

Ocean waves are considered as a promising source of renewable power to generate electricity. The oscillating water column (OWC) is recognized as a reliable device in wave energy conversion (WEC). It has a robust design with no moving parts in-contact with water and contains two main parts; a chamber and a power take-off (PTO). The OWC chamber is partly submerged and open at the bottom and may be either fixed or floating. The chamber is in close contact with the ocean, where incident waves cause the water free surface inside the chamber to fluctuate. The oscillations of the chamber free surface compress and decompress the air in the chamber causing a pressure differential and consequently airflow between the chamber and atmosphere. A duct/turbine connects the chamber to atmosphere. The turbine converts the input pneumatic power to mechanical power by rotating the rotor. Generic OWC designs employ a so-called bi-directional turbine that continues to rotate in the same direction while extracting significant power from air flow in both directions (inhalation and exhalation).

An innovation on the OWC concept, best described as a vented OWC, was recently presented by Fleming et al. (Fleming et al., 2017) who describe the UniWave device, a vented OWC, as an adaption of a typical OWC design to include large passive one-way valves that vent air from the OWC chamber during exhalation. In this configuration, significant air flow through the turbine only occurs during air chamber negative pressure (inhalation), while air primarily passes through the one-way valves during exhalation. Passive check valves/flaps are lightly hinged to the top edge of the chamber permitting the valve to open with minimal positive chamber air pressure (open is to outside, close seals the system). Figure 2.1 shows a schematic of the UniWave OWC operational concept. The rise of the chamber water level causes positive air pressure inside the chamber and in this condition, air escapes the

chamber through the one-way valves (with a small pressure drop). During the second half of the cycle, the water column falls causing a negative pressure inside the chamber, subsequently the one way valves close and air flow is directed entirely through the air turbine (with a high pressure drop). Although the power extraction only occurs during air inhalation, wave power extraction occurs over the entire wave cycle due to temporary energy storage in the form of additional water column heave (Fleming et al., 2017). Pneumatic efficiency of the vented OWC is comparable to a regular bi-directional OWC, but offers opportunity to simplify turbine design. It is acknowledged that this introduces the requirement for bespoke one-way valves and further investigation is still required to determine if there is an overall advantage in adoption of the UniWave concept.

Cost of harnessing energy is a challenge in the current WEC industry (Bull and Ochs, 2013), which can be mitigated through increasing the profitability. Design improvements considering the wave to wire efficiency of a WEC system can increase the power capacity and decrease the related costs (Callaghan and Boud, 2006, Energy, 2005). Efficient designs of the OWC, PTO and the generator are aspects investigated by researchers and are based on maximizing the pneumatic, mechanical and electrical conversion efficiencies of the system (Cui and Hyun, 2016, Liu et al., 2017, López et al., 2016, Liu et al., 2018, Rodríguez et al., 2018).

In comparison to bidirectional turbines, a unidirectional turbine lacks the pressure differentials imposed by the reverse direction of the flow. A turbine customized for a single direction has the potential to have blades with higher stagger angles, adjusted guide vanes angle and modified duct shape. These design modifications improve the performance in the direct flow condition and eliminate the aerodynamic losses imposed by the reverse flow and ensure higher efficiency of the unidirectional turbine. However, geometrical improvement of the PTO unit requires a detailed analysis of the energy losses in different sections of the turbine (Falcão and Henriques, 2016b, Henriques et al., 2016, Liu et al., 2016). Unidirectional version of axial turbines was proposed to be utilized with both fixed and floating twin-turbine-OWC topologies, in which two unidirectional turbines are employed to operate alternately during inhalation and exhalation modes (Dudhgaonkar et al., 2011, Mala et al., 2011b, Okuhara et al., 2012, Setoguchi and Takao, 2006b). Jayashankar et al. (Jayashankar et al., 2009a) carried out numerical simulations of twin unidirectional turbines' performance in an Indian fixed wave power plant and reported a high efficiency of this topology over a wide range of flows. A field test in the Indian OWC plant revealed that airflow velocity profile is not symmetric during inhalation and exhalation and its magnitude is higher when air flows from chamber to atmosphere [61]. Therefore, it was remarked that modifying the rotor blade profile regarding a single direction of flow can result in higher performance compared to conventional symmetric blade profiles. Setoguchi et al. (A. Thakker et al., 2001, Kim et al., 2001, Setoguchi and Takao, 2001) introduced the idea of expanding the pressure

side of a rotor blade by extending the side facing higher incident airflows. They designed a unidirectional impulse rotor with blunt leading edges and extended trailing edges along the camber line.

The scope of this study was restricted to look at radial turbines. Axial turbines are selected as a first choice for a unidirectional turbine configuration with the OWC, due to a significant higher global efficiency compared to the radial impulse turbines (70% versus 40%). However, radial turbines were found to have advantages such as design simplicity, easy manufacturing and lower thrust loads. There was a research gap on improving global efficiency of unidirectional radial air turbines and this topic was selected as the scope of this research. Research on unidirectional radial impulse turbines is limited (Rodríguez et al., 2018) and there is room for design modifications of this type of turbine. In the present study, a unidirectional configuration of a radial turbine for inhalation condition was investigated. The investigation was conducted using Computational Fluid Dynamics (CFD) and the computational model was validated according to the available experimental data of a bidirectional geometry (Case 1) in (Setoguchi et al., 2002).

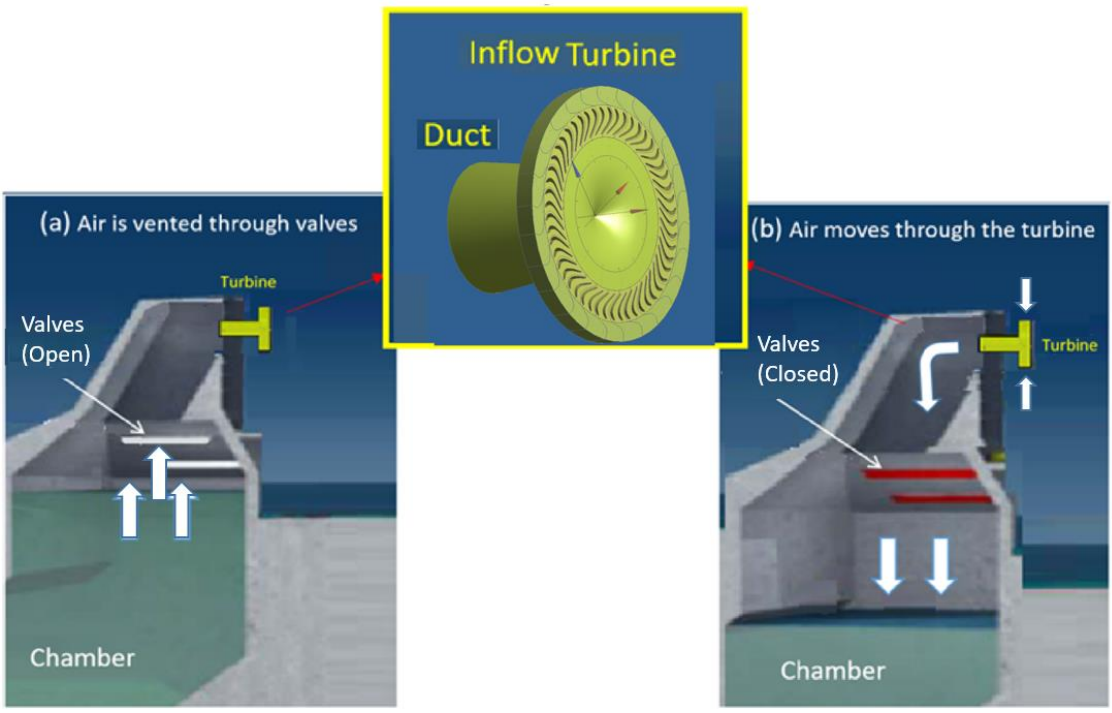

Figure 2.1 Concept of UniWave OWC (Fleming et al., 2017).

2.2 Numerical method

The basis of almost all CFD simulations is the Navier–Stokes equations and computers are used to calculate interaction between fluids and surfaces. Accurate CFD methods and various modelling techniques have been developed in different areas such as heat conduction (Liu, 2012, Zhu and Ye, 2010), hydrodynamics and aerodynamics (Halder et al., 2017, Liu et al., 2017). This study employed

numerical simulation tools to predict the behaviour of a radial air turbine. The numerical simulations were carried out by Star-CCM+ software. The code was based on the finite volume method to resolve the incompressible RANS equations. The steady state simulations were conducted to customize the design of a radial turbine for the UniWave typical operation. Assuming steady flow in these simulations is justifiable considering the quasi-steady assumption (Rodríguez et al., 2018). Since the frequency of the wave cycle in the OWC chamber is significantly lower than the rotating frequency of the turbine, the flow can be treated as steady (Cui and Hyun, 2016). The moving reference frame (MRF) method was used and a fixed mesh was used for the rotor section. The k-ε turbulence model consists of two transport equations (PDEs) and describes the mean flow characteristics for turbulent flow conditions based on them. This model is beneficial for free-shear layer flows with relatively small pressure gradients and in problems in which the Reynolds shear stresses are highly important. The realizable k-ε model has a new transport equation for the turbulent dissipation rate and considers mean flow and turbulence properties (Shih et al., 1995). It has acceptable performance in capturing the mean flow in complex structures, rotating domains, boundary layers, strong adverse pressure gradients, separation, and recirculation. The realizable k-ε turbulence model was employed in this study, this model had previously been used in various investigations in this field and accurate results were obtained (El Marjani et al., 2008, Pereiras et al., 2011c). The Velocity-Pressure coupling was done using the SIMPLE algorithm and thousand iterations were set as the stopping criteria. The convergence criteria was set to an RMS residual target of 10^{-6} and the residual converged after 400 iterations in the simulations. However, the loop of simulations in the optimization study was set on 1000 iterations to assure the solution convergence is perfectly achieved. Since the study was performed in the steady state this number of iterations was sufficient to achieve the solution convergence.

The turbine characteristics were evaluated using a set of mathematical formulations (Setoguchi et al., 2002) for prediction of the torque coefficient C_T, input power coefficient C_A and turbine efficiency η versus flow coefficient ϕ. Equations related to these parameters are as follows:

$$C_T = T_0 / \left\{ \rho \left(V_R^{\,2} + U_R^{\,2} \right) A_R r_R / 2 \right\} \quad (2.1)$$

$$C_A = \Delta p_0 Q / \left\{ \rho \left(V_R^{\,2} + U_R^{\,2} \right) A_R V_R / 2 \right\} \quad (2.2)$$

$$\eta = \frac{T_0 \omega}{\Delta p_0 Q} = \frac{C_T}{C_A \phi} \quad (2.3)$$

$$\phi = V_R / U_R \quad (2.4)$$

Where r_R is the turbine mean radius and is measured at the mid-chord of the rotor blade and ρ is the air density. A_R denotes turbine's flow passage area at r_R ($A_R = 2\pi r_R h$) and h is the height of

casing at r_R, blade speed is shown with U_R and is calculated by $U_R = r_R\omega$, where ω is the rotor angular velocity. V_R refers to the air velocity at the rotor mean radius (r_R) and is the component of air velocity normal to A_R. As the volumetric flow rate Q is constant from the inlet to the outlet of the domain, V_R can be calculated from volumetric flow rate divided by A_R. Δp_0 indicates the total pressure drop between the settling chamber and atmosphere and T_0 is the output torque.

2.2.1 Boundary conditions

The turbine domain consisted of one rotating and two stationary sections. A stationary domain was used at the rotor upstream, including upstream guide vanes (UGVs). The middle domain was set as rotating using the moving reference frame (MRF) tool and is described here as the rotor. The third domain, downstream of the rotor was set as stationary, including downstream guide vanes (DGVs). The downstream section includes the elbow and the duct of the OWC. To save calculation time and minimise CPU usage, a periodic angular section of the turbine was selected as the computational domain, including three rotor blades, four UGVs and three DGVs. Schematics of the turbine domain and the boundary conditions are illustrated in Figure 2.2. Constant total pressure was specified at the inlet and the inlet boundary was set as a stagnation inlet. The outlet boundary was set to pressure outlet, providing constant static pressure at the exit of the domain. The shared planes between each side of the two domains were considered as interface, and periodic boundaries were used. Simulations were performed over a range of total pressure at the inlet between 100 Pa and1500 Pa at a constant rotational speed of 24.5 rad/s, corresponding to a range of flow coefficients from ϕ = 0.4 to 2.5. Experimental studies in (Dixon and Hall, 2013) showed that provided Re > 2×10^5, the effects of Reynolds number on the performance of turbomachines is small. In this research the simulations were performed at a Reynolds number ($\mathrm{Re} = \omega r^2_{in} / \upsilon$) of 2.89×10^5 to reduce the Reynolds number effects on the turbine performance. All simulations were performed under steady conditions. By using the quasi-steady assumption and setting the pitch angle ratio (close to one) at the interface of the fixed and moving domains, the MRF method could be used in this study. The MRF method is a convenient choice in this type studies due to being simple, robust and efficient for the steady-state simulations.

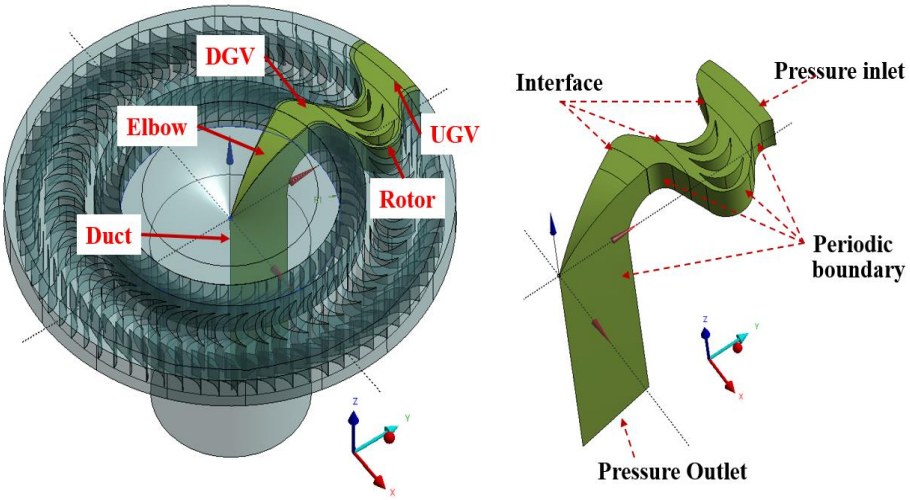

Figure 2.2 Turbine domain and boundary conditions, a section of the turbine was used in the simulations.

2.2.2 Turbine geometries

In order to validate the computational method, experimental results of a fully-developed and well-defined study published in the literature (Setoguchi et al., 2002) were used for a comparison with the current CFD simulations. For this reason, a bidirectional radial turbine geometry was created based on the geometry introduced in (Setoguchi et al., 2002) known as Case (1). This geometry was named M-1 and its main characteristics and operational range were used in this study as a design reference. An initial unidirectional radial turbine geometry was created according to the geometrical dimensions of the bidirectional geometry (M-1), having the same duct geometry, turbine outer diameter (568mm), chord length (54mm), casing height (44 mm) and equal number of 73 upstream guide vanes (UGVs), 51 rotor blades (RBs) and 52 downstream guide vanes (DGVs). This geometry was named M-2 and was different from M-1 due to its asymmetric blade profile and 7.5 degrees blade stagger angle. This stagger angle was set to provide an expanded pressure side facing the upstream guide vanes.

Another unidirectional geometry, referred as M-3, was created according to the main geometrical characteristics of the M-2. However, in contrast to the M-2 with constant casing height of 44 mm, the height of casing in M-3 was increasing from UGV inlet to the DGV outlet in a way to create equal area in each section of the turbine. To keep the sectional area of the turbine constant, the height of casing had to continually increase from 44 mm at the UGV inlet to 74 mm at the DGV outlet, according to the ratio of the diameter at the UGV inlet to the diameter at the DGV outlet ($D_{UGV} / D_{DGV} = 1.68$). This change was applied to study the performance improvement of the unidirectional turbine by

comparing the pressure losses in different sections of the M-2 and M-3, particularly at the DGV section.

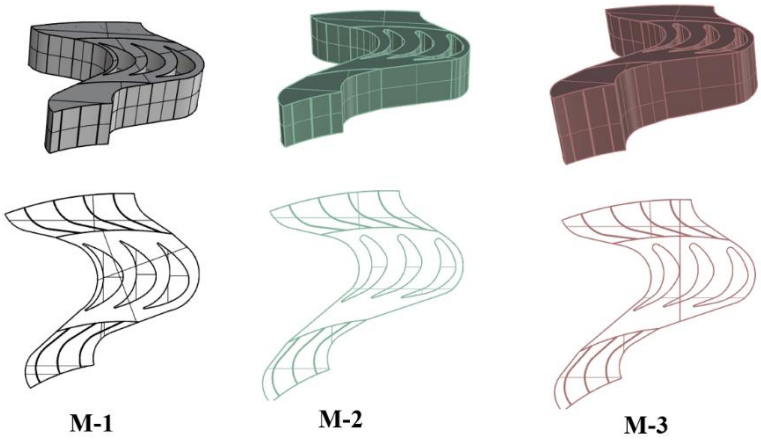

Figure 2.3 shows the main differences of geometries M-1, M-2 and M-3 and Table 2-1 indicates the main characteristics of these geometries. To save calculation time and minimise CPU usage, a periodic angular section of the turbine was selected as the computational domain, including three rotor blades, four UGVs and three DGVs. A pitch change model was used and each blade/GV row section modelled with an individual pitch setting to correctly model the total blades/GVs in the turbine. Then the results of each section were multiplied by a constant to correspond the whole geometry. These constants were $\frac{73}{4} = 18.5$ for the UGVs, $\frac{51}{3} = 17$ for the rotor and $\frac{52}{3} = 17.33$ for the DGVs. It should be noted that these values were selected in a way to keep the pitch angle ratio between the stationary and rotating sections close to 1.

Table 2-1 Main characteristics of geometries M-1 to M-3.

Characteristics	***M-1, case (1) (Setoguchi et al., 2002)***	***M-2***	***M-3***
Configuration type	*Bidirectional*	*Unidirectional*	*Unidirectional*
Blade type	*Symmetric*	*Asymmetric*	*Asymmetric*
Casing height from inlet to DGV exit	*44mm*	*44mm*	*44mm - 74mm*
Setting angle UGV/blade/DGV	*15°/ 0° /25°*	*15°/ 7.5° /25°*	*15°/ 7.5° /25°*

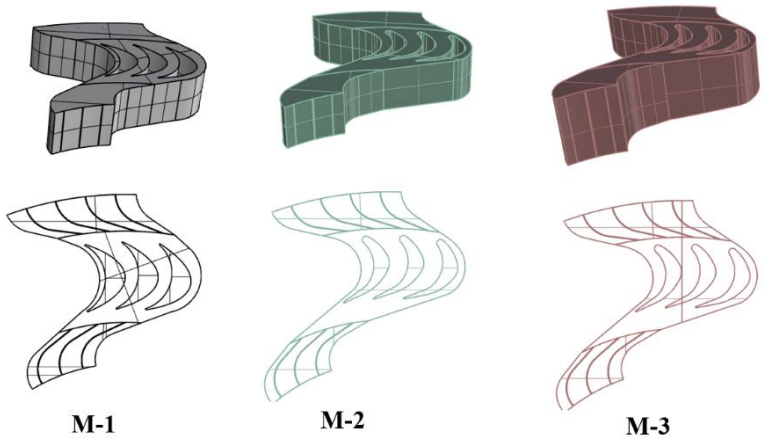

Figure 2.3 Geometries M-1, M-2 and M-3.

2.2.3 Mesh independency study

The M-1 geometry was used for validation of the CFD method, because the performance of this geometry had been previously tested by Setoguchi et al. in (Setoguchi et al., 2002). Various numbers of trimmed mesh elements were investigated using automatic surface repair mesher and prism layers were set to resolve the near wall flow accurately. Prism layers were used in the meshing that allow the solver to determine the forces on walls, flow incidence, secondary flows and separation. Separation affects the drag and pressure drop and its accurate prediction relies on resolving the velocity gradients normal to the wall. In the viscous sublayer of a turbulent boundary layer, these velocity gradients are very steep and use of a prism layer mesh allows to accurately capture near wall flow behaviour and resolve the viscous sublayer directly (low Y^+ ~1) (STAR-CCM+). In this study, 15 prism layers with the total thickness of 33.3% of the base and stretching rate of 1.5 were used and Y^+ in all the simulations was smaller than 1. Schematics of the mesh used in this study are shown in Figure 2.4 . A mesh independence study was performed to analyse the accuracy of converged solutions. Various numbers of cell were considered from 250 thousand to 6 million by changing the base size of the mesh element. As shown in Figure 2.5, the results obtained from the case with 1.5 million cells provided the error of 3.47% and 2.5% for C_T and C_A respectively. In addition, these results were very close to those gained by 6 million cells. Therefore, to save time and the CPU usage in the simulations, the case with lower number of cells (1.5 million) was used. The CFD results of M-1 geometry were compared with the experimental data of case (1) in (Setoguchi et al., 2002) which were reported to have $\pm 1\%$ experimental uncertainty. The deviation of the CFD results from the experimental data were evaluated considering torque coefficient C_T, Input coefficient C_A and efficiency η as defined in equations (2.1) to (2.3) as illustrated in Figure 2.6.

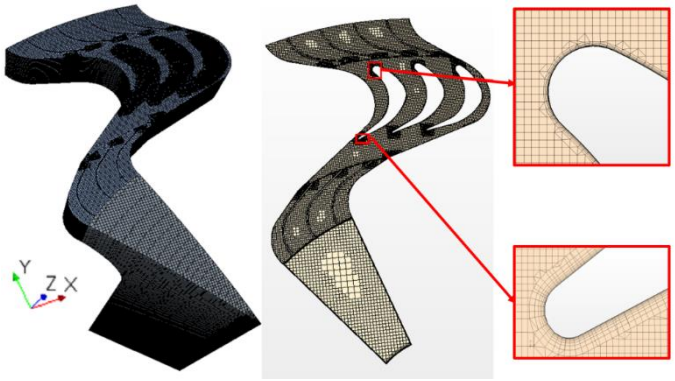

Figure 2.4 Mesh structure used in the simulations, prism layers were used near the walls.

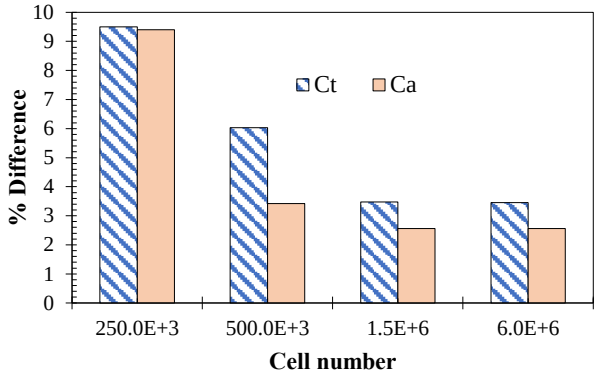

Figure 2.5 Maximum error obtained for numerical simulations of M-1 with various numbers of cell.

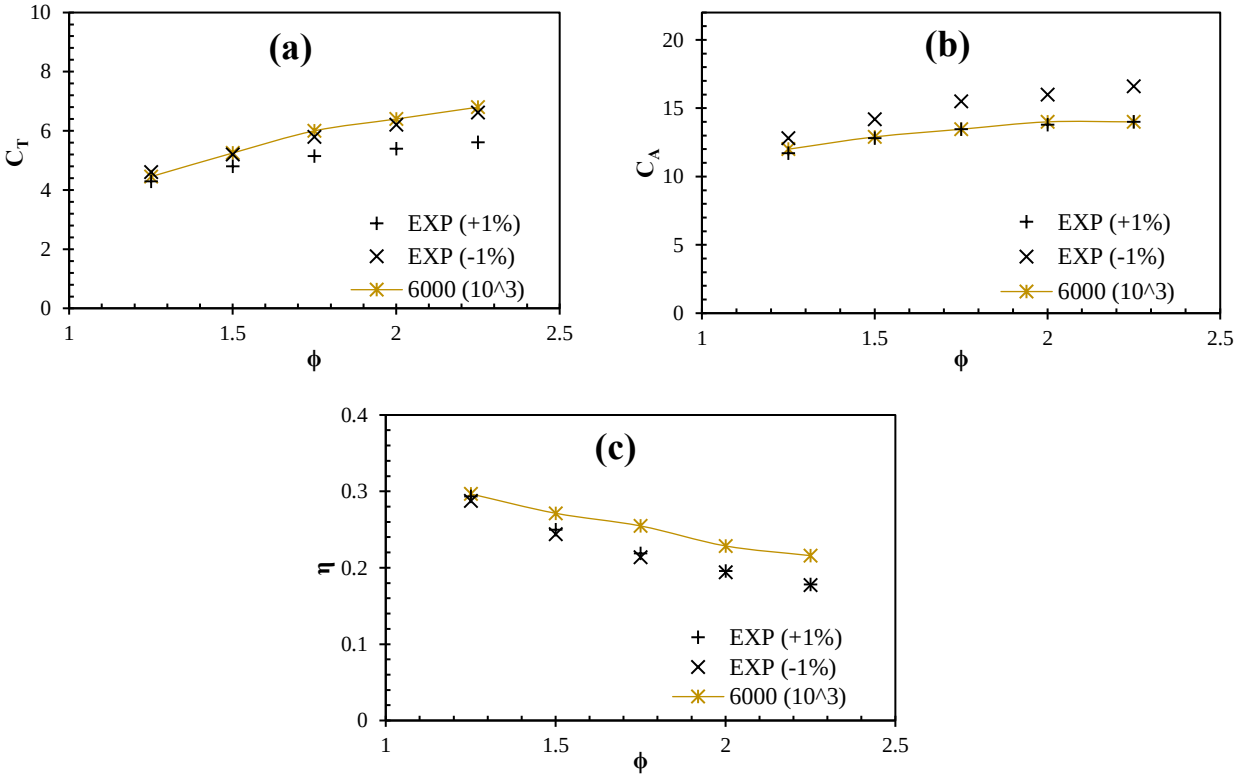

Figure 2.6 Comparison of results for the turbine characteristics of M-1 using the numerical simulation versus experimental results (case 1) (Setoguchi et al., 2002), (a) C_T , (b) C_A and (c) η .

2.3 Results and Discussion

The unidirectional configuration of M-2 was found to provide a higher efficiency compared to M-1 for the inhalation condition. However, flow analysis inside the unidirectional configuration revealed points of flow congestion at the turbine downstream. The design of the inflow turbine had limitations at the rotor downstream associated with the decreased width of the passage.

2.3.1 Impact of the downstream section in the unidirectional configuration

In contrast to the axial turbines, the radial configuration does not have an equal sectional area from inlet to the outlet of the turbine. In the case of the radial inflow turbine the flow passage area at the inlet is significantly larger than at the turbine exit. Therefore, the flow passage becomes narrower from inlet to the outlet and means the air exits the turbine with a higher dynamic pressure. Therefore, the flow entering the turbine at the inlet cannot exit the turbine properly since the downstream works as a point of congestion or blockage. This design issue also has implications for the design of the rotor, where increasing the chord length or setting angle of the blade narrows the interface between the rotor and the DGV. Considering the pressure distribution at various sections inside the turbine reveals that the turbine performance is affected by pressure drops in fixed and rotating sections. To evaluate the effect of the casing shape at the rotor exit, the DGV section was initially removed from the unidirectional turbine configuration (M-2) and the rotor section was directly connected to the duct (as shown in Figure 2.7). This configuration allowed the turbine outlet to be located at a larger radius and avoid the significant pressure losses at the downstream section.

Nevertheless, the turbine performance plots of this configuration in Figure 2.8 revealed that the flow coefficient range is reduced to the maximum point of $\phi = 0.75$ and afterwards moves to $\phi = 0.3$ on a reversed cycle path (as illustrated in Figure 2.8-c). This is because at flow coefficients higher than $\phi = 1$, this configuration generates a negative flow gradient into the domain. Figure 2.9 compares the velocity vectors of M-2 without DGV at different pressure drops. The velocity vectors are poorly directed into the duct as the pressure differential increases and the swirl component of the velocity noticeably grows as the flow coefficient increases. In addition, back flow can be observed inside the duct, particularly at $\Delta p_0 = 1500$ Pa in which the area covered by backflow has expanded dramatically. This phenomenon causes a decreased flow rate while total pressure is increasing.

The rotor-duct interface passage witnessed high swirl flow components, which were caused by the stagger angle of the rotor blades. In addition, because the middle domain was rotating, connecting the duct inlet directly to the rotor outlet negatively affected the torque due to high occurrence of flow separation. Figure 2.8-a illustrates that the torque produced by the M-2 turbine reduces dramatically

due to the noticeable drop of flow rate inside the domain at absence of the DGV section. High losses at the turbine's downstream due to poor adjustment between the rotor and duct sections caused a significant drop of flow coefficient for a given range of pressure differential. The dramatic jump in the input coefficient plot for flow coefficients above $\phi = 0.75$ illustrated in Figure 2.8-b, is due to the sharp decline of flow rate and consequently air velocity at the mean radius of the turbine. This reduction in the flow rate inside the turbine leads to a backward movement of the input coefficient plot toward smaller values of flow coefficients after $\phi = 0.75$.

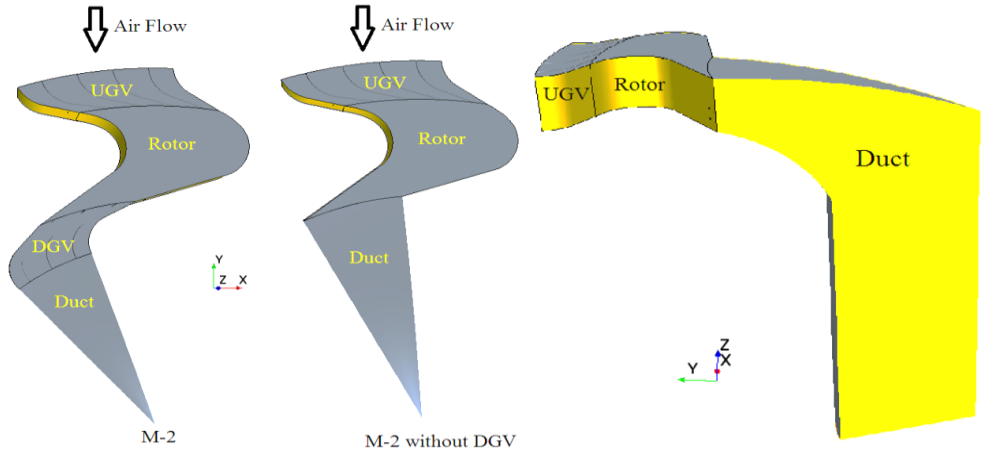

Figure 2.7 Schematics of domain (case M-2), with and without DGV section.

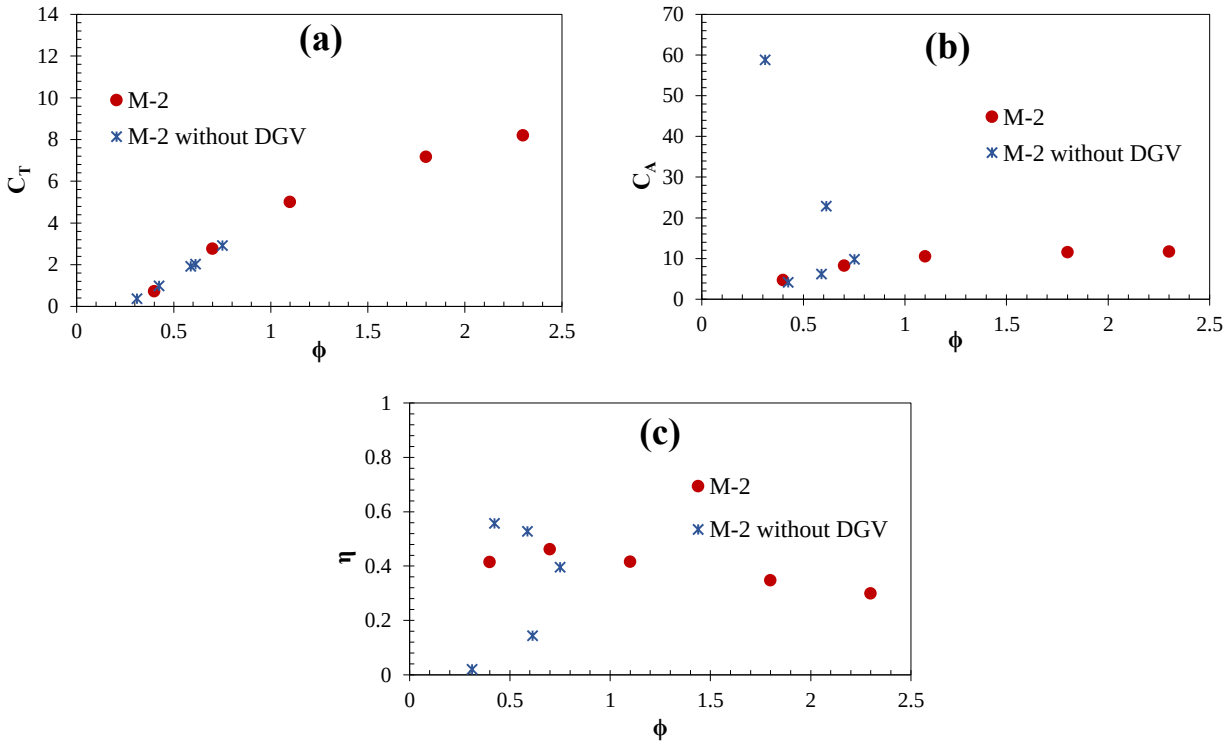

Figure 2.8 Comparison results for turbine performance (case M-2), with and without DGV section. (a) C_T , (b) C_A and (c) η .

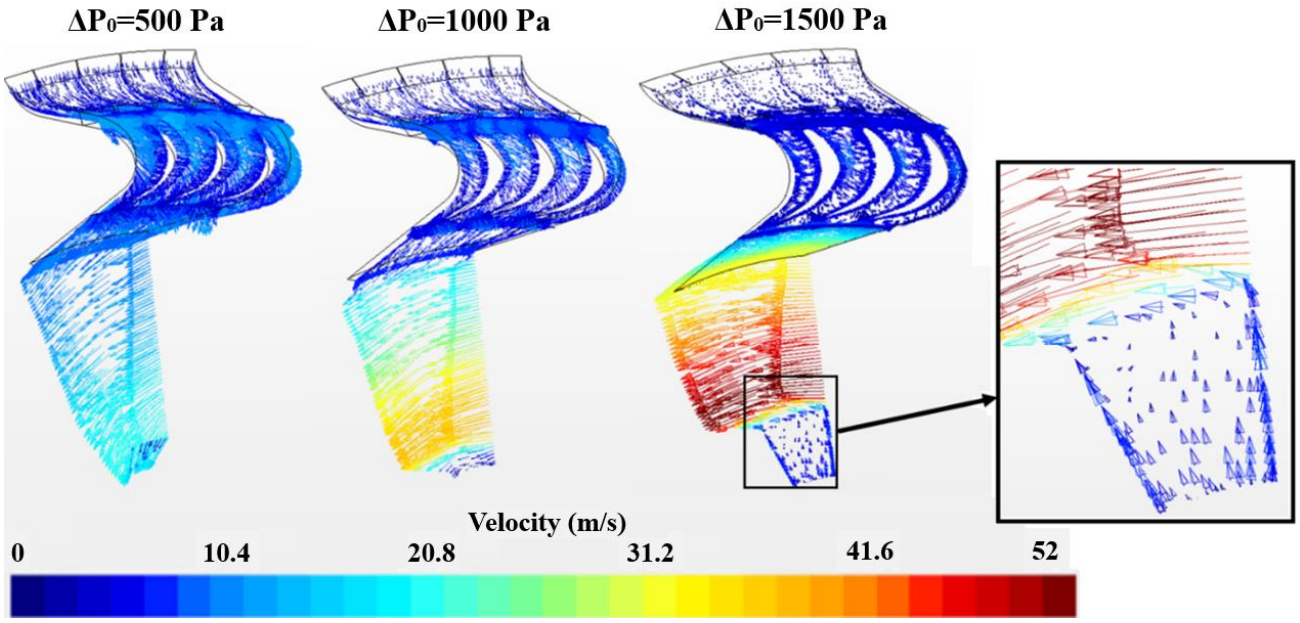

Figure 2.9 Flow behaviour at the duct entrance with absence of the DGV section in the domain for low and high flow coefficients. The back flow inside the duct is noticed at Δp_0 = 1500 Pa.

As the pressure drop increases, for the M-2 without DGV configuration produces huge losses and the airflow cannot move through the turbine properly. Comparison of the pressure and velocity contours of the M-2 with and without DGV section are illustrated in Figure 2.10 and Figure 2.11 respectively. It is clear that for an equal pressure drop of Δp_0 =1000 Pa provided to both geometries, presence of the DGV section has caused a logical pattern of pressure distribution in the turbine domain. In the initial M-2 geometry a significant portion of the pressure drop has been converted by the rotor, while in M-2 without DGV configuration there is a high pressure zone at the rotor exit and the duct entrance (Figure 2.10). Considering Figure 2.11, absence of the DGV section has caused a lower air velocity at the mid-chord radius (V_R) and the flowrate has reduced significantly compared to the M-2 with DGV section. This fact justifies the highly scattered data points around ϕ = 0.5 for M-2 without DGV as shown in Figure 2.8. The input coefficient (C_A) as defined in equation (2.2) has a direct relationship with Δp_0 and a reverse relationship with V_R. Thus, for increased values of pressure drop and lower values of V_R obtained, the C_A data of the M-2 without DGV case increases significantly while the flow coefficient values become smaller. It can be noted that in a turbine geometry similar to M-2, in which the air flows through highly-curved sections in the rotor domain, the downstream section plays a crucial role. This section benefits the configuration by increasing the distance between the rotating domain and the duct. In addition, the curved boundaries applied on the downstream section

allow good adjustment with both the rotor and the duct and prevent poor adjustment at the turbine-duct interface.

The above-mentioned analysis highlights that widening the flow passage at the downstream by locating the turbine-duct connection at a larger radius not only fails to reduce downstream losses, but dramatically decreases the torque and ultimately performance of the turbine. The irregular trend of the efficiency for case “M-2 without DGV” ` that guide vanes at the outlet can ensure turbine operation over a wide range of flows.

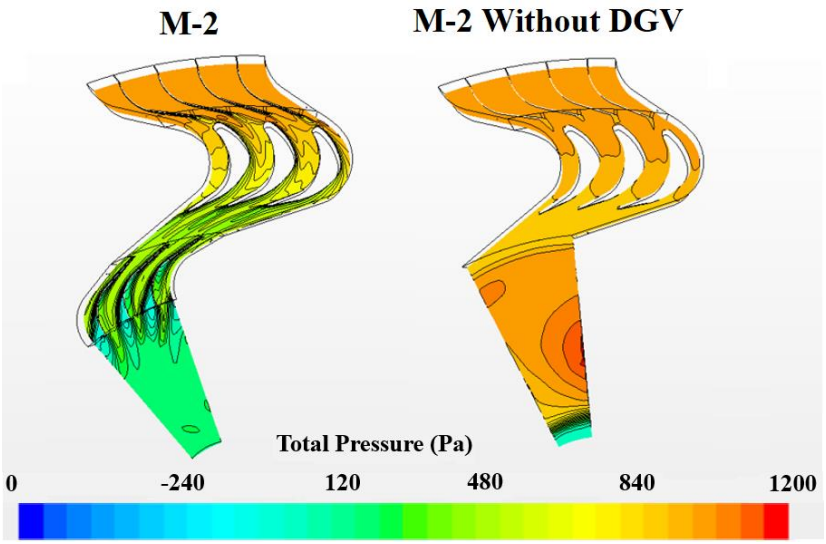

Figure 2.10 Comparison of the pressure contour in M-2 and M-2 without DGV configurations, Δp_0 =1000 Pa.

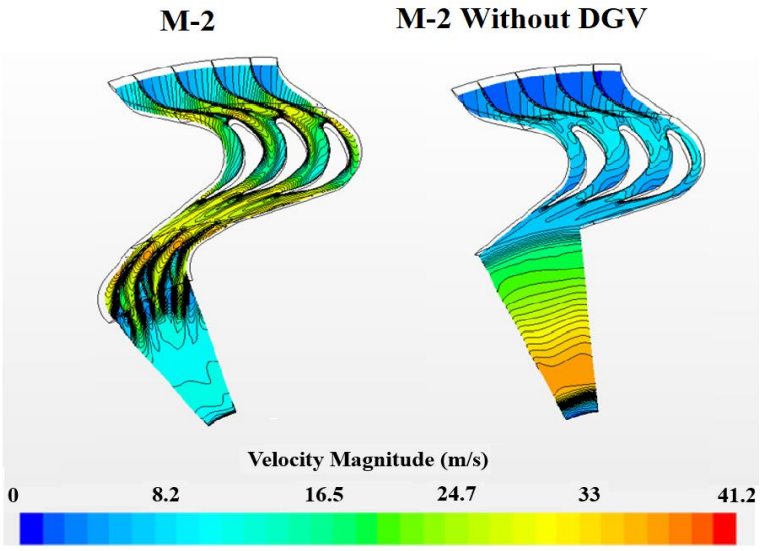

Figure 2.11 Comparison of the velocity contour in M-2 and M-2 without DGV configurations, Δp_0 =1000 Pa.

2.3.2 Design improvement of the downstream section in M-3 configuration

Emphasising on the importance of having a gap between rotor exit and the duct entrance in the domain, the M-3 geometry was proposed with the same order of sections as M-2 (UGV, rotor, DGV, duct). The only difference between two geometries was the increased height of the casing from 44 mm at the inlet to 74 mm at the DGV exit. The height of the duct was modified in a way to appropriately interface with the increased sectional area of the DGV outlet of M-3. The increased height of the geometry was made by increasing the height of the casing, blade span and height of guide vane along axis Z (as shown in Figure 2.3). The tip clearance was kept at a constant gap of 1mm between the casing and turbine elements. The M-3 geometry benefited the turbine by compensating for the flow-passage width reduction from inlet to the outlet and eliminating the flow congestion at the DGV section. In addition, the wider area at the turbine exit was effective in reducing the dynamic pressure. Figure 2.12 compares the operational conditions of M-1 to M-3. As illustrated in Figure 2.12-a, the torque coefficients of M-3 and M-2 are higher than that of M-1. Comparing the C_T plots of M-2 and M-3, it is obvious that the obtained torque is slightly increased by enhancing the turbine height in M-3. The improved C_T can be explained by the increased velocity of the flow at the rotor entry of M-3. As shown in Figure 2.13 for equal total pressure given at the inlet, the airflow is more accelerated by the UGV section in M-3 configuration. While the M-2 accelerates the flow more at the DGV section. The velocity contours of both M-2 and M-3 at the UGV inlet and rotor mean-radius (V_R) are illustrated in Figure 2.14 and Figure 2.15. It is obvious that increased area of M-3 has not reduced velocity and acceleration of the flow. In fact, for equal inlet total pressure and sectional area at the inlet, M-3 allows more flow into the turbine than M-2. The increased flow rate into the turbine leads to higher torque obtained by M-3. A comparison of flow rate/total pressure drop results between M-2 and M-3 has been shown in Figure 2.16 .

According to Figure 2.12-b, the input coefficient mitigates when using the unidirectional configurations, and is the lowest for the case of M-3. It can be mentioned that larger casing area of M-3 enables this turbine to more efficiently produce output power from the available input power than M-1 or M-2. The efficiency plots, shown in Figure 2.12-c, support this statement, where the efficiency of M-3 reaches 60% at $\phi = 0.6$, while the peak efficiency values of M-1 and M-2 are 37% and 48% respectively. In addition, M-3 can maintain an acceptable level of efficiency over a wide range of flow coefficients, which provides above 35% efficiency at flow coefficients higher than 2. This rate for bidirectional geometry is approximately 22% and in case of M-2, it declines to 30%.

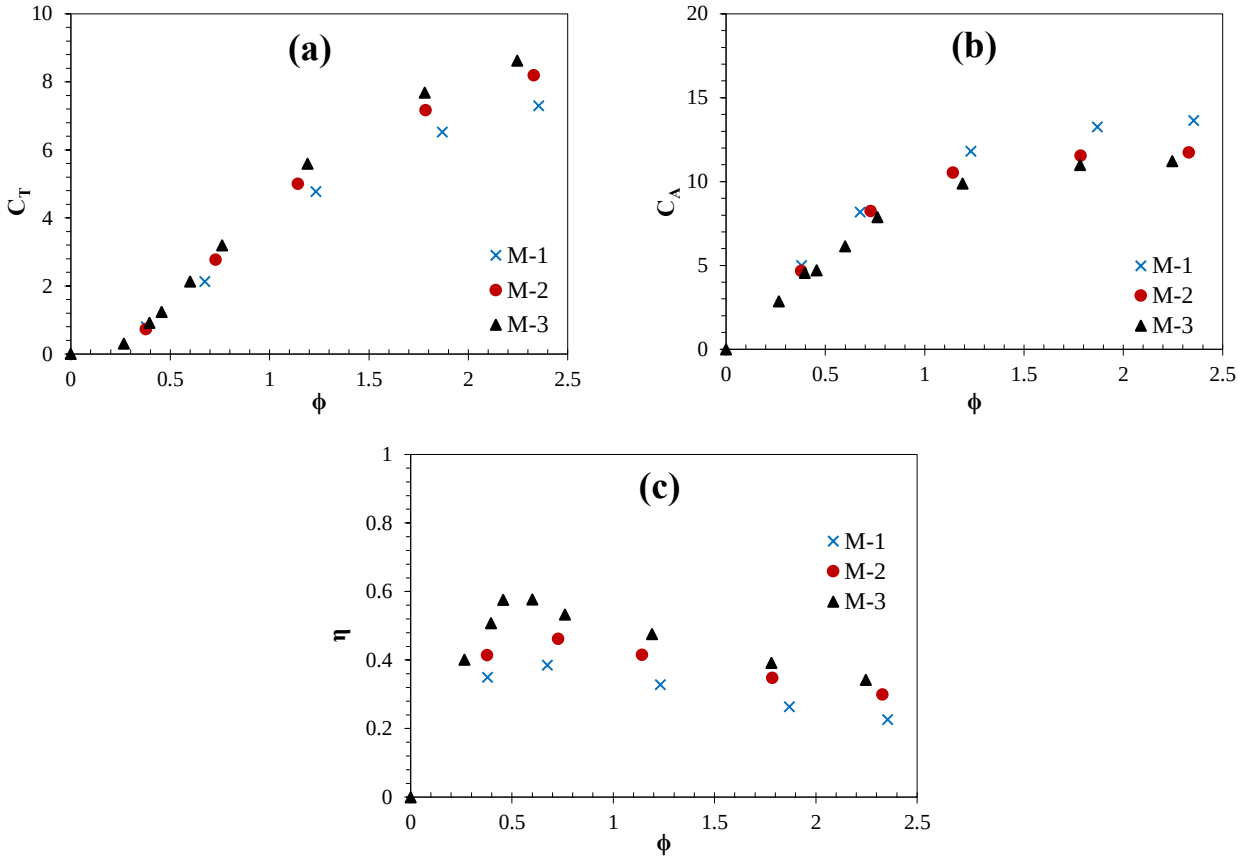

Figure 2.12. Comparison of turbine performance of M-1, M-2 and M-3. (a) C_T , (b) C_A and (c) η .

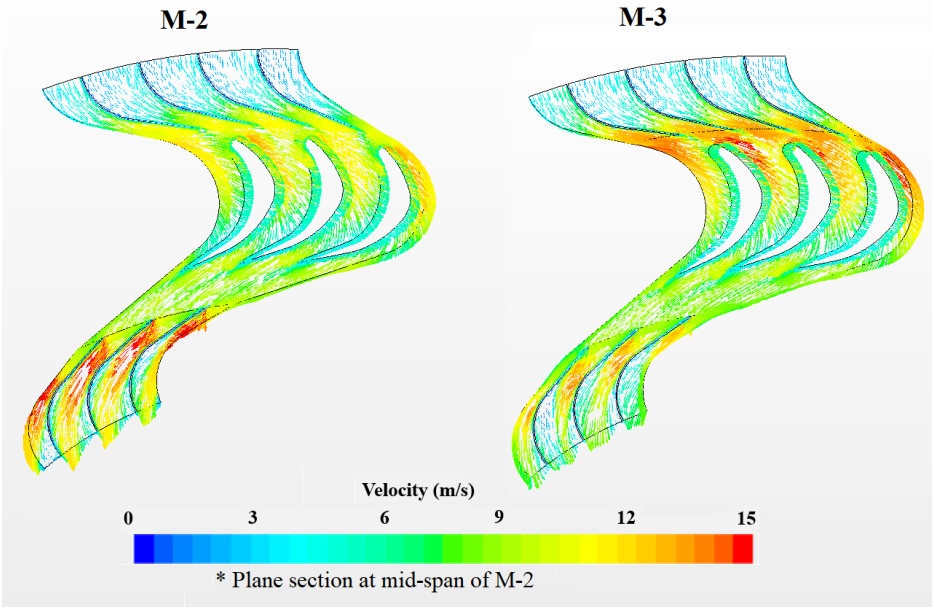

Figure 2.13 Comparison of velocity contour of M-2 and M-3 at a casing height equivalent to mid-span of M-2, ϕ = 0.65.

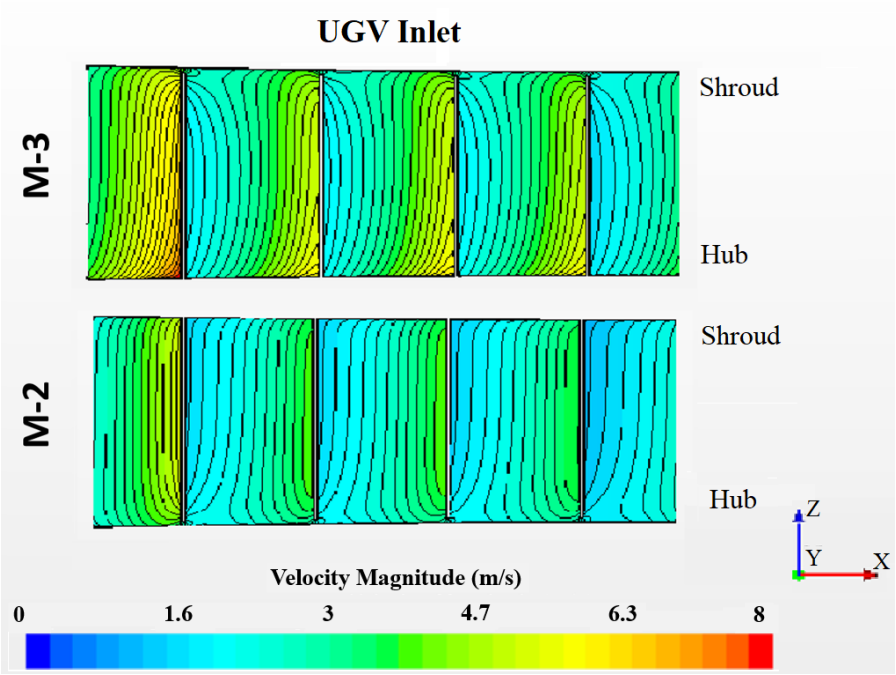

Figure 2.14 Comparison of velocity contour of M-2 and M-3 at UGV inlet, ϕ = 0.65.

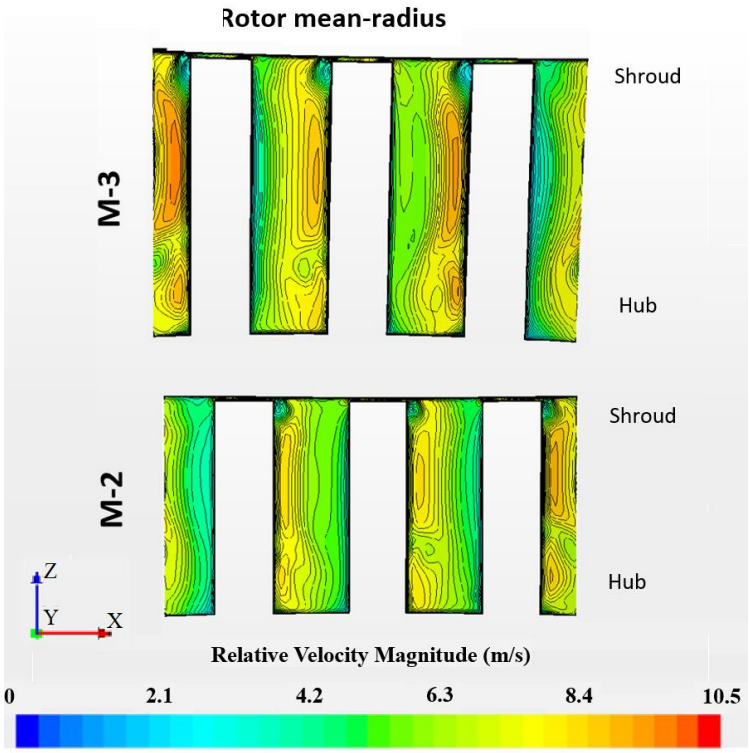

Figure 2.15 Comparison of velocity contour of M-2 and M-3 at rotor mean-radius, ϕ = 0.65.

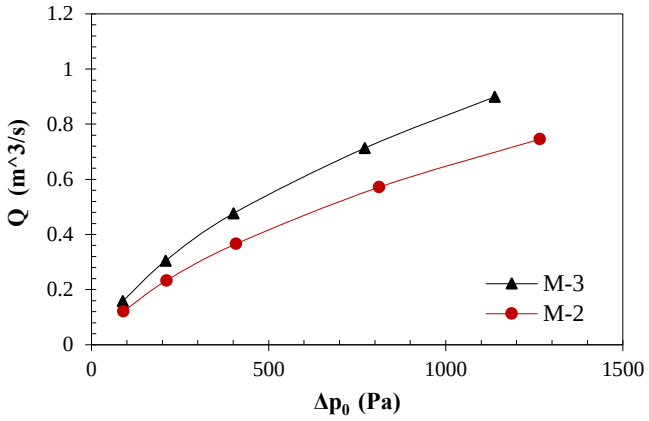

Figure 2.16 Comparison of Flow rate vs. total pressure drop of M-2 and M-3.

2.3.3 Comparison of energy losses of M-2 and M-3

Pressure losses in different parts of the domain were analysed by measuring the pressure drop values at the upstream, rotor and downstream sections separately. The downstream domain includes the DGV and duct. Pressure losses were calculated by subtracting the pressure drop of the rotor from total pressure drop of the whole turbine (Pereiras et al., 2014). The share of energy losses of each fixed element was evaluated by dividing the pressure drop of that element by the total pressure unused by the turbine (total pressure drops after subtracting the rotor pressure drop). The rotor energy exchange was measured regarding the rotor output power with respect to the input power provided to it (pressure differential of the rotor multiplied by the flow rate). The rotor energy losses were obtained considering the power lost in the rotor. The energy losses of M-2 and M-3 are compared in Figure 2.17 to investigate if the idea of increasing the casing height leads to reduced losses in the domain. Analysing the energy losses of M-2 and M-3, shown in Figure 2.17-a, indicates that the upstream section has the lowest share of energy losses in both geometries, with less than 7% losses over the whole range of flow coefficients. It was observed that M-3 causes more upstream losses than M-2, which can be justified by the increased span of the rotor blade and UGV height in case of M-3. The rotor losses of M-3 are less than that of M-2, by about 5% (as shown in Figure 2.17-b). This is largely due to the wider flow passage at the exit of the rotor, which eliminates the intensive bottleneck effects at the downstream of M-2. Considering the energy losses caused at the downstream (Figure 2.17-c), it is obvious that M-3 geometry is better than M-2 in reducing pressure losses in the domain. Where, the downstream domain was considered from rotor exit to the chamber entrance and contains the DGV and duct sections. It is obvious that the downstream losses are below 30% in case of using M-3, while M-2 causes approximately 10% higher losses than M-3 in this section. A comparison of the total pressure contour at DGV outlet of both geometries are shown in Figure 2.18.

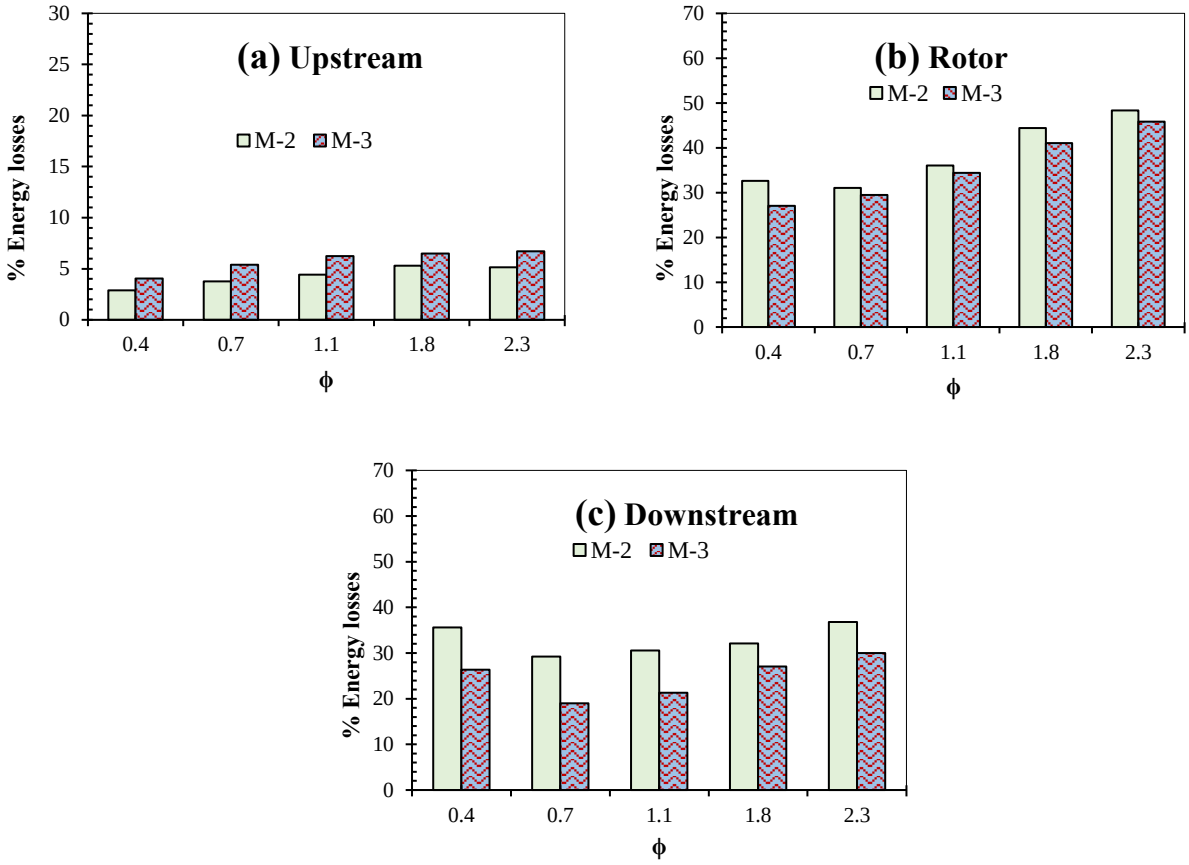

Figure 2.17. Energy losses at different sections of the domain. (a) Upstream (UGV), (b) rotor, (c) Downstream (DGV and duct).

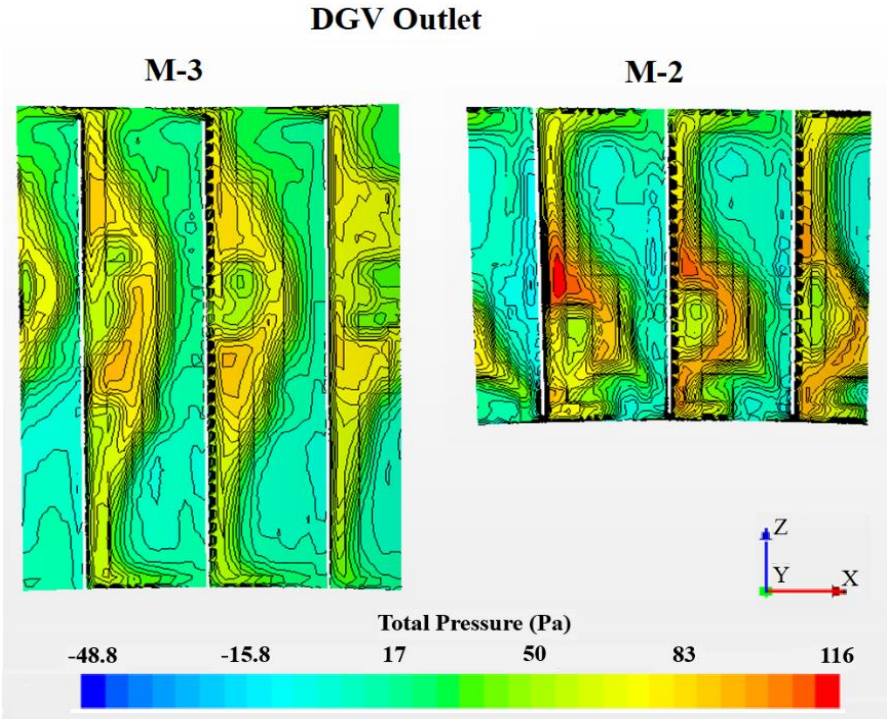

Figure 2.18 Comparison of total pressure contour of M-2 and M-3 at the DGV outlet, ϕ = 0.65.

2.3.4 Impact of downstream guide vanes in M-3

Generally, guide vanes are used in a turbine configuration to act as a nozzle. They are employed at the inlet to accelerate the velocity of the inward flow and are located at the outlet to act the same for the opposite direction of flow. Downstream guide vanes are mostly utilized in bidirectional turbines to increase the air velocity at the rotor inlet during the reverse mode. Nevertheless, even though the M-3 geometry is intended as a unidirectional turbine, use of guide vanes at the rotor downstream was a subject of question. To investigate the impact of the downstream guide vanes in the M-3 configuration, simulations were performed by varying the number of DGVs. First, three DGVs were set at the downstream section corresponding to a total number of 51 DGVs in the whole turbine geometry. Then this number was reduced to one third by setting only one guide vane in the downstream section and finally, all the guide vanes were removed from the downstream section. Figure 2.19 illustrates the changes applied on the guide vanes at the downstream section.

Considering Figure 2.20-a, the plot of torque coefficient versus flow coefficient remains unchanged for various numbers of DGV, which indicates the independency of the obtained torque from guide vanes at the rotor exit. However, when all the guide vanes are removed the range of operational flow

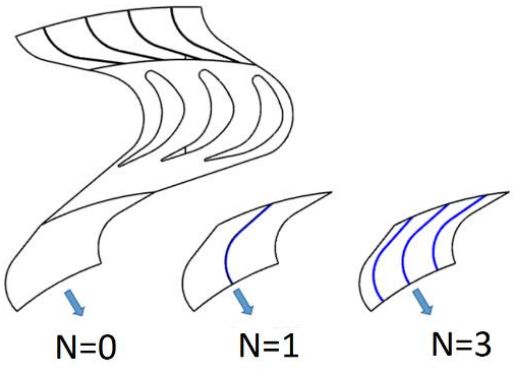

Figure 2.19. Changing the downstream section by removing or reducing the number of guide vanes.

coefficients become limited to flow coefficients lower than ϕ = 0.65. Figure 2.20-b, illustrates the significant change to the range of input coefficient based on the presence or removal of the DGVs. Removing all the downstream guide vanes has made the input coefficient plot to be initially lower than other geometries at smaller flow coefficients (ϕ <0.5), however at ϕ = 0.65 and afterwards it makes a vertical upward trend. This means that after ϕ = 0.65, increase of the pressure differential does not lead to higher flow rate into the turbine and the turbine is unable to extract more energy from the available pneumatic power. This phenomenon narrows the range of operational flow coefficients significantly. As shown in Figure 2.20-c, the efficiency plot of M-3 without DGVs has fluctuations at flow coefficients lower than ϕ = 0.45 and jumps to around 80%. However, the efficiency drops sharply

as the flow coefficient increases and becomes limited to ϕ = 0.65 and after that extreme flow congestion occurs in the turbine. After this point, the input coefficient is increased, but there is no increase in the torque produced by the turbine and ultimately the efficiency plot experiences a sharp downward jump. It should be noted from Figure 2.20-c that despite DGVs introduce incident losses, removing them leads to increased energy losses at the elbow and entrance of the duct. The peak efficiency of almost 0.80 for the M-3 configuration without DGVs is not practical, since the flow congestion has significantly limited the operational range of flow, torque and input coefficients (Figure 2.20) and there is a need to use DGVs in the configuration. In case of reducing the number of guide vanes to one third, the maximum efficiency peaks at 65%, approximately 5% higher than that of the case with 51 DGVs (Figure 2.20-c). However, as the flow coefficient increases, the case with more guide vanes at the downstream section shows the most acceptable performance over the given range of flow coefficients. Considering the desired range of input power and corresponding range of the flow coefficients, either of these cases can be useful. The reason for the flow congestion can be explained by comparing the velocity vectors in case of having zero or three downstream guide vanes. According to Figure 2.21, the lack of guide vanes causes

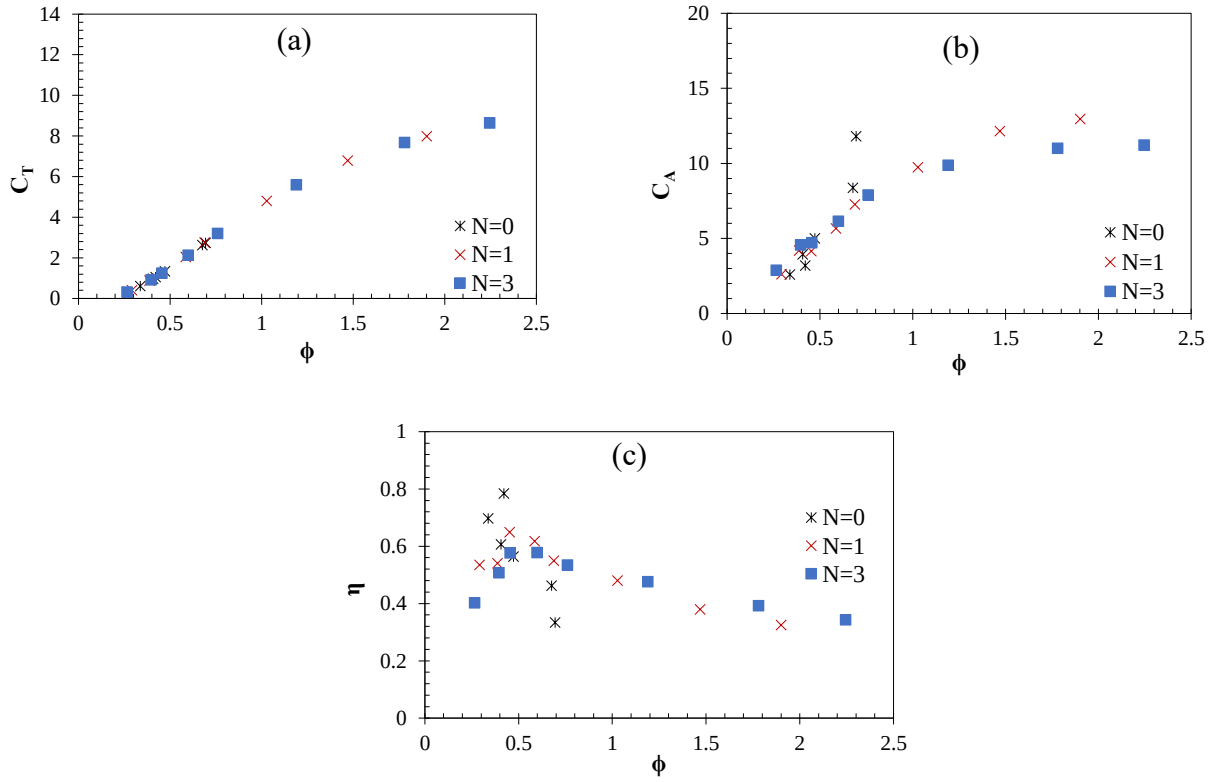

Figure 2.20. Performance of M-3 considering different numbers of guide vanes at the downstream section. (a) C_T , (b) C_A and (c) η .

the air to enter the duct with a relatively high swirl component, while presence of them helps the flow to properly move into the duct. Therefore, removing DGVs leads to increased energy losses at the elbow and entrance of the duct.

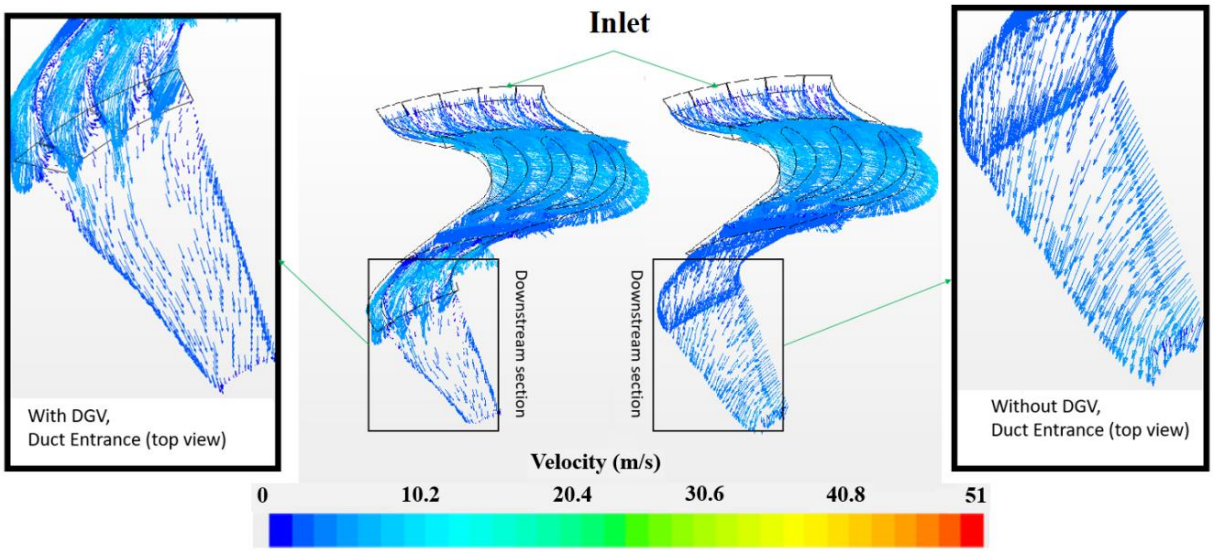

Figure 2.21. Flow behaviour at entrance of the duct (ϕ = 0.4), with downstream guide vanes (Left) and without downstream guide vanes (Right).

A comparison has been made on the pressure and velocity magnitudes of M-3 with and without downstream guide vanes as illustrated in Figure 2.22 and Figure 2.23. It is clear that in case of having downstream guide vanes in the turbine design, the pressure distributes inside the domain properly and there is a significant pressure differential at the rotor boundaries (Figure 2.22). On the other hand, in case of having no DGVs this pressure differential is missing, and the rotor cannot convert energy conveniently. This can be explained by the flow swirl at the duct entrance in case of N= 0, which has caused flow areas of high peripheral velocities at the rotor downstream. The air velocity at the rotor domain has reduced significantly compared to the case with three DGVs (Figure 2.23). Thus, absence of the DGVs has caused decreased flowrate and increased the losses at the downstream section. This is the reason for limited range of operational flow coefficients in Figure 2.20 (case N=0). It is obvious that the lower flow rate and consequently low air velocity values at the rotor mid-chord has led to limited C_T and the upward jump in C_A plot as shown in Figure 2.20-a and b respectively. As a result, the turbine efficiency due to being a function of C_T and C_A and ϕ (as shown in equation (2.2)) observes huge inconsistencies and fluctuations with the absence of downstream guide vanes. Based on the above-mentioned analysis, it is clear that use of downstream guide vanes are necessary for the M-3 configuration, not as a nozzle, but as a means to guide the flow into the duct appropriately, where a wide operational range is required. It should also be noted that the Figure 2.23 illustrates the velocity

contour at a high flow coefficient (near $\phi = 2$). According to the Figure 2.20, the M-3 without DGVs (N=0) does no work at higher flow coefficients and doesn't follow the angular momentum conservation. This is due to the flow congestion and high swirl velocity at the duct entrance. Therefore, it is clear that, compared to the N=3 case, the increase of velocity at the rotor exit is not observed and the efficiency plot has no result at higher flow coefficients.

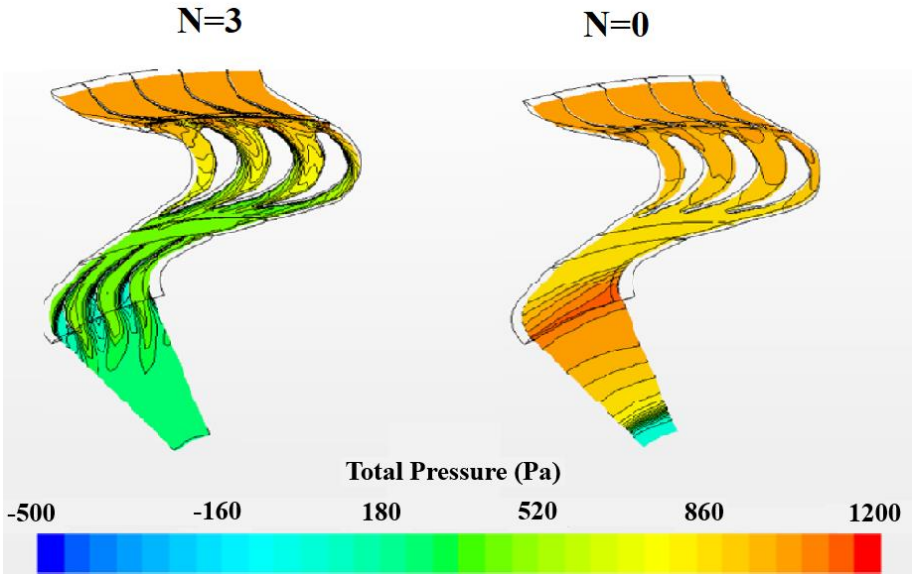

Figure 2.22 Comparison of the pressure contour of M-3 with three DGVs and M-3 without DGVs, Δp_0 =1000 Pa (higher flow coefficients).

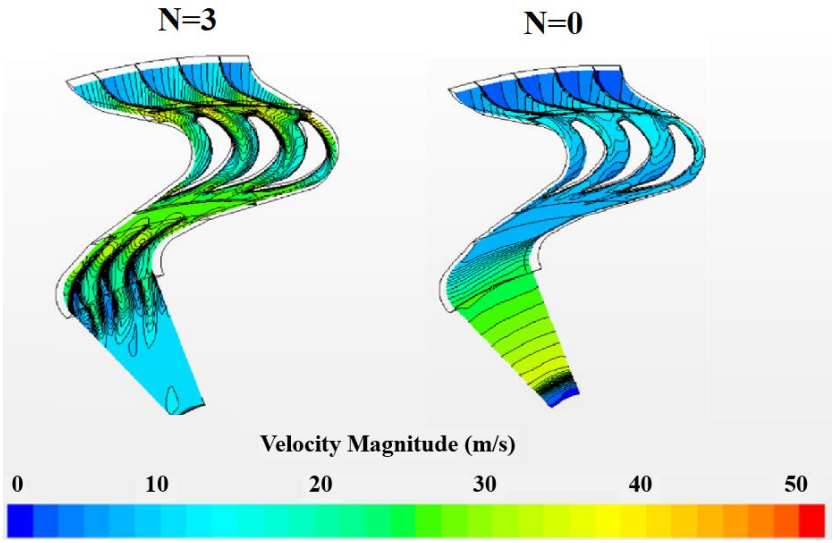

Figure 2.23 Comparison of the velocity contour of M-3 with three DGVs and M-3 without DGVs, Δp_0 =1000 Pa (higher flow coefficients).

2.4 Conclusions

This chapter presents a numerical investigation on the design of a unidirectional radial inflow turbine intended for use in a vented OWC. Some design drawbacks associated with the natural shape of a conventional radial turbine were highlighted. It was revealed in this research that shape of the downstream section can be the source of significant energy losses in the centripetal turbine configuration. A solution investigated to reduce these losses was by increasing the height of the turbine casing. This modification compensated for the reduction of the area at the downstream of the inflow radial turbine. The modified geometry resulted in lower energy losses in the rotor and downstream sections. It also produced significantly higher efficiency compared to a bidirectional radial turbine configuration, where an improvement in efficiency of between 35% to 60% was reached by the M-3 design over the whole range of flow coefficients. In addition, guide vanes at the downstream section are necessary to reduce the flow swirl, direct the flow into the duct section, avoid flow congestion at the downstream section and significantly extend the operational range.

The M-3 geometry still has potential for further improvements on recovering the kinetic energy at the rotor exit. In addition, the increased height of the casing needs to be further evaluated considering the turbine-chamber matching requirements. This parameter is likely to affect the damping coefficient of the turbine. Therefore, by finding the optimum height of the turbine casing the swirl components of the flow velocity at the rotor exit can be recovered more precisely. In addition, the shape and orientation of the downstream guide vanes can be redesigned according to the inhalation operational mode. The turbine downstream and duct entrance may also be reshaped as a diffuser to allow more kinetic energy recovery. This can be done by identifying the most effective geometrical parameters of the duct and DGV sections and using the optimisation techniques to find the optimum turbine geometry.

3 DESIGN MODIFICATION OF A CENTRIPETAL RADIAL AIR TURBINE CONFIGURATION (INFLOW TURBINE)

This chapter is based on two research papers; a conference paper presented at AWTEC 2018 by the candidate (Ansarifard et al., 2018), and a journal paper under review (Revised version is submitted) by the journal of Renewable Energy. The citation for papers are:

Ansarifard, N., Fleming, A., Henderson, A., Kianejad, S., & Chai, S. (2018). Optimisation Study on the Downstream Section of a Radial Inflow Turbine. Paper presented at the 4th Asian Wave and Tidal Energy Conference (AWTEC).

Ansarifard, N., Kianejad, S.S., Fleming, A., Henderson, A., Chai, Sh., "Design optimization of a purely radial turbine for operation in the inhalation mode of an oscillating water column", Renewable Energy, RENE-D-18-00676, (Revised version is submitted, under review).

Abstract

The aim of this study is to improve the efficiency of unidirectional-radial-turbines by integrating the systematic-optimisation-approaches with CFD methods. Efficiency maximization of a centripetal-radial-turbine has been considered in optimisation analysis in steady-state. Nine design variables were used to control the shape of the rotor and its adjustment to the inward-flow direction. The optimized rotor was found to achieve significant efficiency and output power by using asymmetric and non-zero-staggered blades. The downstream section was optimized for an efficient matching with the optimized-inflow-rotor and four parameters were used to control the shape of the downstream section. A diffuser with a 7-degree diffusion-angle was found to be the optimal connection between the turbine and the chamber. The inflow radial turbine obtained 81% peak efficiency in the steady-state, and its average efficiency over the expected flow coefficients is comparable to the axial-turbines used with OWCs.

Introduction

An Oscillating Water Column (OWC) is a Wave Energy Converter (WEC) device that is used to extract pneumatic power from the ocean. A turbine is employed as the Power Take-Off (PTO) unit in the WEC system to produce energy from the pneumatic power. UniWave (Fleming et al., 2017) is a vented OWC, in which, air valves are used to vent to atmosphere during positive air chamber pressure and divert all air flow through the turbine during negative air chamber pressure (air moves from atmosphere into the chamber through the air turbine (Figure 3.1). The airflow direction was chosen due to some specifics of the vents mechanisms and because this mode allows the energy to enter the device with lower impedance. The UniWave concept has been shown experimentally to provide equivalent or better pneumatic power conversion compared to bi-directional OWCs and has a significantly different pressure/flow profile compared to the conventional OWCs (Fleming et al., 2017). During a wave cycle, the rising of water level in the chamber causes positive air pressure, which exits the system through the chamber vents. Because the vents impart a low back pressure the water column rises higher compared to a bi-directional OWC, which temporarily stores the incoming energy as potential energy in the form of water column heave. In the second half cycle the vents are closed and the whole input energy of the negative pressure plus the stored energy of the previous half cycle becomes available to the turbine with higher pressure differential and flow rates compared to a vented OWC. A detailed comparison of pneumatic power of the vented type OWC and the bidirectional type OWC as shown in Figure 3.2, revealed that the vented OWC provides larger negative pressure drops compared to the bidirectional OWC and extracts significantly higher pneumatic power in a half cycle. Using the vented OWC concept can lead to a simpler turbine design, as the losses imposed by the reverse flow direction are significantly reduced in this concept. In addition, the unidirectional turbines

can be custom-designed for maximized efficiency in their unidirectional direct-flow-mode. Reducing the levelized cost of energy is an on-going concern in the WEC industry (Bull and Ochs, 2013). Careful designing of all sections of the chamber-turbine-generator package ensures wave to wire efficiency improvements that contributes towards reducing the cost of energy. Several studies have focused on optimising the turbine designs for OWC and identifying the most sensitive parameters affecting the turbine performance (Falcão et al., 2018, Falcão and Gato, 2012, Falcão and Henriques, 2016b, Rodríguez et al., 2019). The stall and starting characteristics of the Wells turbines were reported to be modified by varying the hub-to-tip ratio and solidity parameters (Raghunathan, 1995). In addition, the turbine efficiency was revealed to be mainly affected by the aspect ratio and tip clearance of the rotor blades (Inoue et al., 1986, Raghunathan and Tan, 1982). In impulse turbines, parameters such as Reynolds number and hub-to-tip ratio (Setoguchi et al., 2004) and guide vane angles (Maeda et al., 1999, Setoguchi et al., 2001) were identified to affect the turbine efficiency. A two-dimensional analysis was carried out by Pereiras et al. (Pereiras et al., 2011b) considering the performance reduction due to the noticeable pressure drop imposed by inner guide vanes. Ansarifard et al. (Ansarifard et al., 2018, Ansarifard et al., 2019) identified a source of energy loss at the elbow of radial impulse turbines, due to the natural reduction of sectional area in a centripetal configuration. They suggested increasing the height of casing from upstream to downstream section in a way to maintain a constant sectional area from the inlet to outlet of the radial inflow turbines. An optimal turbine design, considering the operational conditions of the OWC, can be obtained using a numerical study integrated with the optimisation approaches. These approaches are fast and reliable and predict the optimal designs through identifying the relationship between parameters and responses. Systematic optimisations were applied on the airfoil blade shape to modify the turbine design and improve the efficiency of a reaction turbine by Mohamed et al. (Mohamed et al., 2011). The optimised airfoil design was reported to obtain 11.3% improvement in power output throughout a wide operational range. In addition, performance prediction of self-pitch controlled blades was studied by applying the optimisation techniques on a non-symmetric airfoil shape (Mohamed and Shaaban, 2014). Modifications of the blade camber line and thickness of Wells turbines (Raghunathan et al., 1991, Raghunathan and Tan, 1985) and impulse turbines (Gomes et al., 2012) were also conducted. In the latter study, a 3D geometry of the axial impulse turbine was generated through stacking the previously optimised 2D sections of the blade along the span-wise direction. Comparison showed that the optimal design obtained about 5% efficiency increase. In addition, optimum number of rotor blades and guide vanes were obtained by Badhurshah et al. (Badhurshah and Samad, 2015a) and Samad et al. (Samad et al., 2008) by employing multi fidelity analysis methods. The effect of design variables on pressure drop and shaft power were evaluated and about 11% efficiency improvement was achieved. Optimisation on blade sweep angle

of the wells turbine was also performed based on the surrogate modelling techniques, and the optimised sweep angle improved the rotor torque by over 28% (Halder et al., 2017). However, there are gaps for studying the flow behaviour inside the fixed elements of the turbine and considering the turbine-chamber requirements for efficiency improvements.

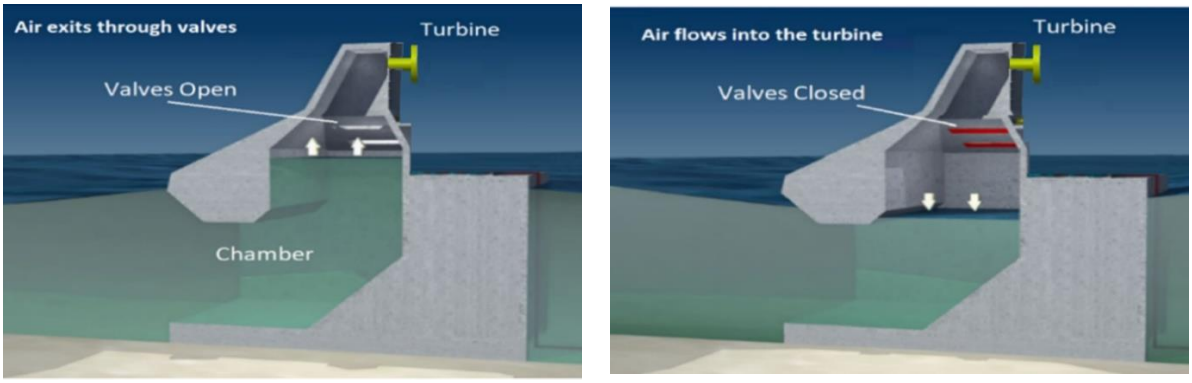

Figure 3.1 Concept of the UniWave OWC, the airflow exits the chamber when valves are open (left) and passes through the turbine when valves are closed (right) (Fleming et al., 2017).

The present study aimed to optimise the design of a unidirectional radial turbine for efficiency maximization in steady state. A centripetal configuration of the radial turbine was considered, and design optimisation was performed in two separate steps. First, by subtracting the duct section from the turbine domain and focusing on design optimisation of the inflow rotor, and second, by finding the shape of downstream section (DS) suited for the operation of the inflow radial turbine. The investigations were performed using CFD simulations (ANSYS, CFX 18.0) and the computational model was validated through a comparison with the available experimental data of a bidirectional radial turbine geometry (M-2 in (Ansarifard et al., 2019) and case (1) in (Setoguchi et al., 2002)). Parametric shapes of rotor blades, downstream guide vanes and duct section were considered by defining a list of parameters and specifying a variation range for each of them. The initial geometry of the unidirectional radial turbine used in optimisation analysis has been defined in section 2, followed by the details of the numerical model in section 3. Section 4 covers the process of exploring an optimum turbine design through performing multiple optimisation studies. Finally, section 5 discusses the characteristics of the optimum unidirectional radial turbine (inflow turbine) in details and compares it with the existing unidirectional turbines.

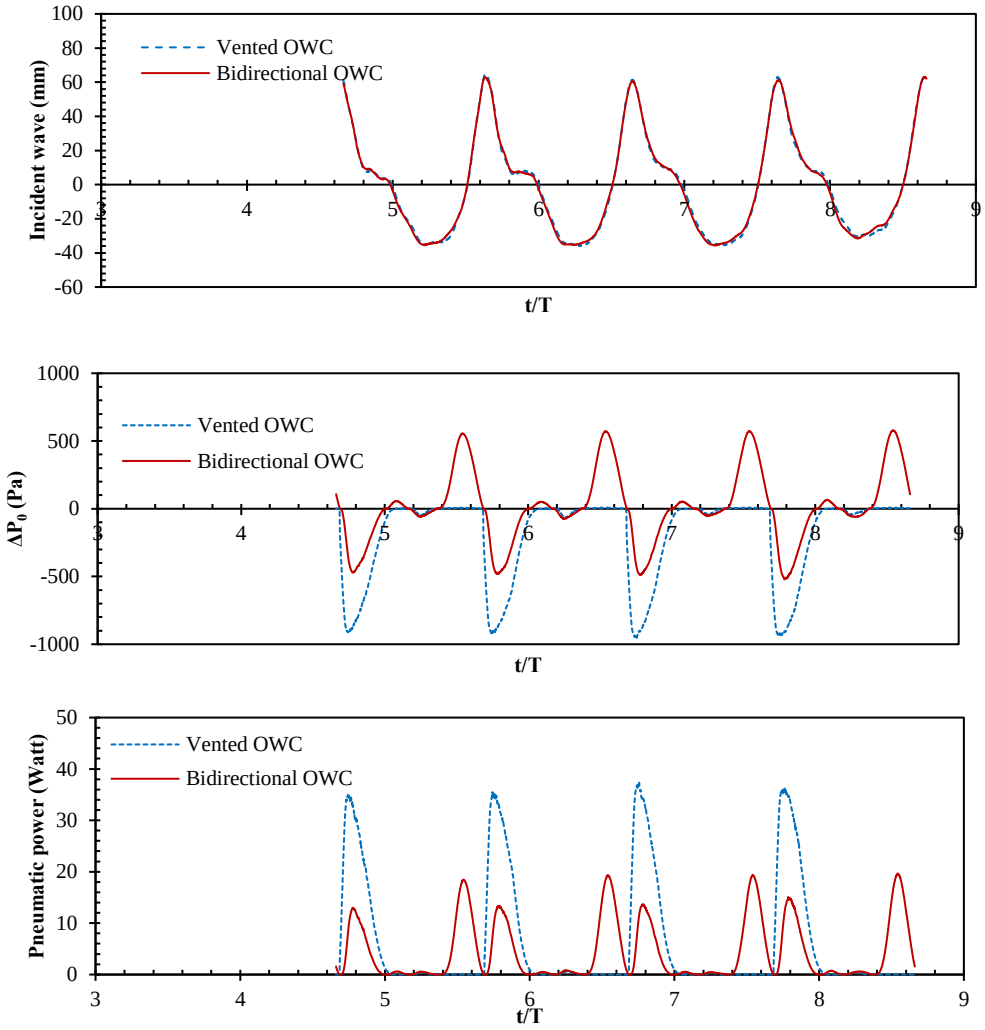

Figure 3.2 Comparison of chamber pressure and pneumatic power in a vented and a bidirectional OWC at model scale, Regular wave H=0.08 m, f=0.311 *Hz*.

3.1 Geometries

A bidirectional configuration of a radial turbine, extracted from Ref. (Setoguchi et al., 2002) and previously investigated by the authors (M-1 in Ref. (Ansarifard et al., 2019)), was used in this study to validate the numerical method and to be used as a reference for creation of an initial centripetal (inflow) radial turbine geometry. The bidirectional turbine geometry has the main characteristics presented in Table 3-1. The initial inflow turbine geometry was designed according to the main geometrical characteristics of the bidirectional turbine with similar geometries of the duct and upstream guide vanes (UGVs) with the bidirectional turbine. In addition, inlet diameter (of the rotor and UGV sections) and the number of upstream guide vanes and rotor blades (RBs) were equal in both turbines (73 UGVs and 51 RBs). The main differences were using asymmetric rotor blades appropriate for an inward flow direction and using 20 downstream guide vanes (DGVs) in an opposite direction to guide the flow into the duct section. Using or removing the guide vanes at the downstream of a

centripetal radial turbine was previously studied by the authors (Setoguchi et al., 2002) and it was found that using DGVs (but decreasing their number) in this turbine geometry is necessary.

Table 3-1 Bidirectional turbine specifications.

	Blade number	***Chord length***	***Setting angle***
DGV	*52*	*50 mm*	*25*
RB	*51*	*54mm*	*19.8°/35.8°*
UGV	*73*	*50mm*	*25°*

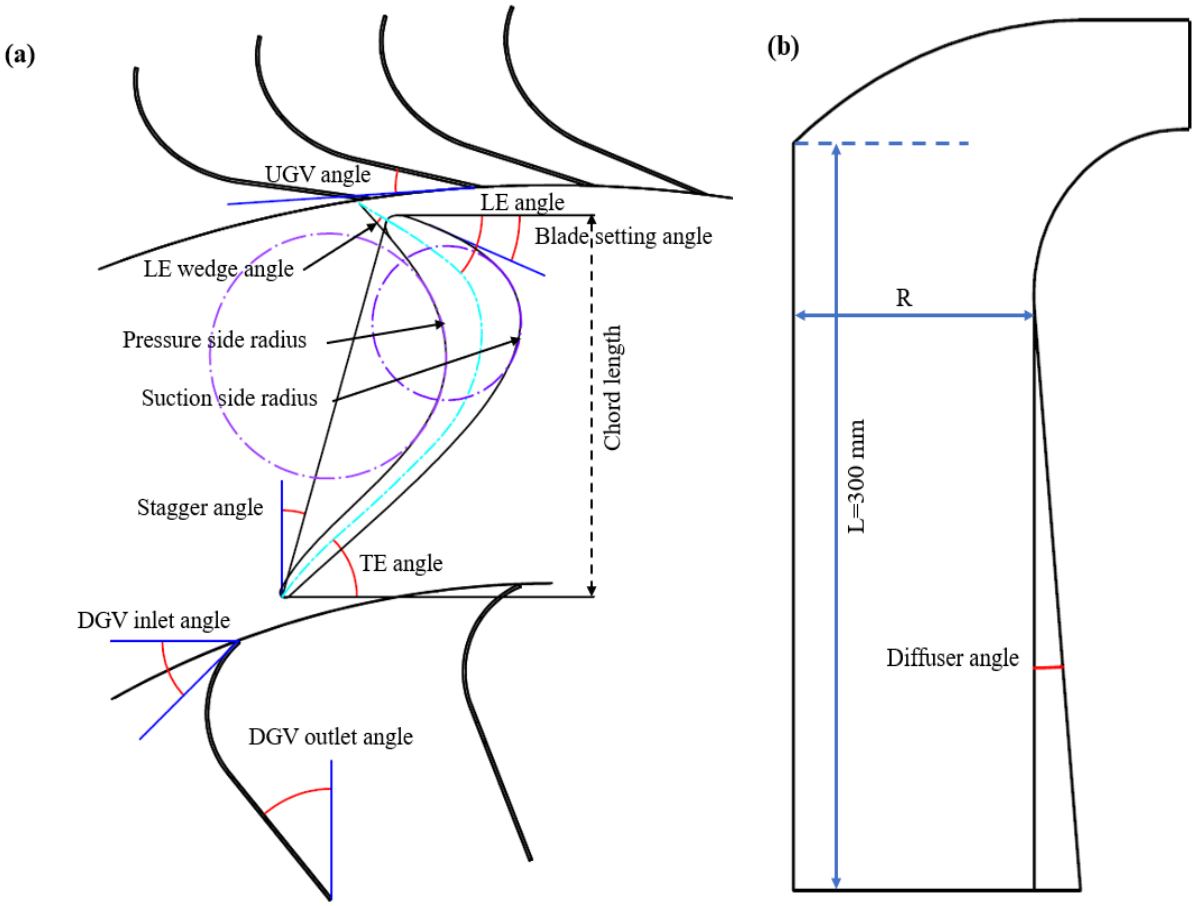

Figure 3.3 Illustration of parameters used in creation of the inflow turbine.

A parametric geometry of the inflow radial turbine was defined by a set of CAD variables. Eight parameters were used to create the rotor geometry, one parameter to enable the adjustment between the rotor blades and the UGVs and four parameters to control the parametric geometry of the downstream section (including duct and DGVs). The parametric turbine geometry and the way each parameter is defined are illustrated in Figure 3.3. The variation range of the rotor parameters was considered in a way to obtain a flexible asymmetric blade profile with highly-curved suction and pressure sides. the shape of DGVs was controlled using two parametric angles at the inlet and outlet of the DGVs row as illustrated Figure 3.3-a. The duct geometry was varied using two main parameters:

radius (R) and diffuser angle as shown in Figure 3.3-b. Table 3-2 indicates the variation range of these parameters and their values in the initial inflow turbine design.

Table 3-2 Design variables in the parametric inflow turbine geometry with upper and lower limits.

Design variables	***Lower bound***	***Upper bound***	***Initial inflow turbine***
Chord Length (mm)	*54*	*74*	*70*
LE Angle (°)	*35*	*45*	*43*
LE Wedge Angle (°)	*10*	*30*	*25*
Pressure Side (PS) Radius (mm)	*0.4*	*0.6*	*0.55*
Stagger Angle (°)	*20*	*30*	*27.6*
Suction Side (SS) Radius (mm)	*0.5*	*0.7*	*0.65*
TE Angle (°)	*30*	*50*	*40*
Blade Setting Angle (°)	*70*	*90*	*75*
UGV Angle (°)	*10*	*45*	*30*
DGV Inlet Angle (°)	*10*	*90*	*20*
DGV Outlet Angle (°)	*0*	*20*	*20*
Duct Radius (R) (mm)	*80*	*120*	*107*
Diffuser Angle (°)	*0*	*10*	*0*

3.2 Numerical model

Numerical simulation tools were employed to perform the aerodynamic and design optimisation of the inflow radial turbine. The computations were conducted using ANSYS CFX, and the parametric 3D model of the rotor was generated using the CAESES software (UserGuide, 2017) with the ability to be integrated with the ANSYS workbench 18.0 for automated mesh and CFD analysis. As CAESES was an external modelling software, the turbo-mode tool in ANSYS-CFX was used to setup the problem and to ease the iterative process of the optimisation study. The quasi-steady assumption was assumed for the flow, considering the frequency ratio between the rotating domain and the period of the wave cycle in the OWC chamber (Rodríguez et al., 2018). Since the wave cycle frequency was noticeably lower compared to the rotor frequency, their interaction was considered negligible and the steady flow assumption was justified (Cui and Hyun, 2016). The Moving Reference Frame (MRF) approach was used to set up the steady model and assume a constant speed of 120 rad/s for the rotor, and a frozen rotor interface between the rotor and the stationary domains. In this approach both stationary and rotating domains are solved in steady state with a frame change model connecting them. It is clear that the actual condition is unsteady as the rotor is rotating, however, to reduce the computational cost, the optimisation study was performed using the MRF model. The results of the optimisation study were later performed in a transient model (as will be described in section 5.3) to evaluate the errors due to ignoring the unsteady interaction between the rotating and the stationary domains. An angular section of the geometry, equivalent to 1/17th of the whole turbine, was used as the computational domain to reduce the computational overhead and periodic boundaries were set on

either sides of the domain, as illustrated in Figure 3.4. A frozen interface was used between the stationary and rotating domains and the pitch angle ratio was maintained close to 1 by applying appropriate passage and alignments between the duct, rotor and guide vane sections. Uniform total pressure at the inlet and uniform static pressure at the outlet were applied as the boundary conditions (Figure 3.4). The total pressure at the inlet was varied in a way to provide the typical range of non-dimensional flow coefficients (ϕ = 0.25 to ϕ = 2.5) for an OWC (ϕ is defined in equation 3.4). The flow was assumed incompressible and the realizable k-ε turbulence model was selected due to being economical in terms of CPU and time. This turbulence model has been utilized in similar studies of the field and accurate results were obtained (El Marjani et al., 2008, Pereiras et al., 2011c). The flow in all simulations was considered steady and unidirectional with a convergence criterion set to an RMS residual target of 10^{-6}. The simulations were performed at a Reynolds number ($\mathrm{Re} = \omega r^2_{in} / \upsilon$) of 1.4×10^6 (Dixon and Hall, 2013). The OWC turbine performance in steady state was described by a set of parameters (Setoguchi et al., 2002); torque coefficient C_T, input power coefficient C_A, turbine efficiency η and flow coefficient ϕ as follows:

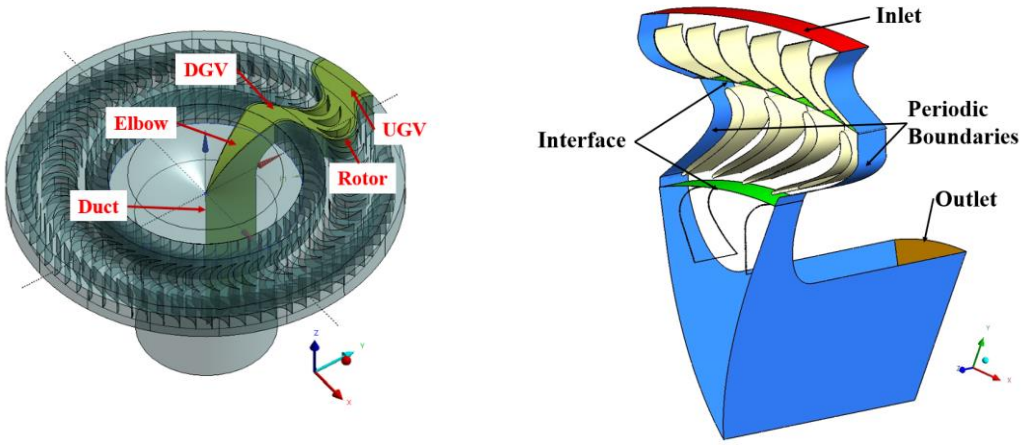

Figure 3.4 Computational domain and boundary conditions of the centripetal radial turbine.

$$C_T = T_0 / \left\{ \rho \left(V_R^{\,2} + U_R^{\,2} \right) A_R r_R / 2 \right\} \tag{3.1}$$

$$C_A = \Delta p_0 Q / \left\{ \rho \left(V_R^{\,2} + U_R^{\,2} \right) A_R V_R / 2 \right\} \tag{3.2}$$

$$\eta = \frac{T_0 \omega}{\Delta p_0 Q} = \frac{C_T}{C_A \phi} \tag{3.3}$$

$$\phi = V_R / U_R \tag{3.4}$$

The detailed definitions of the variables contributing in these coefficients are given in the nomenclature section.

3.2.1 Mesh

The meshing was generated in ANSYS by setting the size function on proximity and curvature to provide greater control over the mesh quality near the edges. Inflation layers were applied in sensitive areas such as near the blade's suction and pressure sides, guide vanes, walls and interfaces to allow the solver to determine the forces on walls, flow incidence, secondary flows and separation. In the viscous sublayer of a turbulent boundary layer, velocity gradients normal to the walls are very steep and using an inflation-layered mesh leads to an accurate capture of near-wall flow behaviour and resolves the viscous sublayer directly (low Y^+ ~1) (ANSYS-User's-Manual). Twenty inflation layers with the

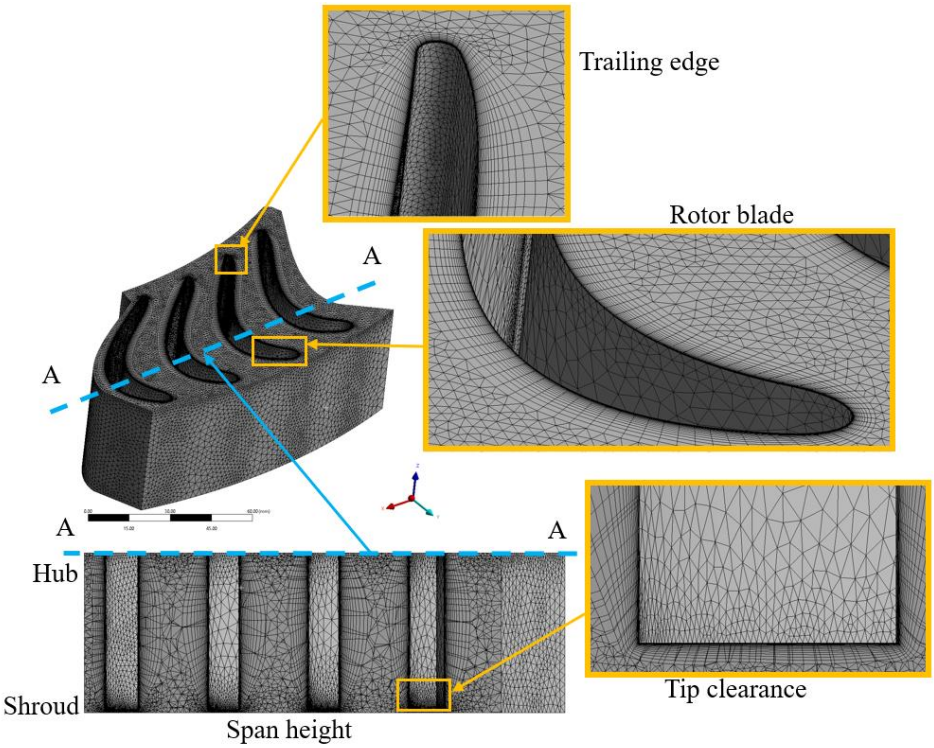

Figure 3.5 Schematics of the mesh configuration with inflation layers.

transition ratio of 0.5 and growth rate of 1.2 were applied for meshing the computational domain, as schematically illustrated in Figure 3.5. The minimum size and proximity settings were varied to study mesh independence by creating four cases with 0.45, 0.7, 1.7 and 5 million tetrahedral mesh cells. This number of cells refers to meshing of an angular section, approximately 1/17th of the whole turbine geometry. As shown in Figure 3.6, the percentages of deviation were evaluated compared to Case 4, with 5 million cells. Where Case 1 denotes the minimum number of cells (0.45 million), and the number of cells increases from Case 1 to Case 3. It is obvious that Case 1 obtained the least accurate results compared to other cases with over 12% deviation in C_T. Case 2 provided a maximum deviation

of about 6% and the discrepancy of results in Case 3 is practically nil. Therefore, Case 3 with a total number of 1.7 million cells was used for the CFD simulations to save time and reduce CPU usage.

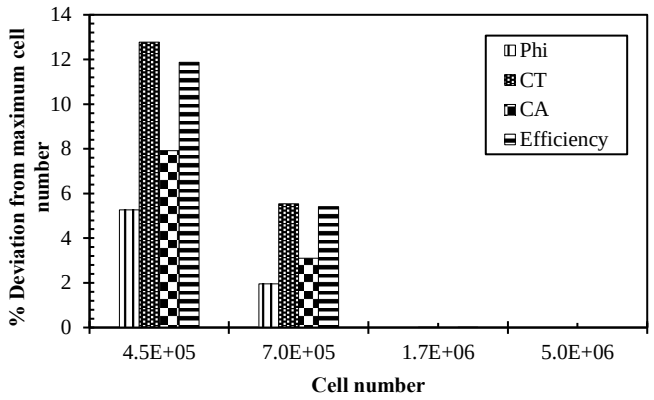

Figure 3.6 Results of grid independency studies and comparison of the deviation from maximum cell number (5×10^6).

3.2.2 Validation of the CFD model using the bidirectional turbine geometry

The bidirectional turbine geometry was experimentally tested by Setoguchi et al. in (Setoguchi et al., 2002) and was used for validation of the numerical model in this study. Geometrical details of this turbine were provided in section 2. A comparison between the turbine characteristics predicted by CFD and the experimental data of Case (1) in (Setoguchi et al., 2002), are shown in Figure 3.7. Under both directions of the flow, the CFD-predicted results follow a similar trend to the experimented data for torque coefficient, input coefficient and efficiency. The CFD results are in better agreement at flow coefficients lower than ϕ =1, where the peak efficiency point of both inhalation and exhalation plots falls in this range. In lower flow rates, the exhalation case shows slightly better agreement than inhalation, and disagreement becomes more obvious as the flow rate increases. Nevertheless, the results predicated by CFD correspond reasonably to the experimental data and provide confidence in the accuracy of the CFD model used in the analysis of the unidirectional radial turbines.

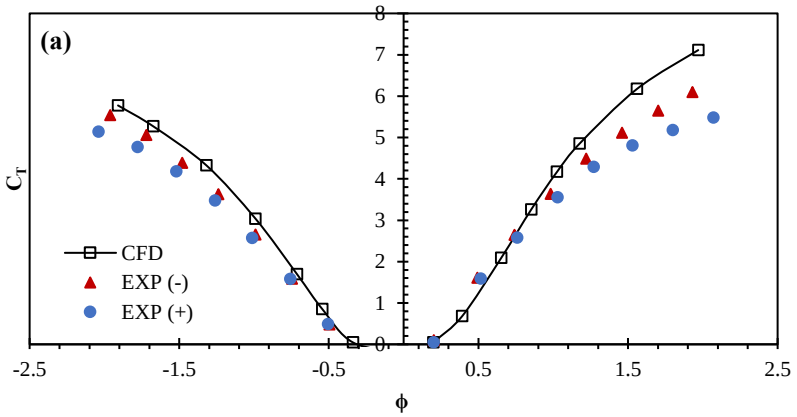

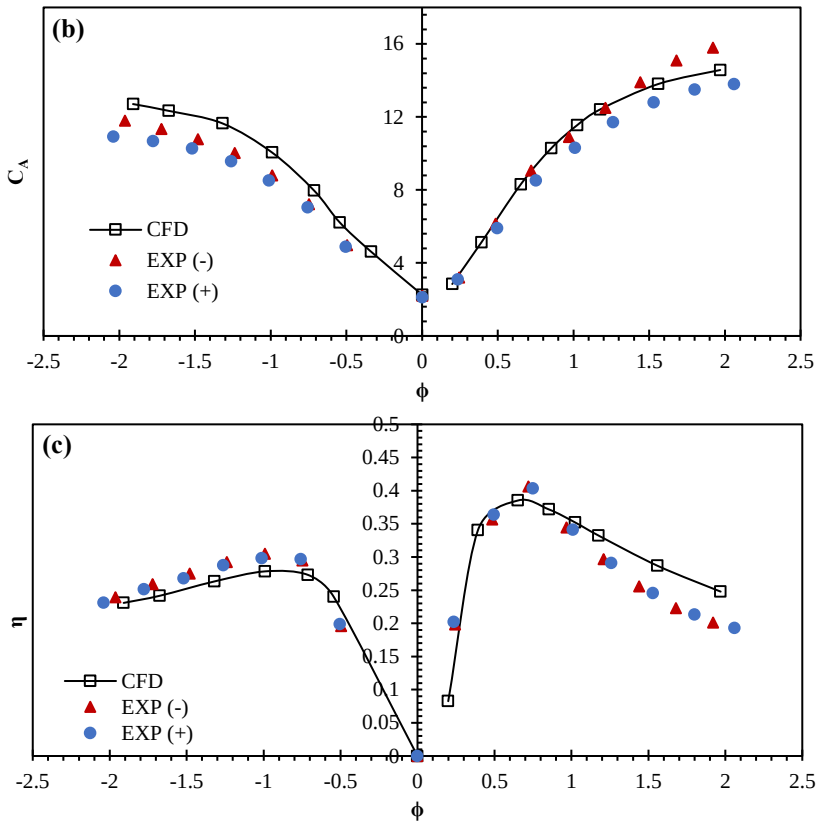

Figure 3.7 Comparing the CFD results of the current study with the published experimental data (Setoguchi et al., 2002) (a) C_T , (b) C_A and (c) η.

3.3 Optimisation

The optimisation study is an iterative process which begins by performing CFD simulations on the initial geometry of the inflow turbine. Then, the output parameters are defined, and the design exploration is used to create a design population by varying the input parameters. In this study, Design of Experiments method (DOE) was used to determine the design space and characterize the turbine performance based on a minimum number of actual analysis runs. The DoE conducts a series of experiments within the specified variation range of the input parameters set and minimizes the quantity of the required analysis runs to determine the parameters impacts. The Central Composite Design (CCD), based on a fractional factorial design was used to reduce the number of experiments by sacrificing less meaningful high-order interactions (Jung et al., 2016). A second order analysis was used with capability to model the interaction between the input parameters and surface curvatures appropriately. The general form of a second-order model explained in Ref. (Hatami et al., 2015) is:

$$y = a_0 + \sum_{i=1}^{n} a_i x_i + \sum_{i=1}^{n} a_{ii} x_i^2 + \sum_{i=1}^{n} \sum_{j=1}^{n} a_{ij} x_i x_j \tag{3.5}$$

Where, x_i and x_j are the design variables, a the tuning parameter and n the number of parameters. In the CCD, an optimal design space is considered with two criteria: the degree of non-orthogonality of regression terms (or Variation Inflation Factor (VIF)), and the position of sample points

(Leverages or the diagonal elements of the design matrix). Using this method, the design space contains a centre point, $2n$ design points located at the -α and +α position on each axis of the selected input parameters and 2^{n-f} factorial points located at -1 and +1 positions along the diagonals of the input parameters space. Where α is selected such that both the maximum VIF and the maximum leverage are the minimum possible and f is the fraction of the factorial design and is a function of n. As an example, CCD for two design variables consists of four factorial points, four axial points, and one central points as schematically shown in Figure 3.8. In this study 13 input parameters were considered, 2^{13-5} fractional factorial designs were used, which significantly reduced the number of experiments from the 2^{13} factorial designs.

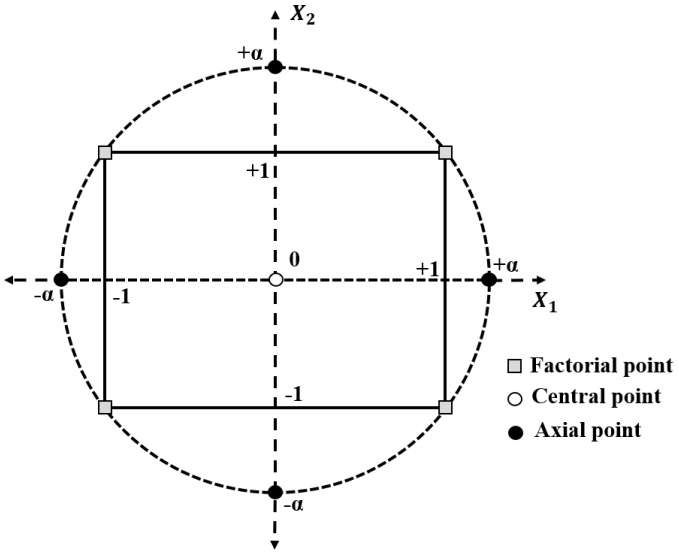

Figure 3.8 Central composite design for two design variables at two levels (Jung et al., 2016).

The response surface function is used in the next step to fit the actual analysis data characterized by the DoE and samples a surrogate model. The response surface optimisation is used to perform an indirect optimisation analysis and evaluate the optimum candidate design predicted by various methods (Ghotli et al., 2013). It provides a smooth and continuous mathematical formulation by interpolating between discrete design points of the DOE. The response surface optimisation method allows the design points to be predetermined by the DOE and permits simultaneous solving of the response-surface design points and performing multiple optimisations. In the current study, three different response surface algorithms were used to predict the optimum design point: Standard Response Surface (SRS), Kriging (KRG) and Genetic Aggregation (GA). The SRS is a regression analysis of the second-order polynomial type, which determines the relationship between the input and output parameters using the descrete design points of the DOE. This regression model is an approximation of

the true input-to-output relationship. Once this relationship is determined, the resulting approximation of the output parameter as a function of the input variables is called the response surface. The KRG is a meta modelling algorithm, which is an accurate multidimensional interpolation approach combined with a polynomial model. It has the capability to automatically and iteratively update and refine the design points during the update of the response surface. GA is a meta model that selects the most appropriate response surface for each output parameter based on the genetic algorithm. It solves different response surfaces in parallel, analyses them regarding their accuracy and the stability in the cross-validation and can be a single response surface or a combination of several different response surfaces.

After creation of the response surfaces, multi-objective genetic algorithm (MOGA) was used as the optimiser. In the MOGA method feasible solutions were specified according to the bounds of the optimisation problem and the optimal solution was explored by analysing the maximum allowable Pareto front (Amouzgar K., 2015). The general process of the optimisation study of this study is illustrated in Figure 3.9. It should be noted that up to 20 parameters could be considered in the DOE Guide (2017), however, this number of parameters causes a large design space. Although the DOE minimizes the number of required analysis runs, still there are a considerable number of experiments to perform. Exploring the optimum design of this study among 283 design points (considering all 13 input parameters and the factorial number of $f = 5$) was not economical in terms of the simulation time and computational resources. Therefore, the optimisation study was performed in two steps:

Step 1: Optimising the shape and adjustment of the rotor blades for a maximized torque generation. In this step, the efficiency was calculated based on the inlet total pressure and variations of the pressure at the outlet boundary were excluded. To evaluate variations of the torque, power coefficient (C_P) was defined as a second output parameter due to being easier to measure compared to the C_T (equation 3.1). Therefore, the optimisation objectives in this step were maximization of the efficiency and power coefficient defined as below:

$$\eta = \frac{T_0 \omega}{p_{t-in} Q} \tag{3.6}$$

$$C_P = T_0 \omega / \rho \omega^3 (2r_R)^5 \tag{3.7}$$

The computational domain in this step was excluded the duct and elbow sections, however, the stationary DGV domain shown in Figure 3.4 without its vanes was maintained at the turbine downstream. The vanes were removed from the DGV section as their primary function is guiding the flow into the elbow and duct sections (however these sections were suppressed from the computational domain). Apart from the above-mentioned function, use of guide vanes at the rotor exit did not benefit

the rotor performance but could cause flow resistance. In addition, according to a previous study by the authors (Ansarifard et al., 2019) it was found that removing or using the DGVs almost had no effect on the torque coefficient of the inflow turbine. This can be explained by the Euler work equation (Aungier, Dixon and Hall, 2013, Howell, 1967), according to which the work transferred in a turbomachinery stage depends on the tangent velocity (V_u), blade speed (U) and the exit flow angles of the UGV and rotor sections. Therefore, the DGVs due to being placed at the rotor exit have no direct effect on the torque, but they can affect the flow field, input coefficient and the efficiency of the turbine.

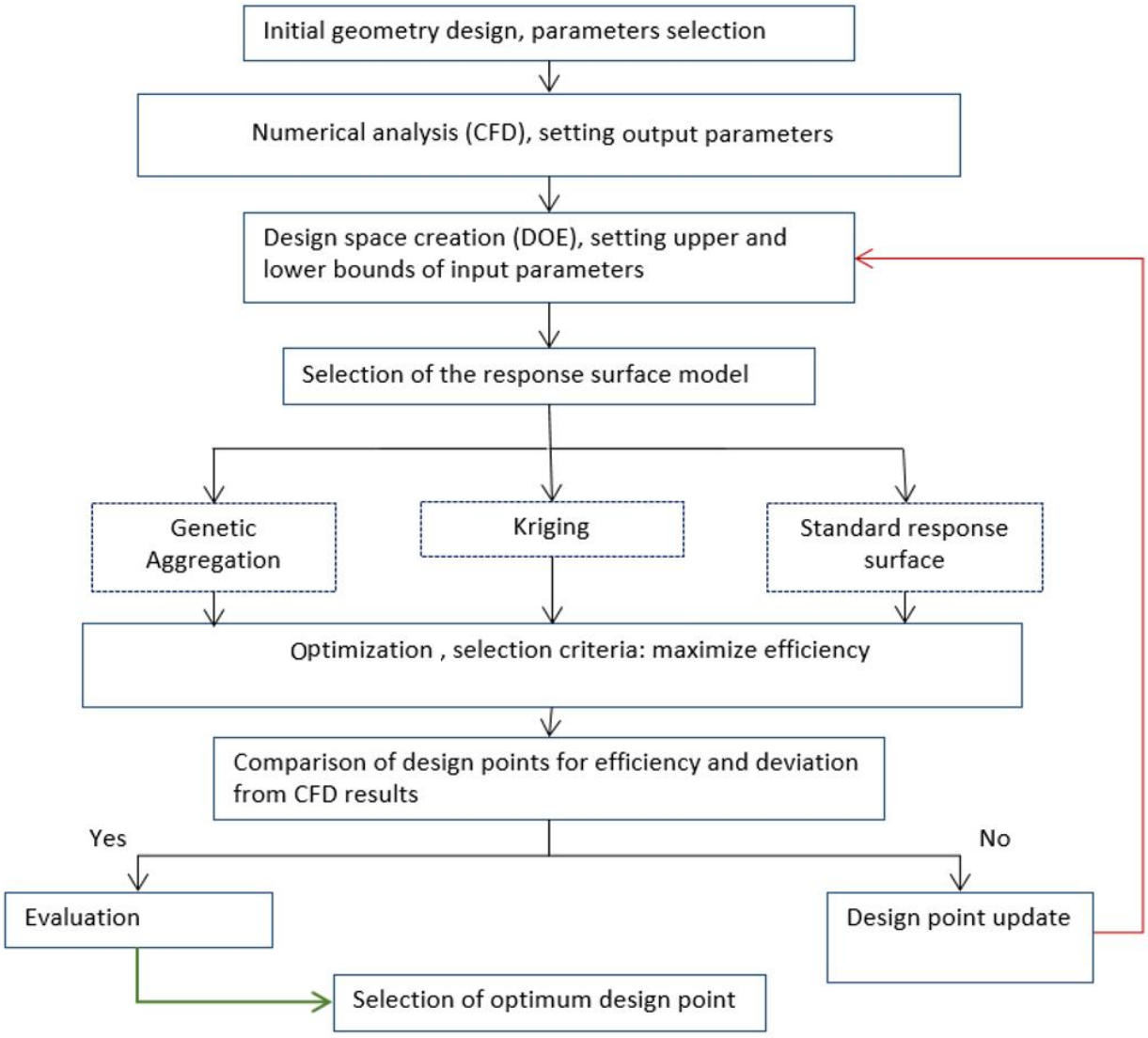

Figure 3.9 Optimisation process.

Step 2: Optimising the geometry of the downstream section for the optimised rotor geometry achieved in the previous step. In this step, maximization of the total to static efficiency of the whole turbine (defined in equation 3.3) was chosen as the objective and the entire computational domain shown in (Figure 3.4) was considered. The impacts of the DGVs and duct on the energy losses and

the turbine-chamber matching, were determined by defining two output parameters of the downstream loss coefficient and the turbine damping. In the optimisation procedure, these parameters were set as the secondary criteria compared to the efficiency and were defined as:

$$\text{Damping} = Q / \sqrt{\Delta p_0} \tag{3.8}$$

$$\text{Downstream loss coefficient} = \Delta p_d / (1/2 \rho V_d^{\,2}) \tag{3.9}$$

The authors acknowledge that combining the steps 1 and 2 in the optimisation process might lead to a slightly different optimum design, however, it was not practical regarding the number of input parameters of this study. As an alternative, the results of this study can be used as a reference to eliminate the unnecessary input parameters in the rotor design and provide scope for an optimisation study including the entire turbine domain at reduced time and computational cost.

3.4 Results and discussion

3.4.1 Step 1 (Design optimisation of the rotor section)

In the first step of the optimisation analysis, 9 design variables in the upstream and rotor sections (Figure 3.3-a) were considered resulting in a design space of 147 experiments ($n = 9$ and $f = 2$). Three parallel optimisation studies were performed using the KRG, SRS and GA response surface algorithms and three candidates for optimum design were predicted by each algorithm. These candidates were verified by the CFD simulations over the specific conditions of the experiments in the ANSYS workbench (without the user interface) (Samad et al., 2008). The accuracy of each algorithm in predicting the relationship between the input and output parameters were compared in Table 3-3. In the table, RS denotes the efficiency predicted by the response surface, CFD shows the efficiency obtained from CFD simulations and %Err determines the percentage of error between the RS and CFD results. It is clear that the candidate 2 of the GA method was the most accurate prediction with the highest efficiency of 65%.

Table 3-3 Comparison of the CFD-verified and predicted results of each response surface model for the optimum turbine design.

Efficiency η	***candidate 1***			***candidate 2***			***candidate 3***		
Response surface	*RS*	*CFD*	*% Err*	*RS*	*CFD*	*%Err*	*RS*	*CFD*	*%Err*
KRG	*0.65*	*0.63*	*-3.82*	*0.66*	*0.62*	*-5.57*	*0.67*	*0.65*	*-2.62*
SRS	*0.69*	*0.64*	*-7.97*	*0.69*	*0.64*	*-7.65*	*0.68*	*0.64*	*-7.68*
GA	*0.62*	*0.62*	*0.12*	*0.65*	*0.65*	*0.81*	*0.62*	*0.63*	*1.17*

The efficiency plots of the optimum candidates predicated by GA, KRG and SRS methods are compared in Figure 3.10. It is obvious that all the response surface algorithms generated close predictions for the optimum design, however, GA provided slightly more accurate results. Thus, the

candidate 2 of the GA algorithm was used as the optimum inflow rotor, with the design characteristics indicated in Table 3-4. Figure 3.11 schematically compares the optimum design of the inflow turbine with respect to the initial turbine geometry. It should be noted that compared to the bidirectional geometry (M-1) which was an impulse type turbine, the optimum inflow turbine has found to be a reaction type turbine, which is due to the criteria for design optimization (optimum efficiency in unidirectional flow).

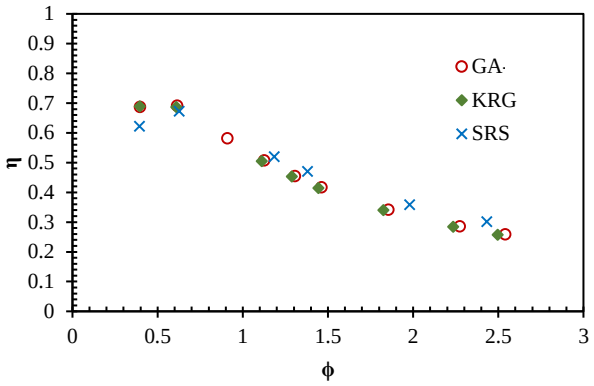

Figure 3.10 Comparison of turbine efficiency of the optimum design candidates predicted by GA, KRG and SRS responses methods.

Table 3-4 Optimum inflow rotor using the GA method (candidate point 2).

Design variables	***Value***
Chord Length	*66 mm*
LE Angle	*41°*
LE Wedge Angle	*17°*
Pressure Side Radius	*0.45 mm*
Stagger Angle	*28.5°*
Suction Side Radius	*0.5 mm*
TE Angle	*45°*
Blade Setting Angle	*83.5°*
UGV Angle	*15°*

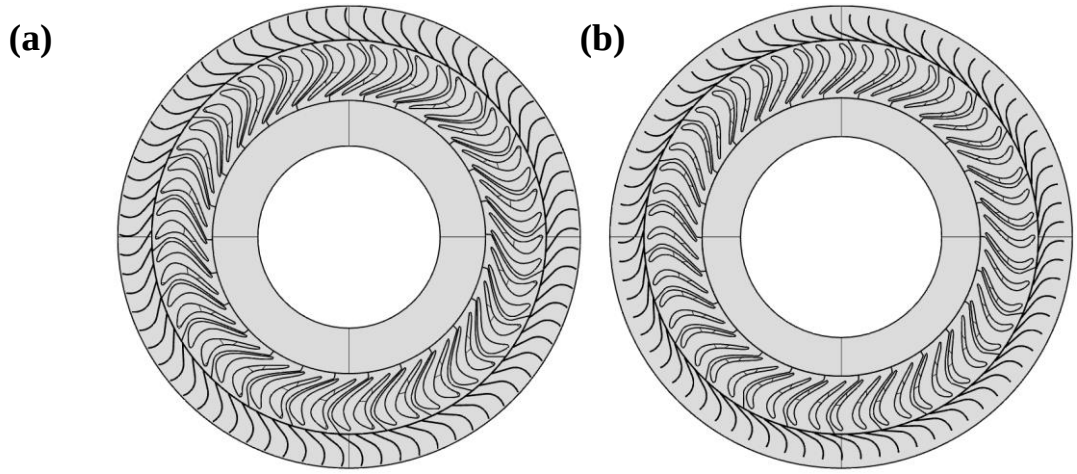

Figure 3.11 Comparison of the initial and optimum inflow rotors, a: initial design, b: optimum design.

The sensitivity of output parameters regarding the rate of changes applied to each input parameter is shown in Figure 3.12. The local sensitivity statistics have been generated regarding the trends of the efficiency and power coefficient of the optimum design point and show the rate of impact of each input parameter on the output parameters. The local sensitivity is an exploration tool included in the response surface, which analyses the weight of each input parameter on the output parameters independently (ANSYS-User's-Manual). If the increase of a parameter fulfils the objective function in the optimisation journey, that parameter is shown with a positive sign. In other words, the positive and negative bars in Figure 3.12. respectively show the increase and decrease of the parameter with respect to the initial values. It is obvious in Figure 3.13 among the list of design variables studied in this step, setting angle of the blade and UGV angle are the most sensitive parameters on efficiency followed by the TE angle and the stagger angle. Similarly, the UGV and blade setting angles have the highest impact on C_P, followed by suction side and chord length.

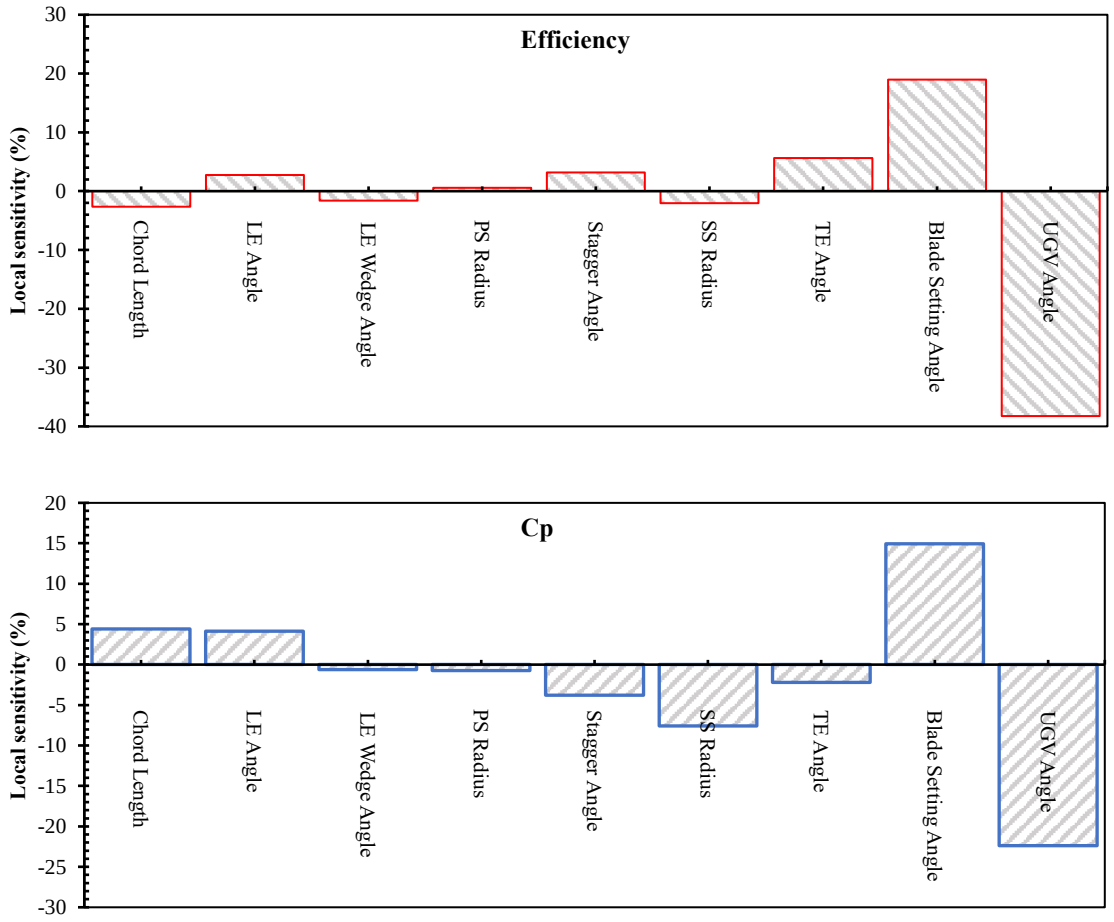

Figure 3.12 Sensitivity analysis of input parameters in step 1 of the optimisation study.

3.4.2 Step 2 (Design optimisation of the downstream section)

The second step of the optimisation analysis was performed considering the design variables of the downstream sections (as determined in Figure 3.3 and Table 3-2). The DOE was created with a total

number of 25 experiments ($n = 4$ and $f = 0$) and the GA response surface was used to find the optimum design of the downstream section to reach a maximization total to static efficiency (equation 3.3). The optimum downstream section was found to have specifications shown in Table 3-5.

The local sensitivity of the input parameters and their rate of impact on the output parameters are shown in Figure 3.13. The DGV inlet angle and the duct radius were found to be the most sensitive parameters in variations of all the output parameters. It is observed that increase of the DGV inlet angle from its reference value has led to higher efficiency and damping and lower downstream losses. In case of the DGV outlet angle, a decrease from the reference value has led to the optimum design. Because, the increase of this parameter causes more downstream losses, due to affecting the DGV shape and the direction of flow at the elbow section. It is also observed that increase of the duct radius and diffuser angle with respect to the initial downstream section geometry can lead to a reduction of the losses at the downstream and increase of the damping.

Table 3-5 Optimum design of the downstream section.

Design variables	***Optimised Geometry***
DGV Inlet Angle	*85.31°*
DGV Outlet Angle	*4.22 °*
Duct Radius	*117.67 mm*
Diffuser Angle	*7.10 °*

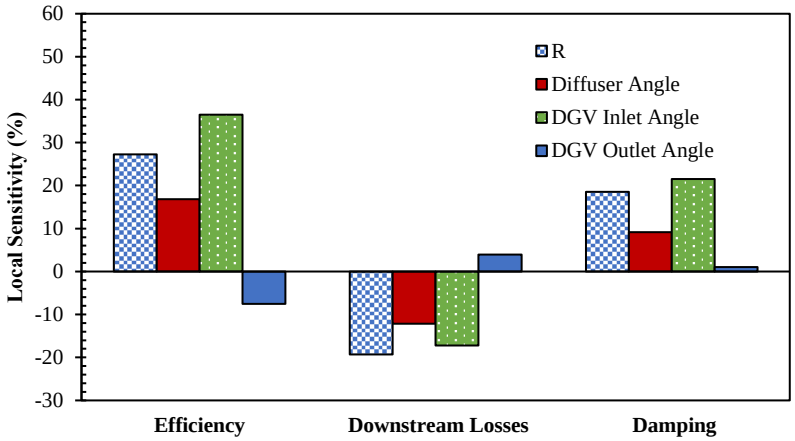

Figure 3.13 Sensitivity analysis of the input parameters in step 2 of the optimisation study.

The response surface of efficiency is shown as a function of the DGV-parameters in Figure 3.14-a, and as a function of duct-parameters in Figure 3.14-b. It is shown that the parameter bounds are selected properly as the most efficient design is clearly distinct in both response surfaces. The optimum efficiency was obtained near higher DGV inlet angles and lower DGV outlet angles. The optimum efficiency is captured near the upper bound of the duct radius and a diffuser angle of 7 degrees.

The effects of the DGV and duct parameters on the downstream losses and damping were analysed and shown in Figure 3.15 and Figure 3.16, respectively. A non-dimensional variation range [0, 1] for each parameter was considered, where 0 denotes the lower bound and 1 refers to the upper bound.

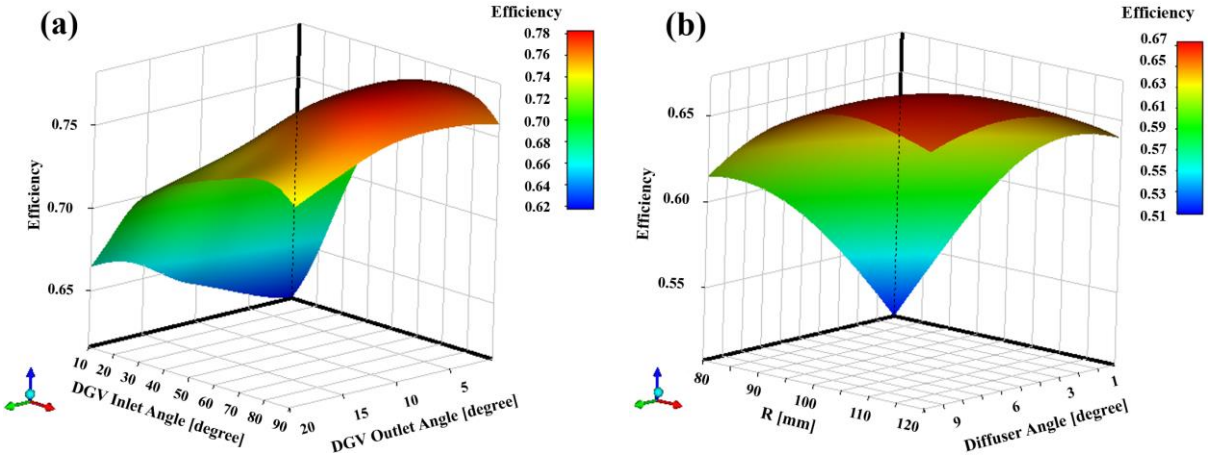

Figure 3.14 Efficiency surface plot against (a): DGV parameters and (b): Duct parameters.

According to the plots shown in Figure 3.15-a, higher DGV-inlet-angles lead to lower losses at the turbine downstream, while increasing the outlet angle gradually increases the losses at the downstream section of the turbine. This can be explained by considering the shape of DGVs in Figure 3.3, which consists of two segments: a curve and a line. Increasing the inlet angle decreases the curvature at the upper segment of the DGV, while increase of the outlet angle intensifies this curvature due to the total length and the specified tangent constraints between the two segments. As shown in Figure 3.15-b, the duct radius is a parameter with clear need of optimising. A small radius value, leading to a lower sectional area, causes more pressure losses in the elbow. On the other hand, a higher radius can also be detrimental probably by causing flow detachment near the walls or causing separation and reverse flow inside the duct. The diffuser angle can also significantly reduce the losses inside the duct since it contributes to a significant reduction of the dynamic pressure at the duct exit.

According to Figure 3.16-a, turbine damping is positively affected by the inlet angle of the DGV, with a peak near the upper bound of this parameter. On the other hand, variations of the outlet angle has negligible effects on the turbine damping. As can be seen in Figure 3.16-b, the duct radius variations in the first half-range have more impact on the turbine damping, and the damping value is approximately unchanged over the second half-range. It can be explained by the fact that a smaller duct radius can lead to pressure losses and cause flow congestion at the duct entrance. The plot of diffuser angle variations shows that use of a diffuser in the duct exit has minor effects on the damping.

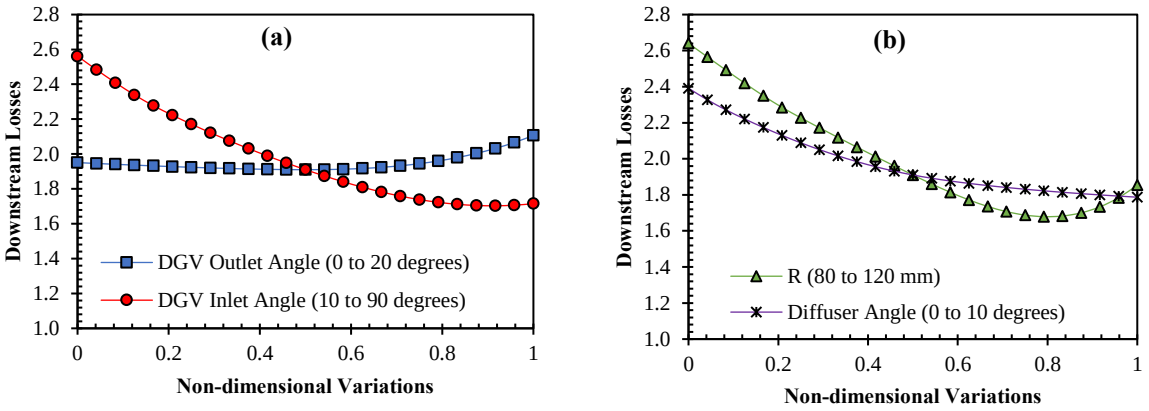

Figure 3.15 Effects of design variables on the downstream loss coefficient.

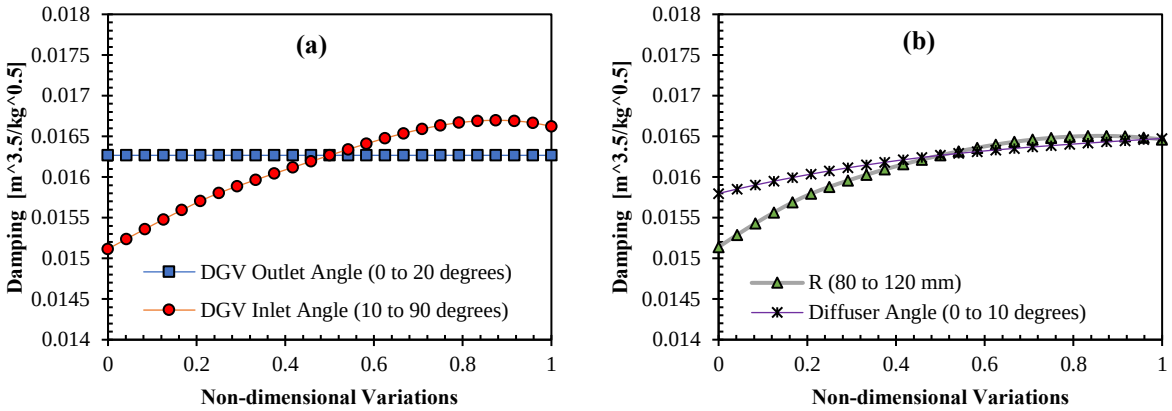

Figure 3.16 Effects of design variables on the turbine damping

The turbine geometry with the initial and optimised downstream sections is illustrated in Figure 3.17. It is observed that the DGVs in the optimum design have lower curvatures compared to the initial DGVs. In addition, the duct radius is obviously larger than the initial geometry to ease the transmission of the flow into the downstream section. The duct also has a diffuser shape with an angle of 7 degrees to recover the kinetic energy and diffuse the flow into the chamber at a lower velocity.

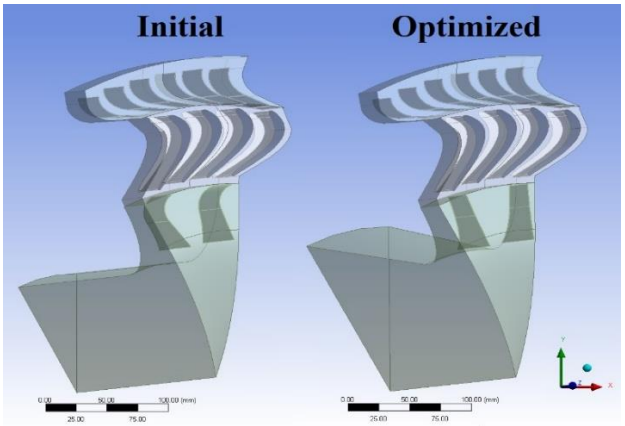

Figure 3.17 Schematic of the inflow turbine with the optimum and initial downstream section.

The turbine characteristics with both downstream sections are compared in Figure 3.18. It can be seen that the torque coefficient curve (Figure 3.18-a) is the same for both geometries. This is because, this step of the optimisation was concerned with design optimisation of the downstream section in presence of a similar rotor section was used with both initial and optimum downstream sections. Considering the input power coefficient plot in Figure 3.18-b, it is observed that at flow coefficients smaller than $\phi = 1.25$ the optimised downstream section has lower input power coefficient than the initial one. This means that the optimised DS geometry causes a more efficient use of the input power in generating the torque. Figure 3.18-c reveals that efficiency of the optimum unidirectional turbine design peaks at near 81.5% at $\phi = 0.47$, with more than 10% of efficiency improvement achieved by modifying the downstream section. This efficiency increment is due to the modified C_A trend of the optimum design. Regarding the damping plots (Figure 3.18-d), it is obvious that the optimum downstream section leads to a higher damping value than the initial design for flow coefficients smaller than ϕ =1.5. This implies the fact that the optimised downstream section permits more flow rates into the turbine-duct configuration compared to the initial downstream section for a given pressure drop which is associated with the lower downstream losses in the optimised DS section as shown in Figure 3.19. In addition, higher curvature of the DGVs in the initial design are likely to cause more downstream losses at the peak efficiency point due to intensifying the swirl component of the flow at the rotor exit. The significant reduction of the downstream losses in the optimum design (in Figure 3.19) can be explained by the use of radial flat plates in the rotor downstream which permits the flow to leave the rotor with no-swirl.

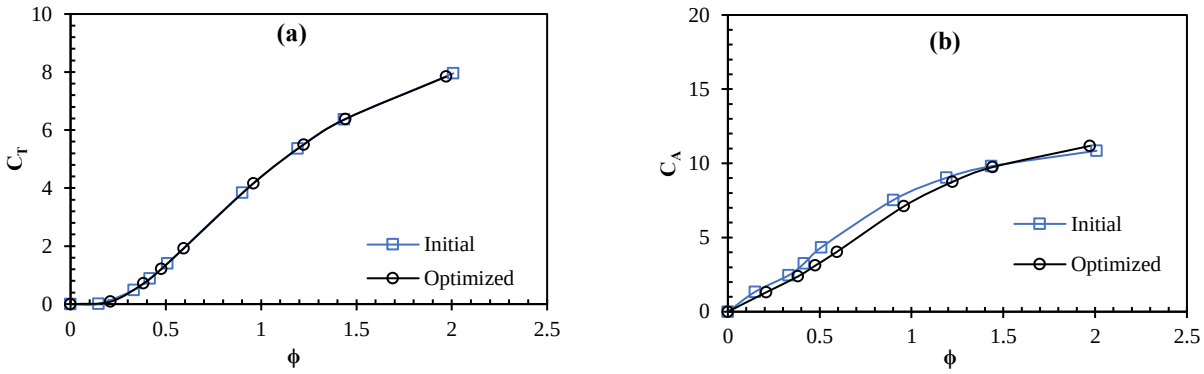

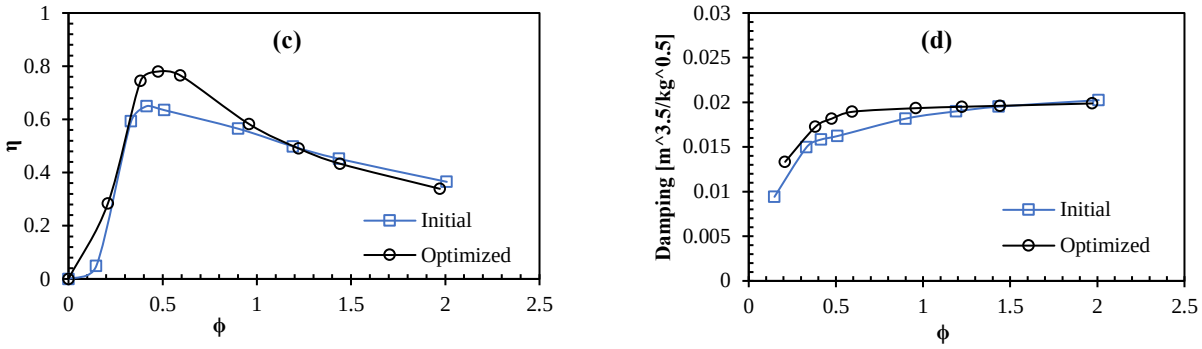

Figure 3.18 Comparison of turbine characteristics between the optimum DS section and the initial DS section, a) Torque coefficient, b) Input coefficient, c) Efficiency and d) Damping.

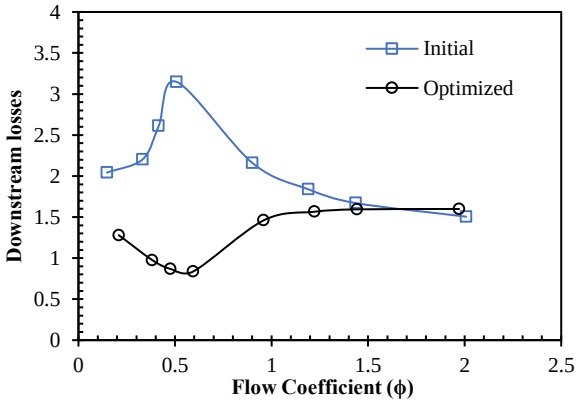

Figure 3.19 Comparison of the downstream losses between the optimum DS section and the initial DS section.

Comparison of the velocity vectors of the initial and the optimised DS sections in Figure 3.20 indicates that the airflow velocity in the rotor section of the optimised DS is higher than the initial DS while the same pressure drop of 1400 Pa is provided to both cases. As the rotor sectional area is equal in both geometries, therefore a higher flow rate has passed through the optimised DS. Reduction of the downstream losses in the optimised DS geometries as illustrated in Figure 3.19 has two main reasons considering the velocity and pressure contours of the DGV and the duct sections. According to Figure 3.20 and Figure 3.21, the optimised DGVs can direct the flow into the duct properly, while flow separation observed near the DGVs curvature of the initial DS. The low-pressure area near the DGV curvature in the initial geometry is observed in Figure 3.21, which clearly shows the negative impact of the initial DGVs on the pressure at the rotor downstream. In addition, regarding the equation 3.6 the downstream losses are related to the total pressure drop and the flow velocity inside the duct. As illustrated in Figure 3.22, the initial DS section allows the airflow to leave the duct at high velocities, meaning that a large amount of kinetic energy leaves the turbine unused. In contrast, the optimised duct has reduced the air velocity at the downstream section to a high extent and the diffuser has recovered the kinetic energy properly. Considering Figure 3.23, it is obvious that the configuration

with optimum DS has lower total pressure at the downstream compared to the configuration with the initial DS, which again implies the recovery of the kinetic energy and reduction of the dynamic pressure at the duct exit in the configuration with optimised DS.

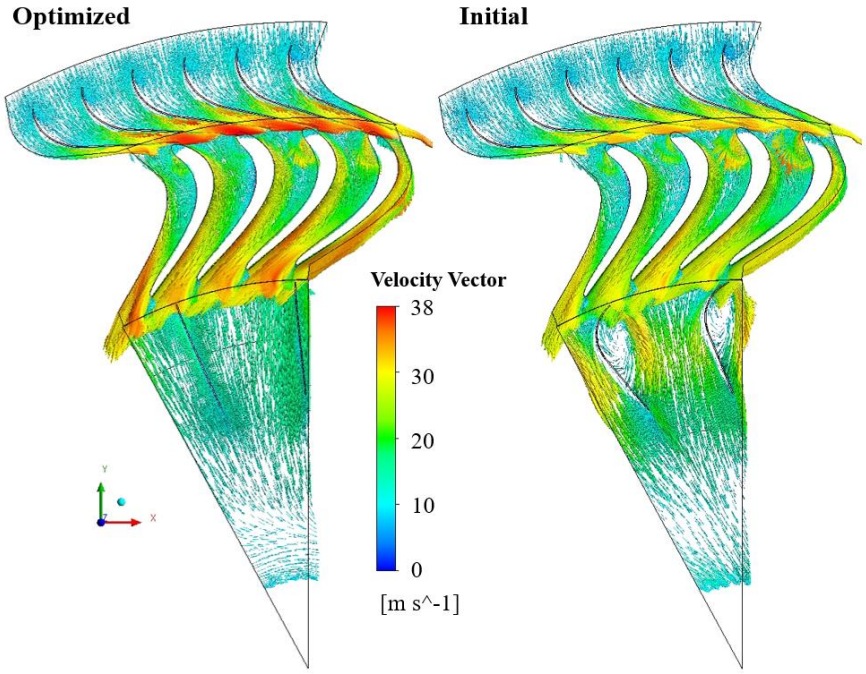

Figure 3.20 Comparison of the velocity vectors of the initial and optimised downstream sections at Δp_0= 1400 Pa equivalent to a point near the peak efficiency.

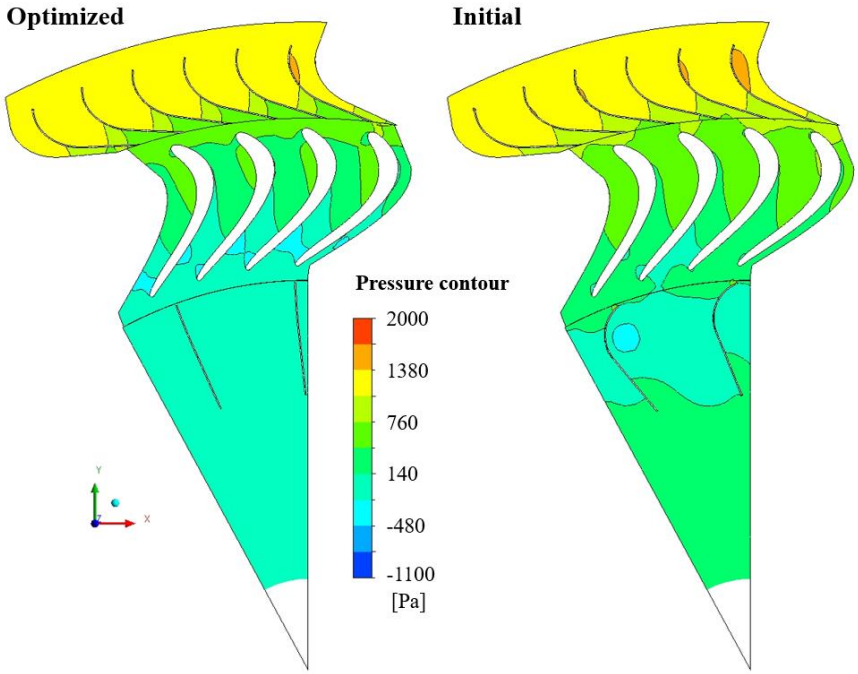

Figure 3.21 Comparison of the pressure contour of the initial and optimised downstream sections at Δp_0= 1400 Pa equivalent to a point near the peak efficiency.

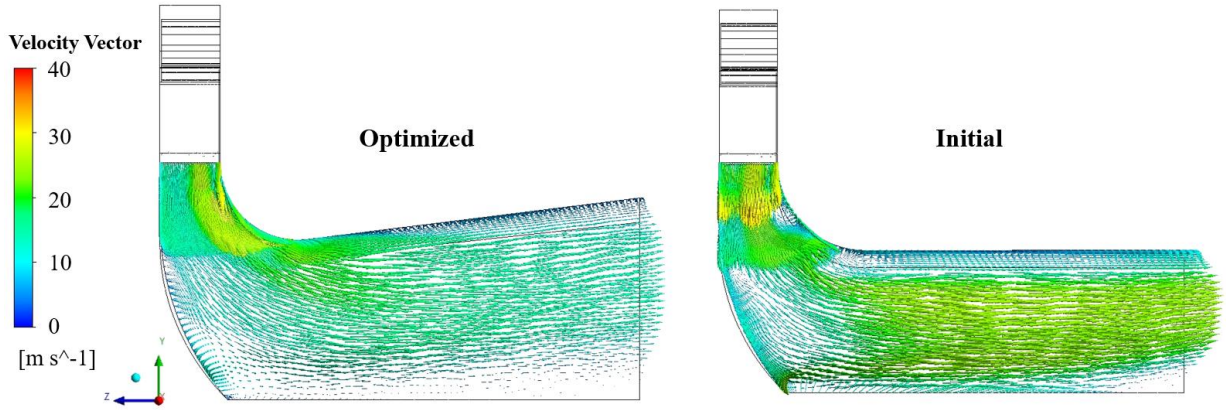

Figure 3.22 Comparison of the flow velocity in the downstream section of initial and the optimised geometries at Δp_0= 1400 Pa equivalent to a point near the peak efficiency.

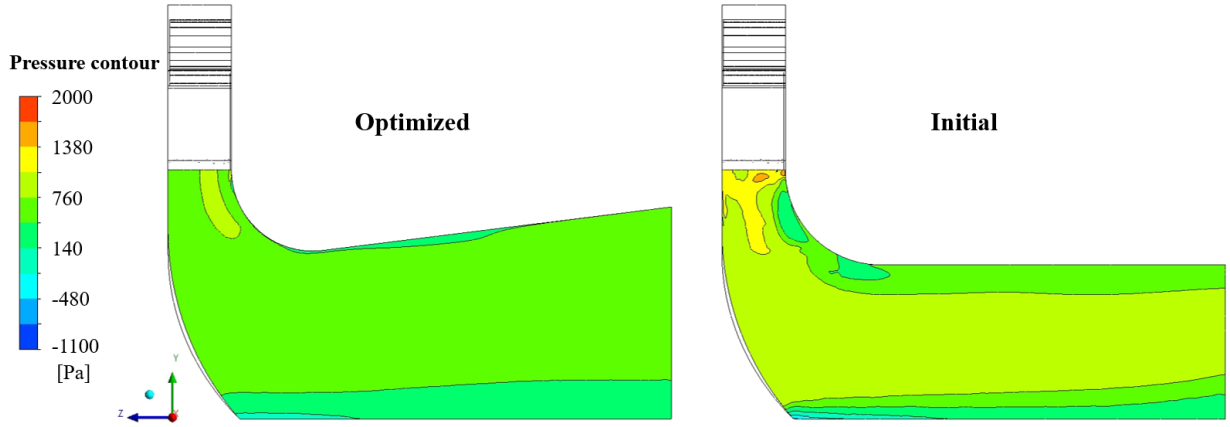

Figure 3.23 Comparison of the total pressure in the downstream section of initial and the optimised geometries at Δp_0= 1400 Pa equivalent to a point near the peak efficiency.

3.4.3 Unsteady performance evaluation of the optimum inflow turbine using a transient model

As mentioned in section 3, the optimisation study was performed using the MRF model to reduce the time and computational cost. However, the actual condition is unsteady since the computational geometry includes rotating domains. Thus, a transient model was used to control the relative motion of the rotor in a purely unsteady fashion and evaluate the accuracy of the obtained efficiency results in the optimisation study. The computational model using the MRF approach (validated in section 4) is named Case 1.

In the transient model, four revolutions of the periodic domain were simulated at a rotational speed of ω =120 rad/s, giving a total time of 0.02464 s. The residuals were set to 1×10^{-6} and a time step study was performed considering three different cases. Courant number (CFL) was utilised to choose a suitable time step and it was less than one for each cell to have numerical stability (Kianejad et al., 2019). First, the time step was set at 5×10^{-4}s, giving a total number of 49 time steps (this setup is

referred as Case 2). Second, a time step of 1×10^{-4}s, giving a total number of 246 time steps (Case 3). Finally, a time step of 1×10^{-5}s, with a total number of 2464 time steps (Case 4). Case 4 was not economical regarding simulation time and was used as a reference to evaluate the accuracy of other cases. Figure 3.24 compares the deviation of the total to static efficiency of the optimum inflow turbine at its best efficiency point, obtained from Cases 1 to 3 with respect to the results of Case 4. According to this figure, the Case 3 shows acceptable accuracy with only 0.73% deviation from the Case 4, but is more economical in terms of the computational cost. Therefore, Case 3 with the time step of 1×10^{-4}s was selected as the final transient model to simulate the optimum inflow turbine's efficiency in an unsteady fashion. In addition, Figure 3.24 shows a maximum of 2-3% deviation in the total to static efficiency of the MRF model (Case 1) and the transient model (Case 3) at ϕ=0.7. However, considering the Figure 3.25, the peak efficiency point of the transient model has slightly shifted toward lower flow coefficients (ϕ =0.5) while the magnitude of peak efficiency is still pretty close to that of the MRF model.

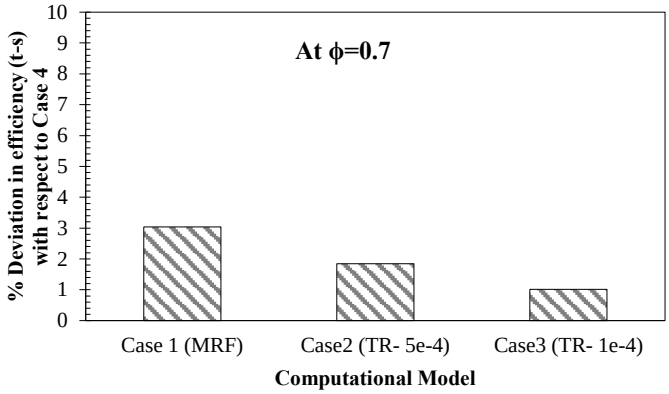

Figure 3.24 Time step study of the transient model and comparison of the deviation of Cases 1 to 3 from the Case 4.

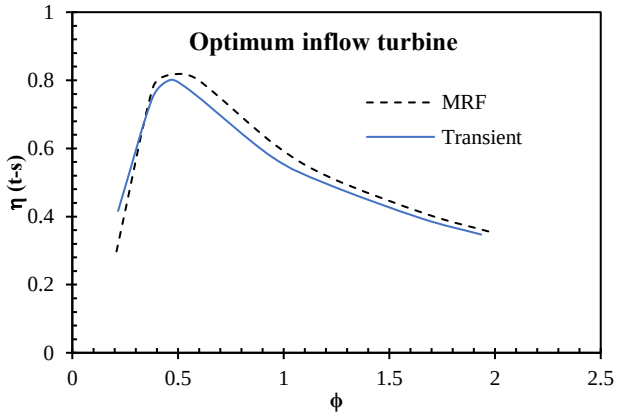

Figure 3.25 Comparison of the total to static efficiency of the optimum inflow turbine using MRF model (Case 1) and the transient model (Case 3).

As the main concern of this study, the plot of the total to static efficiency of the optimum inflow turbine over the entire operational range has been compared for the MRF and the transient models in Figure 3.25. It is obvious that the efficiency plot in both models follows a similar trend and the MRF model has slightly overestimated the efficiency of the turbine when compared to the transient model. Considering the massive computations of the optimisation study, using the MRF model in this study is justifiable and the results of optimisation study can be regarded as valid.

The performance of the optimised inflow turbine, obtained from the transient model, was compared to the existing unidirectional axial and radial turbines (in direct mode) in the literature (Rodríguez et al., 2019, Pereiras et al., 2014). As illustrated in Figure 3.26, the optimisation analysis in this study has significantly improved the efficiency of the unidirectional radial turbines. Where the peak efficiency is higher than that of the existing unidirectional radial turbine by almost 30%. It should be noted that the radial turbine in Ref. (Rodríguez et al., 2019) is design-optimised to work in a twin turbine OWC concept, when maximum efficiency in the direct mode and maximum backflow prevention in the reverse mode are achieved. However, this comparison highlights that a peak efficiency over 80% can be expected for this type of turbine, by focusing on the design optimisation in a single flow direction. The optimum inflow turbine also provides comparable efficiency to the axial turbine (the axial turbine with optimum solidity in the direct mode in Ref. (Pereiras et al., 2014)) with almost 7% peak efficiency and slightly narrower operational range.

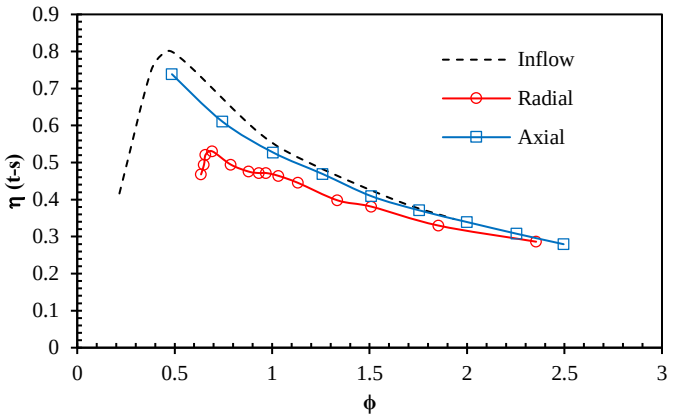

Figure 3.26 Comparison of the efficiency (total to static) of the optimum inflow turbine with the existing radial (Rodríguez et al., 2019) and axial turbines (Pereiras et al., 2014).

3.4.4 Comparison of the performance of the optimum inflow turbine with the bidirectional turbine geometry

To evaluate the importance of the optimization study, the performance of the turbine stage was evaluated in the optimized inflow and the bidirectional turbines considering the velocity triangles of the turbines during the inhalation mode, as illustrated in Figure 3.27. In addition to that the application

of turbomachinery general theory was evaluated in different sections of the turbine, as separated by numbers in Figure 3.28. The performance of the UGV section was evaluated considering the pressure drop in this element using equation 3.10 and the performance of the rotor domain was evaluated based on the Euler's turbine equation using equation 3.11 (Dixon and Hall, 2013).

$$\eta_{UGV} = 1 - \left(\frac{p_{01} - p_{02}}{\Delta p_0}\right), \tag{3.10}$$

$$\eta_{Rotor} = \frac{\rho[U_2 V_{u2} - U_3 V_{u3}]}{[p_{02} - p_{03}]}. \tag{3.11}$$

Where subscript 1, 2 and 3 refers the inlet and outlet boundaries of each section as illustrated in Figure 3.28 and V_u is Tangential component of the absolute velocity.

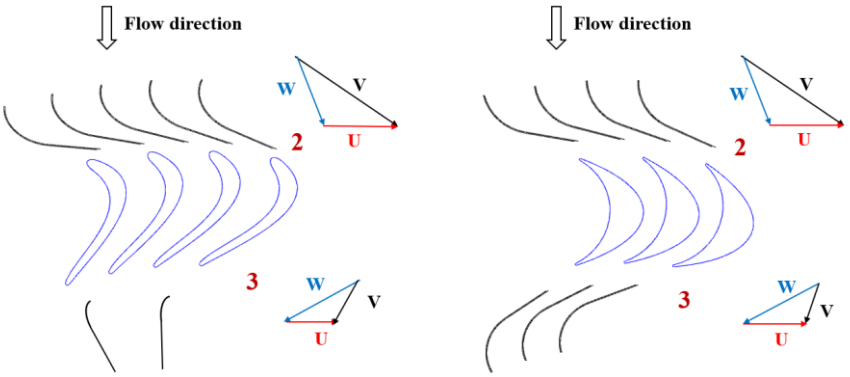

Figure 3.27 Comparison of the airflow velocity triangles at the rotor section of the bidirectional and the inflow turbines during inhalation mode.

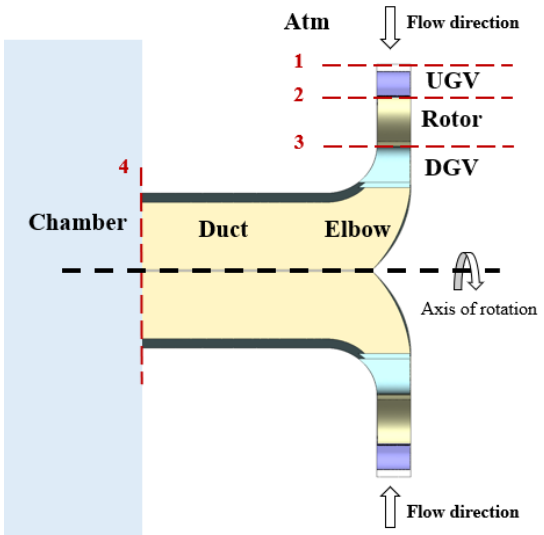

Figure 3.28 Side-view sketch of the radial turbine. Different sections have been separated by labels and surface numbers.

Figure 3.29 compares the performance of the UGV sections in the inflow and bidirectional turbines. The efficiency of this section is over 92% in both geometries which is reasonable for a fixed element at the rotor upstream. It is observed the efficiency of the UGV section in the bidirectional turbine is almost 2.5% lower compared to the inflow turbine. This can be explained by the difference in the UGV angles in both geometries (25° versus 15°).

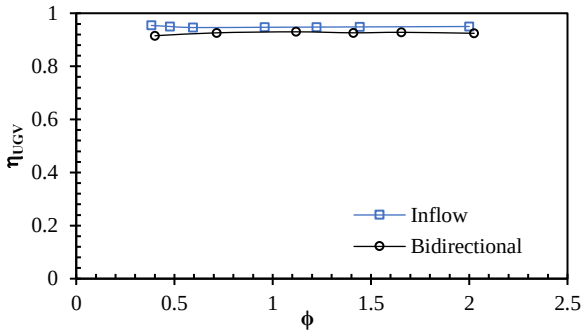

Figure 3.29 Comparison of the performance of UGV section in the bidirectional turbine and the optimized inflow turbine.

Regarding the performance of the rotor section, as compared in Figure 3.30, the inflow turbine has a significantly higher energy exchange at smaller flow coefficients compared to the bidirectional turbine during inhalation. Also, at higher flow rates both rotors have less than 50% efficiency. The significant improved peak efficiency of the inflow rotor compared to the bidirectional rotor (87.5% versus 70%) can be explained considering the flow velocity vectors at both rotors. As illustrated in Figure 3.31, there is a flow incident at the leading edge of the bidirectional blade which causes a growth of the secondary losses from the leading edge to the middle of the blade chord. In case of the inflow turbine, the flow passes smoothly through the rotor domain, which is because the rotor blades are well designed to match the inhalation mode.

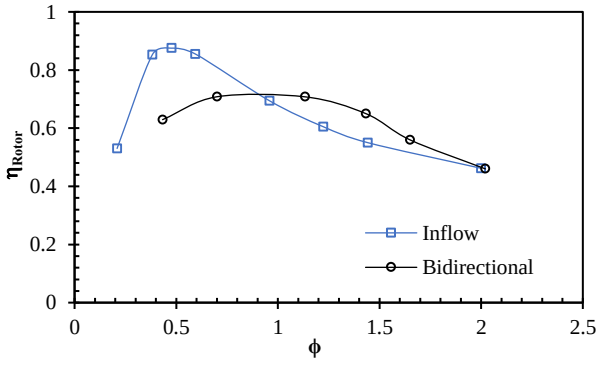

Figure 3.30 Comparison of the performance of rotor section in the bidirectional turbine and the optimized inflow turbine.

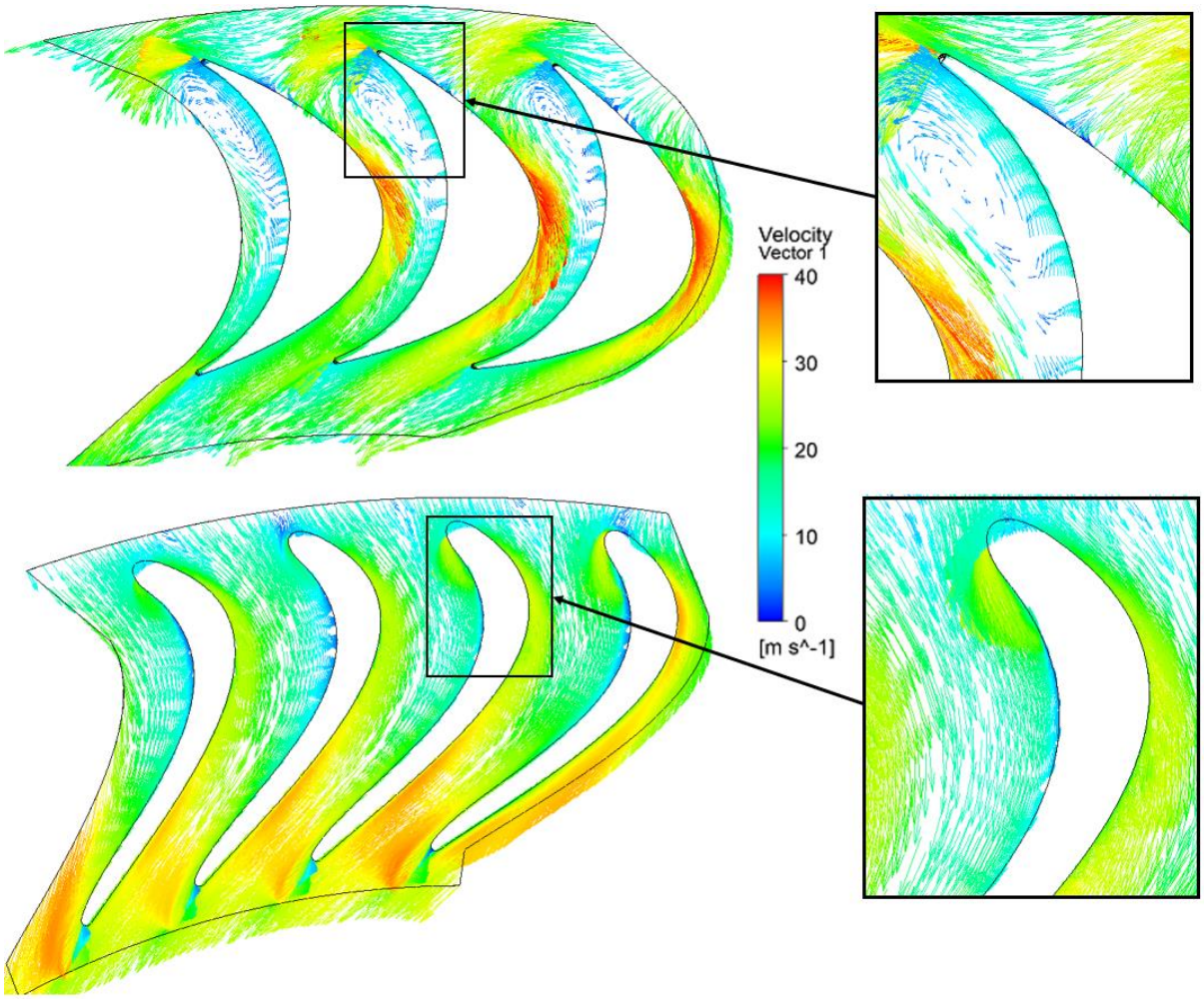

Figure 3.31Comparison of the velocity vectors in the rotor domain of the bidirectional and inflow turbines $\phi = 0.6$.

3.5 Conclusion

A centripetal configuration of a unidirectional radial turbine (also called inflow) was investigated for efficiency maximization. Optimisation techniques integrated with CFD simulations were used to first optimise the shape of rotor blades for efficiency maximization and then to find the proper shape of turbine downstream section (including downstream guide vanes and duct) for the optimised inflow rotor.

Among the list of design variables used for optimising the unidirectional rotor, blade setting angle, UGV angle, TE angle and blade stagger angle showed more sensitivities than other parameters. The inflow rotor obtained a peak efficiency near 70% in a domain excluding the elbow and duct sections. The performance of the inflow turbine was evaluated by considering downstream section (DGVs + duct) in the computational domain and significant pressure losses were observed in CFD simulations. Four parameters associated with the shape of DGVs and the duct geometry were selected as the design variables. The inlet angle and outlet angle parameters were defined to control the curvature and

direction of the parametric DGVs. It was concluded that the DGV inlet-angle had significant effects on the performance of the downstream section. In OWCs the turbine is constantly operating away from the ‘design point’ and based on the analysis in section 2.3.4 the downstream guide vanes are an important inclusion for a radial inflow turbine. The optimised guide vanes of this study were found to have minor curvatures and the optimised duct had a diffuser shape with 7 degrees diffusion angle. Use of diffuser at the turbine-chamber connection led to recovery of the kinetic energy and reduced the losses at the downstream section to a high extent. The inflow turbine obtained a peak efficiency of 80%, where more than 10% of which was due to customizing the downstream section.

It was found that the energy losses decrease significantly in the optimised downstream section. The authors acknowledge that the optimised inflow turbine was obtained based on the list of input/output parameters considered in this study and it might differ by changing the list of input/output parameters. In addition, combining the steps 1 and 2 in the optimisation process might lead to a slightly different optimum design, however, it was not practical regarding the number of input parameters of this study. As an alternative, the results of this study can be used as a reference to eliminate the unnecessary input parameters in the rotor design and provide scope for an optimisation study including the entire turbine domain at reduced time and computational cost.

4 DESIGN MODIFICATION OF A CENTRIFUGAL RADIAL AIR TURBINE CONFIGURATION (OUTFLOW TURBINE)

This chapter is based on a research paper submitted (Revised version submitted) and under review by the journal of Energies. The citation for paper is:

Ansarifard, N., Fleming, A., Henderson, A., Kianejad, S.S., Chai, Sh., "Design optimisation of an outflow radial turbine for a twin turbine OWC wave energy converter", Energies 12(2791).

(https://doi.org/10.3390/en12142791).

Abstract

In this chapter a centrifugal unidirectional-radial-turbine (known as outflow turbine) was evaluated to operate in a vented configuration of oscillating water column (OWC). Most unidirectional turbines used in wave energy conversion (twin-turbine OWC topologies) are of axial flow type. The radial turbine offers an alternative design with the advantage of increased resistance to back flow. However, in general the efficiency of radial turbines is lower than axial turbines. This study describes a CFD-based design optimisation of an outflow radial turbine. The rotor blade geometry is parametrically described in addition to other turbine components. Efficiency optimisation was achieved using the genetic algorithm (GA) over a range of flow coefficients. It was found that the optimised outflow radial turbine can obtain acceptable rotor energy transfer despite having a negative centrifugal energy transfer term. Compared to an inflow radial configuration, the geometrical features of the outflow turbine permit the flow to enter the rotor with higher absolute velocities and increased dynamic pressure change across the rotor. The optimised design was found to have a 72% peak efficiency in steady state which is a significant improvement in this type of turbine.

4.1 Introduction

An oscillating water column (OWC) is a well-known form of wave energy converter (WEC). The incident waves cause the water level inside the OWC chamber to oscillate and compress air into an air turbine mounted on top of the chamber. The pressure differential between the chamber and atmosphere allows the turbine to rotate and produce mechanical power. The mechanical power is converted to electricity by coupling the rotor to a generator.

In the current WEC industry, initiatives to reduce the cost of harnessing energy from renewable sources are highly valuable (Bull and Ochs, 2013). An efficient wave to wire performance of the OWC converter requires design modifications of different parts of the system (Callaghan and Boud, 2006, Energy, 2005). Research on the OWC, Power Take-Off (PTO) and generator units has been expanded in recent years to identify efficient designs of these elements and maximize the energy conversion of the whole system. Different versions of unidirectional turbines have been studied in the twin turbine concepts (Lopes et al., 2019, Okuhara et al., 2014, Pereiras et al., 2014, Setoguchi and Takao, 2006b, A. Falcao et al., 2015). A twin turbine topology employs two unidirectional turbines. Turbines are installed in the chamber and operate regarding the pressure difference between atmosphere and the chamber. Each turbine is active during a single direction of flow in the system (direct mode) and is idle during the reverse direction (reverse mode). The numerical and experimental studies of the twin turbine configurations have mainly been performed on the axial flow unidirectional turbines and design

modifications of this twin-turbine configuration has obtained a peak efficiency of around 70% in the direct mode (Dudhgaonkar et al., 2011, Okuhara et al., 2014, Okuhara et al., 2012, Setoguchi and Takao, 2006b). However, the global efficiency of the twin turbine also requires efficient operation of the turbine in reverse mode (Takao et al., 2011b). Pereiras et al. in (Pereiras et al., 2014) considered the negative torque produced in the reverse turbine in the efficiency calculations of the twin-axial turbines for the first time. Research on application of unidirectional radial impulse turbines in twin-turbine OWC configurations still is in progress. Rodriguez et al. (Rodríguez et al., 2018) improved the geometry of a unidirectional radial turbine in twin-turbine topology for higher resistance to flow in the reverse mode, however, the turbine's direct peak efficiency was significantly low (approximately 40%). They later focused on optimising this turbine's design for efficiency maximization in the active mode, while keeping the strong flow blockage in the reverse mode (Rodríguez et al., 2019).

Employing optimisation tools in the numerical studies can provide a refined approach for identifying different aspects of the turbine design. Employing the response prediction algorithms can help to investigate a larger design space and allow more reliable turbine designs. Understanding the impact of design variables on the objective functions can ensure a fast and reliable exploration of the optimum turbine designs. Several studies have focused on optimising the turbine designs for OWC and identifying the most sensitive parameters affecting the turbine performance (Falcão et al., 2018, Falcão and Gato, 2012, Falcão and Henriques, 2016b, Rodríguez et al., 2019). Impact of the rotor blade profile was studied on performance of the Wells turbines (Raghunathan et al., 1991, Raghunathan and Tan, 1985) and optimisation methods were used to explore an optimum blade design by varying the camber line and blade thickness. A 2D blade profile of an impulse turbine was optimised in (Gomes et al., 2012), a 3D blade geometry was created by stacking the 2D profile span wise and a 5% efficiency improvement was obtained. Mohamed et al. (Mohamed et al., 2011) employed systematic optimisation to investigate the blade shape of a reaction turbine using parameters used in an airfoil design. The genetic algorithm and computational fluid dynamics (CFD) techniques were used to optimise the rotor blade shape of an axial turbine for efficiency maximization and improvement of the power output over a wide range of flowrates. The optimised airfoil obtained an 11.3% increase of the power output compared to the initial design of the blade. Design optimisation methods were also used by Mohamed and Shaaban (2014) to predict performance of a Wells turbine with self-pitch controlled blades. They used parameters in a non-symmetric airfoil shape to identify the optimum design. Optimised sweep angle of the rotor blade of a wells turbine was studied using the surrogate modelling Halder et al. (2017). The optimum blade was reported to have a backward sweep angle at the mid-section and a forward angle at the tip, and improved the torque by 28%. Apart from the blade profile, number of blades and guide vanes were also investigated using the optimisation methods. A

multi fidelity analysis coupled with the CFD was performed to maximize the efficiency of impulse turbine used with an OWC Badhurshah and Samad (2015b).

This study focuses on design optimisation of an outflow radial turbine to maximize the efficiency. The investigation was conducted using CFD and the computational model was validated against experimental data of a bidirectional radial turbine published in Case (1) of (Setoguchi et al., 2002) . The genetic algorithm was used as the optimiser and the design of experiment (DOE) was used to create the design point population. Design optimisation of the rotor and upstream guide vanes in a radially-outward-flow turbine were studied over a range of steady state flowrates. A list of design variables was considered in creation of the parametric CAD geometry of the rotor blades and the upstream guide vanes. The impact of design variables on the turbine efficiency, output power, input power and flow resistance were analysed and the most sensitive parameters were identified.

4.2 Turbine Geometries

A bidirectional configuration of a radial turbine, extracted from Ref. (Setoguchi et al., 2002) and previously investigated by the authors (M-1 in Ref. (Ansarifard et al., 2019)), was used in this study to validate the numerical method and to be used as a reference for creation of an initial centrifugal (outflow) radial turbine. The bidirectional turbine geometry has main characteristics presented in Table 4-1. The initial outflow turbine geometry was designed according to the main geometrical characteristics of the bidirectional turbine. The geometries of the duct and upstream guide vanes (UGVs) were chosen to be similar to that of the bidirectional turbine. In addition, the inner diameter, number of upstream guide vanes and rotor blades (RBs) were equal in both turbines (more details can be found in Ref. (Setoguchi et al., 2002)). The main differences were using asymmetric rotor blades appropriate for an outward flow direction and removing the downstream guide vanes (DGVs), since only outward flow direction was considered as operational. Schematics of the bidirectional geometry and the initial outflow turbine are shown in Figure 4.1.

Table 4-1 Bidirectional turbine specifications

	Blade number	***Chord length***	***Setting angle***
DGV	*52*	*50 mm*	*25°*
RB	*51*	*54mm*	*19.8° / 35.8°*
UGV	*73*	*50mm*	*25 °*

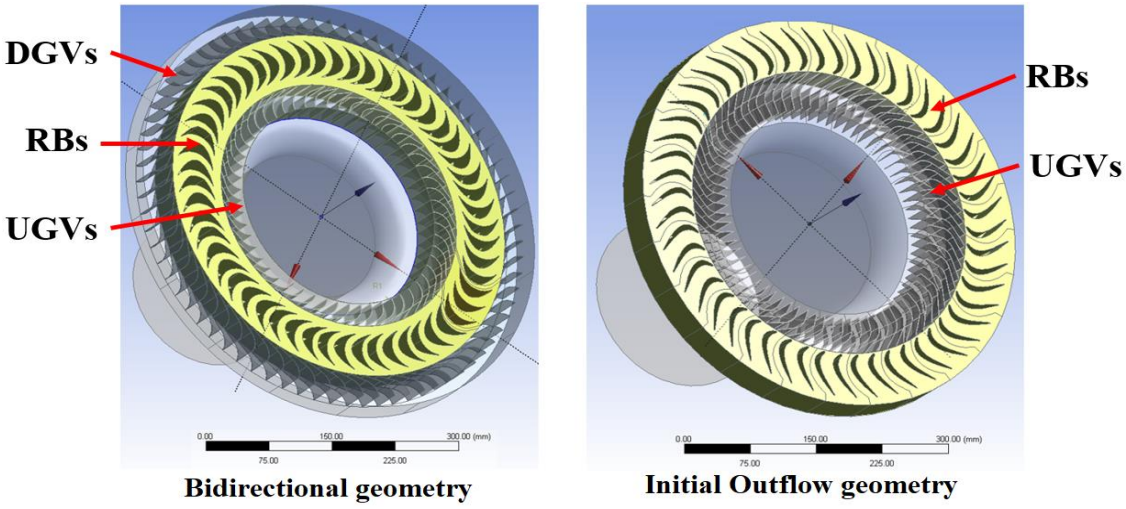

Figure 4.1 Schematics of the bidirectional turbine and initial outflow turbine geometries.

A parametric 3D model of the initial turbine geometry was generated using the CAESES software (UserGuide, 2017). Selection of the base geometry for the rotor blade needed to be done regarding some specific characteristics of the turbine. To ensure acceptable conversion of the input power, an asymmetric blade profile with highly flexible curves in the suction and pressure sides was needed. Therefore, a base blade profile with eleven design variables was created using the software database (UserGuide, 2017). This parametric blade shape could offer enough flexibility to create a large design space by varying a large set of parameters. However, the computational cost and time of simulations were directly associated with the number of input parameters. Therefore, to reduce the computational cost, the optimisation study was focused on the shape of the rotor blades and their adjustment with the guide vanes. Among the parameters available to control the blade's 2D profile, six parameters were considered as more effective through initial literature search (Pritchard, 1985, Wiberg and Anton, 2015). These parameters were radius of the leading edge (LE Radius), chord length, Radius of the pressure side (PS Radius), leading edge angle of the blade (LE angle), stagger angle and trailing edge angle of the blade (TE angle). Figure 4.2 illustrates these parameters in the parametric blade profile. In addition to the blade profile, the setting angle of the upstream guide vanes (GV Angle) was included in the input parameters list. Table 4-2 determines the lower and upper bounds of the input parameters and their values in the reference design (the initial outflow turbine geometry).

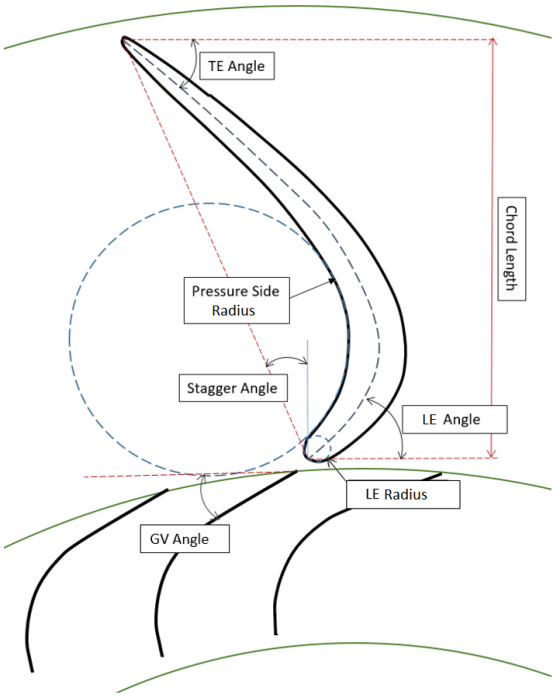

Figure 4.2 Illustration of the parameters used in creation of the blade profile

Table 4-2 Design variables with upper and lower limits

Design variables	*Lower bound*	*Upper bound*	*Initial geometry*
GV Angle (degree)	*15*	*50*	*27*
LE Radius (mm)	*1*	*3*	*1.96*
Chord Length (mm)	*40*	*70*	*62*
PS Radius (mm)	*0.35*	*0.6*	*0.45*
LE Angle (degree)	*30*	*80*	*57.5*
Stagger Angle (degree)	*-30*	*-20*	*-25*
TE Angle (degree)	*30*	*70*	*45*

4.3 Numerical Modelling

Numerical simulation tools were employed to optimise the design of the initial outflow turbine in steady state. The computational simulations were conducted using ANSYS CFX. The turbine performance was described by a set of parameters (Setoguchi et al., 2002): torque coefficient C_T, input power coefficient C_A, turbine efficiency η and flow coefficient ϕ.

$$C_T = T_0 / \left\{ \rho \left(V_R^2 + U^2 \right) A_R r_R / 2 \right\} \tag{4.1}$$

$$C_A = \Delta p_0 Q / \left\{ \rho \left(V_R^2 + U^2 \right) A_R V_R / 2 \right\} \tag{4.2}$$

$$\eta = \frac{T_0 \omega}{\Delta p_0 Q} = \frac{C_T}{C_A \phi} \tag{4.3}$$

$$\phi = V_R / U \tag{4.4}$$

The detailed definitions of the variables contributing in these coefficients are given in the nomenclature section. The quasi-steady assumption of the flow was assumed considering that the ratio of rotating frequency and the period of the wave cycle in the OWC chamber (Rodríguez et al., 2018). Since the frequency of the wave cycle is noticeably lower compared to the turbine frequency, their interaction can be considered as negligible and assuming the airflow as steady becomes justifiable (Cui and Hyun, 2016). As an external modelling software was used for creation of the parametric geometry, the turbo-mode tool in ANSYS-CFX was used to setup the problem, to ease the iterative process of the optimisation study. The Moving Reference Frame (MRF) approach was used to set up the steady model by assuming that the rotor rotates at a constant speed of 120 rad/s and considering a frozen rotor interface between the rotor and the stationary domains. In this approach both stationary and rotating domains are solved at steady state with a frame change model to connect them. It is clear that the actual condition is unsteady as the rotor is rotating, however, to reduce the computational cost, the optimisation study was performed using the MRF model. The optimum design of the optimisation study was later analysed in a transient model (last section of this chapter) to evaluate the errors due to ignoring the unsteady interaction between the rotating and the stationary domains.

The simulations were performed at a Reynolds number ($\mathrm{Re} = \omega r^2_{in} / \upsilon$) of 1.37×10^6. The flow was assumed incompressible and the realizable k-ε turbulence model was selected due to being economical in terms of CPU time. It has acceptable performance in capturing the mean flow in complex structures, rotating domains, boundary layers, strong adverse pressure gradients, separation, and recirculation. This turbulence model has been utilized in many similar studies in the field and accurate results were obtained (El Marjani et al., 2008, Pereiras et al., 2011c). Periodic boundaries were set on the sides of each domain. The interface between domains were set as frozen rotor with a pitch angle ratio close to 1 by applying the passage and alignments of 2/52 for the duct section and 2/51 for rotor upstream and 3/73 for the rotor. The computational domain contained three parts: duct, rotor upstream domain and the rotor domain. To reduce the computational overhead, an angular section of the geometry including three UGVs and two RBs were used instead of the whole geometry as shown in Figure 4.3. The boundary conditions of uniform total pressure at the inlet and uniform static pressure at the outlet were considered. Total pressure values from 0.5 kPa to 20 kPa were set at the inlet to provide a range of non-dimensional flow coefficients from $\phi = 0.25$ to $\phi = 2.5$. The convergence criteria was set to an RMS residual target of 10^{-6}.

The ANSYS meshing program was used to create the mesh for numerical simulations. The size function was set on proximity and curvature to provide a greater control over the mesh. Inflation layers were used in the meshing to allow the solver to determine the forces on walls, flow incidence,

secondary flows and separation. Separation affects the drag and pressure drop and its accurate prediction relies on resolving the velocity gradients normal to the wall. In the viscous sublayer of a turbulent boundary layer, these velocity gradients are very steep and use of inflation layers allows to accurately capture near the wall flow behaviour and resolves the viscous sublayer directly (low Y^+ ~1) (ANSYS-User's-Manual). In this study, twenty inflation layers were applied with the transition ratio of 0.5 and growth rate of 1.2. The minimum size and proximity settings were varied to study mesh independence by creating four cases with 0.25, 0.5, 1 and 2.5 million tetrahedral cells. Figure 4.4 illustrates the percentages of deviation from case 4 with the maximum number of cells (2.5 million), where Case 1 denotes the minimum number of cells (0.25 million). It is obvious that Case 1 obtained the least accurate results in comparison to other cases with over 12% deviation in C_T. Case 2 provides a maximum deviation of about 6% and the discrepancy of results in Case 3 is practically nil. Therefore, Case 3 with a total number of 1 million cells was used for the CFD simulations to save time and the CPU usage. A schematic of the mesh used in the simulations is shown in Figure 4.5. It should be noted that the mesh setting was kept constant while the cell number varied by changes applied to the initial geometry in the optimisation study.

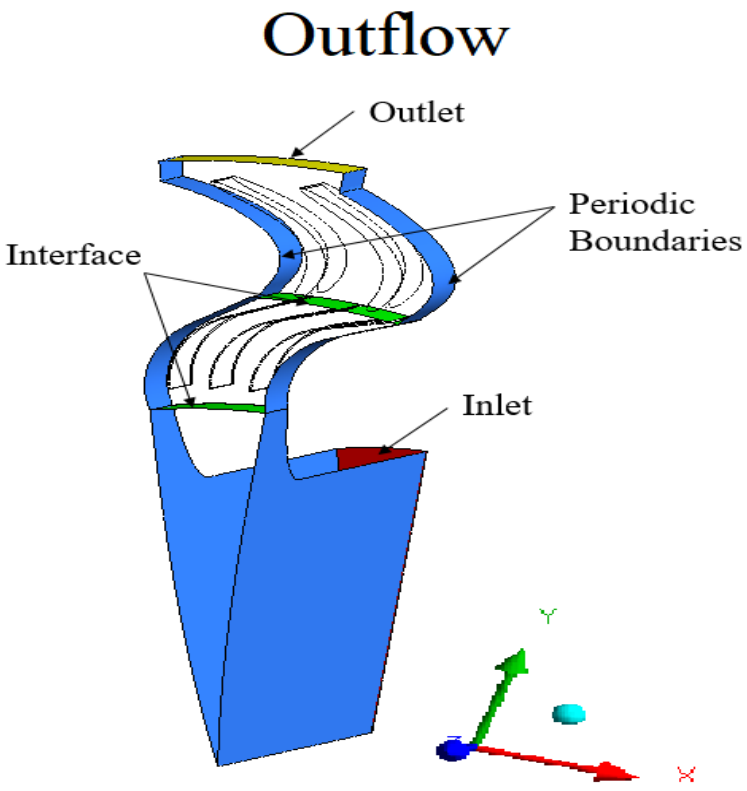

Figure 4.3 Computational domain

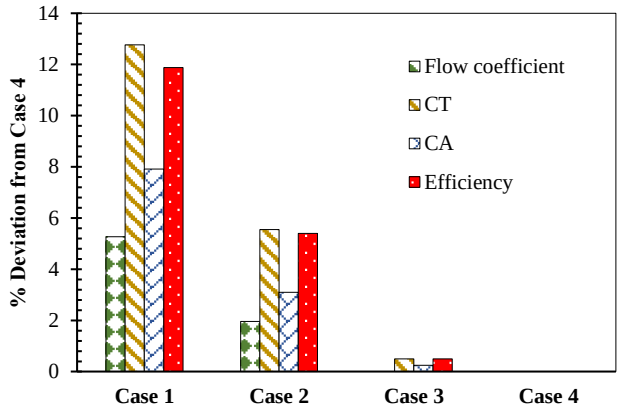

Figure 4.4 Results of grid independency study considering case 4 as the reference.

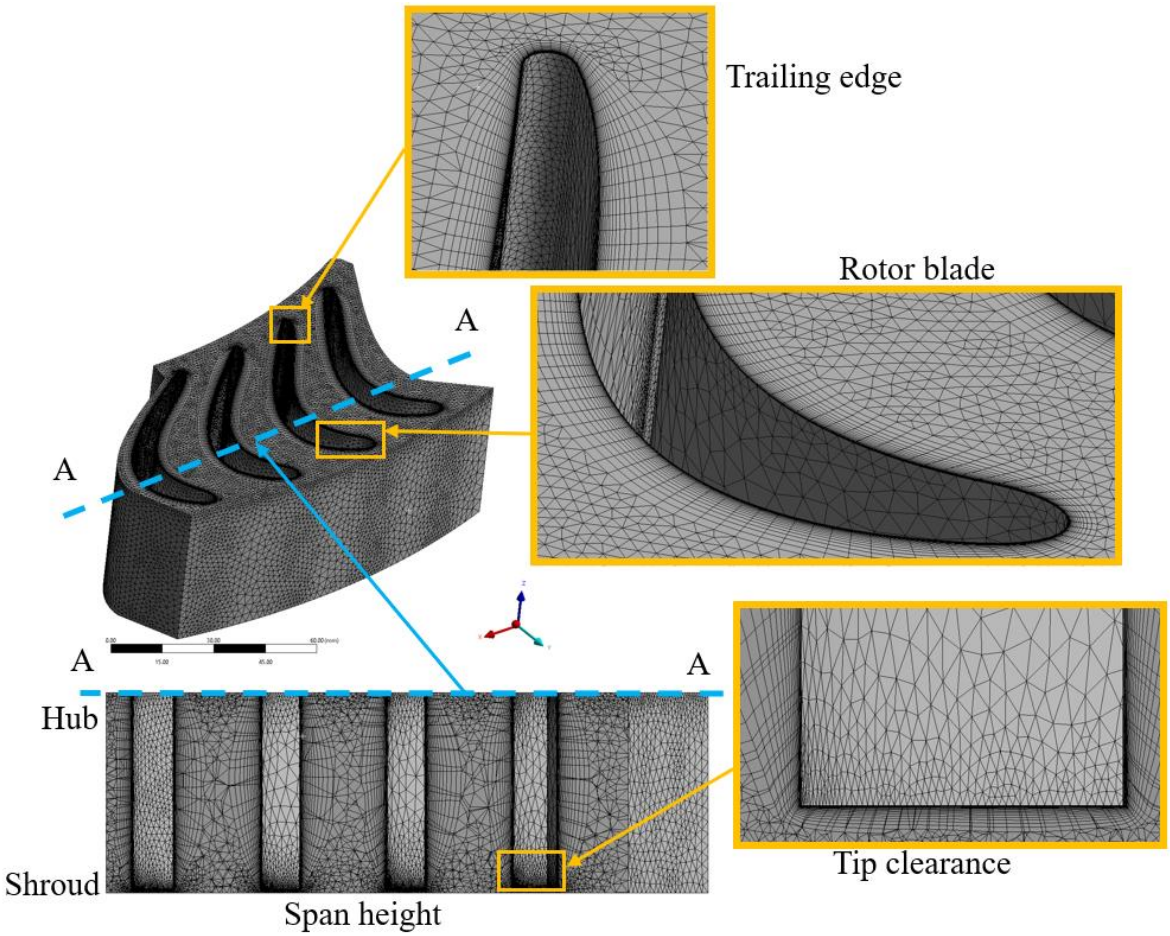

Figure 4.5 Schematic of the mesh used in the simulations (case 3).

4.3.1 Validation of Bidirectional Turbine

The bidirectional turbine (given in Table 4-1) was experimentally tested by Setoguchi et al. (Setoguchi et al., 2002) and was used for validation of the numerical model in this study. The CFD predicted results of the torque coefficient, input coefficient and efficiency were compared with the published experimental measurements of Case (1) in ref. (Setoguchi et al., 2002). The experimental results were reported to have one percent uncertainty and are labelled as EXP (-) (having -1%

uncertainty) and EXP (+) (having +1% uncertainty). As illustrated in Figure 4.6, in both inhalation and exhalation modes, the numerical solution predicts a similar trend to the test results. The simulated results are in a better agreement at lower flow coefficients ($0< \phi <1$) and the peak efficiency points for both inhalation and exhalation fall in this range. Although, the deviation increases at higher flow rates, the CFD results correspond reasonably to the experimental data and provide confidence in the accuracy of the CFD model used to optimise the radial outward flow turbine.

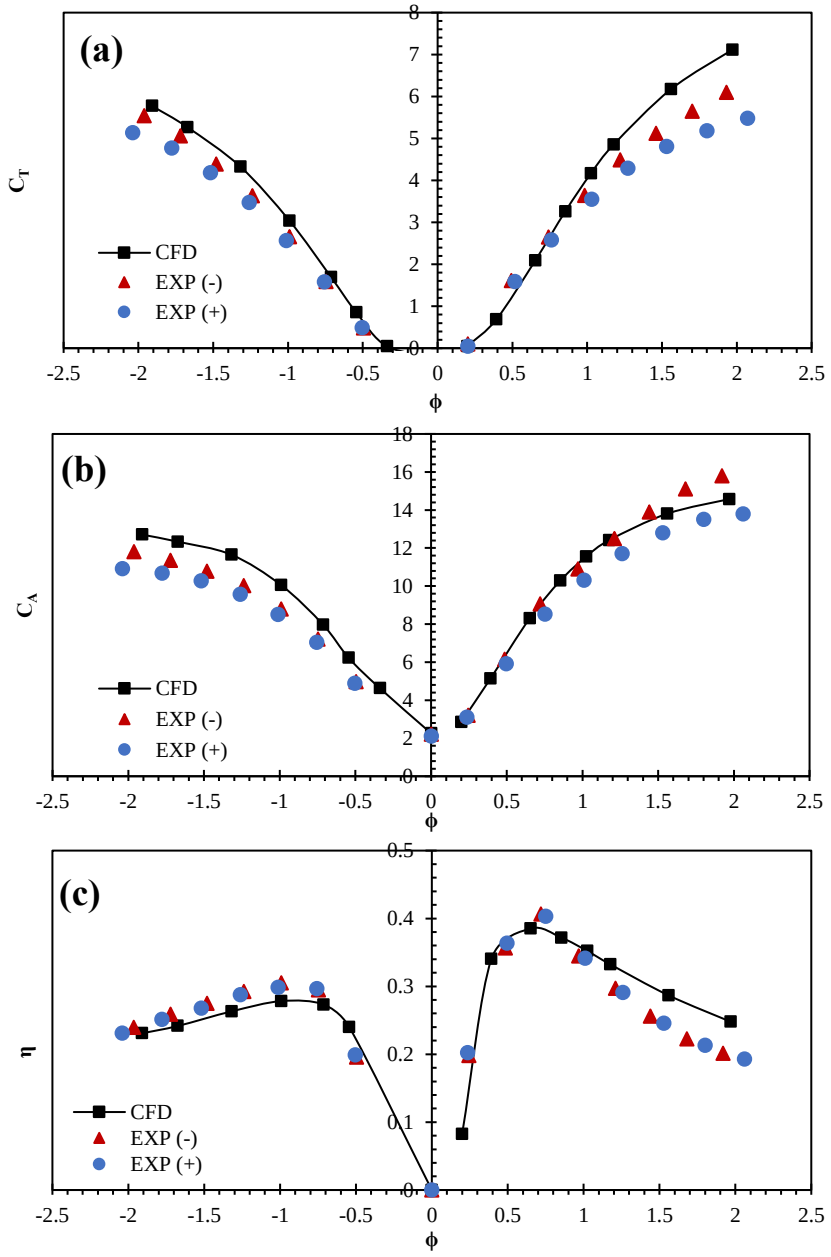

Figure 4.6 Comparing the accuracy of CFD results with published experimental results (Setoguchi et al., 2002); (a) C_T , (b) C_A and (c) η.

4.3.2 Numerical Optimisation of the Outward Flow Radial Turbine

The optimisation study is an iterative process which begins by performing CFD simulations on the initial geometry of the inflow turbine. Then, the output parameters are defined, and the design

exploration is used to create a design population by varying the input parameters. In this study, Design of Experiments method (DOE) was used to determine the design space and characterize the turbine performance based on a minimum number of actual analysis runs. The DOE conducts a series of experiments within the specified variation range of the input parameters set and minimizes the quantity of the required analysis runs to determine the parameters impacts. The Central Composite Design (CCD), based on a fractional factorial design was used to reduce the number of experiments by sacrificing less meaningful high-order interactions (Jung et al., 2016). A second order analysis was used with capability to model the interaction between the input parameters and surface curvatures appropriately. The general form of a second-order model explained in Ref. (Hatami et al., 2015) is:

$$y = a_0 + \sum_{i=1}^{n} a_i x_i + \sum_{i=1}^{n} a_{ii} x_i^{\,2} + \sum_{i=1}^{n} \sum_{j=1}^{n} a_{ij} x_i x_j \tag{4.5}$$

Where, x_i and x_j are the design variables, a the tuning parameter and n the number of parameters. In the CCD, an optimal design space is considered with two criteria: the degree of non-orthogonality of regression terms (or Variation Inflation Factor (VIF)), and the position of sample points (Leverages or the diagonal elements of the design matrix) (Guide, 2017). Using this method, the design space contains a centre point, $2n$ design points located at the -α and +α position on each axis of the selected input parameters and 2^{n-f} factorial points located at -1 and +1 positions along the diagonals of the input parameters space. Where α is selected such that both the maximum VIF and the maximum leverage are the minimum possible and f is the fraction of the factorial design and is a function of n.

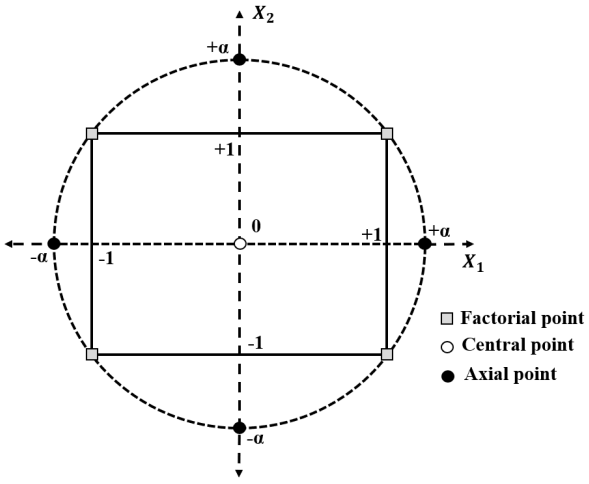

Figure 4.7 Central composite design for two design variables at two levels (Jung et al., 2016).

As an example, CCD for two design variables consists of four factorial points, four axial points, and one central points as schematically shown in Figure 4.7. In this study seven input parameters were considered and 2^6 fractional factorial designs were used, which halved the number of experiments from the 2^7 factorial designs.

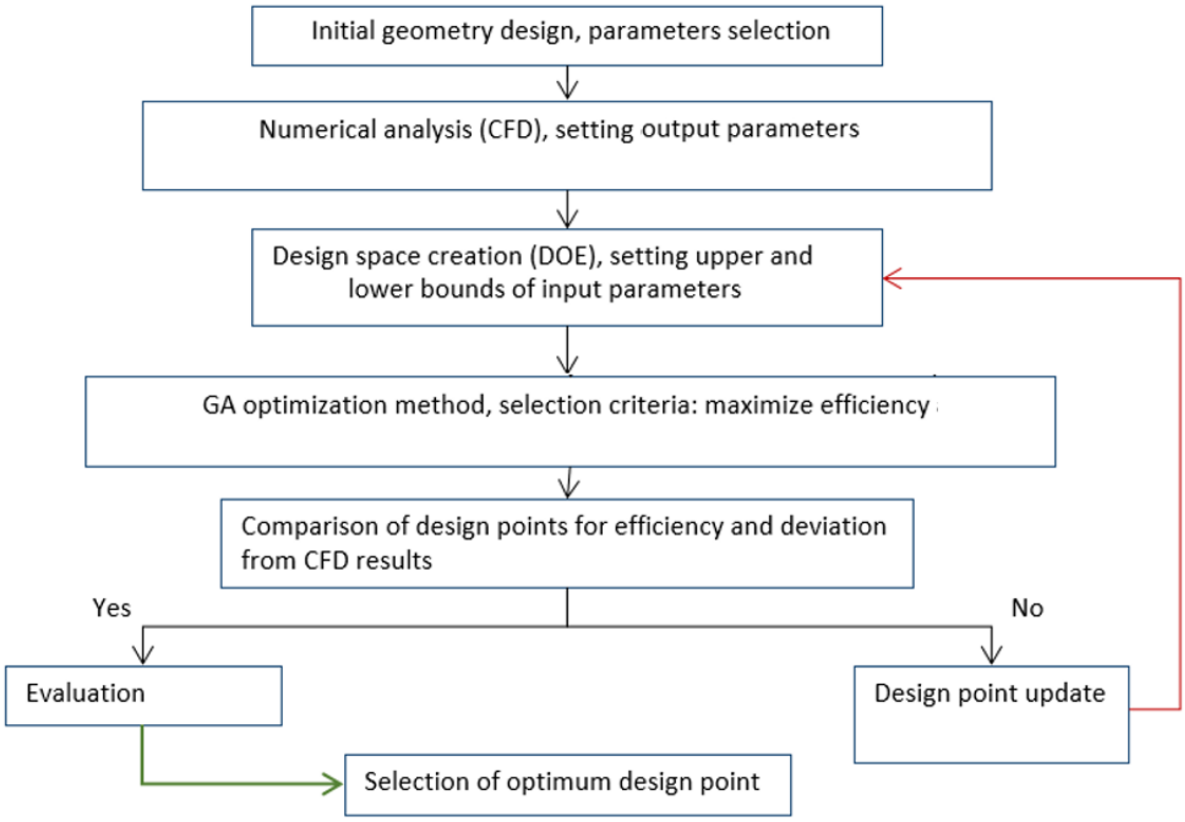

Figure 4.8 Design optimisation process.

The response surface function is used in the next step to fit the actual analysis data characterized by the DOE and sample a surrogate model. The response surface optimisation is used to perform an indirect optimisation analysis and evaluate the optimum candidate design predicted by various methods (Ghotli et al., 2013). It provides a smooth and continuous mathematical formulation by interpolating between discrete design points of the DOE. The response surface optimisation method allows the design points to be predetermined by the DOE and permits simultaneous solving of the response-surface design points and multiple optimisations. In the current study the Genetic Aggregation (GA) response surface algorithm was used to predict the optimum design point. GA is a meta model that selects the most appropriate response surface for each output parameter based on the genetic algorithm. It solves different response surfaces in parallel, analyses them regarding their accuracy and the stability in the cross-validation and can be a single response surface or a combination of several different response surfaces (Guide, 2017). In the optimisation step, genetic algorithm was used as the optimiser which is a well-known approach in turbomachinery design optimisation (Ghotli et al., 2013, Hatami et al., 2015, Jung et al., 2016). In the genetic algorithm feasible solutions are specified according to the bounds of the optimisation problem and the optimal solution is explored by analysing the maximum allowable Pareto front (Amouzgar K., 2015). In this study, maximization of the total to static efficiency

(defined in equation 4.3) was specified as the optimisation objective. In addition, other turbine characteristics such as torque coefficient (equation 4.1), input power coefficients (equation 4.2) and flow coefficient (equation 4.4) were set as the secondary output parameters. Figure 4.8 shows the iterative process of the optimisation study.

4.4 Results and Discussions

The optimised outflow turbine geometry of this study is shown in Figure 4.9 with the design characteristics indicated in Table 4-3.

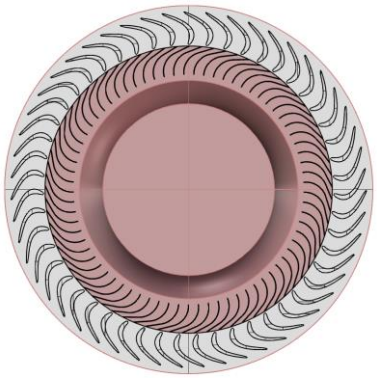

Figure 4.9 Optimised Outflow rotor design.

Table 4-3 Design characteristics of the optimised Outflow turbine.

Design variables	***Optimised geometry***
GV Angle (degree)	*26.5*
LE Radius (mm)	*1.93*
Chord Length (mm)	*50*
PS Radius (mm)	*0.49*
LE Angle (degree)	*67.72*
Stagger Angle (degree)	*-23.1*
TE Angle (degree)	*50*

The sensitivity of output parameters regarding the rate of changes applied to each input parameter was evaluated and shown in Figure 4.10. The local sensitivity statistics were generated regarding the trend of the efficiency at the optimum design point and determined the rate of impact of each parameter on the efficiency variations. The local sensitivity is an exploration tool included in the response surface, which analyses the weight of each input parameter on the output parameters independently (ANSYS-User's-Manual). If the increase of a parameter fulfils the objective function in the optimisation journey, that parameter is shown with a positive sign. In other words, the positive and negative bars in Figure 4.10 show the increase and decrease of the parameter, respectively, with respect to its initial values in the reference geometry.

Considering the local sensitivity data illustrated in Figure 4.10-a, angle of the guide vane (GV angle) affects the flow coefficient significantly. It is obvious that increase of the GV angle leads to a wider area between the upstream guide vanes and reduces the flow incidence and losses at the rotor upstream to a high extent. The LE angle has a reverse effect, which can be explained by the role of this parameter in shaping the flow passage between the rotor blades. Increasing the LE angle in the rotor geometry of this study leads to a narrower blade to blade area and increases the resistance to the flow at the rotor inlet. The input coefficient is mainly sensitive to GV angle and the LE angle as shown in

Figure 4.10-b. It is obvious that a higher GV angle causes a lower input coefficient. As the input parameter is related to the pressure, this can be justified regarding the influence of the GV angle on the pressure drop and losses in the turbine domain. This fact was also reported in a study by Setoguchi et al. (Setoguchi et al., 2002), in which for a fixed LE angle, there is a reverse relationship between the angle of the upstream guide vanes and the C_A parameter.

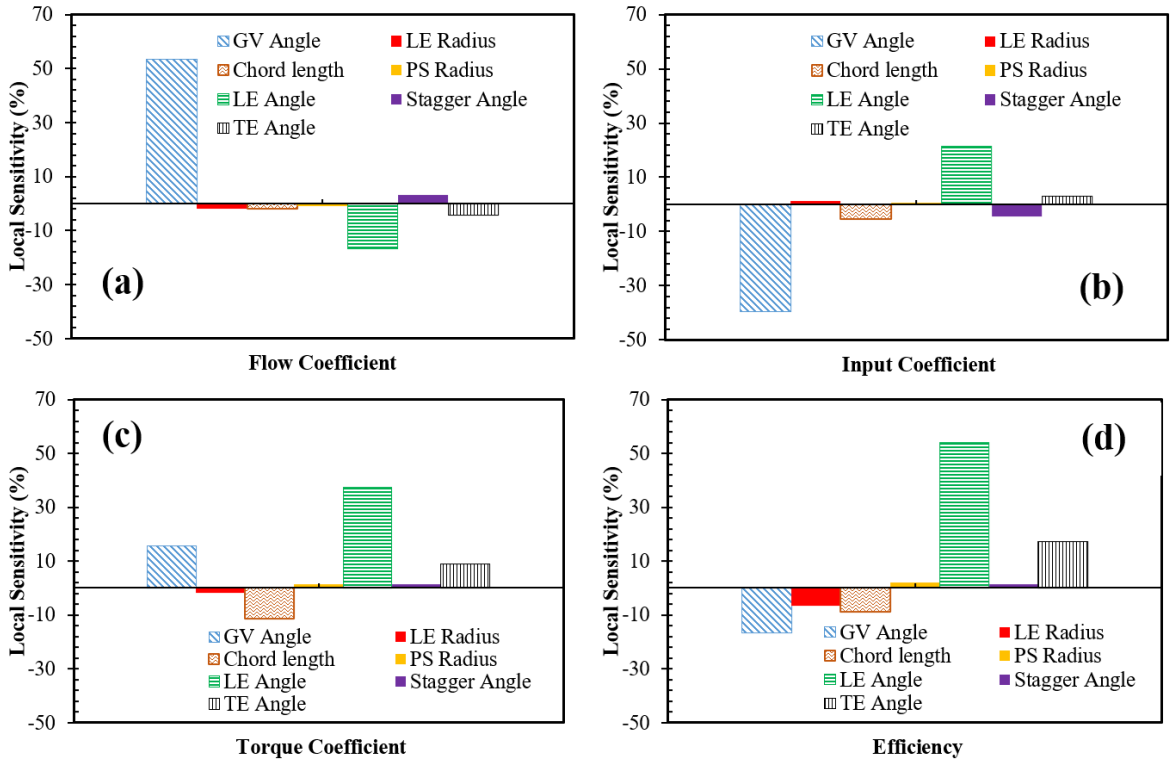

Figure 4.10 Local sensitivity of input parameters at the optimum design point.

The LE angle affects the input coefficient by shaping the blade flow passage and affecting the V_R term in the definition of C_A in equation 4.2. As illustrated in Figure 4.10-c, the LE angle has the highest contribution in variations of the torque coefficient is. Increasing the LE angle causes more inclination of the rotor blade and reduces the area and flow velocity at the mean radius of the rotor (known as A_R and V_R respectively). These terms contribute in the C_T as defined in equation 4.1. The sensitivity of the turbine total to static efficiency to the studied input parameters is shown in Figure 4.10-d. It is observed that the efficiency is mostly affected by the LE angle followed by the GV angle and TE angle. The LE angle being an effective parameter on both C_T and C_A, has a positive effect on the efficiency due to its more impact on the torque coefficient than the input coefficient. The negative effect of the GV angle can also be explained by to its effects on the input power and flow coefficient terms.

It should be noted that changes to the combination of input parameters lead to the optimum design point, however, the 3D response of efficiency based on the two most sensitive parameters (LE angle

and GV angle) is illustrated in Figure 4.11. This figure shows that the optimum efficiency was identified clearly within the specified variation bounds of these two parameters.

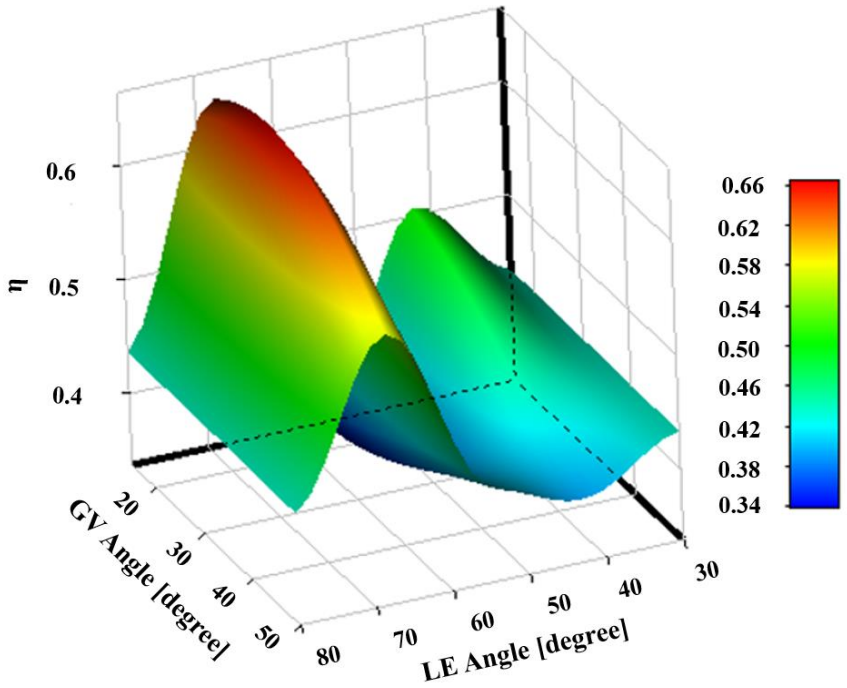

Figure 4.11 Turbine efficiency response versus the most sensitive input parameters.

4.4.1 Comparison of the initial and the optimum outflow turbine geometries

After finding the optimum design for the outflow turbine, its operation was compared to the initial outflow geometry determined in Table 4-2. A comparison of the flow rate versus total pressure drop of the initial and the optimised geometries is illustrated in Figure 4.12-a. It is clearly shown that for a given range of the total pressure drop, the optimised geometry acts more resistive to the flow rate than the initial geometry. Considering the local sensitivity figure of the flow coefficient shown in Figure 4.10-a, the flow rate is mainly affected by the GV angle and the setting angle. According to the geometrical characteristics of the initial and the optimised designs (as mentioned in Table 4-2 and Table 4-3, respectively), both geometries have a close GV angle. Thus, the higher resistance of the optimised geometry can mainly be due to its 10 degrees higher LE angle compared to the initial geometry. For the same reason, the input coefficient of the optimised design (Figure 4.12-b) is significantly higher than that of the initial design, which can be due to the decreased flow velocity at the mean radius (V_R) of the optimised design. This term according to the equation 4.2 leads to more input coefficient values. Comparison of the velocity contours in the rotor domain of both geometries Δp_0=1400 Pa, in Figure 4.13, clearly illustrates the lower air velocity at the mid-chord of the optimised design.

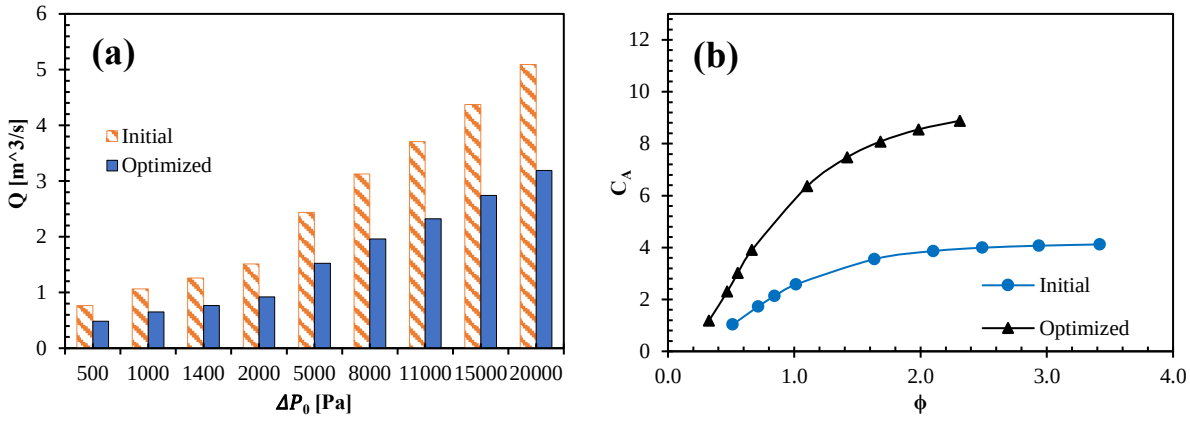

Figure 4.12 Comparison of flow rate (a) and the input coefficient (b) of the optimised design with the initial outflow turbine geometry.

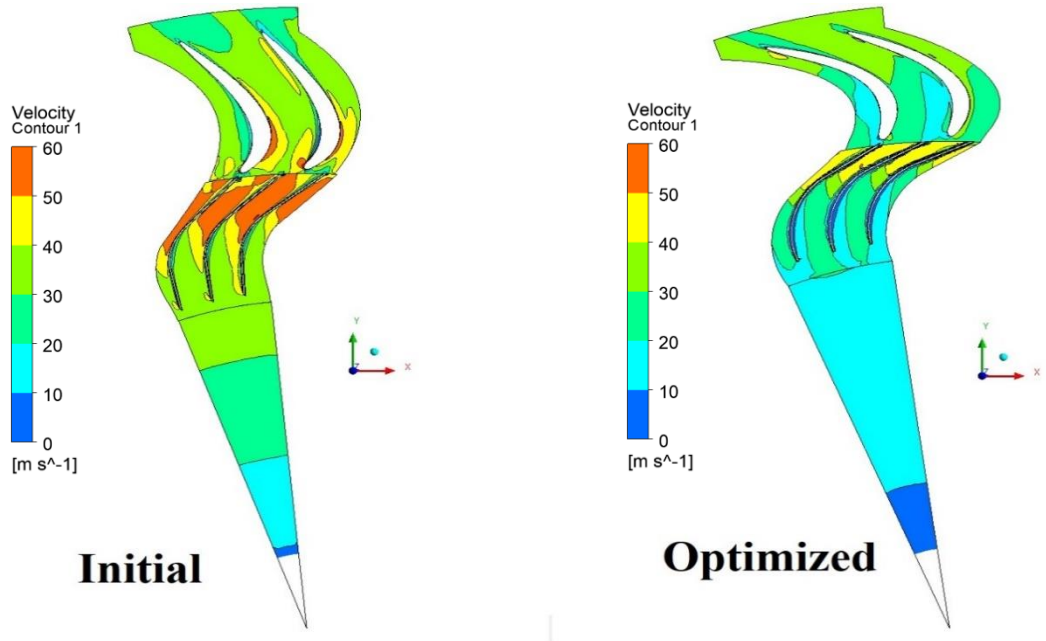

Figure 4.13 Comparison of the velocity contour of the initial and the optimised geometries at ΔP_0=1400 Pa.

As illustrated in Figure 4.14-a, torque coefficient of the optimised design has improved significantly compared to the initial design, which according to the design characteristics of both geometries, is mostly due to 10 degrees higher LE angle and smaller chord length of the optimised design compared to the initial geometry. According to Figure 4.14-b, the optimised geometry has 30% higher Peak efficiency than the initial design, which has been obtained by finding the optimum combination of the input parameters used in this study. For the optimised design, the operational flow range is smaller than the initial design and the peak efficiency point has moved towards smaller flow coefficients. This fact was previously explained by comparing the flowrate versus pressure drop of both geometries in Figure 4.12-a. It can be noted from the above-mentioned results that shape of the

rotor blade can significantly affect the turbine's performance including torque and the power conversion. The velocity vectors in the rotor domain of both geometries near their peak efficiency points (at Δp_0 =1400 Pa) are illustrated in Figure 4.15 and Figure 4.16. Comparing these figures shows that although the initial design allows more flowrate into the turbine domain, the rotor cannot efficiently convert the input power due to the energy losses in the domain. As shown in Figure 4.15, there are huge incident losses at the leading edge of the rotor blades in the initial design while there is a perfect stream of the flow in the turbine domain of the optimised design (Figure 4.16). It can be noted that the well-matched configuration of the rotor blades with respect to the upstream guide vanes is the main reason of low flow incidence in the optimum design.

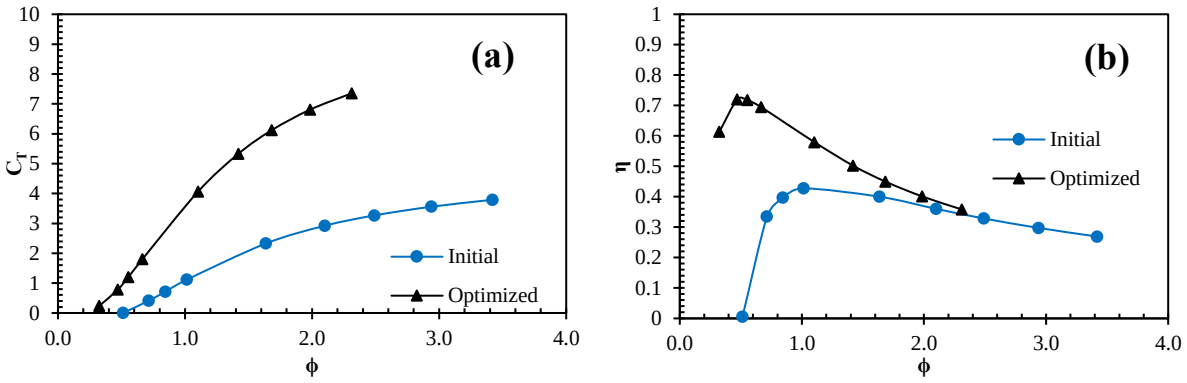

Figure 4.14 Comparison of the torque coefficient (a) and efficiency (b) of the optimised design against the initial outflow turbine geometry.

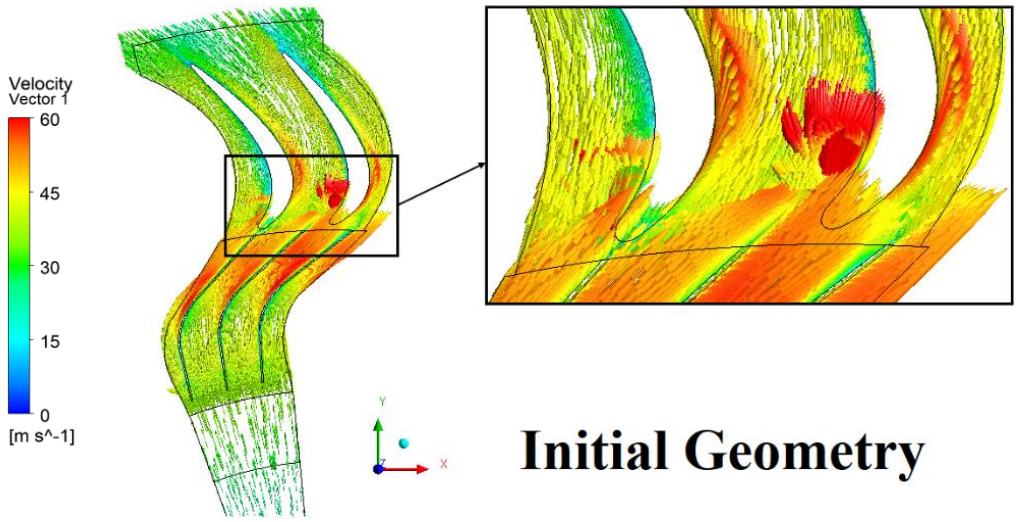

Figure 4.15 Velocity vectors in the turbine domain of the initial geometry at ΔP_0=1400 Pa.

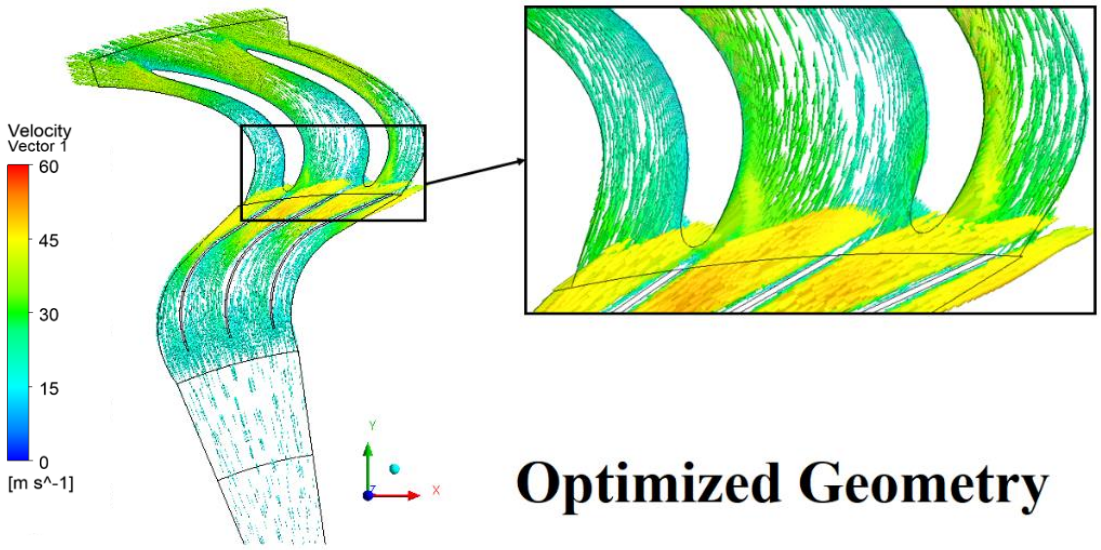

Figure 4.16 Velocity vectors in the turbine domain of the optimised geometry at ΔP_0=1400 Pa.

4.4.2 Energy transfer in radially outward and inward flow turbines

The Euler turbine equation can be written as the summation of energy transfer terms. These energy terms are change in dynamic head (associated with absolute velocity), change in centrifugal energy (associated with blade speed) and change in relative kinetic energy (associated with relative velocity) (Dixon and Hall, 2013, Hans, 1966):

$$\Delta W = \frac{(V_1^2 - V_2^2) + (U_1^2 - U_2^2) + (W_2^2 - W_1^2)}{2} \tag{4.6}$$

Here V and W are the absolute and relative velocities of the fluid, respectively. U is the blade speed and is calculated by multiplying the blade mean radius with the blade rotational speed ($r_R\omega$). Subscript 1 refers to the fluid entering into the rotor and subscript 2 shows flow leaving the rotor.

In a radially outward flow machine, due to changes in radius of rotation, U_1 is less than U_2 and this configuration is usually used for pumps and compressors to increase the static head. Nevertheless, an outward flow radial configuration was investigated in this research to be employed as a rotor. This design was optimised to have a maximized efficiency and its energy transfer capability was compared against the previously optimised inflow rotor design (Ansarifard et al., 2018). The inflow turbine has 73 guide vanes at the upstream, 34 guide vanes at downstream and 51 rotor blades; more details of this turbine can be found in chapter 3 of this thesis. Figure 4.17 schematically illustrates both rotors with arbitrary angles at the entry and exit. In addition, the efficiency plots and the total pressure changes across the rotor (ΔP_R) of both configurations are shown in Figure 4.18 and Figure 4.19, respectively. The total pressure change across the rotor was evaluated using the equation below (Hall and Dixon, 2013, Logan Jr, 2013,Nancarrow et al., 1974):

$$\Delta p_R = p_{01} - p_{02} = \frac{1}{2}\rho[(V_1^2 - V_2^2) + (U_1^2 - U_2^2) - (W_1^2 - W_2^2)] + E_{Rl} \quad (4.7)$$

Here $E_{Rl} = \int_1^2 Tds$ is the rotor losses and has been disregarded in the calculations. As Figure 4.18 and Figure 4.19 illustrate the performance plot of the outflow turbine is comparable to that of the inflow turbine. Also, the total pressure across the outflow rotor is very close to that of the inflow rotor over the whole range of turbine pressure drops.

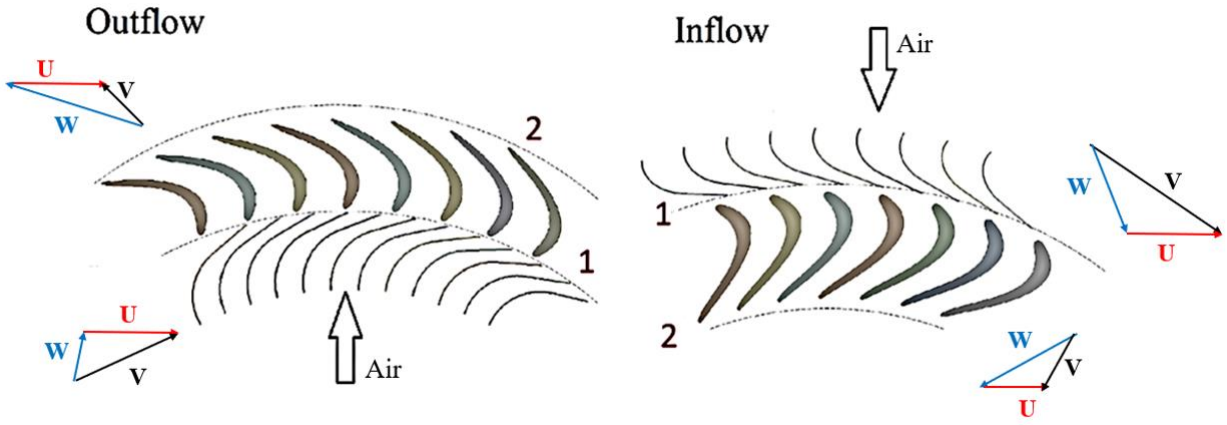

Figure 4.17 Schematics of the airflow velocity components at the rotor section of the outflow and inflow turbines.

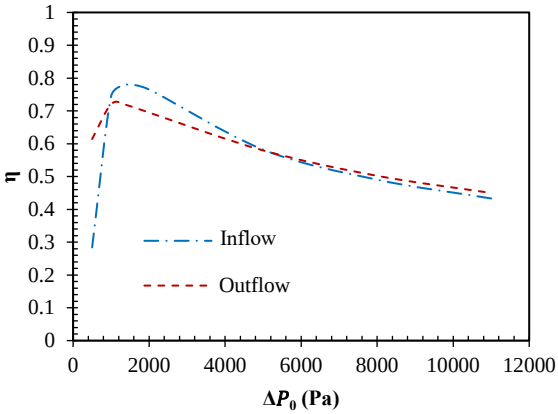

Figure 4.18 Comparison of the efficiency of outflow and inflow turbines over a range of turbine pressure differentials.

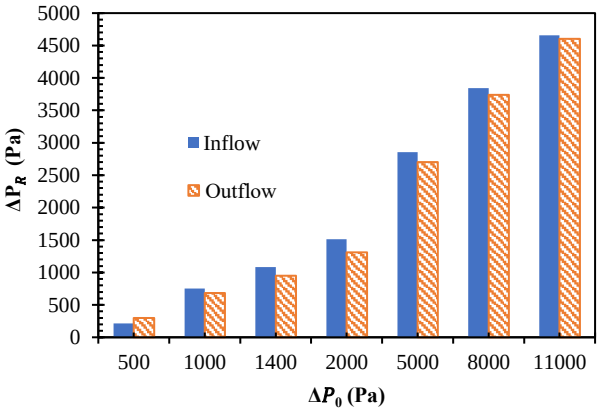

Figure 4.19 comparison of the total pressure changes across the rotor of the outflow and inflow turbine configurations.

To investigate the inflow and outflow turbine configurations in further details, three terms of the energy transfer associated with changes in absolute velocity, blade speed and relative velocity were defined as below:

$$Term1 = (V_1^2 - V_2^2),\ Term2 = (U_1^2 - U_2^2),\ Term3 = -(W_1^2 - W_2^2) = (W_2^2 - W_1^2) \quad (4.8)$$

Comparison of the Term1 illustrated in Figure 4.20 shows that the outflow turbine provides a higher change in absolute kinetic energy compared to the inflow turbine over the whole range of pressure differentials. It can be described by the geometrical features of the outflow turbine, which causes a higher change in dynamic pressure across the rotor. A comparison of the air absolute velocity at the inlet and outlet of each rotor is shown in Figure 4.21, which shows higher absolute velocities of the outflow turbine design compared to the inflow turbine. As illustrated Figure 4.22-a, Term2 which refers to the change in centrifugal energy is constant for each turbine. This term is negative for the outflow turbine due to the change in radius for the flow direction. Term3 (Figure 4.22-b) is the change in relative kinetic energy which initially increases by the raise of pressure drop, peaks in the middle range and then reduces at high pressure drop values. Compared to the inflow configuration, the outflow turbine has a faster response to variations of this velocity component and reaches negative values at pressure differentials higher than 8000 Pa. Generally, Term1 affects the change in dynamic pressure through the machine while Term2 and Term3 affect the static pressure changes across the rotor. It was found from this analysis that although, Term2 negatively affects the energy transfer in the outward turbine, the improvements of Term1 and Term3 compensate the negative portion and provide acceptable total pressure across the rotor for the specified operational range of this study.

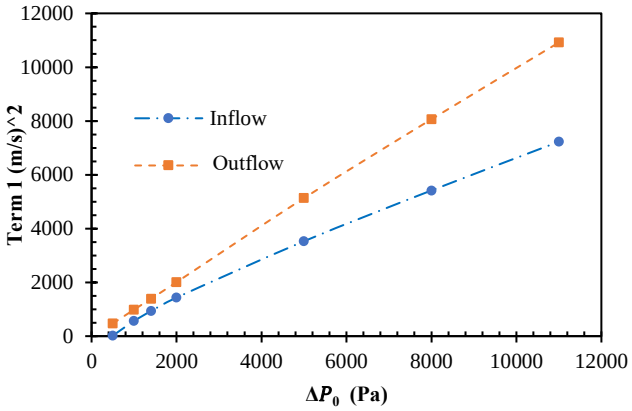

Figure 4.20 Comparison of the energy transfer term 1 of the outflow and inflow turbines.

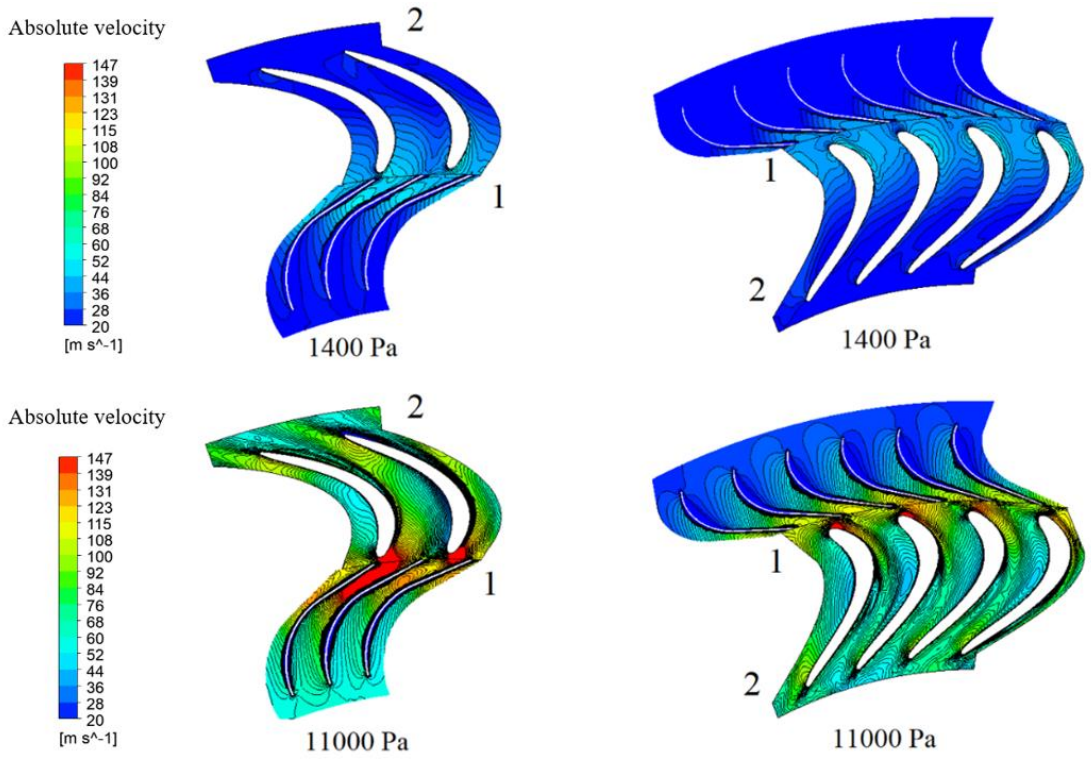

Figure 4.21 Comparison of the absolute velocity contours of the outflow and inflow turbines at Δp_0 =1400 Pa and Δp_0 =11000 Pa.

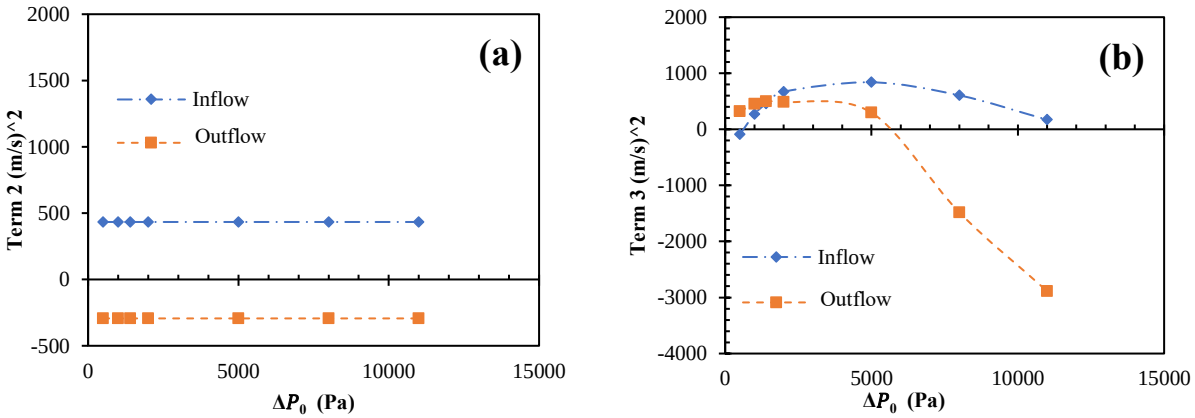

Figure 4.22 Comparison of the energy transfer terms of the outflow and inflow turbines.

4.4.3 Unsteady performance evaluation of the optimum outflow turbine

As mentioned before, the optimisation study was performed using a steady computational model to reduce the time and computational cost. However, the actual condition is unsteady since the computational geometry includes rotating domains. Thus, a transient model (TR) was used to control the relative motion of the rotor in a purely unsteady fashion and to evaluate the accuracy of the obtained efficiency results in the optimisation study. The steady model is called Case 1, which was set up using a Moving Reference Frame (MRF) approach and was validated in previous section.

In the transient model, six revolutions of the periodic domain were simulated at a rotational speed of ω =120 rad/s, giving a total time of 0.01232s. The residuals were set to 10^{-6} and a time step study was performed considering three different cases. First, the time step was set on 5×10^{-4}s, giving a total number of 24 time steps (this setup is referred as Case 2). Second, a time step of 1×10^{-4}s, giving a total number of 123 time steps (Case 3). Finally, a time step of 1×10^{-5}s, with a total number of 1232 time steps (Case 4), this case was not economical regarding the simulation time and was used as a reference to evaluate the accuracy of other cases. Figure 4.23 compares the deviation of the total to total efficiency (η_{t-t}) and total to static efficiency (η_{t-s}) of the optimum outflow turbine at its best efficiency point, obtained from Cases 1 to 3 with respect to the results of Case 4. According to Figure 4.23, the Case 3 shows minor deviation from the Case 4 (1% in η_{t-t} and 0.73% in η_{t-s}) but is more economical in terms of the computational cost. Therefore, Case 3 with the time step of 1×10^{-4}s was selected as the final transient model to simulate the optimum outflow turbine's efficiency in an unsteady fashion. In addition, Figure 4.23 shows that there is a 2% deviation in the η_{t-t} and less than 1% deviation in the η_{t-s} of the MRF model (Case 1) and the transient model (Case 3) at the maximum efficiency point.

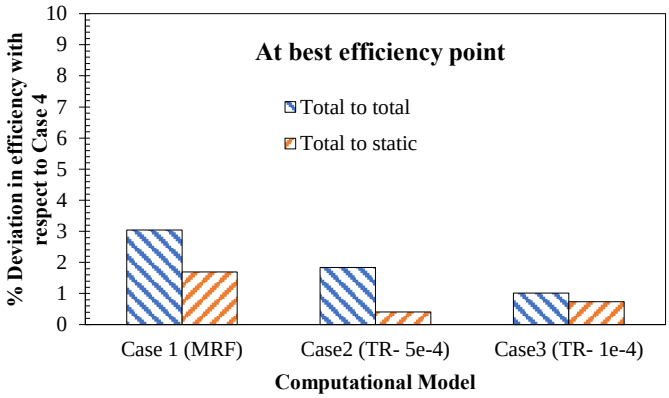

Figure 4.23 Time step study of the transient model (TR) and comparison of the deviation of Cases 1 to 3 from the Case 4.

As the main concern of this study, the plot of the total to static efficiency (η_{t-s}) of the optimum outflow turbine over the entire flow coefficient is compared for the MRF and the transient model in Figure 4.24. It is obvious that the efficiency plots in both models follows a similar trend and the steady model (MRF) has slightly overestimated the efficiency of the turbine for the whole flow coefficients. Considering the volume of the computations in the optimisation studies, benefits of using the steady model in this study strongly outweigh the 2% discrepancy and the MRF model can be regarded as an accurate model.

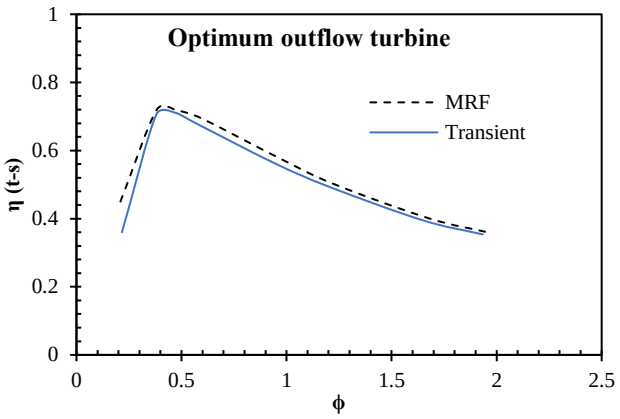

Figure 4.24 Comparison of efficiency of the optimum outflow turbine using MRF model (Case 1) and the transient model (Case 3).

The performance of the optimised outflow turbine, obtained from the transient model, was compared to the existing unidirectional axial and radial turbines (in their direct mode) in the literature (Rodríguez et al., 2019, Pereiras et al., 2014). As Figure 4.25 illustrates, the outflow turbine has a peak efficiency of 71% which has 21% improvement compared to the radial geometry suggested in Ref. (Rodríguez et al., 2019). It should be noted that the radial turbine in Ref. (Rodríguez et al., 2019) is design-optimised to work in a twin turbine OWC concept, when maximum efficiency in the direct mode and maximum backflow prevention in the reverse mode are desired. However, this comparison highlights that a peak efficiency over 70% can be expected for this type of turbine, by focusing on the design optimisation in a single flow direction. The optimum outflow turbine also provides comparable efficiency to the axial turbine (the axial turbine with optimum solidity in the direct mode) in Ref. (Pereiras et al., 2014), with almost 2% lower peak efficiency and slightly narrower operational range.

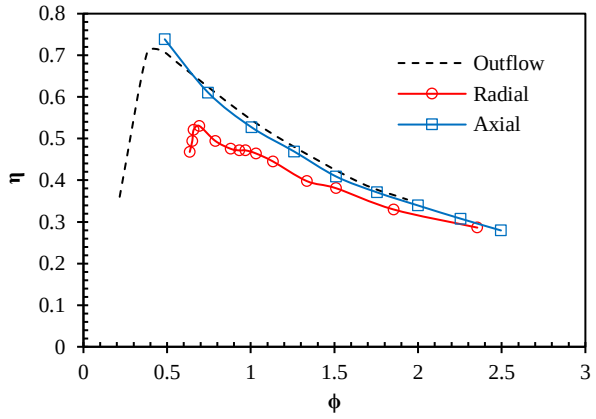

Figure 4.25 Comparison of the efficiency (total to static) of the optimum outflow turbine with the existing radial (Rodríguez et al., 2019) and axial turbines (Pereiras et al., 2014).

4.4.4 Importance of adding a diffuser at the outlet of the optimised outflow turbine

The geometry of the optimised outflow turbine was further investigated regarding the unsteady effects of the flow at the rotor exit. A stationary section was considered at the outer boundary of the turbine domain with inlet and outlet diameters of 0.45 mm and 0.49 mm respectively. Due to the centrifugal configuration of the turbine, this extra section could be considered as a diffuser and was added to the turbine geometry to prevent the flow interactions between the blade trailing edge and the outlet boundary. Figure 4.26 shows the configuration of the diffuser in the periodic computational domain of the outflow turbine.

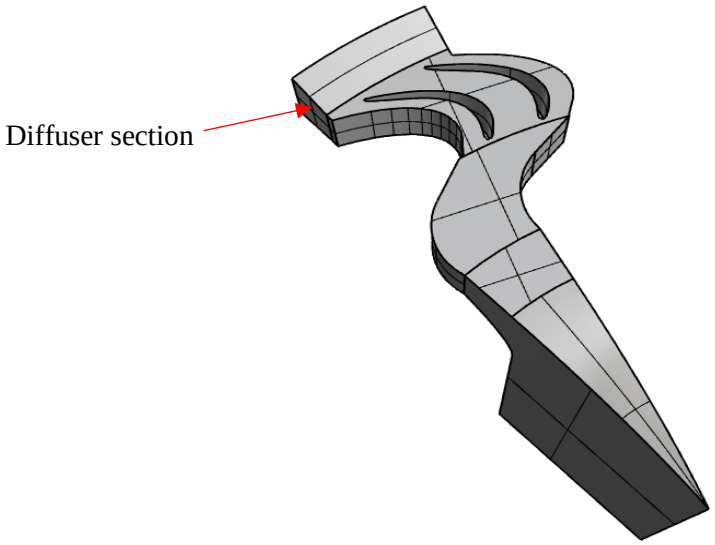

Figure 4.26 The periodic domain used in CFD simulations of the outflow turbine with diffuser.

The transient CFD simulations were performed to compare the performance of the outflow turbine with and without the diffuser section as illustrated in Figure 4.27. As can be observed in Figure 4.27a and b, the main effect of the diffuser is on the input power coefficient and the torque coefficient is almost unaffected. The input coefficient (C_A) plot of the outflow turbine is droped lower to that of the turbine without diffuser. This can explain the role of the diffuser in reducing the pressure losses at the rotor exit. Regarding the total to static efficiency shown in Figure 4.27c, the turbine with diffuser obtains almost 2% higher peak efficiency and this efficiency improvement is more noticeale at higher flow rates, which abviously is due to the trend of the input coefficient plot.

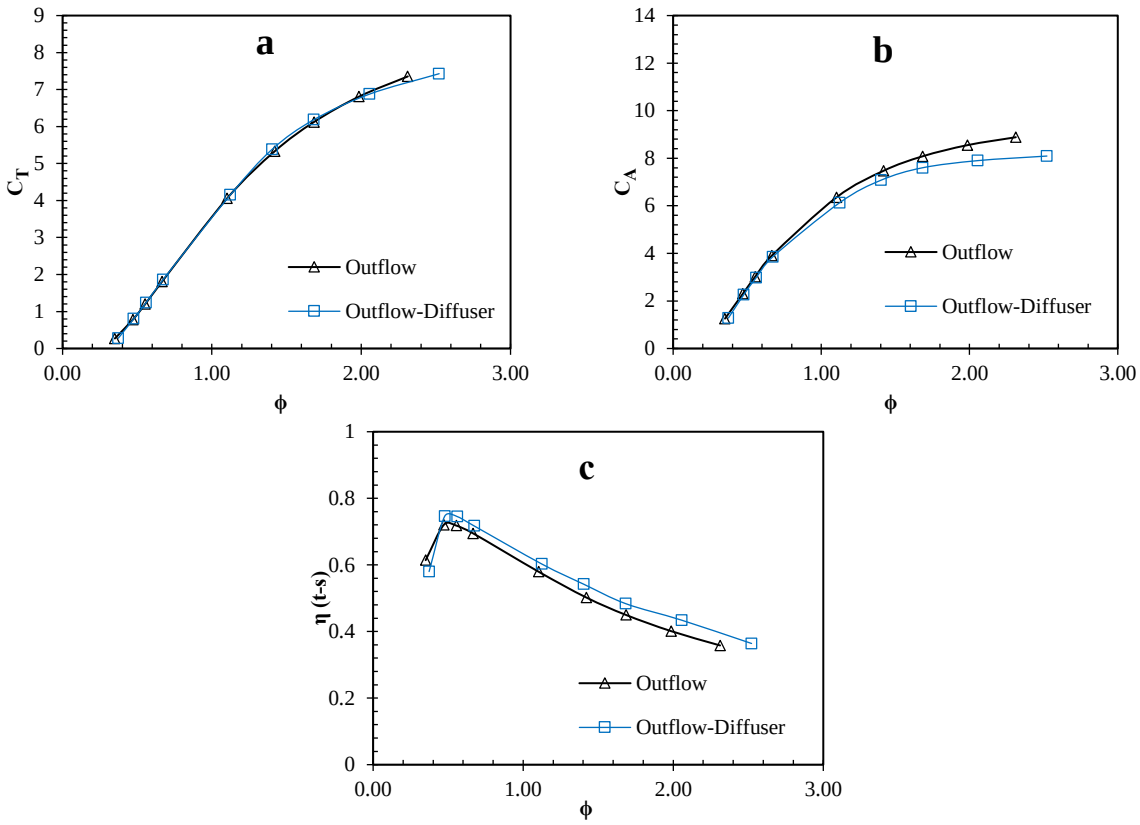

Figure 4.27 Comparison of the performance of the optimum outflow turbine with and without diffuser (using the transient model). (a) C_T , (b) C_A and (c) η.

Figure 4.28 compares the velocity contours at the turbine domain of the outflow turbine with and without the diffuser section. It is clearly observed that the flow velocity is reduced as it moves to the diffuser domain, which can show the application of the diffuser in recovery of the kinetic energy at the rotor downstream. As a result, the outflow turbine equipped with a diffuser can be considerd as the final outflow turbine geometry with a peak total to static efficiency of 74%.

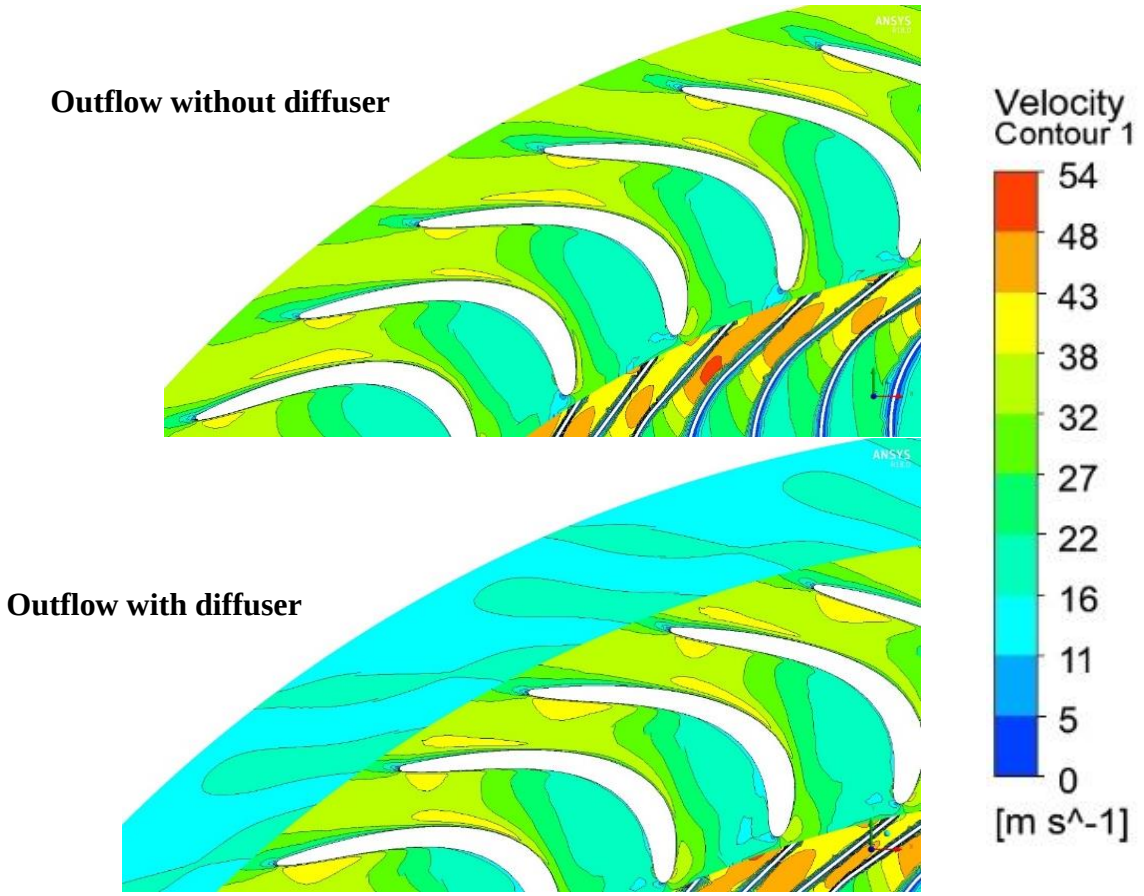

Figure 4.28 Comparison of the velocity contours in the optimum outflow turbine with and without the diffuser section.

4.5 Conclusion

A design optimisation study was performed to maximize the total to static efficiency of a centrifugal radial turbine (also called outflow turbine). Seven CAD parameters were used as the design variables and their effects on the turbine performance were analysed. The optimum outflow turbine obtained 30% higher efficiency than the reference geometry. Although changes to a combination of parameters has led to the optimum turbine geometry, the LE angle was found to be the most sensitive parameter, followed by the GV angle, TE angle and the chord length. Therefore, from the point of view of the authors including these parameters in future optimisations can lead to a more accurate exploration of the optimum rotor design. The performance of the optimum outflow turbine was evaluated in a transient model and close results were obtained compared to the MRF model. This comparison revealed that using the steady model to conduct the optimisation studies of this research was a reliable approach with lower computational cost.

The energy transfer of the optimum centrifugal turbine was compared to an optimum centripetal alternative. It was found that change of the rotor radius causes a negative centrifugal energy transfer,

however, this configuration provides a significant change of the dynamic pressure across the rotor. Thus, the total pressure changes across the turbine maintained comparable efficiency to that of a previously-optimised centripetal inflow radial turbine.

The optimised outflow radial turbine obtained 72% peak efficiency (in steady state), highlighting its comparability with the unidirectional axial alternatives in the field. There are other parameters that can affect the shape of the rotor and the flow passage between two rotor blades such as number of rotor blades and solidity. These parameters were not included in the list of input parameters of this research. Thus, it is recommended to investigate their potential effects on the efficiency of the turbine and the turbine-chamber interactions.

5 COMPARISON OF INFLOW AND OUTFLOW RADIAL AIR TURBINES IN VENTED AND BIDIRECTIONAL OWC WAVE ENERGY CONVERTERS

This chapter is based on a research paper submitted (Revised version is submitted) and under review by the journal of Energy. The citation for paper is:

Ansarifard, N., Fleming, A., Henderson, A., Kianejad, S.S., Chai, Sh., Jarrah Orphin," Comparison of inflow and outflow radial air turbines in vented and bidirectional OWC systems", Energy, 182, 159-176. (https://doi.org/10.1016/j.energy.2019.06.041)

Abstract

This chapter analyses the aerodynamic performance of two configurations of a unidirectional-radial-air-turbine; inflow and outflow. These turbines were studied as the Power-Take-Off (PTO) unit for application on a vented-OWC and a conventional bidirectional-OWC with a twin-turbine configuration, forming four different turbine-OWC configurations. These configurations were evaluated in terms of full-scale power extraction using extrapolated hydrodynamic experimental data of irregular waves of King Island test site. The power extraction capacity was evaluated by defining a lower and upper bound of power generation under fixed and controlled RPM schemes and the energy produced in each configuration was then compared against a state-of-the-art bidirectional turbine. It was found that the difference between these power extraction bounds was lower in case of the outflow turbine, which shows this turbine is less sensitive to RPM variations than the inflow turbine. In addition, due to its lower resistance to the flow in direct mode, the outflow turbine has a smaller full-scale size than the inflow turbine. It was concluded that the outflow turbine provides better efficiency in a twin-turbine-OWC system, while the inflow turbine yields better performance in a vented-OWC system. The inflow turbine when used in a vented OWC can obtain comparable power to a bidirectional turbine-OWC systems fitted with a state-of-the-art bi-directional turbine.

5.1 Introduction

An oscillating water column (OWC) is one of the most studied wave energy converter plants in the world. It has a concrete or steel structure, called a chamber, which is partially submerged in the sea and open at the bottom. Incident waves cause oscillations in the chamber water level; therefore, positive and negative pressure drops between the chamber and atmosphere. A Power-Take-Off (PTO), typically a turbine, is mounted at the top of the chamber and extracts energy from the pressure differential between the chamber and atmosphere. The air flow moving into the turbine in an OWC system is bidirectional and a conventional stator plus rotor type turbine is used to extract power from the air flow induced by the pneumatic pressure of the OWC.

A unidirectional concept of OWC, known as vented OWC, was investigated by Fleming et al. (Fleming et al., 2017). A fundamental difference between the vented OWC and the conventional ones is the use of passive air flow valves in the chamber structure to rectify the flow and expose the turbine to air flow from one direction. Although in the vented OWC air is limited to pass through the air turbine for only half the wave cycle, almost all the energy from the entire wave cycle is available for extraction. This is because during the reversed half-cycle, air exits the system through the valves with very little pressure drop, so the energy becomes stored in the form of water column heave and becomes added to

the pneumatic power of the next half-cycle. Using the vented OWC concept results in a simpler turbine design, as the efficiency penalty imposed by the reverse flow operation of the turbine is significantly reduced. In addition, the unidirectional turbines can be custom-designed for maximized efficiency in their unidirectional direct-flow-mode.

Other types of air rectifying systems were designed to extract ocean pneumatic power, such as Tupperwave (Benreguig et al., 2018) and Bombora (Manasseh et al., 2017). In the Tupperwave, the airflow becomes significantly pressurized and is rectified between two fixed-volume accumulator chambers. These chambers are connected to the OWC chamber using passive valves and a unidirectional turbine is employed to produce energy (Benreguig et al., 2018). The Bombora, utilizes a flexible membrane system to convert the wave energy to pressurized air. It is divided into a number of cells which are inflated with the compressed air. As a wave passes over a chamber, air is compressed into a plenum chamber using one-way valves and the resulting air flow drives a unidirectional generator (Manasseh et al., 2017). Design of unidirectional turbines for OWC was mainly investigated in the form of twin-turbine topologies. The idea of twin-turbine configuration of the OWC was proposed by Jayashankar et al. and Mala et al. in (Jayashankar et al., 2009a, Mala et al., 2011b), to rectify the flow by employing a pair of unidirectional turbines instead of using control valves. In this configuration each turbine acts in a single direction of flow (either inhalation or exhalation) and is idle during the reversed flow direction. Most proposed twin-unidirectional configurations in the literature employ axial turbines, except the study by Rodriguez et al. (Rodríguez et al., 2018) which investigated centrifugal turbines for a twin-turbine purpose. They focused on improving the global efficiency through strengthening the flow blockage in the reverse turbine and optimising the performance of the turbine in the direct mode (Rodríguez et al., 2019). A big challenge in twin-turbine designs is associated with the flow leakage through the reverse turbine, which takes around 30% of the total flow generated by the OWC (Dudhgaonkar et al., 2011). This issue not only limits the power conversion to only 70% of the available pneumatic power but contributes in production of negative torque. Radial turbines (centrifugal configuration) were shown to better prevent backflow in the reverse mode than the axial turbines (Rodríguez et al., 2018). However, the power conversion performance of these turbines are still significantly lower than the axial turbines. This is due to the low global efficiency of the radial impulse turbine which hardly reaches 50%, while this efficiency for axial turbines is over 70% (Dudhgaonkar et al., 2011, Okuhara et al., 2014, Okuhara et al., 2012, Setoguchi and Takao, 2006b). The aim of improving the efficiency of radial turbines has led to investigations of centripetal and centrifugal configurations of the radial turbines by the authors, these geometries are referred as inflow and outflow turbines respectively. These turbines were designed by studying various geometrical parameters to find an optimised design for each configuration. The inflow and outflow

turbines are illustrated in Figure 4.1 and were initially designed to operate in a vented OWC system, where a single-turbine and one-way valves are used to limit power extraction to a single air flow direction. The inflow and outflow turbines obtained high peak efficiency of 81% and 74%, respectively, which is a significant improvement for this type of turbines.

In this study, numerical simulations were employed to analyse the performance of air turbines in steady and unsteady conditions. Two inflow and outflow radial turbines, previously optimised for efficiency maximization, were used for further analysis. The performance of the turbines was assessed by means of CFD simulations using the commercial code of ANSYS CFX. The numerical model was validated by using a bidirectional radial turbine published in the literature (Case 1, by Setoguchi et al. in (Setoguchi et al., 2002)) and a good degree of agreement with the published experimental results was obtained. The inflow and outflow turbines were analysed in a vented OWC system which was their initial design purpose. These turbines were also compared regarding their overall power extraction in a twin-turbine concept in a bidirectional OWC and their drawbacks in reverse mode were highlighted. To analyse the turbines' operation under unsteady conditions, model scale hydro/aero dynamic experimental data of irregular waves corresponding to King island, Tasmania were used. Different configurations of the inflow and outflow turbines in vented and bidirectional OWC systems were compared in terms of size, rotational speed and power in full scale using the data of irregular waves tested at Australian Maritime College (AMC). Finally the turbines were compared with a state-of-the-art twin-rotor turbine (Rodríguez et al., 2019) regarding the power extraction with fixed and optimum rotational speeds under irregular waves in full scale.

5.2 Geometry

Two different designs of a unidirectional radial turbine were studied in this research, these geometries are named inflow and outflow turbines with the specifications outlined in Table 5-1. These geometries are illustrated in Figure 5.1, and were previously optimised for efficiency maximization for a single flow direction. Each turbine has 51 rotor blades with 73 guide vanes at the rotor upstream (according to the geometry Case (1) in (Setoguchi et al., 2002)). The inflow turbine has a second row of guide vanes at the rotor downstream to eliminate the swirl and direct the flow into the duct (logics behind this can be found in (Ansarifard et al., 2019)). Design of the downstream section of the inflow turbine was separately optimised in (Ansarifard et al., 2018) regarding the damping coefficient and energy losses. Parametric geometries of both turbines were studied by the authors, Considering a set of CAD variables. These parameters are defined in Figure 5.2 and Figure 5.3 where their values in the optimum design of the inflow and outflow turbines are determined in Table 5-2 and Table 5-3, respectively.

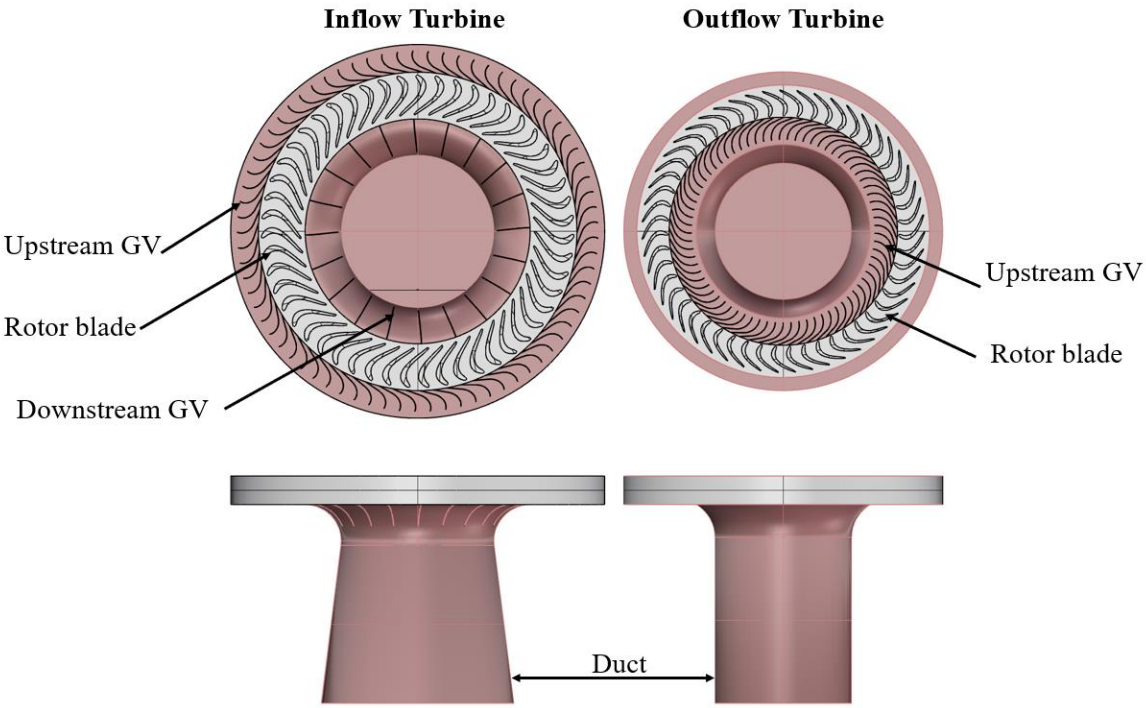

Figure 5.1 schematics of the inflow and outflow turbine geometries.

Table 5-1 Main characteristics of inflow and outflow turbines in model scale.

Characteristics	***Inflow***	***Outflow***
Configuration type	*Centripetal*	*Centrifugal*
D_R	*0.414 m*	*0.408 m*
$D_{Overall}$	*0.575 m*	*0.490 m*
Number of blades	*51*	*51*
Number of upstream guide vanes	*73*	*73*
Number of downstream guide vanes	*20*	*-*

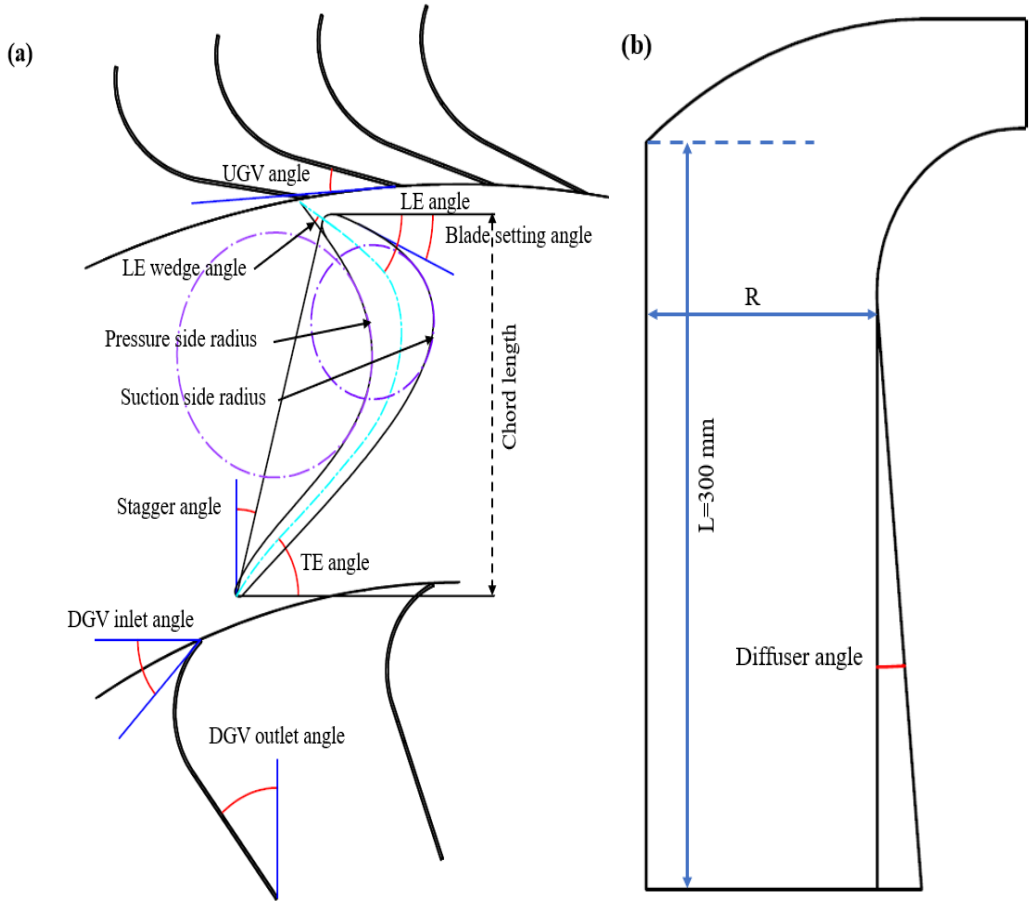

Figure 5.2 Illustration of the parameters used in creation of the inflow turbine.

Table 5-2 Design characteristics of the optimised inflow turbine.

Design variables	***Value***
Chord Length	*66 mm*
LE Angle	*41°*
LE Wedge Angle	*17°*
Pressure Side Radius	*0.45 mm*
Stagger Angle	*28.5°*
Suction Side Radius	*0.5°*
TE Angle	*45°*
Blade Setting Angle	*83.5°*
UGV Angle	*15°*
DGV Inlet Angle	*85.31°*
DGV Outlet Angle	*4.22°*
Duct Radius (R)	*117.67 mm*
Diffuser Angle	*7.10°*

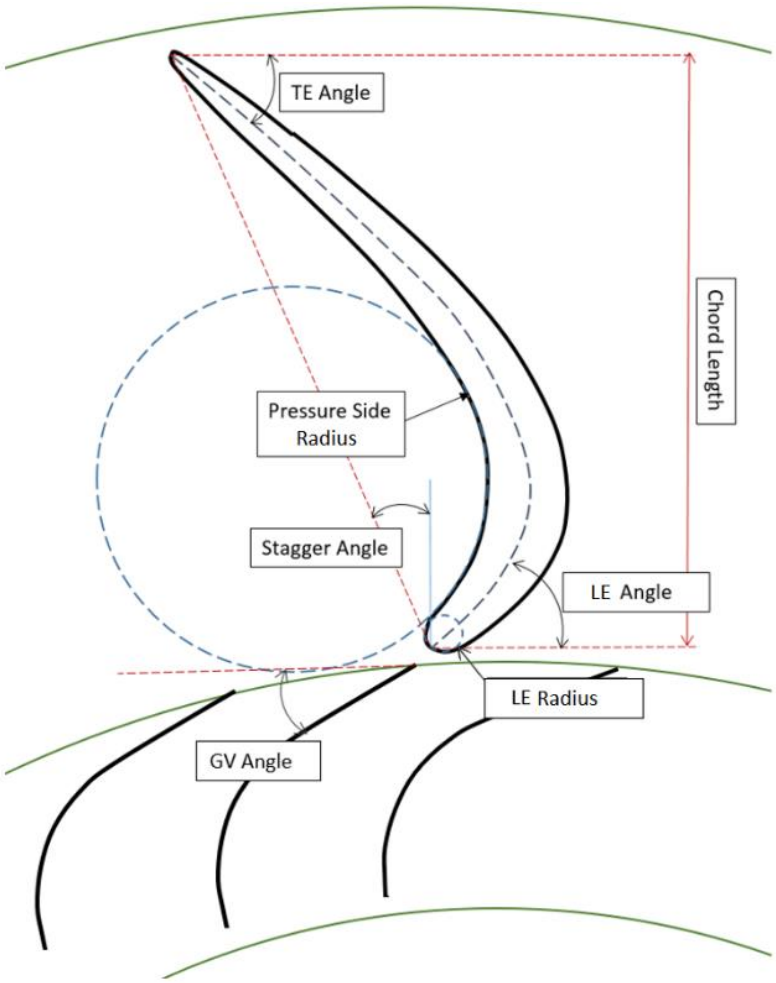

Figure 5.3 Illustration of the parameters used in creation of the outflow turbine.

Table 5-3 Design characteristics of the optimised outflow turbine.

Design variables	***Optimised geometry***
GV Angle (degree)	*26.5*
LE Radius (mm)	*1.93*
Chord Length (mm)	*50*
PS Radius (mm)	*0.49*
LE Angle (degree)	*67.72*
Stagger Angle (degree)	*-23.1*
TE Angle (degree)	*50*

The duct and upstream guide vane (UGV) geometries of the outflow turbine were chosen to be similar to that of the bidirectional turbine geometry (case 1) extracted from Ref. (Setoguchi et al., 2002). The outflow turbine has a diffuser at the rotor outlet with the inlet and exit diameters of 0.45 mm and 0.49 mm respectively.

5.3 Numerical model

A transient model was used to simulate the turbine operation in a purely unsteady fashion and control the relative motion of the rotor. Angular sections of the geometries equivalent to $1/17^{th}$ of the

whole inflow turbine and 1/25th of the outflow turbine were used as the periodic computational domains to reduce the computational overhead as illustrated in Figure 5.4. Therefore, six and four revolutions of the periodic domains were simulated for the inflow and the outflow turbines, respectively, at a rotational speed of ω =120 rad/s. Boundary conditions of uniform total pressure at the inlet and uniform static pressure at the outlet were applied. Total pressure at the inlet was varied in a way to provide the typical range of dimensionless flow coefficients, ϕ = 0.25 to ϕ = 2.5, for an OWC (ϕ is defined in equation (5.4)). The flow was assumed incompressible and the realizable k-ε turbulence model was selected due to its wide acceptance as a design tool in industry. This turbulence model has been utilized in similar studies of the field and accurate results were obtained (El Marjani et al., 2008, Pereiras et al., 2011c). The flow in all simulations was considered steady and unidirectional with a convergence criterion set to an RMS residual target of 10^{-6}. A quasi-steady assumption was assumed for the flow, considering the frequency ratio between the rotating domain and the period of the wave cycle in the OWC chamber (Rodríguez et al., 2018). Since the wave cycle period was substantially longer compared to the rotor rotational period, their interaction was considered as negligible and quasi-steady flow assumption was justifiable (Cui and Hyun, 2016).

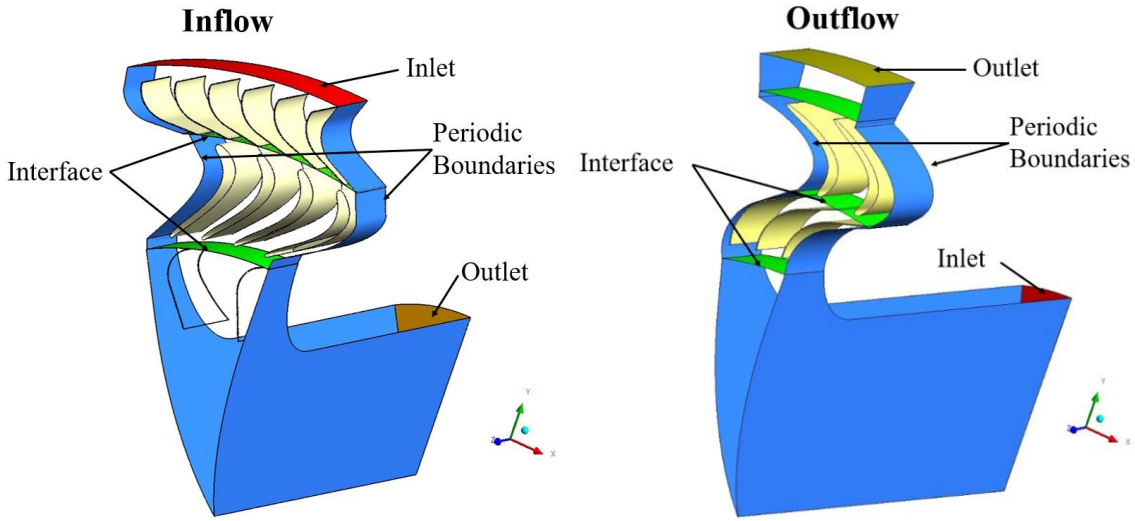

Figure 5.4 Computational domain.

A second order implicit scheme was used to approximate the time dependent term and the SIMPLE algorithm was used to create the pressure-velocity coupling. Turbine performance in steady state was described by a set of parameters (Setoguchi et al., 2002), being torque coefficient C_T , input power coefficient C_A , turbine efficiency η and flow coefficient ϕ :

$$C_T = T_0 / \left\{ \rho \left(V_R^2 + U_R^2 \right) A_R r_R / 2 \right\} \tag{5.1}$$

$$C_A = \Delta p_0 Q / \left\{ \rho \left(V_R^{\,2} + U_R^{\,2} \right) A_R V_R / 2 \right\} \tag{5.2}$$

$$\eta = \frac{T_0 \omega}{\Delta p_0 Q} = \frac{C_T}{C_A \phi} \tag{5.3}$$

$$\phi = V_R / U_R \tag{5.4}$$

The detailed definitions of the variables contributing in these coefficients are given in the nomenclature section.

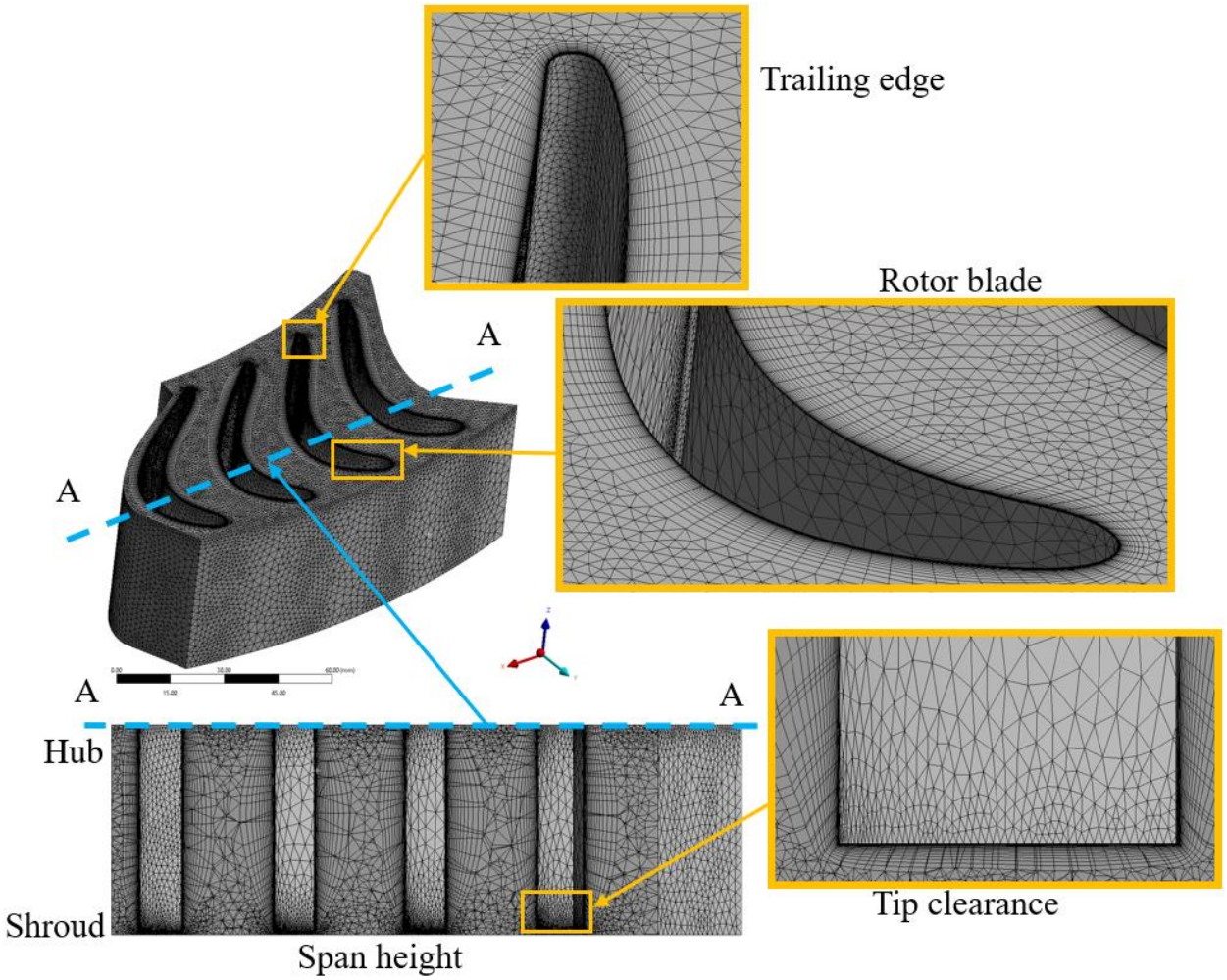

Figure 5.5 Schematics of the mesh used in the simulations (Case 3).

The computational meshing was performed in ANSYS by setting the size function on proximity and curvature to provide a good flow resolution near curved surfaces and edges. Inflation layers were applied to blade suction and pressure sides, guide vanes, walls and interfaces to allow the solver to determine forces on walls, flow incidence, secondary flow and separation. The viscous sublayer of a turbulent boundary layer has high velocity gradient close to the wall and the inflation-layered mesh accurately resolves the viscous sublayer directly (low Y^+ ~1) (ANSYS-User's-Manual). Twenty inflation layers with the transition ratio of 0.5 and growth rate of 1.2 were applied for meshing the

whole computational domain in a way to have the entire blade cells and 70% of the upstream guide vanes cells with $Y^+ < 1$. There was 1mm tip clearance in the unidirectional radial turbine geometry, similar to the reference geometry (Case (1) in Ref. (Setoguchi et al., 2002)). The rotor mesh has been illustrated in Figure 5.5, with a cut in the spanwise direction (A-A view) to show the mesh layers in the tip gap.

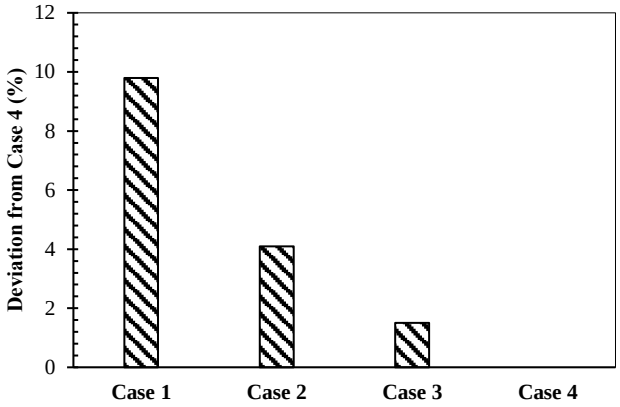

Figure 5.6 Grid independency study, comparing the deviation of efficiency (at ϕ =0.7) with reference to the Case 4 (2.5×10^6 cells).

The mesh skewness value was less than 0.5 and a high quality unstructured grid was obtained using global and local sizing parameters. Minimum size and proximity settings were varied to study mesh independence by creating four cases with 0.25, 0.5, 1 and 2.5 million tetrahedral mesh cells. This number of cells refers to meshing of an angular section, approximately $1/25^{th}$ of the whole turbine geometry. In addition, A time step study was performed considering three different time steps: 5×10^{-4} s, 1×10^{-4} s and 1×10^{-5} s. The case using time step 1×10^{-5} s was not economical regarding the simulation time and was used as a reference to evaluate the accuracy of other cases. As shown in Figure 5.6, Grid independency study was performed by considering the percentage of deviation from the Case 4 with 2.5 million cells. Where Case 1 denotes the minimum number of cells (0.25 million), and the number of cells increases from Case 1 to Case 3. Obviously, the discrepancy of results in Case 3 were practically nil (almost 1.5%). Therefore, the Case 3 was chosen to conduct the time step study by taking the time step 1×10^{-5}s as the reference. As illustrated in Figure 5.7, the time step 1×10^{-4}s obtained close results at considerably lower computational cost. Therefore, Case 3 with a total number of 1 million cells and the time step 1×10^{-4}s were used for the computational model.

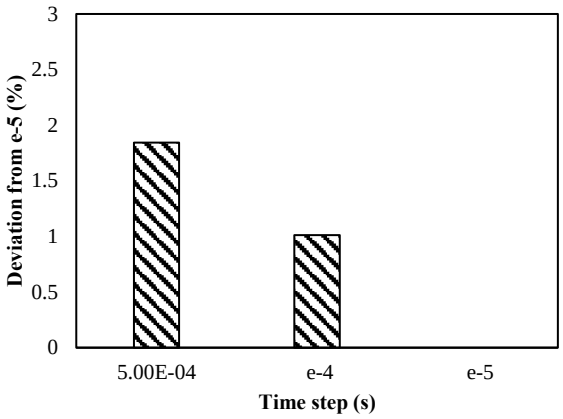

Figure 5.7 Time step study, comparing the deviation of efficiency (at ϕ =0.7) in Case 3 with reference to the time step 1×10^{-5}s.

5.3.1 Validation of the CFD model using a bidirectional turbine geometry

A bidirectional radial turbine geometry experimentally tested by Setoguchi et al. (Setoguchi et al., 2002) was used for validation of the numerical model. Geometrical details of this turbine presented in (Setoguchi et al., 2002) have been used in previous studies of the authors as a reference to design the inflow and outflow geometries (geometry M-1 in (Ansarifard et al., 2019)). A comparison between the turbine characteristics predicted by CFD and the experimental data in (Setoguchi et al., 2002) Case (1) is shown in Figure 5.8. Under both flow directions, the simulated results follow a similar trend to the experimented data in terms of torque coefficient, input power coefficient and efficiency. The CFD results are in better agreement at flow coefficients lower than ϕ =1, where the peak efficiency points for both inhalation and exhalation plots fall in this range. In lower flow rates, the results show good agreement, but the deviation becomes more obvious as the flow rate increases which can be explained by the surface roughness and frictional losses during the experiments. Nevertheless, the results predicated by CFD correspond reasonably well to the experimental data and provide confidence in the accuracy of the CFD model used in the analysis of the unidirectional radial turbines.

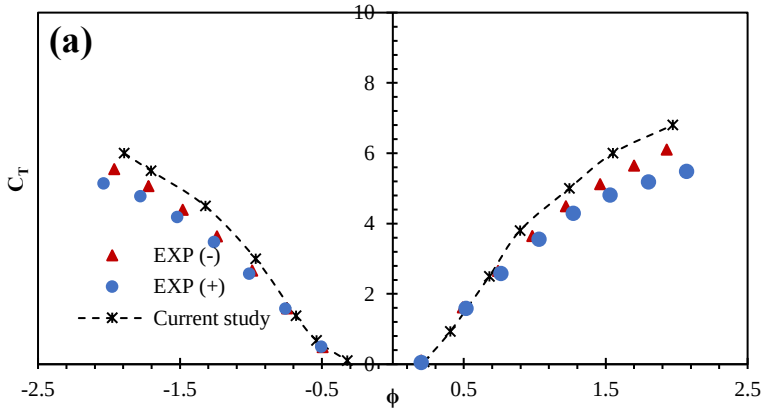

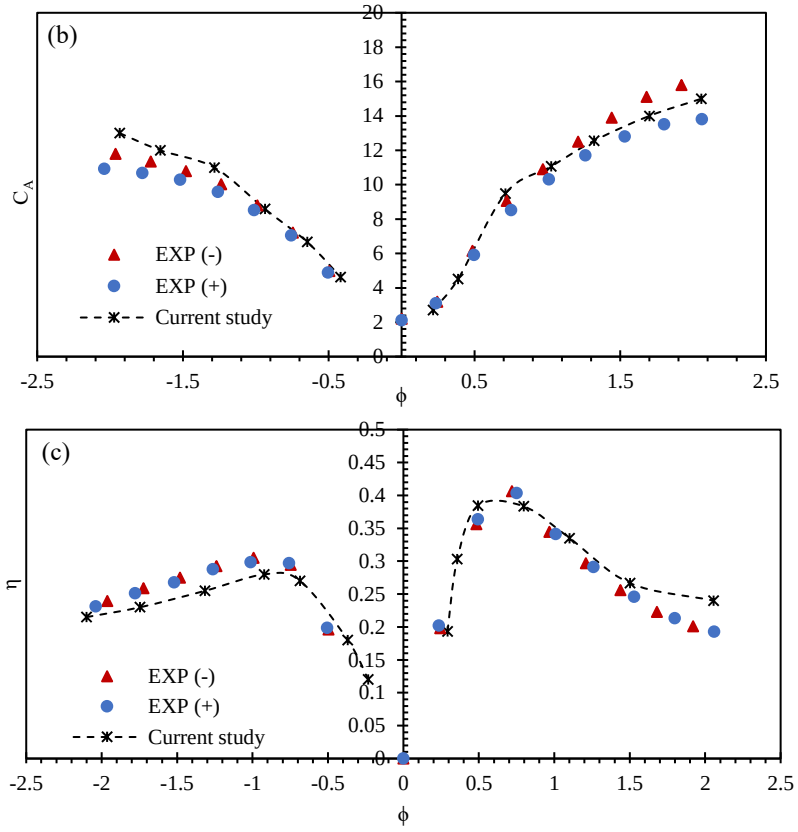

Figure 5.8 Comparing the accuracy of CFD results with published experimental data in (Setoguchi et al., 2002) for C_T , C_A and η. Experimental data were reported with ±1% uncertainty which are illustrated in the figure by EXP(-) and EXP (+).

5.4 Performance comparison of inflow and outflow turbines

For a more realistic performance comparison of the turbines, it was necessary to first consider the friction torque in each turbine. The Friction torque ($T_{friction}$) is associated with the aerodynamic and bearing losses of the turbine and can be measured when the flow rate in the turbine is zero (at ϕ =0). The aerodynamic/windage losses or windage losses are proportional to the square of the rotational speed and the bearing torque losses are approximately independent of the rotational speed (Lopes et al., 2019). The windage torque ($T_{Windage}$) corresponding to ϕ =0 was measured over a range of rotational speeds and its variation versus the rotational speed (ω) was plotted for the inflow and outflow turbines (in model scale) as shown in Figure 5.9. The equations associated with the windage torque for the inflow and the outflow turbines were found to be:

$$T_{Windage} = 5E^{-6}\omega^2 \text{ N.m (Inflow turbine)} \quad (5.5)$$

$$T_{Windage} = 3E^{-6}\omega^2 \text{ N.m (Outflow turbine)} \quad (5.6)$$

The bearing losses were not considered in this study, as they do not depend on the turbine characteristics. In addition, the windage torque in this study was calculated by the extrapolation of the

CFD results to ϕ =0 which limits its reliability. The authors acknowledge that experimental studies are required for a more accurate analysis of the windage losses. The windage power losses in the nondimensional form were measured using the expression:

$$C_{p-Windage} = \frac{T_{Windage}\omega}{\rho\omega^3 D_R{}^5} \tag{5.7}$$

The nondimensional values of the windage losses for the inflow and the outflow turbines were found to be $1.77 \times 10^{-3}$and 1.04×10^{-3}, respectively. Figure 5.10 compares the relative windage power losses as a function of flow coefficient in the inflow and the outflow turbines.

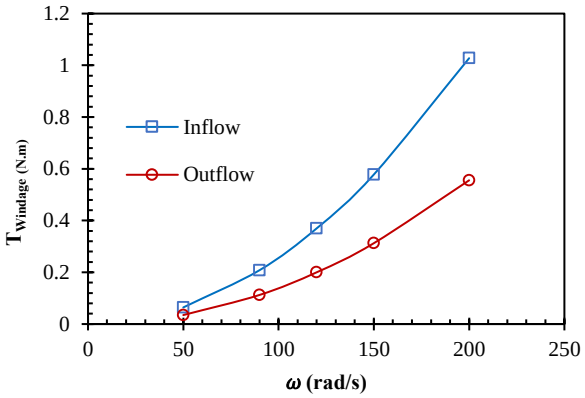

Figure 5.9 Variations of the windage torque of the inflow and outflow turbines versus *ω* (for the scale shown in Table 5-1).

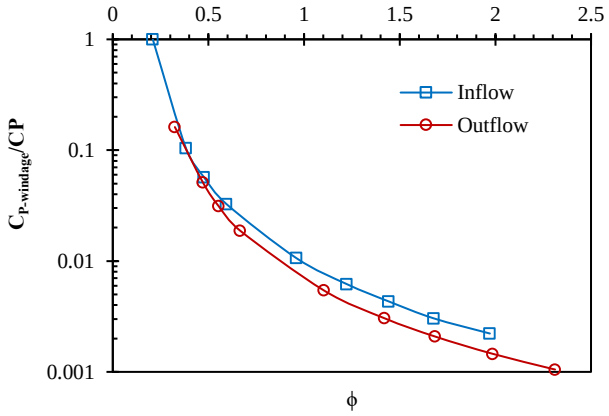

Figure 5.10 Comparison of the non-dimensional windage power losses of the inflow and outflow turbines.

The windage losses were found to reduce the peak efficiency of the inflow and the outflow turbines by 2.5% and 1.5%, respectively. In addition, the peak efficiency of both turbines was found to have a small shift to the right, as illustrated in Figure 5.11. This can be explained by the fact that the peak efficiency of these turbines falls on smaller flow coefficients, where, the effects of windage losses are more noticeable.

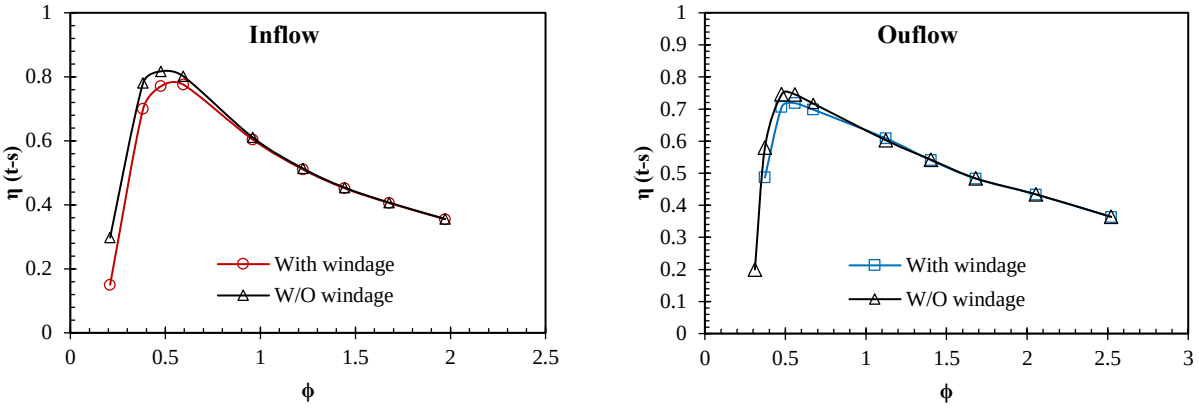

Figure 5.11 Comparison of the total to static efficiency of the inflow and outflow turbines with and without the windage losses.

The performance characteristics of the inflow and outflow turbines were compared taking the windage losses into account. As illustrated in Figure 5.12 a and b, the torque and input coefficients of the inflow turbine (C_T and C_A respectively) are higher than that of the outflow turbine over the whole range of flow coefficients. Comparing the efficiency plots of the turbines (Figure 5.12 c), it is observed that the inflow turbine obtains 7% higher peak efficiency than the outflow turbine and reaches an efficiency of 79% at ϕ =0.5. From ϕ =1 afterwards, the outflow turbine surpasses the inflow turbine, providing up to 10% higher efficiency in higher flow rates. Higher efficiency of the outflow turbine at higher flow coefficients can be explained by the trends of the C_T and C_A plots of this turbine compared to the inflow turbine after ϕ =1. The increasing difference between C_T and C_A shows that the outflow turbine can extract more energy from the input power compared to the inflow turbine. This can be justified by the ratio between flow rate and pressure drop across each turbine. As Figure 5.12 d illustrates, for a similar pressure drop provided to both turbines, the outflow turbine allows a higher volume flowrate. This is due to less resistance of the outflow turbine to the flowrate and possibly lower losses at the downstream of the outflow rotor (in model scale).

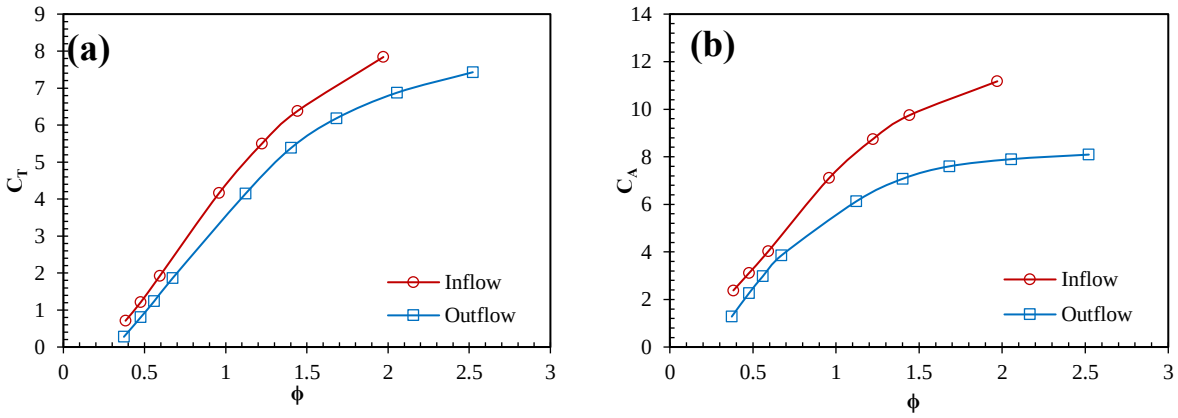

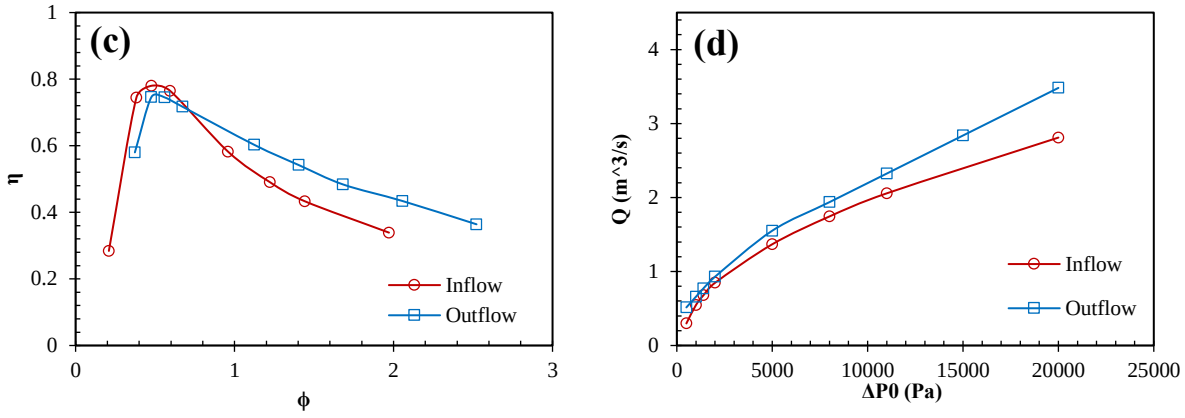

Figure 5.12 Comparison of the aerodynamic characteristics of the inflow and outflow turbines in steady state condition.

5.5 Twin-turbine concept in a bidirectional OWC system

A twin-turbine topology in a bidirectional OWC was investigated by introducing configurations A and B as illustrated in Figure 5.13. In the former (configuration A), a pair of inflow turbines were employed to configure a twin-turbine-OWC system. While in the latter (Configuration B), two identical outflow turbines were employed with the OWC.

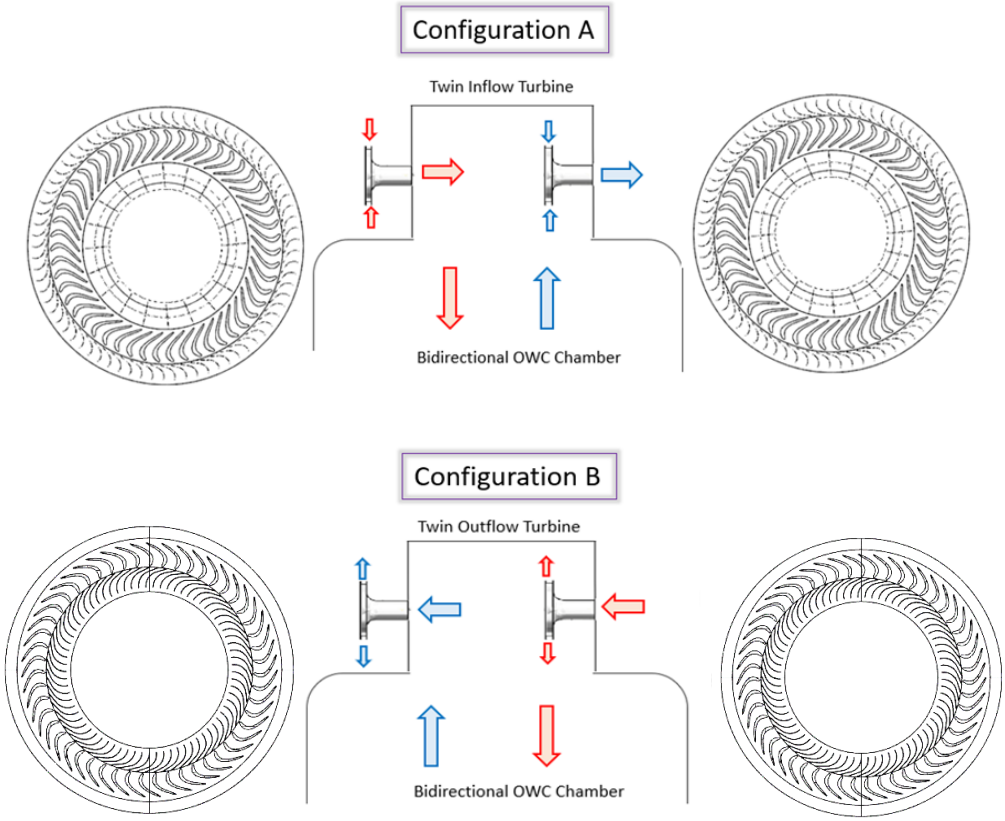

Figure 5.13 Schematics of configurations A and B. A: twin-inflow turbines, B: twin-outflow turbines.

In a twin-turbine configuration, both the unidirectional turbines work under identical pressure drops between the chamber and the atmosphere. The turbines are placed in an opposite direction, allowing

them to alternate their roles throughout a full wave cycle. Therefore, during each half-cycle one turbine acts in the direct mode (producing energy) and the other acts in the reverse mode (producing backflow and negative torque).

A non-steady analysis was performed to evaluate the turbines performance using a quasi-steady assumption the time variations of the chamber pressure drop were defined as below (Pereiras et al., 2014):

$$\Delta p_0 = p_{\max} \sin(2\pi t / T) \tag{5.8}$$

$$\Delta p_{0-direct} = \Delta p_{0-reverse} \tag{5.9}$$

$$Q_{Total} = q_{direct} + q_{reverse} \tag{5.10}$$

$$\omega = \omega_1 = \omega_2 \tag{5.11}$$

$$\phi = (Q_{\max} / A_R) / U_R \tag{5.12}$$

The term total means in a full wave cycle, and subscripts direct and reverse denote the operational mode of the turbines in a twin turbine topology. To evaluate the system performance, two different mean efficiency terms were analysed. These terms were $\bar{\eta}_{input}$ which denotes the percentage of flow rate contributing in energy production (direct mode) in a full cycle, and $\bar{\eta}_{twin}$ which refers to mean efficiency of twin turbines to extract power from the pneumatic power available in the direct mode:

$$\bar{\eta}_{system} = \bar{\eta}_{input}\bar{\eta}_{twin}$$

$$\bar{\eta}_{system} = \frac{1/T\int_0^T \omega T_{0-Total}\,dt}{1/T\int_0^T \Delta p_0 Q_{Total}\,dt} = \tag{5.13}$$

$$\underbrace{\frac{1/T\int_0^T \Delta p_0 q_{direct}\,dt}{1/T\int_0^T \Delta p_0 Q_{Total}\,dt}}_{\bar{\eta}_{input}} \underbrace{\frac{1/T\int_0^T \omega(T_{0-direct}+T_{0-reverse})\,dt}{1/T\int_0^T \Delta p_0 q_{direct}\,dt}}_{\bar{\eta}_{twin}}$$

It should be noted that the windage losses were considered in the calculation of the $\bar{\eta}_{twin}$ (in this section). The inflow and outflow turbines were compared regarding their twin-turbine efficiency and system performance in Figure 5.14. It is observed that twin-outflow turbines (configuration B) perform more efficient in an OWC than twin-inflow turbines (Configuration A). However, in the steady state condition, (shown in Figure 5.12 c), a single inflow turbine had 7% higher peak efficiency than the

outflow turbine. Thus, lower system efficiency of configuration A can be explained by higher impact of the second turbine working in the reverse mode and higher friction torque due to windage losses (as shown in Figure 5.9). Considering the distribution of flowrate in each configuration, as illustrated in Figure 5.15, a higher portion of flowrate escapes from the system through the reverse turbine in the configuration A. This causes a lower $\bar{\eta}_{input}$ of configuration A which directly affects its system efficiency. In addition, the reversed flowrate produces negative torque and consumes some power from the generator, ultimately reduces the twin efficiency ($\bar{\eta}_{twin}$). As can be seen in Figure 5.15, both the inflow and outflow turbines have a poor resistance to flow in the reverse mode. This is because the main purpose of their design was to operate in a vented OWC system, in which the power extraction is limited to unidirectional flow and effects of the reverse flow should be minimal. The next section discusses use of these turbines in a vented OWC system in details.

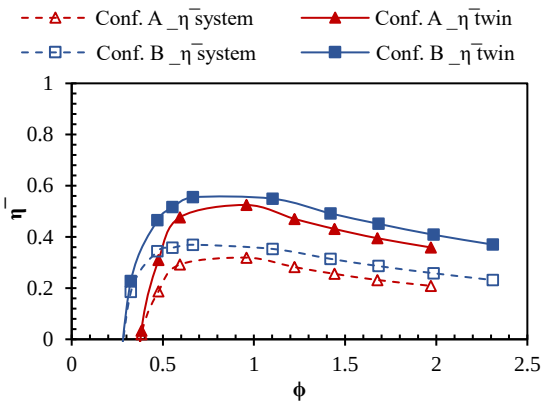

Figure 5.14 Mean performance of turbines in a twin-turbine concept (Configurations A and B).

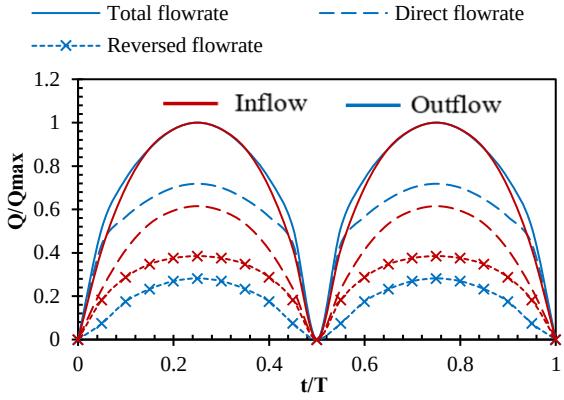

Figure 5.15 Comparison of the flow contribution in inflow and outflow turbines during the direct and reverse modes at ϕ =0.5.

5.6 Single turbine + valve concept in a vented OWC system

The unidirectional inflow and outflow turbines were investigated in a vented OWC system in which the second turbine is replaced by a one-way valve. Configurations B and C, in Figure 5.16, schematically show using the inflow and outflow turbines in a vented OWC system, respectively. As shown in Figure 5.16, turbines employed in vented OWC operate when the chamber water level falls and the flow in the opposite direction becomes discharged to atmosphere through the check valves. In this way, the negative effects of the reverse flow on the turbine are significantly reduced and efficiency of the single turbine is evaluated through a half-cycle of the wave.

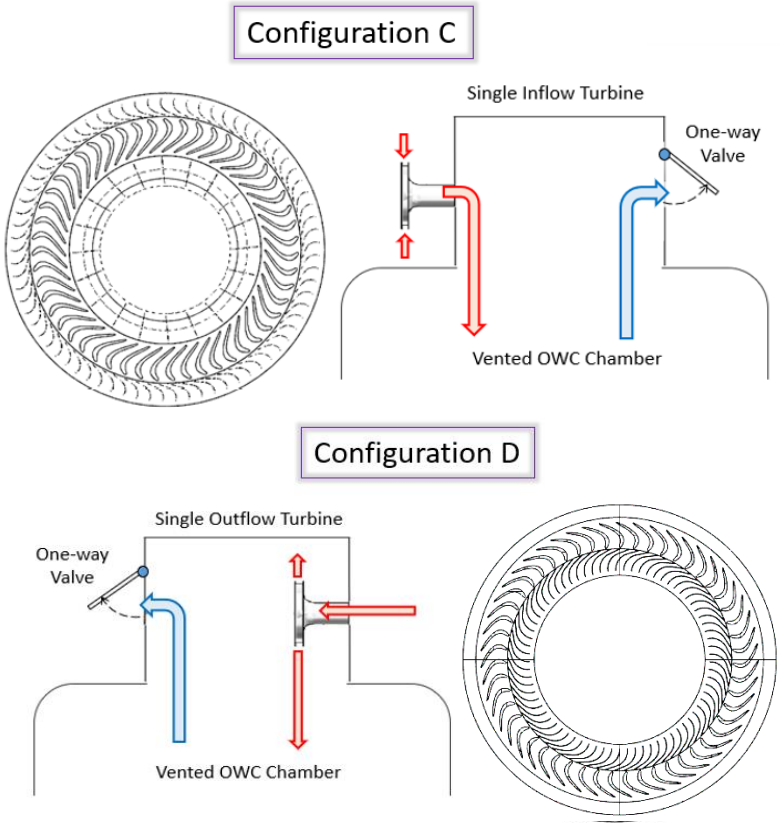

Figure 5.16 Schematics of configurations C and D. C: employs a single inflow turbine, B: employs a single outflow turbine.

Evaluating the exact performance of the check valve is out of the scope of this research. However, a leakage rate of 5% of the flow through the check valves was assumed in this analysis. Therefore, a mean input efficiency of $\bar{\eta}_{input} = 0.95$ was considered in the calculation of mean system efficiency. Thus, as illustrated in Figure 5.17, the mean system efficiency in the both configurations is slightly lower than the mean efficiency of the single turbine. It can be noted that these plots follow a similar trend to that of the turbines' efficiency in steady states (Figure 5.12 c), where the inflow turbine has approximately 10% higher peak efficiency in the vented OWC system. The mean system efficiency of turbines in vented OWC is almost doubled the system efficiency in the bidirectional OWC (Figure 5.14), which is due to elimination of the reverse mode in the system. Similar to the previous section, the mean system efficiency is defined as:

$$\bar{\eta}_{system} = \bar{\eta}_{input}\bar{\eta}_{\sin gle}$$

$$\bar{\eta}_{system} = \frac{1/T\int_0^T \omega T_{0-Total}\,dt}{1/T\int_0^T \Delta p_0 Q_{Total}\,dt} = \tag{5.14}$$

$$\underbrace{\frac{2/T\int_0^{T/2}\Delta p_0 q_{direct}\,dt}{2/T\int_0^{T/2}\Delta p_0 Q_{Total}\,dt}}_{\bar{\eta}_{input}}\ \underbrace{\frac{2/T(\int_0^{T/2}\omega T_0\,dt)}{2/T\int_0^{T/2}\Delta p_0 q_{direct}\,dt}}_{\bar{\eta}_{single}}$$

Where the $\bar{\eta}_{input}$ is 0.95 over the whole cycle (considering 5% leakage of the valves), and $\bar{\eta}_{input}$ refers the mean efficiency of the turbine to extract power from the pneumatic power available in the direct mode. It is worth mentioning that since in the vented OWC the input power available in a half cycle (reverse mode) is negligible compared to the direct-mode half cycle, the input and mean efficiency of the turbine were evaluated in a half cycle only (the direct mode), however, the equation 5.14 still can be referred to the mean efficiency in the whole wave cycle. Also, it should be noted that the friction torque due to windage losses was considered in the calculation of $\bar{\eta}_{input}$.

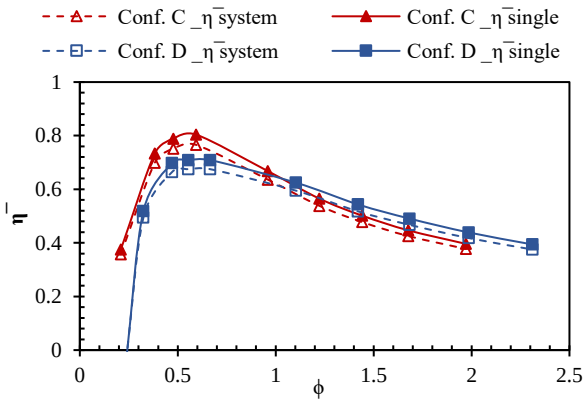

Figure 5.17 Mean performance of turbines in a vented OWC (Configurations C and D).

5.7 Falcao Turbine

A twin-rotor radial inflow turbine experimentally tested by Falcao et al. (Falcão et al., 2015) and later by Lopes et al. (Rodríguez et al., 2019) was considered as a reference to analyse the performance of the afore-mentioned turbine-OWC configurations. The twin-rotor turbine geometry includes two identical conventional single stage radial inflow gas turbines, a connecting duct and two identical sets of circular curved-duct manifolds. Also, a two-position axially-sliding cylindrical valve was used at the duct entrance to prevent air from flowing into the reversed turbine. In this study, this geometry is referred as “Falcao turbine” and is compared with turbine geometries of configuration A to D regarding the full-scale sizing, rotational speed and power extraction in the bidirectional and vented OWC systems. The Falcao turbine consists of two identical rotors with their curved-duct manifolds

(Rodríguez et al., 2019). Therefore, the Falcao turbine in the bidirectional OWC is represented by the twin-rotor configuration and in the vented OWC by the single-rotor configuration.

As the Falcao turbine was fitted with sliding valves to rectify the flow into the turbines, the analysis of the flow leakage by the valves is ignored and the input efficiency of $\bar{\eta}_{input} = 1$ was considered for the Falcao turbine. Thus, the Falcao turbine's efficiency in the system, $\bar{\eta}_{system}$, depended only on the turbine's mean efficiency $\bar{\eta}_{turbine}$. The windage losses were considered in the performance of the twin-rotor turbine as reported in Ref. (Rodríguez et al., 2019). Figure 5.18 compares the mean efficiency of the inflow, outflow and Falcao turbines when employed in the bidirectional and vented OWC systems. Table 5-4 shows the peak mean efficiency of all the turbines in vented and bidirectional OWCs. These data were used in the next section to calculate the ideal power extracted by the turbine under irregular waves, when the rotational speed is optimised.

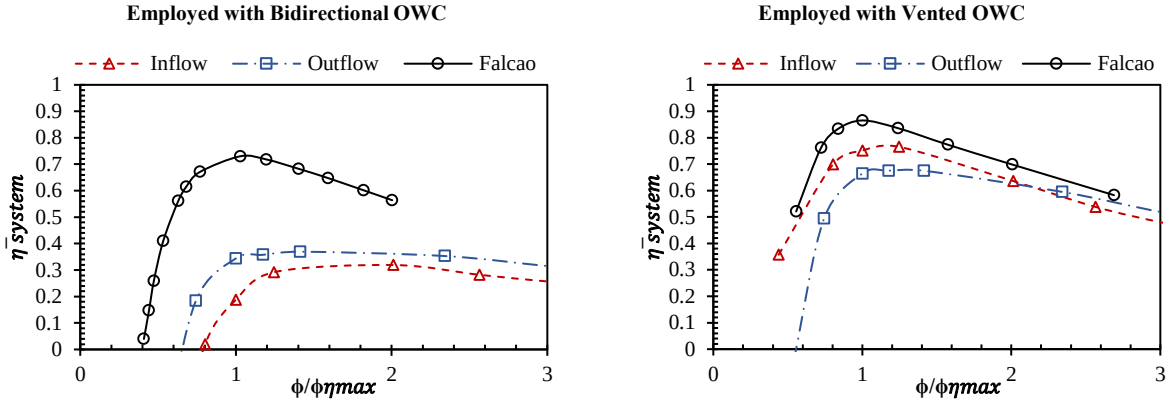

Figure 5.18 Comparison of mean efficiency of the Falcao turbine (A. Falcao et al., 2015) with inflow and outflow turbine geometries. Efficiency versus non-dimensional flow rate coefficient $\phi / \phi_{\eta_{\max}}$, where subscript $\eta_{\max}$ means maximum efficiency conditions.

Table 5-4 Peak mean efficiency ($\bar{\eta}_{system}$) of the inflow, outflow and Falcao turbines in vented and bidirectional OWC systems.

Turbine type	*Bidirectional OWC*	*Vented OWC*
Inflow	*0.302*	*0.753*
Outflow	*0.354*	*0.664*
Falcao	*0.739*	*0.866*

5.8 Performance comparison under irregular waves

In this section, the hydro–aero conversion of the configurations A to D (described in the previous sections) were investigated using the experimental data of irregular waves, expected to occur at the King island Tasmania test site. The experiments were conducted in the Australian Maritime College

Model Test Basin (MTB), with dimensions 35 m long x 12 m wide x 1 m deep, 16 piston type wavemaker paddles at one end, and an absorbing beach at the other end (Figure 5.19, bottom). The table in Figure 5.19 shows model parameters in model- and full-scale, and water depth. The model was positioned on the centre line of the basin and 11 m from the wavemaker. Plywood and clear acrylic were used as the structural materials for the model. For the vented OWC condition, five 3D printed passive check valves/flaps were arranged on the sides and back of the model as shown in Figure 5.19. The flaps were made from acetate sheets, lightly hinged to the top edge permitting the valve to open with minimal positive chamber air pressure. For the bidirectional OWC condition, these flaps were sealed completely. The power take-off was simulated using an orifice plate that exhibits a quadratic pressure/flow relationship similar to that of a single stage turbine, as described in (Fleming et al., 2017). It should be noted that the same size orifice plate was used for both configurations, thus the system was not necessarily optimised for both configurations.

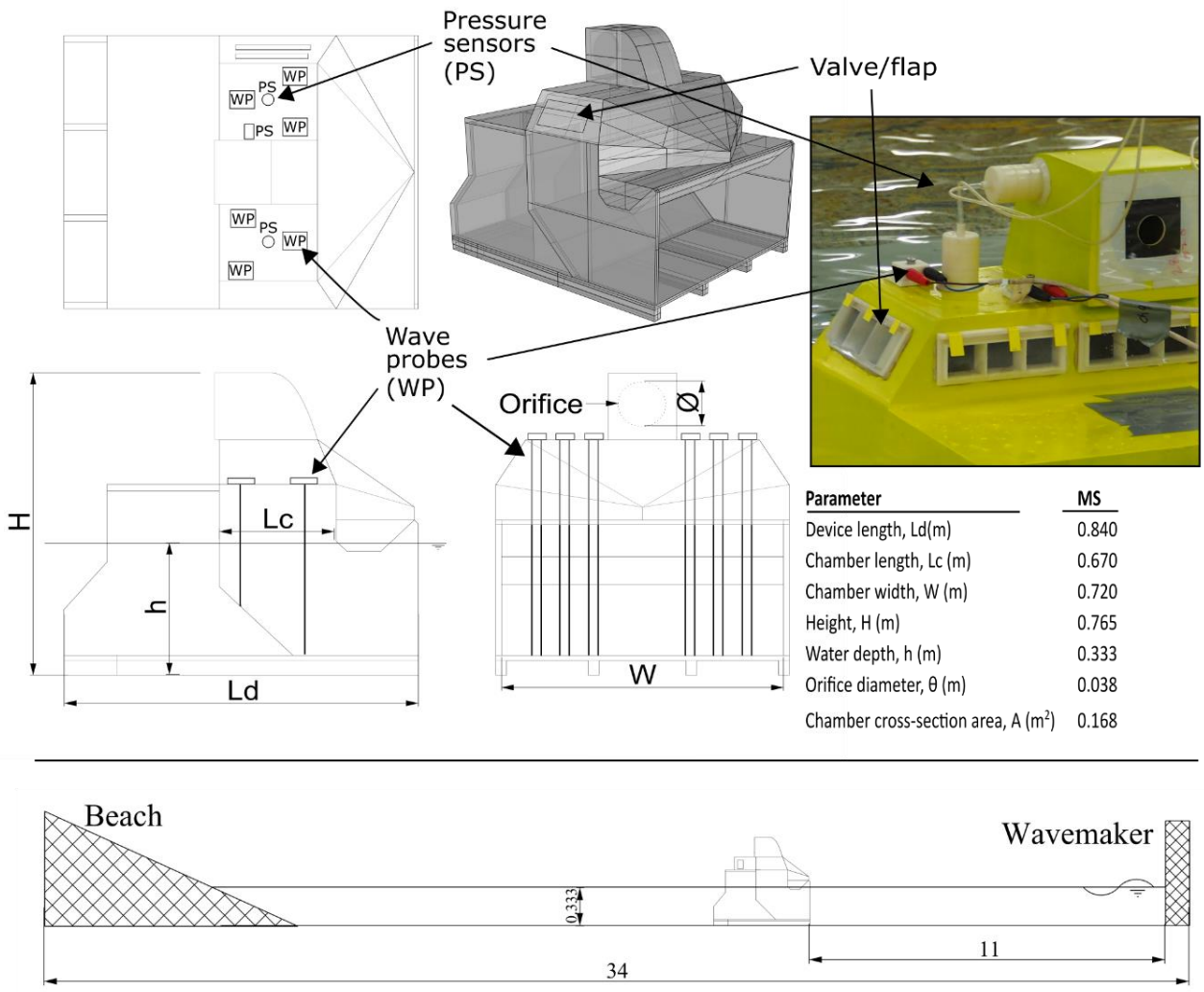

Parameter	MS
Device length, Ld(m)	0.840
Chamber length, Lc (m)	0.670
Chamber width, W (m)	0.720
Height, H (m)	0.765
Water depth, h (m)	0.333
Orifice diameter, θ (m)	0.038
Chamber cross-section area, A (m^2)	0.168

Figure 5.19 TOP, model drawing with principle dimensions in model- and full-scale; wave probe and pressure sensor locations; and a cropped picture of the model showing the passive check valves/flaps

that are operational (vented OWC condition), as well as some of the instruments. BOTTOM, diagram of model in the Australian Maritime College Model Test Basin, not to scale.

However, there is a reasonable compromise for comparison. Air pressure inside the OWC chamber was measured with three pressure transducers (1 psi Honeywell TSC sensor conditioned by an Ocean Controls instrument amplifier KTA 284), with positions shown in Figure 5.19. Each pressure sensor was found to produce near identical values (Fleming et al., 2017). Water surface elevation inside the OWC chamber was measured using six resistive type wave probes; however, this data was not used for production of results in this paper except for an orifice flow coefficient check. Wave probes were connected to the data acquisition system through a HR Wallingford wave probe signal conditioning box. Data was acquired at a rate of 200 Hz using a 16 bit National Instruments PCI card (NI PCI-6254) connected to a BNC terminal box. Data recording was triggered by wave paddle motion and was recorded for a duration of 30 seconds for regular waves and 600 seconds (30 minutes full scale equivalent) for irregular waves. The full scale irregular wave conditions were selected based on common waves occurring at the King Island test site (Fleming et al., 2017). Figure 5.20 maps the H_S and T_P of the tested irregular waves denoted by KI-1 to KI-48. These wave conditions were used to compare the system performance of the turbine-OWC configurations described in previous sections.

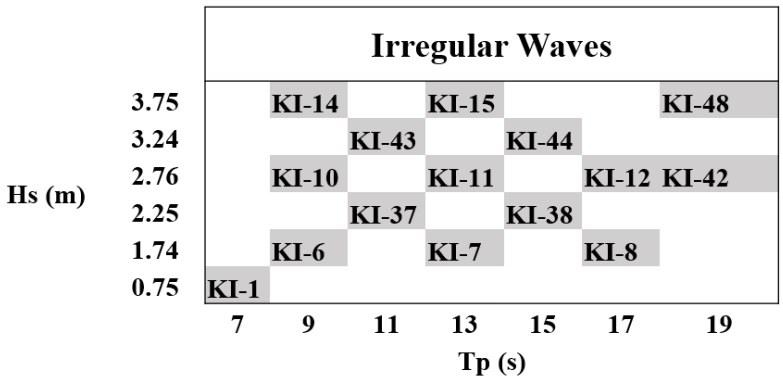

Figure 5.20 Wave height (H_S) and period (T_P) characteristics of the investigated irregular waves.

Chamber pneumatic power and the flow rate were calculated as (Evans, 1982):

$$P_{Pneumatic} = \Delta p_0 Q \tag{5.15}$$

$$Q = C_d A_O \sqrt{2|\Delta p_0| / \rho} \tag{5.16}$$

Where an orifice discharge flow coefficient of $C_d = 0.6$ was chosen in the calculations of the flow rate. Use of air valves in the vented OWC configuration leads to discharge of flow to the atmosphere in a half cycle (during positive air chamber). However as also mentioned in (Fleming et al., 2017) "energy

is being stored in the form of potential energy as water column heave" and for the second half cycle (during negative air chamber) the air valves close and the whole incoming wave energy plus energy stored in water column heave is available to the turbine. Figure 5.21 compares chamber pressure and pneumatic power of the vented and conventional OWCs under a regular wave (H=0.08 m, f=0.311 Hz). It is clearly seen that the air chamber pressure in the vented OWC is slightly positive but significantly negative. Also, the amplitude of pneumatic power for negative air chamber pressure is significantly higher than that of the conventional OWC. It should be noted that the dead band in Figure 5.21 is due to the shallow water which causes non-sinusoidal and sometimes a secondary wave crest. Analysis of the experimental data of phase wave probe and water column level illustrated that water surface is nearly stationary in some segments.

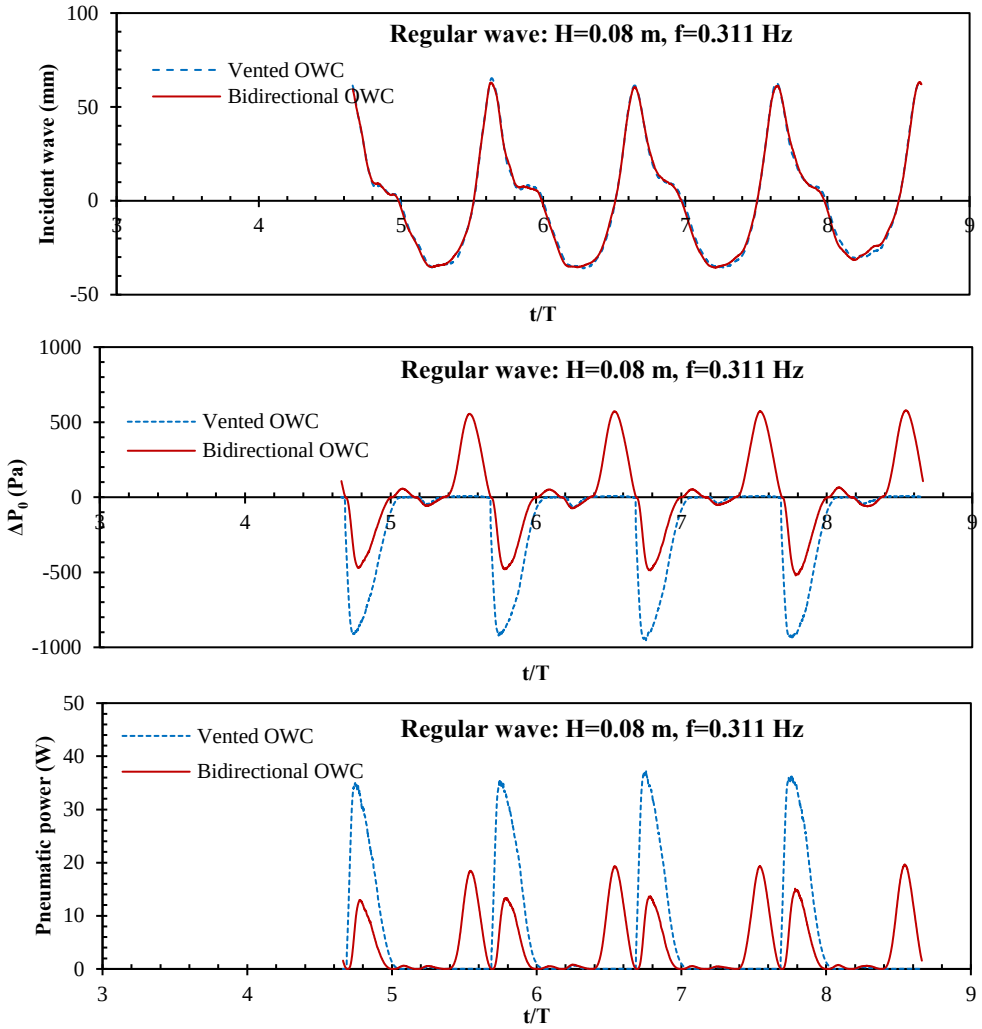

Figure 5.21 Comparison of chamber pressure and pneumatic power in a vented and a bidirectional OWC at model scale.

5.8.1 Histogram Analysis of pressure domain

The pressure domain of each OWC configuration was recorded over a duration of 30 seconds for regular waves and 600 seconds for irregular waves. The recorded pressure drops during full wave

cycles were categorized into small-continuous intervals of 10 Pascal. These pressure intervals were compared considering their occurrence over the entire recording time and were divided by the total number of pressure records, to calculate the proportion of occurrence of each interval. A comparison of the pressure domain in vented and bidirectional OWCs is shown in Figure 5.22. It is obvious that pressure drops around -60 Pa and 60 Pa are more likely to happen in the bidirectional OWC, while in the vented OWC pressure drops between -60 Pa and 20 Pa are most repeated, however there is very little extractable power in this range. High pressure drops take place over a noticeable portion of time in both configurations. It is clear that the magnitude of negative pressure drops is significantly higher in the vented OWC, which corresponds to the chamber pressure plots in Figure 5.21.

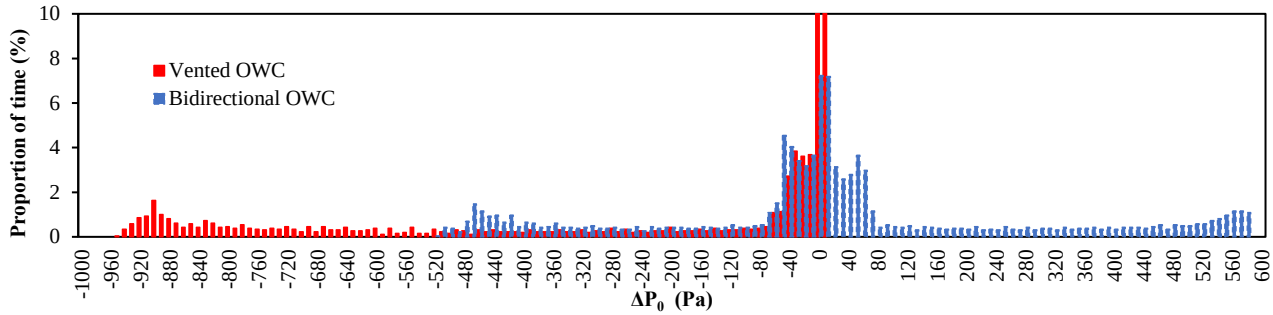

Figure 5.22 Comparison of vented and bidirectional OWCs in a pressure domain (regular wave: H=0.08 m, f=0.311 Hz).

Using equations 5.15 and 5.16 the pneumatic power can be obtained for a given pressure differential. The calculated power is then multiplied by the percentage of occurrence of each pressure interval to produce the pneumatic power content plot. Figure 5.23 illustrates the model-scale pressure histogram, pneumatic power content and mean output power of the configuration A (bidirectional OWC with twin-inflow turbines) under a regular wave (H=0.08 m, f=0.311 Hz). The mean output power of the system is calculated by multiplying the mean system efficiency of configuration A in the pneumatic power content values (as shown in Figure 5.23, middle):

$$\bar{P}_{system} = \bar{\eta}_{system} P_{Pneumatic} \tag{5.17}$$

Here $\bar{P}_{system}$ is the mean power extracted by the PTO in the turbine-OWC configuration, $P_{pneumatic}$ is the pneumatic power of the OWC and $\bar{\eta}_{system}$ is the turbine's mean efficiency in the system. As mentioned, pressure drops between 60 Pa and -60 Pa are most repeated, however the pneumatic power is more significant at higher pressure drops. Therefore, a choice of RPM can lead to a decision to extract power from either the most occurred pressure drops or the strongest ones. Studying three constant rotational speeds of 500, 1000 or 1500 RPM revealed that, 500 RPM permits the turbine's non-dimensional peak efficiency to fall over the most repeated pressure drops (lower range), however

1000 RPM and 1500 RPM more efficiently cover the middle and higher ranges of the pressure histogram respectively.

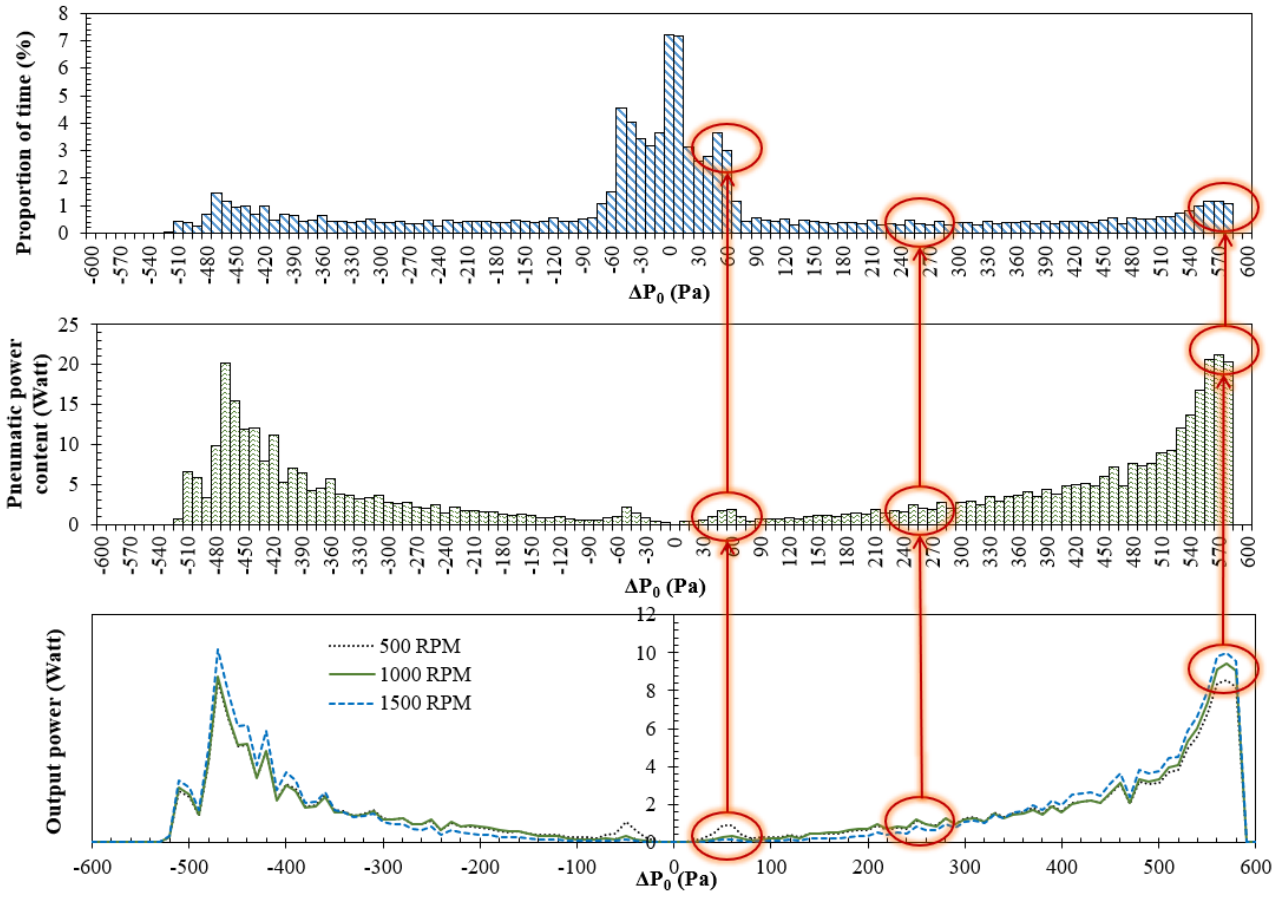

Figure 5.23 Pressure histogram and power contents of configuration A (in model-scale) under a regular wave: H=0.08 m, f=0.311 Hz.

Figure 5.24 compares the system efficiency plot of configuration A (in model-scale) at various RPMs. It should be noted that a constant rotational speed should be considered as a lower bound for the turbine performance, while the optimal rotational speed is the maximum bound. In a turbine control scheme, concerned with maximising energy extraction, the real turbine performance lies between those two bounds.

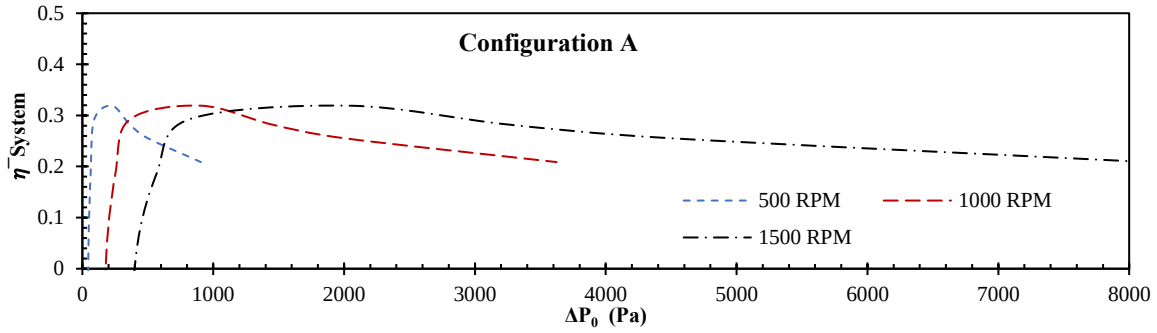

Figure 5.24 Distribution of mean system efficiency (configuration A) over a given range of ΔP_0 at various RPMs.

5.8.2 Power extraction in full scale:

Froude Similitude scaling (Holmes, 2009) was used to scale up the results of pressure and pneumatic power of the experiments to full scale ($\lambda = 30$) as shown in Table 5-5.

Table 5-5 Froude scaling (Holmes, 2009).

Unit	*Factor*
Length	λ
Pressure	λ
Power	$\lambda^{7/2}$
Time	$\lambda^{1/2}$

The full-scale size of the inflow, outflow and Falcao turbines for each of the vented and bidirectional OWCs were considered regarding the damping parameter in each turbine defined as (Pereiras et al., 2015):

$$\Psi = C_q D_R{}^2 / \sqrt{\rho C_H} \quad (m^{3.5}\, kg^{-0.5}) \tag{5.18}$$

Where C_q and C_H are non-dimensional flow rate and pressure drop respectively (more details can be found in the nomenclature section) and are the same for model and full-scale. The value of damping parameter in model scale was found from the values of C_q and C_H corresponding the peak efficiency point of the turbine. For the Falcao turbine C_q and C_H were reported to be 0.0517 and 0.0264 respectively, (Case $R_3/R_1 = 1.2$ in (Falcão et al., 2015)). Using equation (18) and considering the model-scale damping at peak efficiency of each turbine, the full-scale diameter can be obtained so that the OWC has optimum operation.

Figure 5.25 compares the full-scale damping in the inflow, outflow and Falcao turbines with the damping of the orifice in full-scale (at the best efficiency point of the OWC). A main limitation of this analysis is that the turbine analysed is assumed to have the same influence as the orifice plate used in the experiments. However, in the reality the orifice fails to fully mimic the turbine's behaviour. Since the PTO was simulated by the same orifice in both conditions (vented and bidirectional OWCs), a similar full-scale damping of $\Psi = 1.2$ ($m^{3.5}\, kg^{-0.5}$) was used in all wave conditions. All the turbines were sized to have their peak efficiency at a full-scale damping equal to that of the orifice (the intersection of the turbine damping plot with the orifice damping plot in Figure 5.25 is the peak efficiency point of each turbine). As shown in Table 5-6, the outflow turbine obtains the specified

damping with a lower size than both Falcao and inflow turbines. This can be explained by less resistance of this turbine geometry to flowrate which leads to a higher flow/pressure ratio as illustrated in Figure 5.12 d.

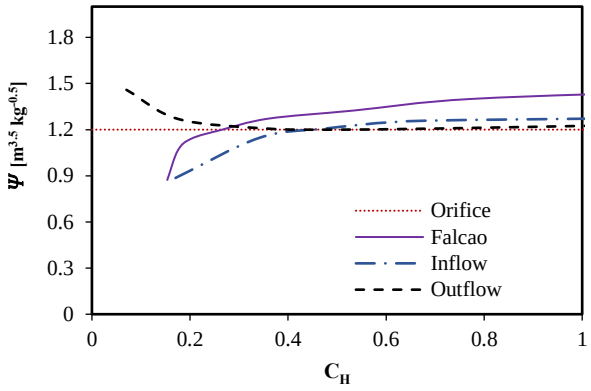

Figure 5.25 Comparison of damping of orifice with the turbines investigated.

Table 5-6 Full scale size of turbines.

Turbine	D_R
Inflow	*3.38 m (*$1.58 \times 10^7 < Re < 5.54 \times 10^7$*)*
Outflow	*3.13 m (*$1.35 \times 10^7 < Re < 4.75 \times 10^7$*)*
Falcao	*3.61 m (*$1.8 \times 10^7 < Re < 6.29 \times 10^7$*)*

Effect of rotational speed on power extraction was evaluated considering the mean output power of the system at each wave condition, defined as:

$$\sum(\bar{P}_{system} = \bar{\eta}_{system} P_{Pneumatic}) \tag{5.19}$$

The system output power is calculated considering the pneumatic power in each pressure interval (as shown in Figure 5.23), and the efficiency of the turbine during that pressure interval (depending on the rotational speed chosen) and their summation over entire ΔP_0 range. Six different rotational speeds were used for the full-scale turbines both the vented and bidirectional OWC systems. In addition, five irregular wave conditions, including the lowest (KI-1) and the highest energetic (KI-14) wave conditions, were chosen to consider various power levels of the incident waves. As Figure 5.26 illustrates, the inflow turbine in a twin-turbine-OWC system (Configuration A) is highly affected by variations of the rotor's rotational speed and the proper RPM falls in the range of 200 to 250 RPM for this configuration. This configuration obtains the least power output among other systems with a peak of 250 kW. The power extracted in a twin-outflow-OWC system (Configuration B) is over 250 kW

for rotational speeds between 200 RPM to 400 RPM. This turbine has less dependency on RPM variations than the inflow turbine, however its proper operation occurs at a higher rotational speed (325RPM). The inflow turbine when employed in a vented OWC system (Configuration C), operates at a higher rotational speed (400 RPM) and reaches a power of 600 kW in the highest energetic wave condition. Comparing configuration C and D, it is clear that the outflow turbine operates at higher RPMs and is less sensitive to the rotational speed than the inflow turbine (similar to that observed in the bidirectional OWC system). However, the peak power obtained by the inflow turbine is by 60 kW higher than that of the outflow turbine. In a bidirectional OWC system, the Falcao turbine obtains a significantly higher output power than the inflow and outflow turbines (Configurations A and B respectively), but at a slightly higher rotational speed (400 RPM). In case of the vented OWC, the output power of all the turbines is comparable. Where, the peak power of the inflow turbine (Configuration C) is approximately 50 kW lower than the Falcao turbine, however both the inflow and outflow turbines operate more consistently with variations of the RPM.

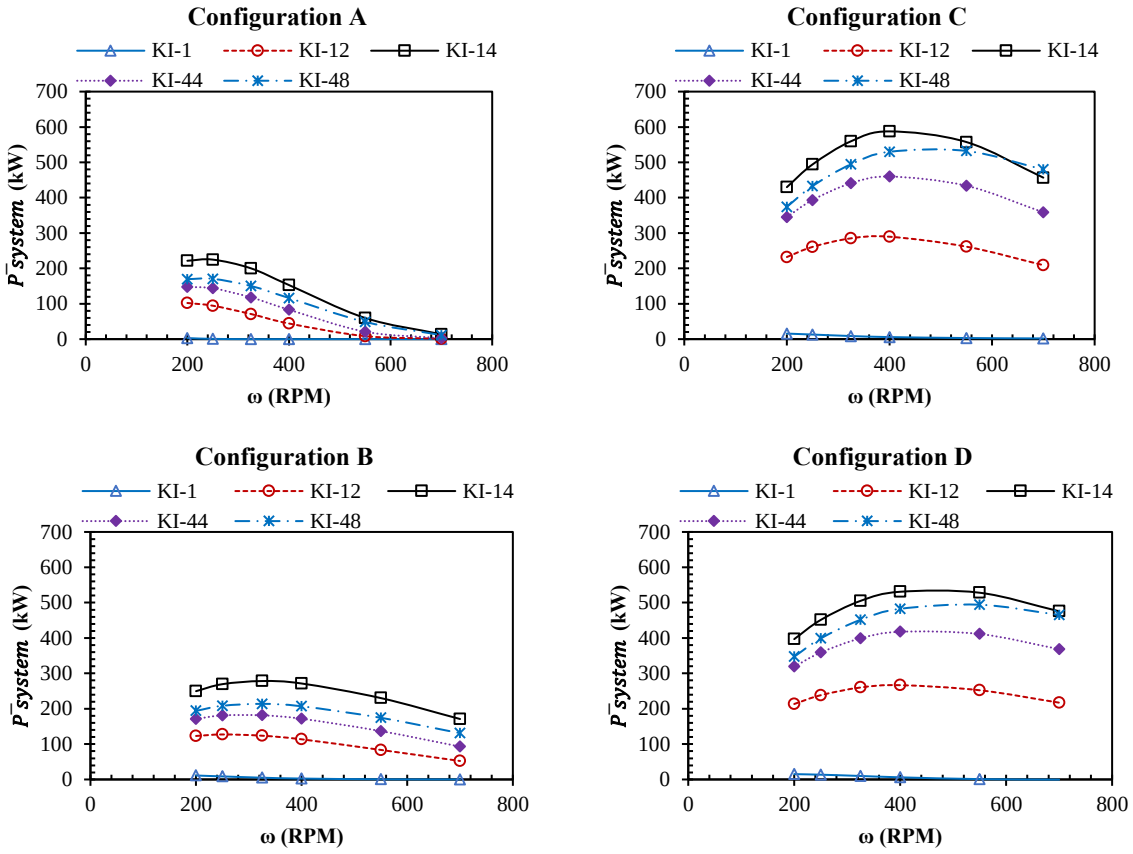

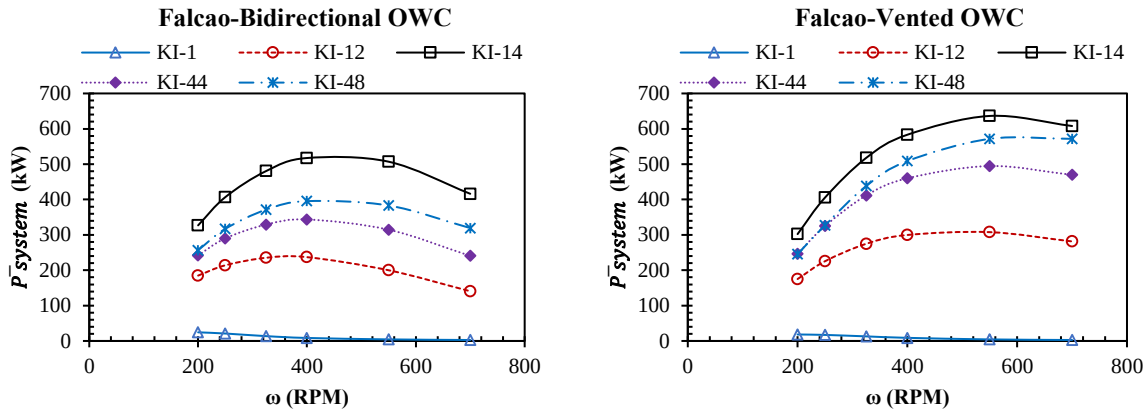

Figure 5.26 Effect of rotational speed on power extraction of turbines in different configurations and various wave conditions.

A comparison of the pneumatic power provided to the turbines in each configuration is shown in Figure 5.27. It is observed that over a range of studied irregular waves, pneumatic power extracted by the both vented and bidirectional OWCs are almost equivalent. Hence, discharging the flow to atmosphere during positive chamber pressure drops in the vented OWC does not imply that half of the pneumatic power is untapped (Fleming et al., 2017).

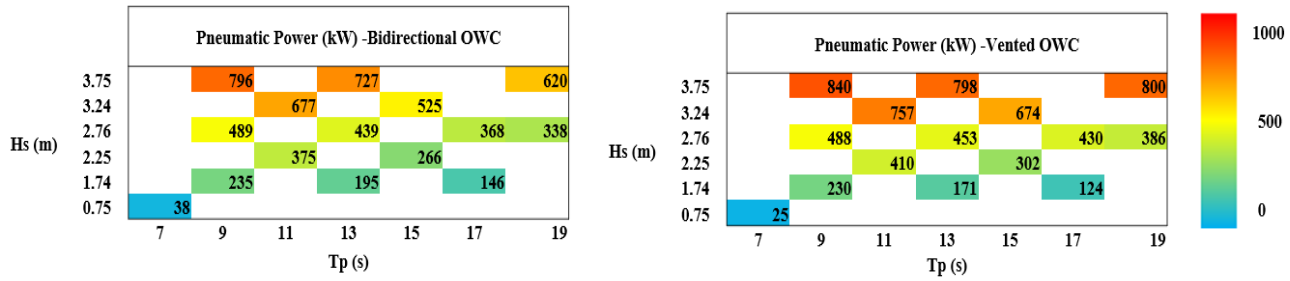

Figure 5.27 Comparison of the pneumatic power obtained by the bidirectional and vented OWCs over the range of irregular waves investigated in this study.

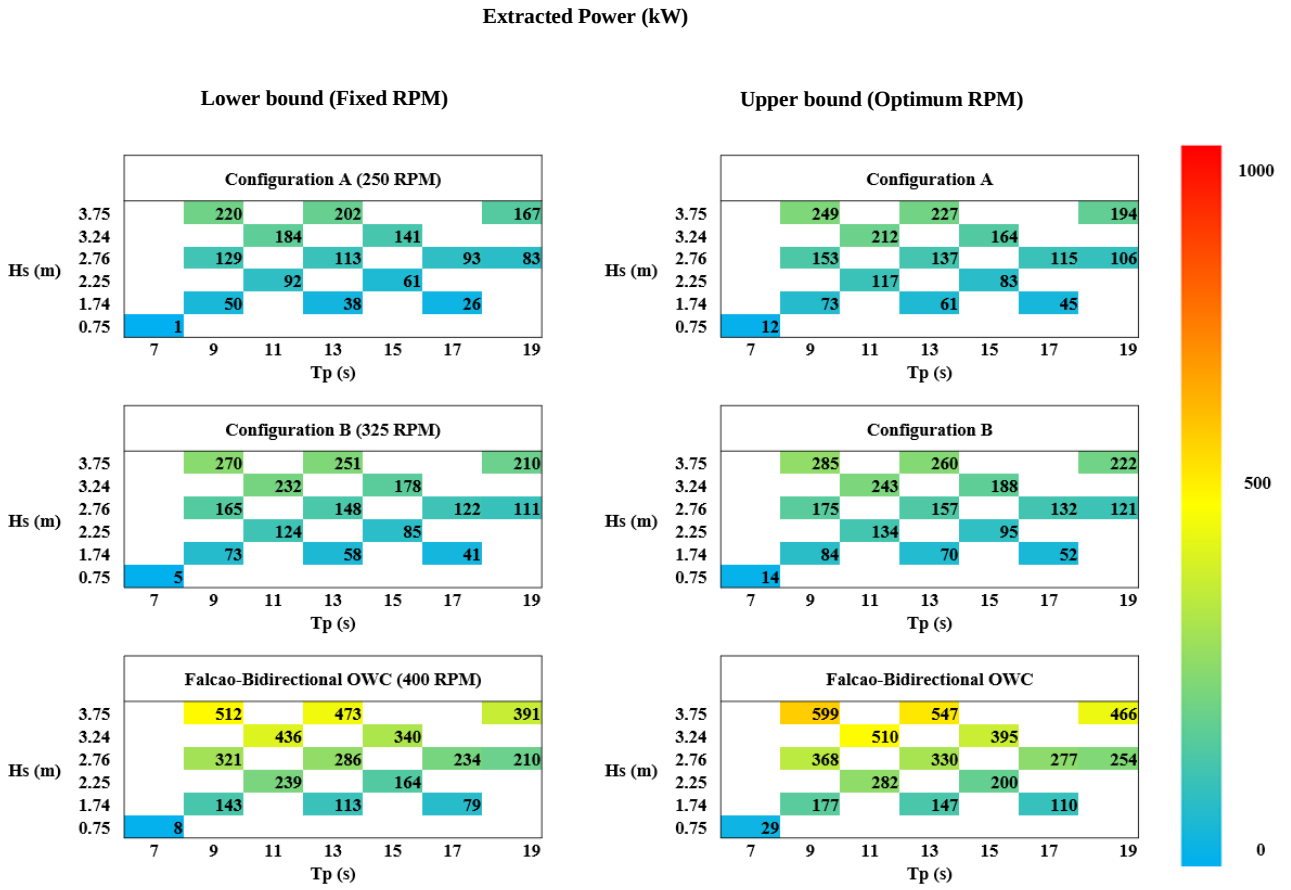

Figure 5.28 Extracted power matrix of turbines in a bidirectional OWC configuration with lower bound (constant rotational speed) and upper bound (optimum rotational speed).

Figure 5.28 and Figure 5.29, illustrate the output power matrix of each turbine in the bidirectional and vented OWC configurations respectively. The power extraction of the turbine has been evaluated in lower and upper bounds associated with its performance in constant and optimum rotational speed. The constant rotational speed differs for each turbine-OWC configuration and was decided regarding the peak power extracted at the fixed RPM sets illustrated in Figure 5.26. The upper bound shows the ideal system performance when the optimum rotational speed is set, and the turbine's peak efficiency is maintained over each incident wave. The peak mean efficiency of each turbine when employed in vented or bidirectional OWC was determined in Table 5-4. These values were used instead of $\overline{\eta}_{system}$ in the equation 5.19 to calculate the ideal power extraction by each turbine-OWC configuration. It should be noted that a simplified analysis has been performed considering the turbine control scheme of this study, where the turbine speed has been changed in every wave and the portion of the incoming power required to accelerate the turbine has been disregarded. Therefore, in an ideal case the real turbine performance lies between the two bounds of the extracted power.

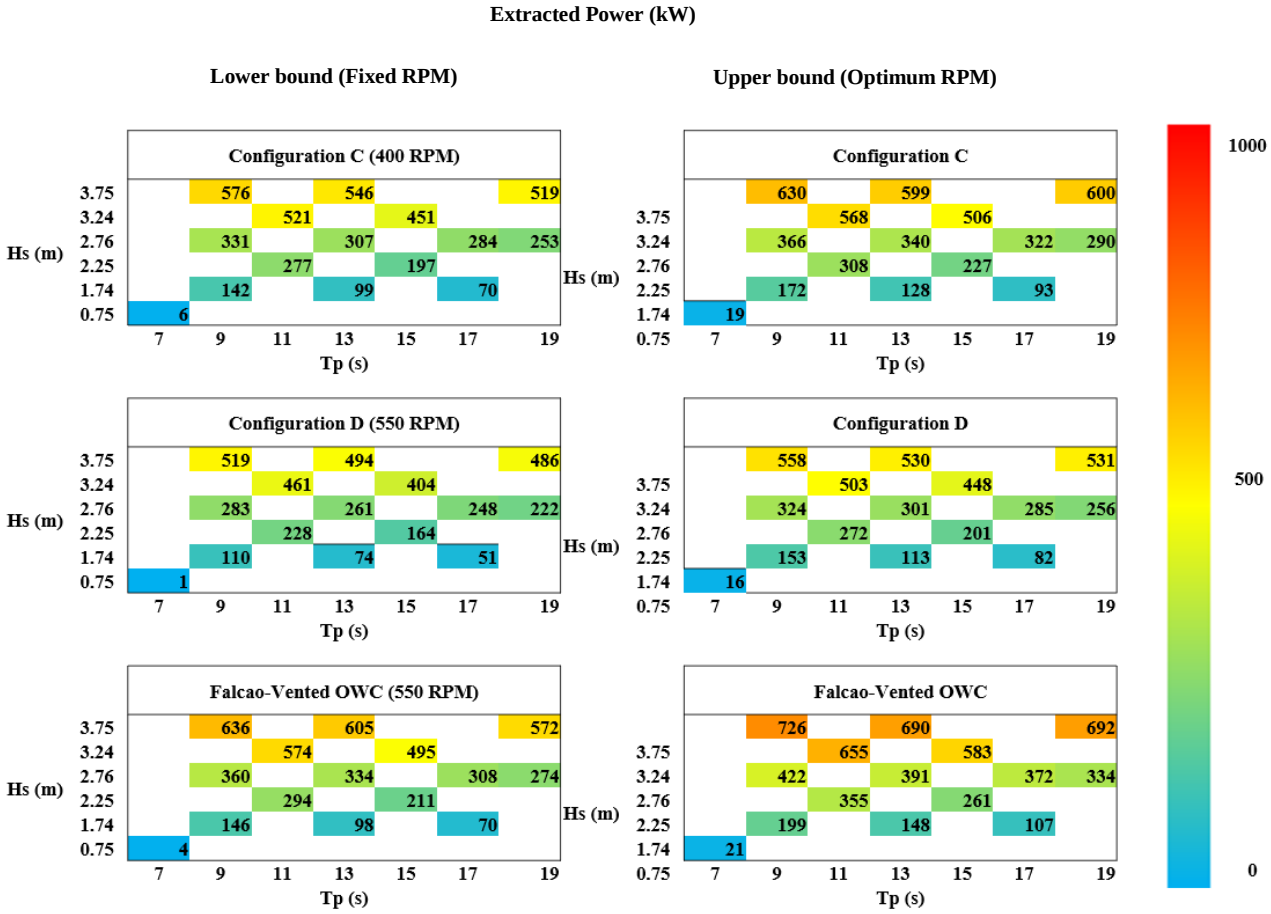

Figure 5.29 Extracted power matrix of turbines in a vented OWC configuration with lower bound (constant rotational speed) and upper bound (optimum rotational speed).

By comparing the bounds of the extracted power (in Figure 5.28 and Figure 5.29), it can be concluded that a power harvesting increase can be obtained by speed control of the Falcao turbine, where the maximum output power has improved by 90 to 100 kW by optimising the rotational speed in both systems. The outflow turbine has a lower dependency on the RPM control compared to other turbines. Where optimising the rotational speed of this turbine leads to only 40 kW and 15 kW improvements of the maximum power in vented and bidirectional OWC systems respectively. This happening can also reveal that the optimum RPM of the outflow turbine can be a value very close to 325 RPM. The inflow turbine operates more efficiently than the outflow turbine in a vented OWC, where there is a single turbine working in the system and the negative effects of the reversed turbine are eliminated. The inflow turbine extracts comparable power to that of the Falcao turbine in the vented OWC, with 60 kW and 96 kW less maximum power in fixed and optimum RPM situations respectively. There is a noticeable difference between the performance of the inflow and outflow turbines in a vented and bidirectional OWC. This can be explained by the design purpose of these geometries which was based on efficiency maximization in a single direction of the flow. The low

input efficiency, $\overline{\eta}_{input}$, of these turbines in a twin-turbine configuration is the main reason for their unacceptable performance in a bidirectional OWC. This is because about one third of the flow rate escapes the system through the reverse turbine and does not contribute in power extraction, while it causes negative torque.

5.9 Conclusions

Two unidirectional radial turbines were evaluated in single and twin-turbine configurations with vented and bidirectional OWCs, respectively. These turbines were investigated regarding their efficiency in steady state and their operation under irregular waves of King Island test site (Fleming et al., 2017) in Tasmania.

The inflow turbine is more noticeably affected by the backflow and negative torque when used in a twin-turbine configuration. This can be explained by the fact that the outflow turbine, due to having a centrifugal configuration, shows better performance during the reverse mode than the inflow turbine with a centripetal configuration. However, for a vented OWC system, replacing the second turbine with a one-way valve is a preferred option. Compared to the outflow configuration, the inflow turbine yielded better performance for a vented-OWC system and obtained comparable power to a bidirectional-turbine-OWC system fitted with a state-of-the-art twin-turbine. However, the outflow turbine offers interesting features such as smaller size in full scale, higher backflow prevention and less sensitivity to RPM variations. In addition, this turbine showed a lower difference between the ideal and the extracted power at a fixed rotational speed. Regarding the afore-mentioned advantages, more improvements on the peak efficiency of this turbine in steady state can lead to higher performance of the outflow turbine in a vented OWC.

Comparison of the vented and bidirectional OWCs revealed that the pneumatic power provided to the PTO in both OWC configurations is almost equivalent. The vented OWC can be regarded as a simpler and more economical design, as it extracts comparable ideal power to the conventional OWC, but with using a single turbine. However, the scope remains for future investigations of the valves in a vented OWC concept regarding their energy loss and maintenance.

Acknowledgement

The comparative tests of the conventional and vented OWCs were performed at the Model Test Basin (MTB) of the Australian Maritime College (AMC). We specially thank Mr. Jarrah Orphin and Mr. Damon Howe for performing the tests and providing the experimental data of this analysis and the WSE company for providing the OWC model.

6 SUMMARY AND CONCLUSIONS

In this thesis, numerical simulations were employed to investigate airflow behaviour through the entire sections of a radial turbine and steps were taken to customize the turbine design for the typical operation of a vented oscillating water column. A 3D model of the turbine plus the elbow and duct sections were created and used in the studies. The efficiency of the turbine was evaluated as the main factor for improvement over the whole steps of the research.

In chapter 2 of this research, the flow distribution in a centripetal turbine (inward flow direction in the radial turbine domain) was analysed and energy losses in rotating and stationary sections were evaluated. It was found that a significant energy loss occurs in the elbow and entrance to the duct section in the inward flow direction. In fact, the variation of the radius from inlet to the outlet leads to reduction of the flow passage from upstream to downstream of the centripetal turbine configuration. As a result, it was found that use of guide vanes at the rotor downstream of the centripetal radial turbine is necessary, however scope remained for design optimisation of the downstream section in the inward flow radial turbine.

In chapter 3, design optimisation techniques were used to improve the efficiency of the centripetal radial turbine. Parametric geometries of rotor blades, downstream guide vanes and the duct were created by allowing variations of a list of geometrical parameters in each section. Response surface optimisation algorithms were used to evaluate the impact of these parameters on the turbine performance. The downstream guide vanes were maintained in the turbine design by a change of application. In contrast to conventional bidirectional turbines, this row of vanes was not provided to guide the flow in the reverse direction, but to reduce the swirl flow at the rotor downstream under direct flow. Therefore, downstream guide vanes were employed to direct flow into the duct section over the inward flow condition, while causing more impendence during the opposite direction. The optimised inflow turbine was found to have highly asymmetric and non-zero staggered rotor blades with significant torque production. Parameters such as setting angle of the rotor blades, angle of upstream guide vanes, trailing edge (TE) and stagger angle of the rotor blades were found to have the highest contribution to the efficiency and torque improvement of the inflow radial turbine.

The duct section is the linking element between the turbine and the OWC chamber and plays a significant role in the integration of the PTO and OWC. Damping coefficient and pressure losses were investigated in design optimisation of the downstream section. It was concluded that use of a diffuser with 7 degrees diffusion angle leads to recovery of the kinetic energy at the turbine exit and improves the total efficiency of the turbine by over 10 percent. The optimised centripetal radial turbine, also

called inflow turbine, obtained a peak efficiency of 80 percent, which was a significant improvement of this turbine category.

As an alternative, in chapter 4 design of a centrifugal turbine configuration was investigated for operation over the outward flow direction. This turbine geometry is called outflow turbine, and its efficiency maximization was studied by employing the design optimisation methods. The efficiency of the outflow turbine was significantly affected by the leading edge (LE) angle of rotor blades. Similar to the inflow turbine, setting angle of upstream guide vanes and trailing edge (TE) angle of rotor blades were the other highly effective parameters. In this chapter, the optimised inflow and outflow turbines were compared regarding their energy transfer terms through the rotor. It was found that increase of radius from inlet to outlet of the outflow rotor causes a negative centrifugal energy transfer, however the change of dynamic pressure across the rotor is more significant in the outflow turbine. Thus, the total pressure change across the outflow turbine is comparable to that of the inflow turbine.

The inflow and outflow turbines were further compared regarding their operation in a vented-OWC and a twin-turbine-OWC wave energy converter in chapter 5. It was found that the inflow turbine, despite higher peak steady-state efficiency than the outflow turbine (80% versus 72%), is more affected by the windage losses and negative torque when used in a twin-turbine configuration. The better performance of the outflow turbine in a twin-turbine OWC concept was due to the direction of flow in this configuration, which naturally causes more flow resistance in the reverse mode. However, in the vented-OWC wave energy converter, the inflow turbine showed a better performance than the outflow turbine, which was comparable to the performance of a recent high-efficient twin-rotor turbine in the field. This was due to use of one-way valves to rectify the flow in the vented-OWC system, which reduced the negative effects of reverse mode and provided more capacity for the turbine to operate in the direct mode.

Performance of both turbines was compared in unsteady conditions using extrapolated experimental data of irregular waves corresponding to a King Island test site. Effects of variations of the rotational speed on power extraction of each turbine were investigated under various irregular wave conditions. The sensitivity of power conversion to RPM variations was evaluated considering a lower and upper bound for the power extraction:

- In a fixed RPM, corresponding to maximum output power in all irregular wave conditions.
- In an optimum RPM, assuming a control scheme is used to maintain peak efficiency over the entire pressure domain.

The real power extraction of the turbine was considered to fall within the bounds specified above. It was found that the difference between these power extraction bounds was lower in case of the

outflow turbine, which shows the turbine is less sensitive to RPM variations than the inflow turbine. In addition, due to its lower resistance to the flow in direct mode, the outflow turbine has a smaller full-scale size than the inflow turbine when employed with a similar OWC. It was also concluded that limiting air flow to a single direction and using a single unidirectional turbine (in the vented OWC configuration) can be regarded as a simpler and more economical design, with comparable power extraction to the conventional OWCs.

In summary, all chapters of this thesis were designed in a way to illustrate the journey of this research in answering the research questions. The chapter 2 was presented to introduce potential flexibilities in the turbine design when limiting energy capture to a single flow direction (inward flow). This chapter created a background for design improvement of the downstream section in a centripetal radial turbine configuration. Chapters 3 and 4 were presented to answer the research questions 1 and 2. In which, the flow characteristics were investigated in the inward and outward flow directions, respectively. Comparing the performance characteristics and the energy transfer terms in both inflow and outflow turbines indicates how the overall performance of the turbine-OWC system is affected by the direction of the flow in the radial turbine domain. The chapter 5 was presented in answering the research questions 1 and 3, in which, the inflow and outflow turbines were configured with vented and bidirectional OWCs and their power extraction was compared to a high-efficient twin-rotor turbine used in a bidirectional OWC configuration. Finally, the main conclusions of this study are given in the form of bullet points:

- Using guide vanes at the rotor exit of the inflow turbine is necessary to improve the transition of the flow from elbow to the duct section. In addition to that, in OWCs the turbine is constantly operating away from the ‘design point’ so the downstream guide vanes are an important inclusion for a radial inflow turbine.
- The setting angle of the rotor blades, angle of upstream guide vanes, trailing edge (TE) and stagger angle of the blades have the highest contribution to the efficiency and torque improvement of the inflow radial turbine.
- Using a diffuser with 7 degrees diffusion angle leads to recovery of the kinetic energy at the turbine exit and improves the total efficiency of the inflow turbine by over 10 percent.
- The leading edge (LE) angle, trailing edge (TE) angle and setting angle of the upstream guide vanes are the most effective parameters on efficiency variations of the outflow turbine.
- The outflow turbine due to its axial-radial flow transition has a negative centrifugal energy transfer term, nevertheless its total pressure change is still comparable to that of the inflow turbine.

- In a twin-turbine configuration, the windage losses and negative torque have more impacts on the inflow turbine compared to the outflow turbine.
- The outflow turbine is less sensitive to RPM variations than the inflow turbine.
- The outflow turbine, due to its lower resistance to the flow in direct mode, has a smaller full-scale size than the inflow turbine when employed with a similar OWC.
- The inflow turbine embedded in the vented OWC offers a simpler and more economical design, yet comparable power extraction to the conventional turbine-OWC configurations.

7 FURTHER WORK

The list of input parameters defined in the optimisation study of this research had a direct impact on the optimised geometry obtained for the turbines. In case of the outflow turbine, there is still scope for further efficiency improvements by considering additional parameters that affect blade to blade area and air velocity through the rotor. Parameters such as number of rotor blades and solidity are suggested to be considered in future optimisation studies of the outflow rotor.

The focus of this numerical study was on design modification of the PTO unit and only turbine, elbow and duct sections were modelled in the computational domain. However, considering the whole turbine-chamber configuration in the CFD simulations can lead to a more comprehensive analysis, including both model and full-scale operations. Air compressibility is a factor that affects the performance of the OWC chamber in full scale (Elhanafi et al., 2017). Analysing the air compressibility effects on the pneumatic power and chamber pressure drop in full-scale, and evaluating the corresponding turbine operation and wave-to-wire efficiency of the OWC can be a subject for further investigation. However, this matter requires a large computational domain consisting of turbine and the chamber, and computational resources to precisely model their interaction.

In addition, the OWC experimental data used in the analysis of chapter 5, were obtained by using an orifice to simulate the turbine behaviour. However, this assumption applies some limitations to the analysis as in the reality the orifice lacks to fully mimic the turbine's behaviour. The 3D models of the inflow and outflow turbine designs suggested by this research can be created and tested with the OWC model for a more accurate analysis of the turbine effects on the OWC damping.

There are other types of turbines that can be custom-designed for operation with a vented OWC. Axial unidirectional turbines and impeller-shaped turbines can be used as alternative reference geometries in optimisation studies and their performance can be compared with the inflow and outflow turbines of this research.

BIBLIOGRAPHY

A. FALCAO, L.M.C GATO, J.C .HENRIQUES & PEREIRAS, B. 2015. A novel twin-rotor air turbine for bidirectional flows in wave energy conversion. 11th European Wave and Tidal Energy Conference 6-11th Sept 2015, Nantes, France.

A. THAKKER, P. FRAWLEY, H.B. KHALEEQ, Y. ABUGIHALIA & T. SETOGUCHI 2001. Experimental and CFD Analysis of 0.6m Impulse Turbine with Fixed Guide Vanes. international Offshore and Polar Engineering Conference Stavanger, Norway.

AMOUZGAR K., C. M., SALOMONSSON K. 2015. Multi-objective optimization of material model parameters of an adhesive layer by using SPEA2. In 11 th World Congress of Structural and Multidisciplinary Optimization (WCSMO-11), 249–254.

ANSARIFARD, N., FLEMING, A., HENDERSON, A., KIANEJAD, S. & CHAI, S. Optimization Study on the Downstream Section of a Radial Inflow Turbine. The 4th Asian Wave and Tidal Energy Conference (AWTEC), 2018. 1-11.

ANSARIFARD, N., KIANEJAD, S., FLEMING, A. & CHAI, S. 2019. A radial inflow air turbine design for a vented oscillating water column. Energy, 166, 380-391.

ANSARIFARD, N., FLEMING, A., HENDERSON, A., KIANEJAD, S. & CHAI, S. 2019a. Design Optimisation of a Unidirectional Centrifugal Radial-Air-Turbine for Application in OWC Wave Energy Converters. Energies, 12(14).

ANSARIFARD, N., FLEMING, A., HENDERSON, A., KIANEJAD, S., CHAI, S. & ORPHIN, J. 2019b. Comparison of inflow and outflow radial air turbines in vented and bidirectional OWC wave energy converters. Energy.

ANSYS-USER'S-MANUAL 11.0, ANSYS,User's-Manual. Inc.

AUNGIER, R. Turbine aerodynamics: axial-flow and radial-inflow turbine design and analysis. 2006. ASME Press.

BADHURSHAH, R. & SAMAD, A. 2015a. Multiple surrogate based optimization of a bidirectional impulse turbine for wave energy conversion. Renewable Energy, 74, 749-760.

BADHURSHAH, R. & SAMAD, A. 2015b. Multiple surrogate based optimization of a bidirectional impulse turbine for wave energy conversion. Renewable Energy, 74, 749-760.

BALJE, O. 1981. Turbomachines-A guide to design, selection, and theory, John Wiley & Sons.

BENREGUIG, P., MURPHY, J. & SHENG, W. Model Scale Testing of the Tupperwave Device With Comparison to a Conventional OWC. ASME 2018 37th International Conference on Ocean, Offshore and Arctic Engineering, 2018. American Society of Mechanical Engineers, V010T09A048-V010T09A048.

BULL, D. & OCHS, M. E. 2013. Technological Cost-Reduction Pathways for Oscillating Water Column Wave Energy Converters in the Marine Hydrokinetic Environment. SAND2013-7205.

CALLAGHAN, J. & BOUD, R. 2006. Future Marine Energy. Results of the Marine Energy Challenge: Cost competitiveness and growth of wave and tidal stream energy. Carbon Trust.

CRUZ, J. 2007. Ocean wave energy: current status and future prespectives, Springer Science & Business Media.

CUI, Y. & HYUN, B.-S. 2016. Numerical study on Wells turbine with penetrating blade tip treatments for wave energy conversion. International Journal of Naval Architecture and Ocean Engineering, 8, 456-465.

DARABI, A. & PORIAVALI, P. Guide vanes effect of Wells turbine on OWC wave power plant operation. World Congress of Engineering, 2007.

DE O FALCÃO, A. 2002. Control of an oscillating-water-column wave power plant for maximum energy production. Applied Ocean Research, 24, 73-82.

DIXON, S. L. & HALL, C. 2013. Fluid mechanics and thermodynamics of turbomachinery, Butterworth-Heinemann.

DREW, B., PLUMMER, A. R. & SAHINKAYA, M. N. 2009. A review of wave energy converter technology. Sage Publications Sage UK: London, England.

DUDHGAONKAR, P. V., JAYASHANKAR, V., JALIHAL, P., KEDARNATH, S., SETOGUCHI, T., TAKAO, M., NAGATA, S. & TOYOTA, K. Fluidic components for oscillating water column based wave energy plants. ASME-JSME-KSME 2011 Joint Fluids Engineering Conference, 2011. American Society of Mechanical Engineers, 1979-1983.

DURGUDE, A., VIPRADAS, A., KISHORE, S. & NIMSE, S. 2016. DESIGN OPTIMIZATION OF BRAKE DISC GEOMETRY.

EL MARJANI, A., RUIZ, F. C., RODRIGUEZ, M. & SANTOS, M. P. 2008. Numerical modelling in wave energy conversion systems. Energy, 33, 1246-1253.

ELHANAFI, A., MACFARLANE, G., FLEMING, A. & LEONG, Z. 2017. Scaling and air compressibility effects on a three-dimensional offshore stationary OWC wave energy converter. Applied energy, 189, 1-20.

ENERGY, A. 2005. Oscillating water column wave energy converter evaluation report. The Carbon Trust, Marine Energy Challenge.

EVANS, D. 1982. Wave-power absorption by systems of oscillating surface pressure distributions. Journal of Fluid Mechanics, 114, 481-499.

FADAEENEJAD, M., SHAMSIPOUR, R., ROKNI, S. & GOMES, C. 2014. New approaches in harnessing wave energy: With special attention to small islands. Renewable and Sustainable Energy Reviews, 29, 345-354.

FALCÃO, A. F., GATO, L. M., HENRIQUES, J. C., BORGES, J. E., PEREIRAS, B. & CASTRO, F. 2015. A novel twin-rotor radial-inflow air turbine for oscillating-water-column wave energy converters. Energy, 93, 2116-2125.

FALCÃO, A. F. & HENRIQUES, J. C. 2014. Model-prototype similarity of oscillating-water-column wave energy converters. International Journal of Marine Energy, 6, 18-34.

FALCÃO, A. F. & HENRIQUES, J. C. 2016a. Oscillating-water-column wave energy converters and air turbines: A review. Renewable Energy, 85, 1391-1424.

FALCÃO, A. F., HENRIQUES, J. C. & GATO, L. M. 2018. Self-rectifying air turbines for wave energy conversion: a comparative analysis. Renewable and Sustainable Energy Reviews, 91, 1231-1241.

FALCÃO, A. F. D. O. 2010. Wave energy utilization: A review of the technologies. Renewable and Sustainable Energy Reviews, 14, 899-918.

FALCÃO, A. F. O. & GATO, L. M. C. 2012. Air Turbines. 111-149.

FALCÃO, A. F. O. & HENRIQUES, J. C. C. 2016b. Oscillating-water-column wave energy converters and air turbines: A review. Renewable Energy, 85, 1391-1424.

FALNES, J. 2002. Ocean waves and oscillating systems: linear interactions including wave-energy extraction, Cambridge university press.

FLEMING, A., MACFARLANE, G., HUNTER, S. & DENNISS, T. Power performance prediction for a vented oscillating water column wave energy converter with a unidirectional air turbine power take-off. The 12th European Wave and Tidal Energy Conference (EWTEC), 2017. 1-7.

FRID, C., ANDONEGI, E., DEPESTELE, J., JUDD, A., RIHAN, D., ROGERS, S. I. & KENCHINGTON, E. 2012. The environmental interactions of tidal and wave energy generation devices. Environmental Impact Assessment Review, 32, 133-139.

GHOTLI, R. A., AZIZ, A. A., IBRAHIM, S., BAROUTIAN, S. & ARAMI-NIYA, A. 2013. Study of various curved-blade impeller geometries on power consumption in stirred vessel using response surface methodology. Journal of the Taiwan Institute of Chemical Engineers, 44, 192-201.

GOMES, R., HENRIQUES, J., GATO, L. & FALCÃO, A. 2012. Multi-point aerodynamic optimization of the rotor blade sections of an axial-flow impulse air turbine for wave energy conversion. Energy, 45, 570-580.

GUIDE, A. F. U. 2011. Release 14.0, ANSYS. Inc., USA, November.

GUIDE, A. U. M. 2017. Release 17.0, ANSYS. Inc., USA, November.

HALDER, P., RHEE, S. H. & SAMAD, A. 2017. Numerical optimization of Wells turbine for wave energy extraction. International Journal of Naval Architecture and Ocean Engineering, 9, 11-24.

HALDER, P., SAMAD, A., KIM, J.-H. & CHOI, Y.-S. 2015. High performance ocean energy harvesting turbine design–A new casing treatment scheme. Energy, 86, 219-231.

HALL, C. & DIXON, S. L. 2013. Fluid mechanics and thermodynamics of turbomachinery, Butterworth-Heinemann.

HANS, E. 1966. Energy transfer machine. Google Patents.

HARRIS, R. E., JOHANNING, L. & WOLFRAM, J. 2004. Mooring systems for wave energy converters: A review of design issues and choices. Marec2004.

HATAMI, M., CUIJPERS, M. & BOOT, M. 2015. Experimental optimization of the vanes geometry for a variable geometry turbocharger (VGT) using a Design of Experiment (DoE) approach. Energy conversion and management, 106, 1057-1070.

HEATH, T. 2012a. A review of oscillating water columns. Phil. Trans. R. Soc. A, 370, 235-245.

HEATH, T. V. 2012b. A review of oscillating water columns. Philos Trans A Math Phys Eng Sci, 370, 235-45.

HEMER, M. & GRIFFIN, D. 2010. The wave energy resource along Australia's southern margin. Journal of Renewable and Sustainable Energy, 2, 043108.

HENRIQUES, J. C. C., GOMES, R. P. F., GATO, L. M. C., FALCÃO, A. F. O., ROBLES, E. & CEBALLOS, S. 2016. Testing and control of a power take-off system for an oscillating-water-column wave energy converter. Renewable Energy, 85, 714-724.

HOLMES, B. 2009. Tank testing of wave energy conversion systems: marine renewable energy guides, European Marine Energy Centre.

HOWELL, A. 1967. Axial Flow Turbines. JH Horlock. Butterworths, London. 1966. 275 pp. Diagrams. 97s. 6d. The Aeronautical Journal, 71, 57-58.

INIOUE, M., KANEKO, K. & SETOGUCHI, T. 2000. One-dimensional analysis of impulse turbine with self-pitch-controlled guide vanes for wave power conversion. International Journal of Rotating Machinery, 6, 151-157.

INOUE, M., KANEKO, K., SETOGUCHI, T. & RAGHUNATHAN, S. Simulation of starting characteristics of the Wells turbine. 4th Joint Fluid Mechanics, Plasma Dynamics and Lasers Conference, 1986. 1122.

JAYASHANKAR, V., ANAND, S., GEETHA, T., SANTHAKUMAR, S., JAGADEESH KUMAR, V., RAVINDRAN, M., SETOGUCHI, T., TAKAO, M., TOYOTA, K. & NAGATA, S. 2009a. A twin unidirectional impulse turbine topology for OWC based wave energy plants. Renewable Energy, 34, 692-698.

JAYASHANKAR, V., ANAND, S., GEETHA, T., SANTHAKUMAR, S., KUMAR, V. J., RAVINDRAN, M., SETOGUCHI, T., TAKAO, M., TOYOTA, K. & NAGATA, S. 2009b. A twin unidirectional impulse turbine topology for OWC based wave energy plants. Renewable Energy, 34, 692-698.

JUNG, U.-H., KIM, J.-H., KIM, J.-H., PARK, C.-H., JUN, S.-O. & CHOI, Y.-S. 2016. Optimum design of diffuser in a small high-speed centrifugal fan using CFD & DOE. Journal of Mechanical Science and Technology, 30, 1171-1184.

KIANEJAD, S., ENSHAEI, H., DUFFY, J. & ANSARIFARD, N. 2019. Prediction of a ship roll added mass moment of inertia using numerical simulation. Ocean Engineering, 173, 77-89.

KIM, T., SETOGUCHI, T., KANEKO, K. & TAKAO, M. 2001. The optimization of blade pitch settings of an air turbine using self-pitch-controlled blades for wave power conversion. Journal of solar energy engineering, 123, 382-386.

LIU, H., XU, K.,ZHU, T.,YE, W., 2012. Multiple temperature kinetic model and its applications to micro-scale gas flows. Computers & Fluids, 67, 115-122.

LIU, Z., CUI, Y., KIM, K. W. & SHI, H. D. 2016. Numerical study on a modified impulse turbine for OWC wave energy conversion. Ocean Engineering, 111, 533-542.

LIU, Z., CUI, Y., LI, M. & SHI, H. 2017. Steady state performance of an axial impulse turbine for oscillating water column wave energy converters. Energy, 141, 1-10.

LIU, Z., CUI, Y., XU, C., SHI, H. & KIM, K. 2018. Transient simulation of OWC impulse turbine based on fully passive flow-driving model. Renewable Energy, 117, 459-473.

LOGAN JR, E. 2013. Turbomachinery: basic theory and applications, CRC Press.

LOPES, B. S., GATO, L. M., FALCÃO, A. F. & HENRIQUES, J. C. 2019. Test results of a novel twin-rotor radial inflow self-rectifying air turbine for OWC wave energy converters. Energy, 170, 869-879.

LÓPEZ, I., PEREIRAS, B., CASTRO, F. & IGLESIAS, G. 2016. Holistic performance analysis and turbine-induced damping for an OWC wave energy converter. Renewable Energy, 85, 1155-1163.

MAEDA, H., SANTHAKUMAR, S., SETOGUCHI, T., TAKAO, M., KINOUE, Y. & KANEKO, K. 1999. Performance of an impulse turbine with fixed guide vanes for wave power conversion. Renewable Energy, 17, 533-547.

MALA, K., JAYARAJ, J., JAYASHANKAR, V., MURUGANANDAM, T., SANTHAKUMAR, S., RAVINDRAN, M., TAKAO, M., SETOGUCHI, T., TOYOTA, K. & NAGATA, S. 2011a. A twin unidirectional impulse turbine topology for OWC based wave energy plants–Experimental validation and scaling. Renewable energy, 36, 307-314.

MALA, K., JAYARAJ, J., JAYASHANKAR, V., MURUGANANDAM, T. M., SANTHAKUMAR, S., RAVINDRAN, M., TAKAO, M., SETOGUCHI, T., TOYOTA, K. & NAGATA, S. 2011b. A twin unidirectional impulse turbine topology for OWC based wave energy plants – Experimental validation and scaling. Renewable Energy, 36, 307-314.

MANASSEH, R., MCINNES, K. L. & HEMER, M. A. 2017. Pioneering developments of marine renewable energy in Australia. The International Journal of Ocean and Climate Systems, 8, 50-67.

MASUDA, Y. 1986. An experience of wave power generator through tests and improvement. Hydrodynamics of ocean wave-energy utilization. Springer.

MOHAMED, M., JANIGA, G., PAP, E. & THÉVENIN, D. 2011. Multi-objective optimization of the airfoil shape of Wells turbine used for wave energy conversion. Energy, 36, 438-446.

MOHAMED, M. H. & SHAABAN, S. 2014. Numerical optimization of axial turbine with self-pitch-controlled blades used for wave energy conversion. International Journal of Energy Research, 38, 592-601.

NANCARROW, J., EGLI, H. & BURDETTE, F. 1974. Energy transfer machine. Google Patents.

O'SULLIVAN, D. L., LEWIS & W, A. 2011. Generator selection and comparative performance in offshore oscillating water column ocean wave energy converters. IEEE transactions on energy conversion, 26, 603-614.

OKUHARA, S., TAKAO, M., SATO, H., TAKAMI, A. & SETOGUCHI, T. 2014. A Twin Unidirectional Impulse Turbine for Wave Energy Conversion—Effect of Fluidic Diode on the Performance. Open Journal of Fluid Dynamics, 04, 433-439.

OKUHARA, S., TAKAO, M., TAKAMI, A. & SETOGUCHI, T. 2012. A Twin Unidirectional Impulse Turbine for Wave Energy Conversion. Open Journal of Fluid Dynamics, 02, 343-347.

PEREIRAS, B., CASTRO, F., EL MARJANI, A. & RODRÍGUEZ, M. A. 2011a. An improved radial impulse turbine for OWC. Renewable Energy, 36, 1477-1484.

PEREIRAS, B., CASTRO, F., EL MARJANI, A. & RODRÍGUEZ, M. A. 2011b. Tip clearance effect on the flow pattern of a radial impulse turbine for wave energy conversion. Journal of Turbomachinery, 133, 041019.

PEREIRAS, B., CASTRO, F., MARJANI, A. E. & RODRÍGUEZ, M. A. 2011c. An improved radial impulse turbine for OWC. Renewable Energy, 36, 1477-1484.

PEREIRAS, B., LÓPEZ, I., CASTRO, F. & IGLESIAS, G. 2015. Non-dimensional analysis for matching an impulse turbine to an OWC (oscillating water column) with an optimum energy transfer. Energy, 87, 481-489.

PEREIRAS, B., VALDEZ, P. & CASTRO, F. 2014. Numerical analysis of a unidirectional axial turbine for twin turbine configuration. Applied Ocean Research, 47, 1-8.

PEREIRAS, B., VALDEZ, P., CASTRO, F. & GARRIDO, J. C. CFD analysis of a unidirectional axial turbine for twin turbine topology in OWC plants. ASME 2013 32nd International Conference on Ocean, Offshore and Arctic Engineering, 2013. American Society of Mechanical Engineers, V008T09A020-V008T09A020.

PRITCHARD, L. An eleven parameter axial turbine airfoil geometry model. ASME 1985 International Gas Turbine Conference and Exhibit, 1985. American Society of Mechanical Engineers, V001T03A058-V001T03A058.

RAGHUNATHAN, S. 1995. The Wells air turbine for wave energy conversion. Progress in Aerospace Sciences, 31, 335-386.

RAGHUNATHAN, S., SETOGUCHI, T. & KANEKO, K. Aerodynamics of monoplane Wells turbine-a review. The First International Offshore and Polar Engineering Conference, 1991. International Society of Offshore and Polar Engineers.

RAGHUNATHAN, S. & TAN, C. 1982. Performance of the Wells turbine at starting. Journal of Energy, 6, 430-431.

RAGHUNATHAN, S. & TAN, C. 1985. Effect of blade profile on the performance of the Wells self-rectifying air turbine. International journal of heat and fluid flow, 6, 17-22.

RODRÍGUEZ, L., PEREIRAS, B., FERNÁNDEZ-ORO, J. & CASTRO, F. 2018. Viability of unidirectional radial turbines for twin-turbine configuration of OWC wave energy converters. Ocean Engineering, 154, 288-297.

RODRÍGUEZ, L., PEREIRAS, B., FERNÁNDEZ-ORO, J. & CASTRO, F. 2019. Optimization and experimental tests of a centrifugal turbine for an OWC device equipped with a twin turbines configuration. Energy, 171, 710-720.

SAMAD, A., KIM, K.-Y., GOEL, T., HAFTKA, R. T. & SHYY, W. 2008. Multiple surrogate modeling for axial compressor blade shape optimization. Journal of Propulsion and Power, 24, 302-310.

SETOGUCHI, T., SANTHAKUMAR, S., MAEDA, H., TAKAO, M. & KANEKO, K. 2001. A review of impulse turbines for wave energy conversion. Renewable energy, 23, 261-292.

SETOGUCHI, T., SANTHAKUMAR, S., TAKAO, M., KIM, T. H. & KANEKO, K. 2002. A performance study of a radial turbine for wave energy conversion. Proceedings of the Institution of Mechanical Engineers, Part A: Journal of Power and Energy, 216, 15-22.

SETOGUCHI, T. & TAKAO, M. State of art on self-rectifying air turbines for wave energy conversion. Proc 4th Int Conf on Mech Eng, 2001. 117-126.

SETOGUCHI, T. & TAKAO, M. 2006a. Current status of self rectifying air turbines for wave energy conversion. Energy conversion and management, 47, 2382-2396.

SETOGUCHI, T. & TAKAO, M. 2006b. Current status of self rectifying air turbines for wave energy conversion. Energy Conversion and Management, 47, 2382-2396.

SETOGUCHI, T., TAKAO, M., SANTHAKUMAR, S. & KANEKO, K. 2004. Study of an impulse turbine for wave power conversion: effects of Reynolds number and hub-to-tip ratio on performance. Journal of Offshore Mechanics and Arctic Engineering, 126, 137-140.

SHIH, T.-H., LIOU, W. W., SHABBIR, A., YANG, Z. & ZHU, J. 1995. A new k-ϵ eddy viscosity model for high reynolds number turbulent flows. Computers & Fluids, 24, 227-238.

STAR-CCM+ user guide. https://www.sharcnet.ca/help/index.php/STAR-CCM+.

TAKAO, M. & SETOGUCHI, T. 2012. Air Turbines for Wave Energy Conversion. International Journal of Rotating Machinery, 2012, 1-10.

TAKAO, M., SETOGUCHI, T., KANEKO, K., KIM, T., MAEDA, H. & INOUE, M. 2002. Impulse turbine for wave power conversion with air flow rectification system. International journal of offshore and polar engineering, 12.

TAKAO, M., TAKAMI, A., OKUHARA, S. & SETOGUCHI, T. 2011a. A twin unidirectional impulse turbine for wave energy conversion. Journal of Thermal Science, 20, 394.

TAKAO, M., TAKAMI, A., OKUHARA, S. & SETOGUCHI, T. 2011b. A twin unidirectional impulse turbine for wave energy conversion. Journal of Thermal Science, 20, 394-397.

TEASE, W., LEES, J. & HALL, A. Advances in oscillating water column air turbine development. Proc. of the Seventh European Wave and Tidal Energy Conference, Porto, Portugal, 2007.

THAKKER, A., JARVIS, J. & SAHED, A. 2009. Design charts for impulse turbine wave energy extraction using experimental data. Renewable Energy, 34, 2264-2270.

USERGUIDE, C. 2017. Available: https://www.caeses.com/ [Accessed].

UY, M. & TELFORD, J. K. Optimization by Design of Experiment techniques. Aerospace conference, 2009 IEEE, 2009. IEEE, 1-10.

WATERS, R. 2008. Energy from ocean waves: full scale experimental verification of a wave energy converter. Universitetsbiblioteket.

WIBERG, W. & ANTON, N. 2015. Aerodynamic design of a gas turbine rotor blade for the KTH test turbine.

YUSAF, T., GOH, S. & BORSERIO, J. 2011. Potential of renewable energy alternatives in Australia. Renewable and sustainable energy reviews, 15, 2214-2221.

ZHU, T. & YE, W. 2010. Theoretical and numerical studies of noncontinuum gas-phase heat conduction in micro/nano devices. Numerical Heat Transfer, Part B: Fundamentals, 57, 203-226.